UNIVERSITY OF SOUTHAMPTON

FACULTY OF SCIENCE

PHYSICS

THE CHARACTERISATION OF CLEAN AND OXIDISED TIN SINGLE CRYSTAL SURFACES

by

MARTIN EDWARD WOODS

A thesis submitted for the degree of Doctor of Philosophy

October 1983

To my parents, sisters and brother

UNIVERSITY OF SOUTHAMPTON

ABSTRACT

FACULTY OF SCIENCE

PHYSICS

Doctor of Philosophy

THE CHARACTERISATION OF CLEAN AND OXIDISED TIN SINGLE CRYSTAL SURFACES

by Martin Edward Woods

Auger electron spectroscopy, electron energy loss spectroscopy, and low energy electron diffraction, have been used to study the clean and oxidised Sn(001) and Sn(101) single crystal surfaces. The argon ion bombarded and annealed Sn(001) surface exhibited a terrace array with steps both up and down along the [01] and [10] directions of the surface net. The terraces consisted of bulk (001) planes, each of which was separated by a step of height 1.59Å. The argon ion bombarded Sn(101) surface exhibited a low energy electron diffraction pattern characteristic of a bulk (101) plane. Minor detail in the diffraction patterns of the (101) surface was attributed to the presence of steps. The Sn(101) surface structure observed in the present study differed from that of a previous study by Rider (1981).

Oxidation of the surfaces was carried out at 5×10^{-7} torr under a number of temperature conditions. Under most temperature conditions the oxygen uptake curves obtained from A.E.S. peak height measurements indicated the formation of a single chemisorbed oxide layer. The oxidised Sn(001) surface was amorphous over the temperature range 115K to 473K. The oxidised Sn(101) surface also formed an amorphous oxide below $\approx$ 383 - 393K. Above this temperature two main structures were observed: at sub-monolayer exposures ($\lesssim$ 1000L) a Sn (101) p 1 x 2 -O island structure was present; and at higher exposures (up to 30,000L) a Sn(101) c 7/8 x 4/5 -O structure with rotational disorder was formed. The electron energy loss spectra were characteristic of the Sn(II) oxide under all conditions. Auger shifts were noted on oxidation of Sn(001) at 135K. The main $M_{4,5}$ $N_{4,5}$ $N_{4,5}$ tin Auger peaks were shifted by 5eV to lower energies.

CONTENTS

CONTENTS PAGE

CONTENTS PAGE

CONTENTS

PAGE

LIST OF FIGURES PAGE

LIST OF FIGURES PAGE

LIST OF FIGURES PAGE

LIST OF FIGURES PAGE

LIST OF FIGURES PAGE

CHAPTER 1

INTRODUCTION

There have been many ultra-high vacuum and high vacuum studies of β-tin films and foils, and of polycrystalline tin oxides. In several cases these reports have given contradictory conclusions (e.g. for the identity and distribution of the oxides on oxidised tin films and foils; and the size of the tin Auger peak shifts of SnO and SnO_2 with respect to clean tin). Some of the results indicated that further studies under controlled experimental conditions were necessary, in particular there was a need for investigations on the well defined surfaces of single crystals. The initial oxidation of the (100), (101), and (110) single crystal surfaces of tin was investigated in this laboratory by G C Rider (1981) using electron diffraction and electron spectroscopic techniques. The present study extended the investigation to the (001) surface. The (101) surface was also re-examined as Rider's work indicated that the surface structure was altered during its preparation. The clean and oxidised surfaces have been studied at a number of temperatures, and wherever possible the experimental conditions have been kept identical to those of Rider.

There are a number of properties of tin and its oxides which make them interesting materials to study. Firstly, β-tin has a structure which is unique at atmospheric pressure. Metallic β-tin also undergoes a reversible phase change to the semi-metallic α-tin on cooling below 13.2°C. The use of tin as a protective coating in the prevention of corrosion leads to an interest in its oxidation characteristics.

A number of the oxide studies have also been initiated by the interest in stannic oxide (SnO_2) for use as optically transparent electrodes. A summary of the properties, and a review of the recent investigations on the surfaces of tin and its oxides has been given in chapter 2.

The techniques of Auger electron spectroscopy, electron energy loss spectroscopy, and low energy electron diffraction have been used in the present study. These techniques have been outlined in chapter 4, while the theoretical background to these techniques has been presented in chapter 3. Particular attention has been given to the L.E.E.D. kinematic theory relevant to the understanding of the stepped (001) surface. The A.E.S. and E.L.S. data have been presented separately to the L.E.E.D. data in chapter 5. Also included in this chapter are the uptake curves for the oxidation of the clean surfaces. The L.E.E.D. results from the clean and oxidised (001) and (101) surfaces are given in chapters 6 and 7 respectively. The extent to which a kinematic model predicts the L.E.E.D. patterns from the terraced (001) surface has also been considered in chapters 6 and 8. A discussion of the results obtained in the present study has been given in chapter 8, together with a summary of all the known structures at the clean and oxidised tin single crystal surfaces. Chapter 9 summarises and concludes the present study. Suggestions for further work have also been presented in this chapter.

CHAPTER 2

A REVIEW OF THE PROPERTIES OF TIN; AND RECENT SURFACE STUDIES

2.1 STRUCTURE OF TIN AND ITS OXIDES

There are two allotropes of tin. Above 13.2°C tin forms a body-centred tetragonal structure (fig. 2.1). This, the β-phase, has unit cell dimensions a = 5.83Å, c = 3.18Å (R W G Wyckoff, 1960), and is stable to the melting point of 231.9°C. Each atom is surrounded by a distorted tetrahedron of neighbours at a distance of 3.02Å, with two more in the c-direction at 3.17Å. The body-centred tetragonal structure is unique to β-tin at atmospheric pressure, and is only formed by germanium and silicon at high pressures (J C Jamieson, 1963).

Below 13.2°C tin exists in a second form, the α-phase, with the diamond structure (fig. 2.2) and a nearest neighbour separation of 2.80Å. The two phases are very close in energy, α-tin having an energy of ≈ 0.04 eV/atom lower than β-tin) (J. Ihm et al, 1981). The change from the body-centred tetragonal structure to the diamond structure leads to an increase in volume of 21% (E O Hall, 1956).

Tin forms two stable bulk oxides, both of which exist as tetragonal structures (figs. 2.3,4): these are stannous oxide (SnO) and stannic oxide (SnO_2).

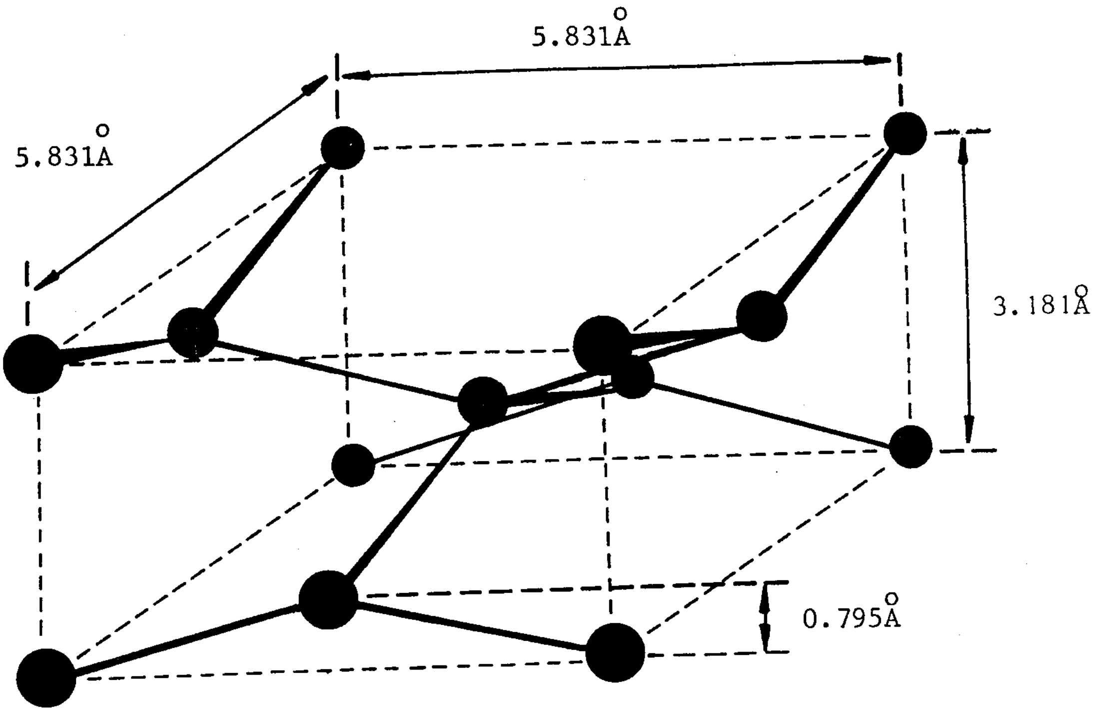

FIG. 2.1a The unit cell of β-Sn.

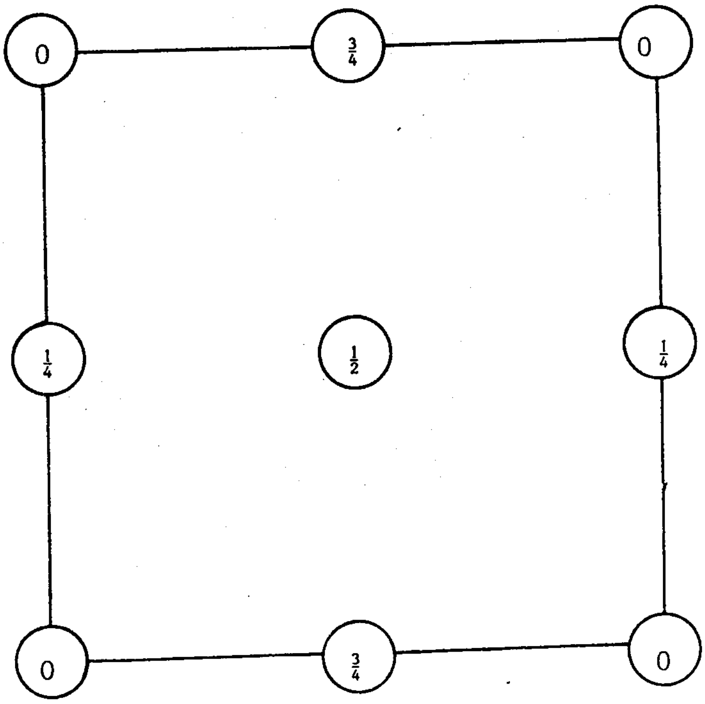

FIG. 2.1b The atomic arrangement within a unit cell of β-Sn projected on the (001) face.

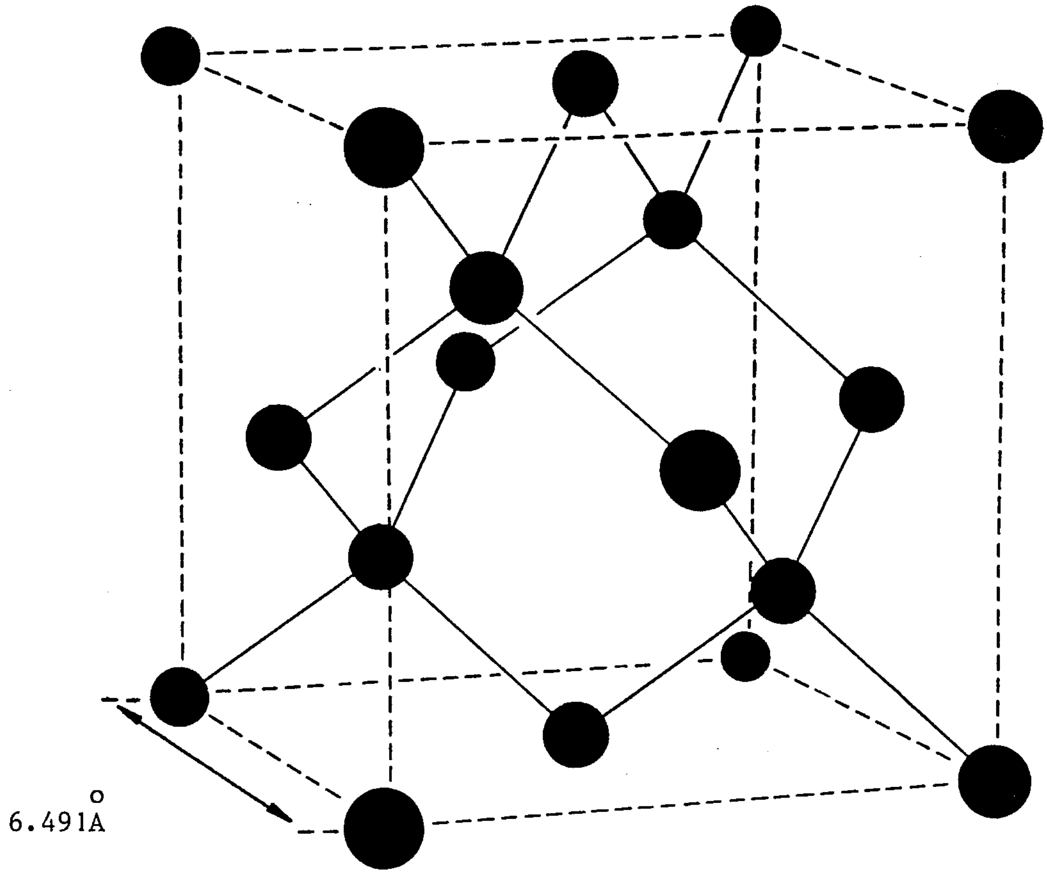

FIG. 2.2a Conventional cubic cell of α-Sn (Diamond Structure)

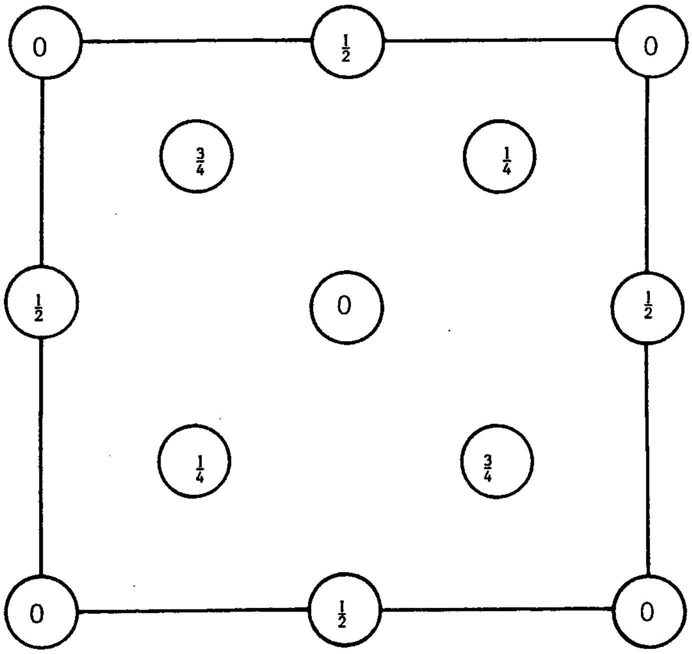

FIG. 2.2b The atomic positions in the cubic cell of α-Sn projected on a cube face.

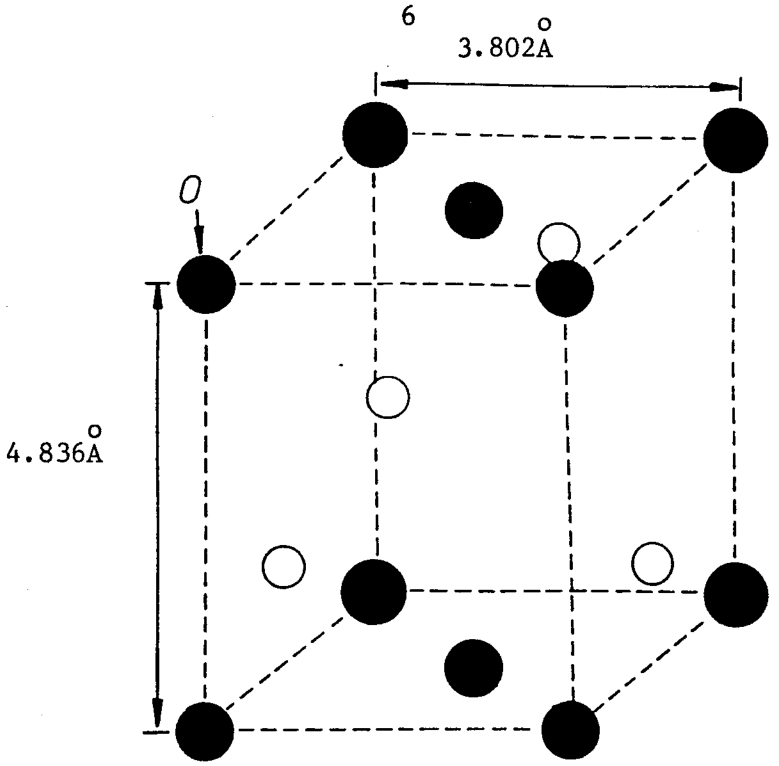

FIG. 2.3 Unit cell of tetragonal SnO

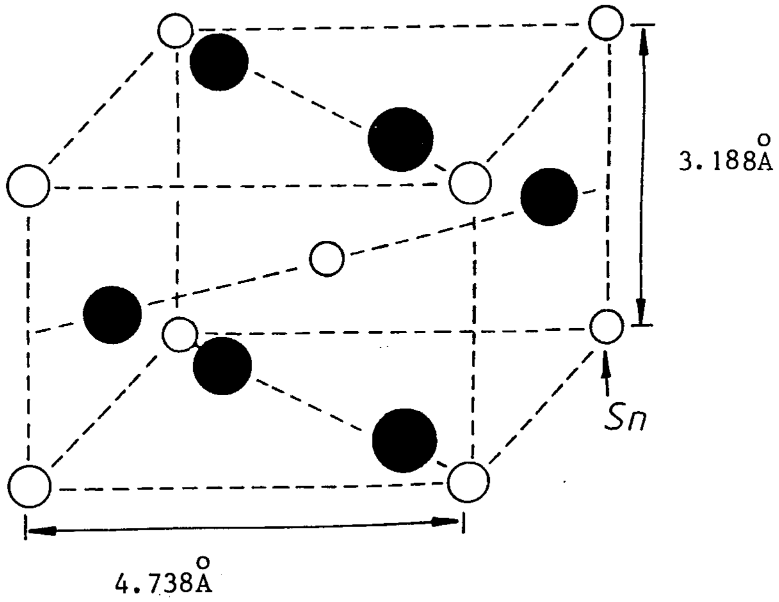

FIG. 2.4 Unit cell of tetragonal SnO_2

2.2 ELECTRONIC PROPERTIES

White tin is metallic. L S Darken et al (1953) determined the electronic configuration for white tin by using the Pauling model of the metallic bond as a resonating covalent bond. This model predicts that three quarters of the tin atoms have the configuration {Kr} $5s^2p^2$ and one quarter {Kr} $5s^1p^3$.

Band structure calculations have been carried out by G Weisz, 1966; J E Craven, 1969; and M.A.E.A. Ament et al, 1974 (fig. 2.5). Both Weisz and Craven used semi-empirical local pseudopotential models to determine the band structure and Fermi surface, but Craven made use of data from de Haas - van Alphen investigations, which was unavailable at the time of Weisz's calculation. Ament et al based their calculations on a relativistic augmented plane wave model.

Grey tin is a semi-metal. Its electronic configuration at OK is {Kr} $5s^1p^3$. A model for its band structure has been determined by S. Groves et al (1963) based on experimental data and previous theoretical calculations by F Herman (1955) and L Liu et al (1963). The gap between the main valence and conduction bands at $k = 0$ is zero (fig. 2.6), but there is an indirect band gap of $\approx$ 0.09eV between the upper valence band and a second conduction band. This small band gap has led to recent interest in the development of room-temperature stable α-Sn films (R F C Farrel et al, 1981) for application as long wavelength infra-red detectors.

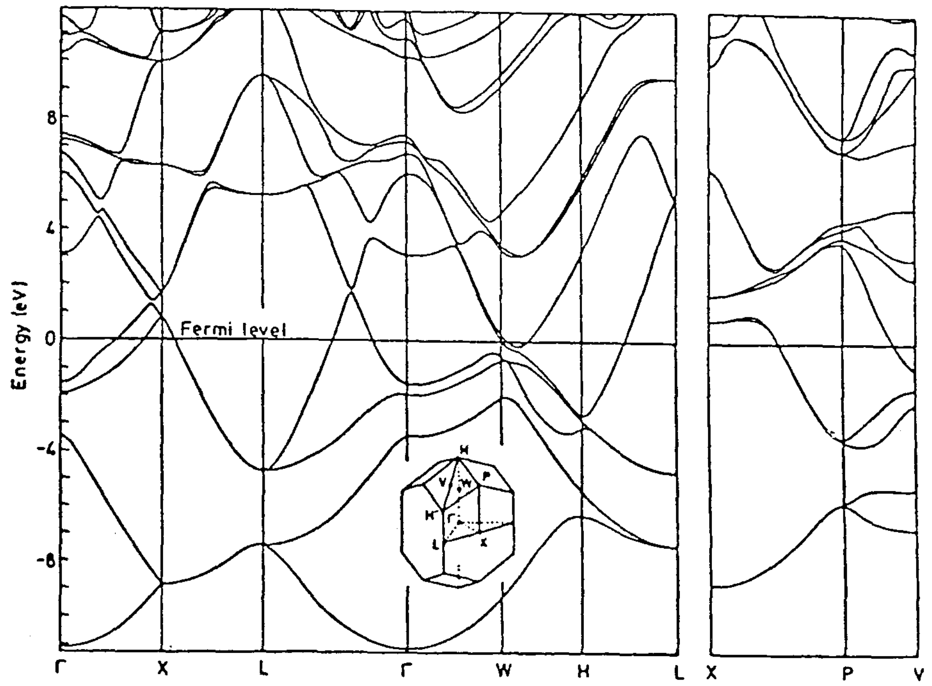

FIG. 2.5 Band structure of β-Sn (after M A E A Ament et al, 1974).

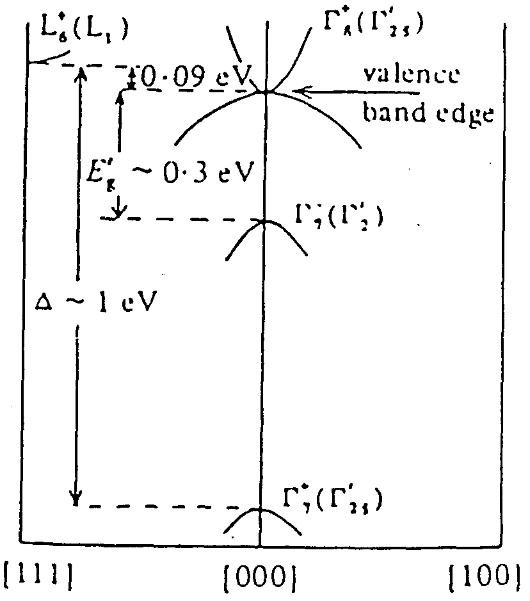

FIG. 2.6 Band structure model of α-Sn (after S Groves et al, 1963).

Pure stannic oxide (SnO_2) is an n-type wide band gap semiconductor with either ionized oxygen vacancies or interstitial tin ions acting as donors. Its good electrical conductivity and high optical transparency in the visible region of the electromagnetic spectrum has led to interest in its use (pure and doped) as electrodes in photovoltaic devices. A review of the physical properties and uses of stannic oxide has been published by Z M Jarzebski et al, 1976.

2.3 GENERAL SPECTROSCOPIC STUDIES

All of the u.h.v. studies on tin involving the Auger technique have referred to the $M_{4,5}\,N_{4,5}\,N_{4,5}$ transitions. The fine structure of these transitions has been assigned by A C Parry-Jones et al, 1979; and S M Barlow et al, 1979. A difference of 12.6 eV was measured by M Pessa et al (1979) in the $M_5\,N_{4,5}\,N_{4,5}$ $^1G_4$ line between the gas phase and the solid phase. The line width also broadened by 0.45 eV for the solid phase for the $M_{4,5}\,N_{4,5}\,N_{4,5}$ transitions. The major Auger transitions of tin foil and powdered SnO, SnO_2, have been summarised by S K Sen et al (1981). Previously unreported minor Auger peaks in the clean tin Auger spectra were presented by G C Rider (1981).

The characteristic electron energy loss features of tin have been studied by a number of authors (C J Powell, 1961; G Rasigni et al, 1966; G C Rider, 1981; R A Powell, 1979; R A Pollak et al, 1974; and P Bayat-Mokhtari et al, 1979) under high vacuum and ultra-high vacuum conditions.

Losses at $\approx$ 10eV and 14eV were identified as surface and bulk plasmon losses respectively. Multiples of these were also observed. At low primary electron beam energies a loss of $\approx$ 3-5 eV was attributed to an interband transition by G Rasigni et al, and Macrae et al (labelled as $\Gamma_5^+ - \Gamma_4^-$) whereas A J Bevolo et al labelled it an intraband transition.

Electron energy loss spectra of oxidised tin have been presented by P Bayat-Mokhtari (1979), A J Bevolo(1982), G C Rider (1981), and R A Powell (1979). Characteristic spectra from SnO and SnO_2 have been published by R A Powell and A J Bevolo. Bevelo's spectra were in the first order differential form (figs. 2.7-9) as were those of the present study with which they were compared. Bevolo noted that the main difference between the spectra of SnO and SnO_2 was a feature at 55eV in the SnO_2 spectrum (representing a 17eV loss) which was not present in the SnO spectrum. Powell did not identify any of the losses in his bulk oxide spectra, and Bevolo only noted the 4d tin interband transition which was found to shift by 1.8 ± 0.1 eV on going from pure tin to either oxide.

2.4 ELECTRON SPECTROSCOPIC STUDIES OF OXIDISED β-TIN FOIL AND FILM SUBSTRATES; AND OF α-TIN FILMS

The majority of electron spectroscope studies on tin have been carried out on clean and oxidised foils and films under ultra-high or high vacuum conditions. In a number of cases the properties of the oxidised surfaces have been compared with polycrystalline SnO or SnO_2.

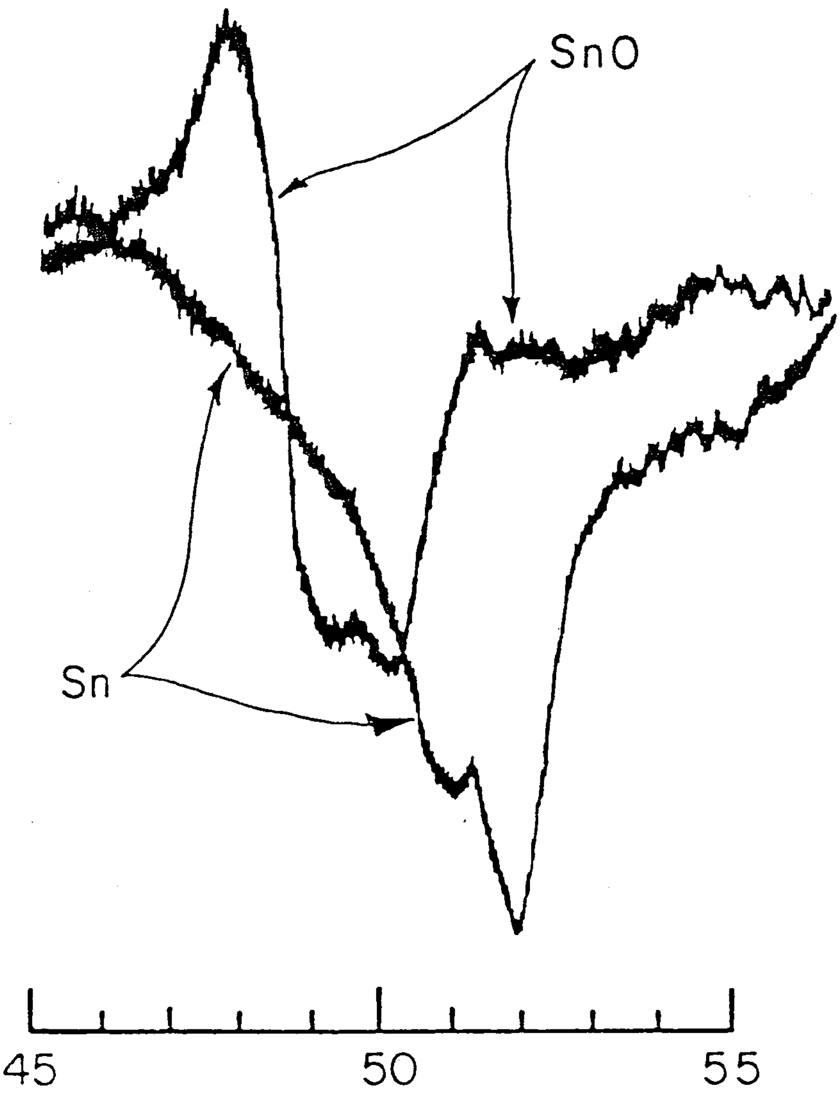

FIG. 2.7 The interband 4d doublet in the first derivative ELS spectra of SnO and Sn with an incident energy of 75.0V (after A J Bevolo et al, 1982).

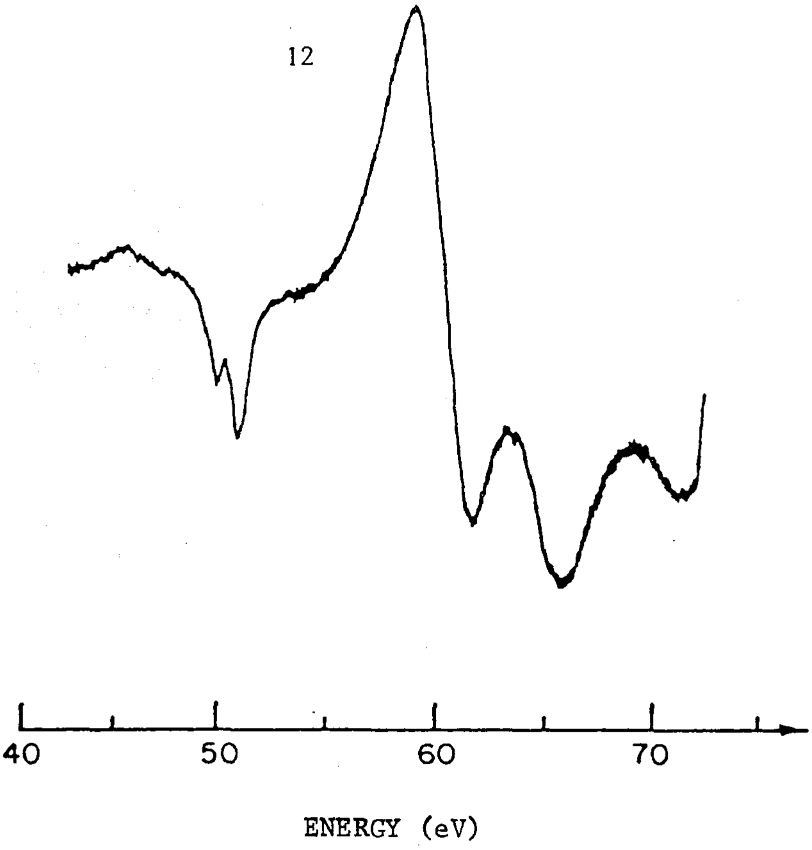

FIG. 2.8 First derivative ELS spectrum of pure tin with an incident energy of 75.0V (after A J Bevolo et al, 1982).

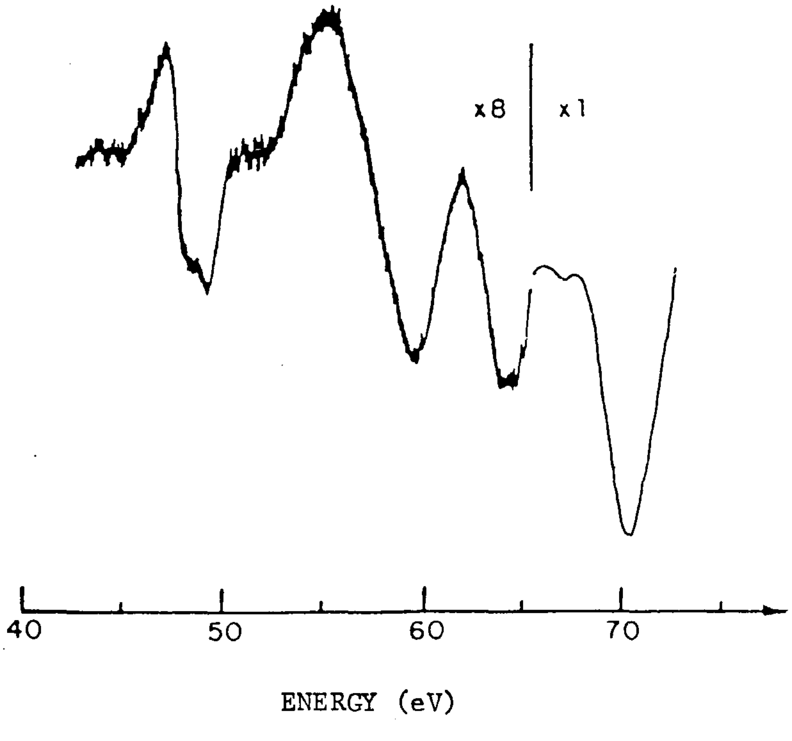

FIG. 2.9 First derivative ELS spectrum of SnO_2 powder with an incident energy of 75.0V (after A J Bevolo, et al, 1982).

A U.P.S. study of polycrystalline tin film has been carried out by J.H.P. Castelijns et al (1977). Comparisons were made with photoemission curves from liquid tin, and between smooth and rough surfaces. Photoemission from localized surface states was identified on the rough surface. The main features of the photoemission spectra were identified using the band structure of white tin obtained by M.A.E.A. Ament et al (1974).

An early U.P.S. study by R A Powell et al (1976) on evaporated tin films tentatively identified the grown oxide as SnO_2, although no experimental density of states were available for SnO or SnO_2 for comparison. Later U.P.S. studies of SnO_2 (P L Gobby et al, 1976; P L Gobby, 1977) and the X.P.S. study by C L Lau et al (1978) of SnO and SnO_2 indicated that the assignment by Powell was incorrect.

There have been several X.P.S. studies on clean tin, oxidised tin, and bulk tin oxides. The X.P.S. valence band spectrum of tin has been measured by H Höchst et al (1976). T Farrell (1976) reported chemical shifts between SnO and SnO_2 for the tin 3d binding energies. The presence of SnO and metallic tin were noted on a tin sample oxidised in air at 80°C. R J Bird (1973) also suggested that SnO was the oxide on tin foil oxidised in air. This conclusion was made after a chemical shift half that of SnO_2 was measured for the tin 3d binding energy of the oxidised sample. No core level binding energy shifts were detected between SnO and SnO_2 by W E Morgan et al (1973) and C L Lau et al (1978). Lau et al did note differences in the valence band spectra from SnO and SnO_2. These differences were used to characterise the surface of an oxidised tin film. Both SnO and SnO_2 were identified at the surface of the oxidised tin film.

A C Lin et al (1977) have performed a combined X.P.S. and A.E.S. study of the removal of the surface oxide from an as-mounted tin foil. Comparisons were made with SnO and SnO_2 powders. The as-mounted tin foil had an O/Sn Auger peak height ratio close to that of SnO_2. After argon ion bombardment to produce a clean surface the tin $M_{4,5}\,N_{4,5}\,N_{4,5}$ doublet shifted to a 5eV higher energy. At intermediate stages of oxidation the doublet was poorly defined. The Auger and X.P.S. spectra were almost identical for SnO and SnO_2 except for differences in relative peak heights and widths of the tin and oxygen peaks.

The characteristic electron energy loss spectra (E.E.L.S) were measured by R A Powell (1979) for SnO and SnO_2 powders. These spectra were used to identify the surface oxide species of oxidized tin shot: SnO was found to be the surface species. By considering the X.P.S. results of C L Lau et al, and the U.P.S. results of R A Powell et al, Powell suggested that the SnO/SnO_2 mixture seen in these previous studies after oxidation of a tin substrate could be accounted for by the poorer surface sensitivity of U.P.S. and X.P.S. compared with E.E.L.S. Powell considered that SnO may have been located at the surface with an underlying layer of SnO_2 such that the more surface-sensitive E.E.L.S. technique would primarily detect SnO whereas the photoelectron techniques would detect both oxides.

In Powell's A.E.S., U.P.S., and E.E.L.S. spectra, structure characteristic of metallic tin was observed. As no work function change was measured on oxidation, the possibility of a metallic tin-rich surface was proposed.

A further X.P.S. and A.E.S. study has been undertaken by P Sen et al (1982) on the oxidation of a polycrystalline tin film. The presence of the metal conduction band Fermi edge again suggested the presence of metallic tin at the oxidised surface. An increase of 0.4eV was measured in the positions of the 3d and 4d tin metal peaks on oxidation. The oxide thickness was estimated from the ratio of the oxygen to tin peak heights, the bulk plasmon intensity, and the metal 4d X.P.S. peak height.

There is a certain amount of disagreement on the size of the chemical shifts of the tin $M_{4,5}$ $N_{4,5}$ $N_{4,5}$ Auger peaks for SnO and SnO_2. Both R A Powell (1979) and C D Wagner et al (1973) measured almost identical shifts for the two oxides, although Powell observed a shift of 5.5eV whereas Wagner et al observed a shift of 3.9eV. In contrast S K Sen et al (1981) measured a shift of 3 ± 1eV for SnO and 7 ± 1eV for SnO_2. After prolonged ion bombardment Sen observed no changes in the Auger spectra of Sn or SnO_2; whereas after approximately three hours bombardment of SnO some reduction of Sn was noted by the superposition of the $M_{4,5}$ $N_{4,5}$ $N_{4,5}$ Auger spectra of Sn and SnO.

By comparing the Sn/O Auger peak height ratio and the Auger shifts of tin foils oxidised at 200°C, 100k Pa, with those of SnO, and SnO_2, Sen concluded that only SnO was present. This differed with the results of R A Powell and C L Lau et al, who found both SnO and SnO_2 present after oxidising their foils at 100°C. Transmission electron diffraction photographs taken by S K Sen et al after annealing the oxidised foil at 200°C for 72 hours indicated the presence of both SnO and SnO_2.

2.5 SINGLE CRYSTAL STUDIES

There have been few reported u.h.v. studies on single crystal tin or its oxides. Y C Jean et al (1980) measured the positronium fraction from an Sn (100) surface after initial bombardment by a positron beam. A constant positronium fraction at sub-monolayer exposures during oxidation at 473K indicated that the surface was tin-rich and that the oxygen had diffused below the surface, there still being an oxygen Auger signal. No change was found in the positronium fraction when the Sn(100) crystal was exposed to hydrogen suggesting that no adsorption took place.

The (100) surface was also examined by G C Rider (1981) in conjunction with the (110) and (101) surfaces. The L.E.E.D. patterns obtained from the (100) surface were interpreted in terms of a buckling of the surface. The (110) surface above 350K was a bulk exposed plane. Below this temperature reconstruction occurred which was interpreted in terms of two possible models. The L.E.E.D. patterns produced by the (101) surface were in disagreement with those of the present study (chapters 7, 8). The surface was composed of (112) facets which underwent a reversible transition to an α-Sn ($\sqrt{3} \times \sqrt{3}$) structure on cooling the surface below 270K. In the present study the surface plane was that of a bulk exposed (101) plane under all temperature conditions considered.

Rider interpreted his oxidised surfaces in terms of three oxide structures: at 290K the oxide on the (100) surface was amorphous; a 3.5Å x 4.0Å oxide structure was formed on the (110) and (101) surfaces at 290K; and a 4.8Å x 5.0Å oxide structure was formed on annealing the single crystal surfaces above 470K. The 4.8Å x 5.0Å structure was also observed on an oxidised tin foil. These, and the present L.E.E.D results from single crystal surfaces, have been summarised in chapter 8. All of the oxides in Rider's study and the present study produced an E.E.L.S. spectrum with features similar to those noted by Bevolo in SnO.

R F C Farrel et al (1981) have grown single crystal α-Sn films on clean (001) InSb and (001) CdTe surfaces which have closely-matched lattice spacings to that of α-Sn. The films exhibited a (2 x 2) reconstruction throughout growth. The reversible α-β transformation was found to occur at $\sim 70^{\circ}C$ for films of thickness below 0.5μm. Above 0.5μm nucleation of β-Sn occurred. As the bulk transition temperature is $13.2^{\circ}C$, the α-Sn films had been substrate-stabilised. In the case of 1% Ge-doped α-Sn the α-β phase change at $70^{\circ}C$ was found to be irreversible on cooling to $20^{\circ}C$. In a further transmission electron microscope study of single crystal α-Sn films on InSb, A G Cullis et al (1982) found the transformation of the α-phase to the β-phase above $60^{\circ}C$ took place at pre-existing irregularities. The β-phase thus formed as islands in the α-phase. After complete transformation the film was polycrystalline. Cullis et al also carried out electrical measurements which showed that the α-Sn films exhibited p-type conductivity. Angular resolved photoemission of heteroepitaxial films of α-Sn (001) on InSb (001) have recently been reported by H Höchst et al (1983). The experimentally obtained dispersion (E(k)) along ΓX was found to agree well with the non-local pseudopotential band structure calculation of J R Chelikowsky et al (1976).

The (100), (101) and (110) faces of SnO_2 have been studied by E de Frésart et al (1980, 1982, 1983). A number of temperature-dependent surface phase transitions were identified by L.E.E.D. with corresponding changes in Auger signal peak heights, work function, surface conductance, and electron energy loss spectra (the (110) face only). Preferential sputtering of oxygen during ion bombardment was suggested to explain the initially oxygen-deficient clean surfaces. The temperature-dependent structural changes were interpreted in terms of tin segregation and oxygen diffusion from the bulk.

CHAPTER 3

THEORY OF THE ELECTRON SPECTROSCOPIC AND ELECTRON DIFFRACTION TECHNIQUES

3.1 THE SECONDARY ELECTRON SPECTRUM

When a solid is irradiated with electrons of energy E_p, the distribution N(E) of secondary electrons with energy E from the surface takes the form of fig.3.1.

There are three distinct regions:

a) A sharp peak at the primary energy E_p corresponding to elastically reflected electrons (region 3).

b) A broad peak near E = 0 (region 1) as a result of the secondaries emitted from the solid after ionization by the primary electrons. These electrons in turn create more secondaries by further ionization.

c) A region between 1 and 3 containing inelastically scattered primary electrons and the higher energy secondaries. Many of the Auger electrons occur in this region. Also there are peaks due to electrons which have undergone well-defined energy losses (eg plasmons, interband transitions, phonons).

The electrons of interest in the present study were the Auger electrons and those with characteristic losses in the electron spectroscopic spectra; and the elastically reflected electrons in low energy electron diffraction.

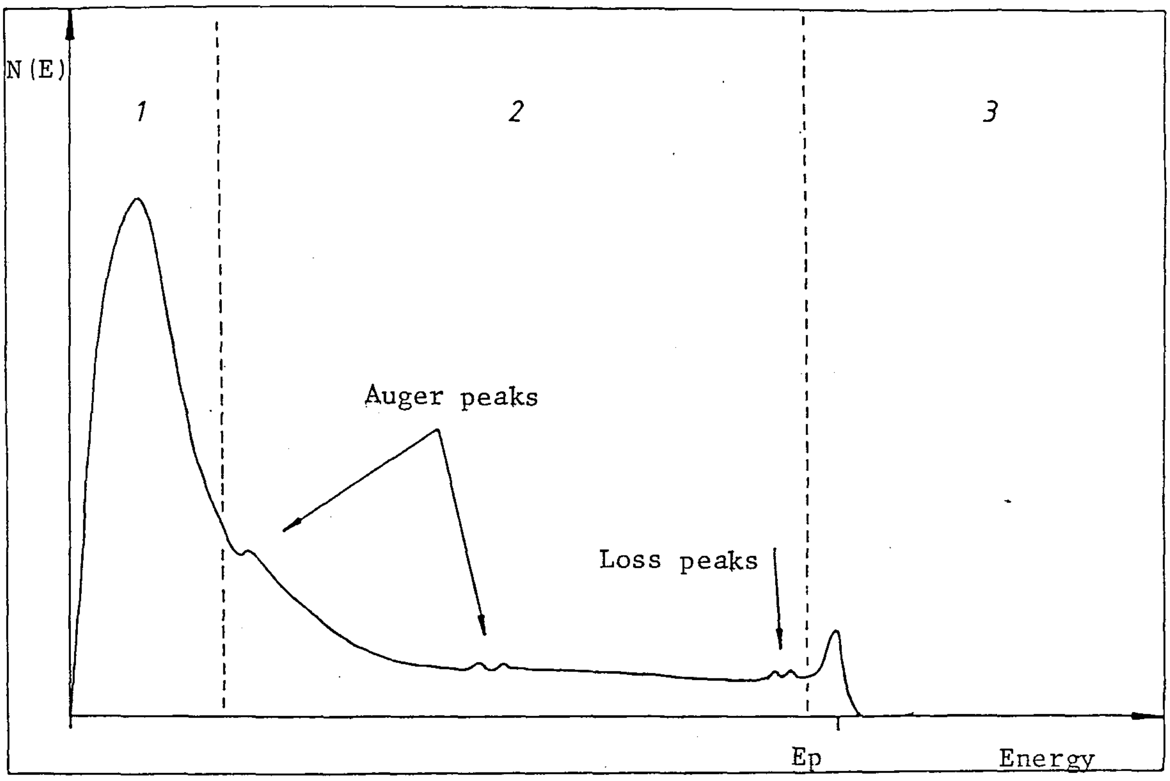

Fig. 3.1 Regions of the secondary electron spectrum.

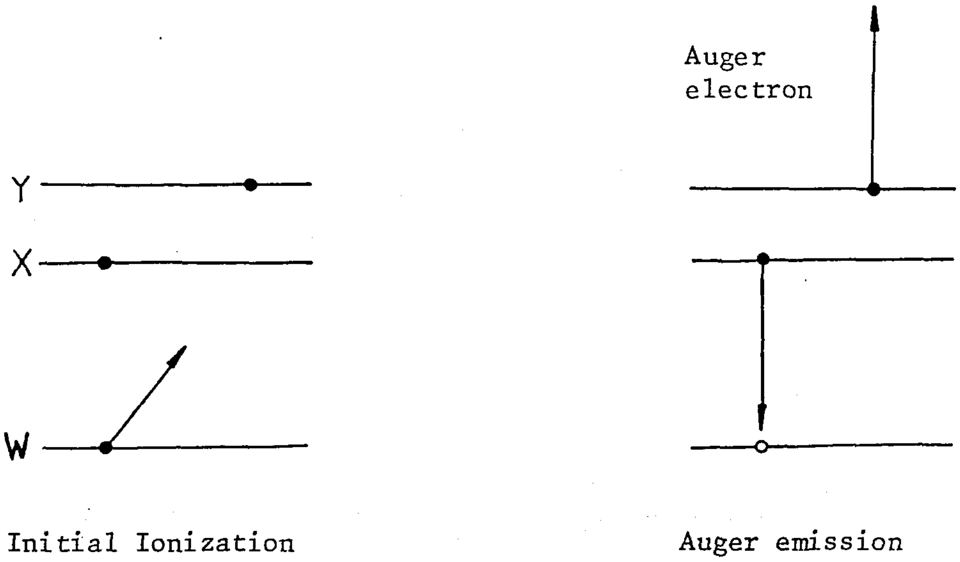

Fig. 3.2 The Auger process.

3.2 AUGER ELECTRON SPECTROSCOPY

When an atom is ionized by the removal of an electron from an inner shell W it will reorganise its structure to attain a lower energy state by two possible processes:

1) The inner shell vacancy may be filled by an electron from a higher shell X with the emission of a photon (X-ray), frequency ν. The energy change involved is given by

$$h\nu = E_X - E_W \tag{3.1}$$

2) The inner shell vacancy may be filled by an electron from shell X with the release of the excess energy by the ejection of an electron from shell Y (fig. 3.2). The electron has kinetic energy T which may be approximated by

$$T = E_W - E_X - E_{Y'} \tag{3.2}$$

and is known as an Auger electron. E_W, E_X refer to binding energies for electrons in shells W and X in the neutral atom; $E_{Y'}$ refers to the ionization energy for an electron in shell Y from a singly ionized atom.

Chung et al (1970) have improved on equation 3.2 by taking the binding energy for a doubly ionized shell to be given by the average of the binding energies corresponding to atomic number Z and $Z + 1$.

$$T(Z) = E_W(Z) - \tfrac{1}{2}\{E_X(Z) + E_X(Z+1) + E_Y(Z) + E_Y(Z+1)\} - \Phi_A \qquad (3.3)$$

The averaging has been done for both X and Y shells as the holes created in them are indistinguishable. The work function of the analyser has also been included which takes account of the work done in overcoming the work functions of the crystal surface and the analyser.

The Auger transitions are labelled as $W_a X_b Y_c$ where W_a, X_b, Y_c are written in terms of standard X-ray notation (e.g. the tin $M_4\ N_{4,5}\ N_{4,5}$ transition of fig. 5.3).

(a) TYPES OF AUGER TRANSITIONS

A normal Auger transition consists of the ionization of an electron from a core level W_a, the vacancy being filled by an electron from level X_b. The line width ΔE_{wxy} is dependant on the transition rate τ. By the uncertainty principle this is

$$\Delta E_{wxy} = \hbar / T \qquad (3.4)$$

Typically $\tau \simeq 10^{-16}$S with $\Delta E \simeq 0.1$eV. If the initial vacancy is filled by an electron from the same major shell (i.e. with the same principal quantum number N), but a different sub-shell, the Auger transition ($W_a W_b Y_c$) is termed a Coster-Kronig transition. These electrons have faster transition rates than normal Auger electrons with ΔE typically a few eV. Finally, if all three levels lie in the same shell the transition $W_a W_b W_c$ is termed a Super Coster-Kronig Transition.

(b) SOLID STATE EFFECTS ON THE AUGER PEAKS

The most important solid state effects on the shape, width, and position of Auger lines are:

1) Valence band effects.
2) Chemical shifts.
3) Energy loss processes.

The broadening of discrete energy levels of free atoms to bands for valence electron states of solids leads to a broadening of the corresponding Auger peaks of the solid. The shape of the peaks is dependant on the density of states of the band.

Changes in the electronic structure of an element due to chemical bond changes in different chemical environments (e.g. after gas adsorption) can lead to shifts (e.g. the oxidation of Sn(001) at 135 K (see p.68) and shape changes in Auger peaks.

Finally, energy losses due to ionization lead to low energy tails on the Auger peaks. Other loss processes (e.g. plasma excitations) lead to peaks which are normally distinguishable from the Auger peaks (e.g. the bulk plasmon losses of the clean tin Auger spectrum, fig. 5.3).

Apart from these solid state effects, the width of the Auger peaks is also affected by instrumental effects such as the size of the modulation voltage, local potential variations in the vicinity of the analyser grids, the finite primary beam size, etc.

3.3 ELECTRON ENERGY LOSS SPECTROSCOPY

The loss peaks of the secondary electron spectrum are characteristic of the surface layers of a solid, and may be used to identify adsorbed surface species. The principal loss processes are:-

1) Collective excitation of valence electrons (plasmons).
2) Interband and intraband transitions.
3) Excitation of lattice vibrations (phonons).

The technique used in the present study was able to resolve plasmon peaks and interband/intraband transitions but not phonon losses. The detection of phonon losses (which requires a high resolution spectrometer) gives information on the bonding between atoms of the surface layers. A review of high resolution electron energy loss spectroscopy has been given by B A Sexton (1981).

Primary and Auger electrons can lose discrete amounts of energy by the collective excitation (plasmon) of the electron 'gas' of the conduction electrons. A free electron model for the excitation of a plasmon gives the value E_p for the plasmon energy as

$$\begin{aligned} E_p &= \hbar W_p \\ &= \hbar \left(\frac{4\pi n e^2}{M_e}\right)^{\frac{1}{2}} \end{aligned} \tag{3.5}$$

where M_e is the mass of the electron, n is the electron density, W_p is the plasmon frequency. In a crystal M_e is replaced by $M_e{}^*$, the effective mass, as the band structure has to be taken into account.

A collective excitation of electrons at the surface of a metal has an energy

$$\begin{aligned} E_s &= \hbar W_s \\ &= \hbar W_p/\sqrt{2} \end{aligned} \tag{3.6}$$

where W_s is the surface plasmon frequency. The energy E_{s1}, of a surface plasmon of a surface layer with a dielectric constant ε is

$$E_{s1} = (1/\sqrt{1 + \varepsilon}\,)\ \hbar W_p \tag{3.7}$$

3.4 LOW ENERGY ELECTRON DIFFRACTION (LEED)

(a) INTRODUCTION

The diffraction of low energy electrons (0-1000eV) by crystals was first identified by Davisson and Germer in 1927. Electrons with energies ≃ 100eV have de Broglie wavelengths of the same order of magnitude (a few Å) as the interatomic separation of crystals, with inelastic mean free paths of a few atomic separations. Thus, it is possible to study the diffraction effects of the surface layers of crystals. The positions of the diffraction spots may be predicted by considering that the incident electrons interact weakly with the sample atoms so that only single scattering processes need be considered. This, the kinematic theory outlined in section 3.4b, correctly predicts many of the features of perfect and disordered surfaces. This theory does not give a correct interpretation of the diffraction beams as the interaction of low energy electrons with solids involves multiple scattering processes. Multiple scattering has been considered in the dynamic theories (see e.g. Pendry, 1974) to give further structural information.

(b) THE KINETIC THEORY

Consider a monochromatic electron beam incident on a surface. Far away from the crystal the wavefunction of an incident electron may be represented by a plane wave

$$\Psi_i\,(\underline{r},\ t) \;=\; A\exp\{i(\underline{K}_o\cdot\underline{r} + Et/h)\} \qquad (3.8)$$

$$= \Psi_i(\underline{r})T_i(t)$$

where $\underline{K}_o$ is the wavevector; E is the energy; and $\underline{r}$ is the position of the incident electron at time t.

As the electrons involved in LEED are elastically scattered, energy conservation implies that far away from the crystal the scattered wavevector $\underset{\sim}{K}_s$, satisfies

$$|\underset{\sim}{K}_s| \quad = \quad |\underset{\sim}{K}_o| \tag{3.9}$$

Momentum conservation gives the change in momentum ($\Delta \underline{K}$, the scattering vector) as

$$\Delta \underline{K} \quad = \quad \underset{\sim}{K}_s - \underset{\sim}{K}_o \tag{3.10}$$

The motion of the electrons in the vicinity of the surface is satisfied by the time-independant Schrödinger equation:

$$(-h^2/2M_e)\nabla^2 \; \Psi(\underline{r}) + V(\underline{r}) \; \Psi(\underline{r}) = E \; \Psi(\underline{r}) \tag{3.11}$$

(symbols have their usual meaning).

The periodicity of the crystal surface is denoted (fig. 3.3) by a vector

$$\underline{R} \quad = \quad l\underline{a} + m\underline{b} \tag{3.12}$$

where l and m are integer and $\underline{a}$, $\underline{b}$ are basis vectors of the surface net.

The potential acting on an electron has the two dimensional periodicity of the surface such that

$$V(\underline{r} + \underline{R}) \quad = \quad V(\underline{r}) \tag{3.13}$$

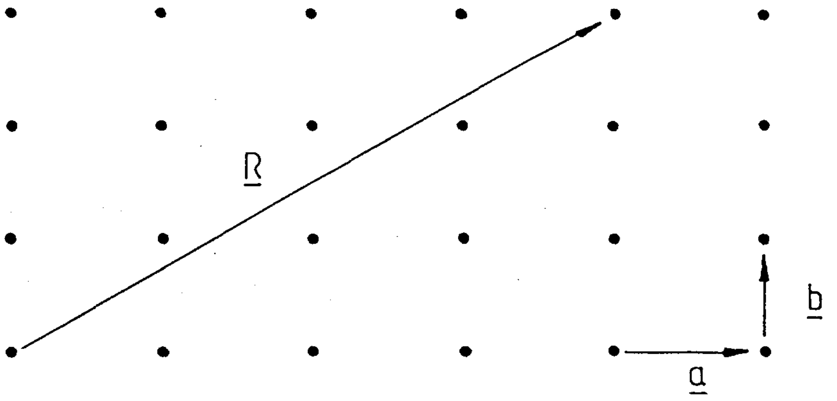

Fig. 3.3 Atom position co-ordinates of a crystal lattice.

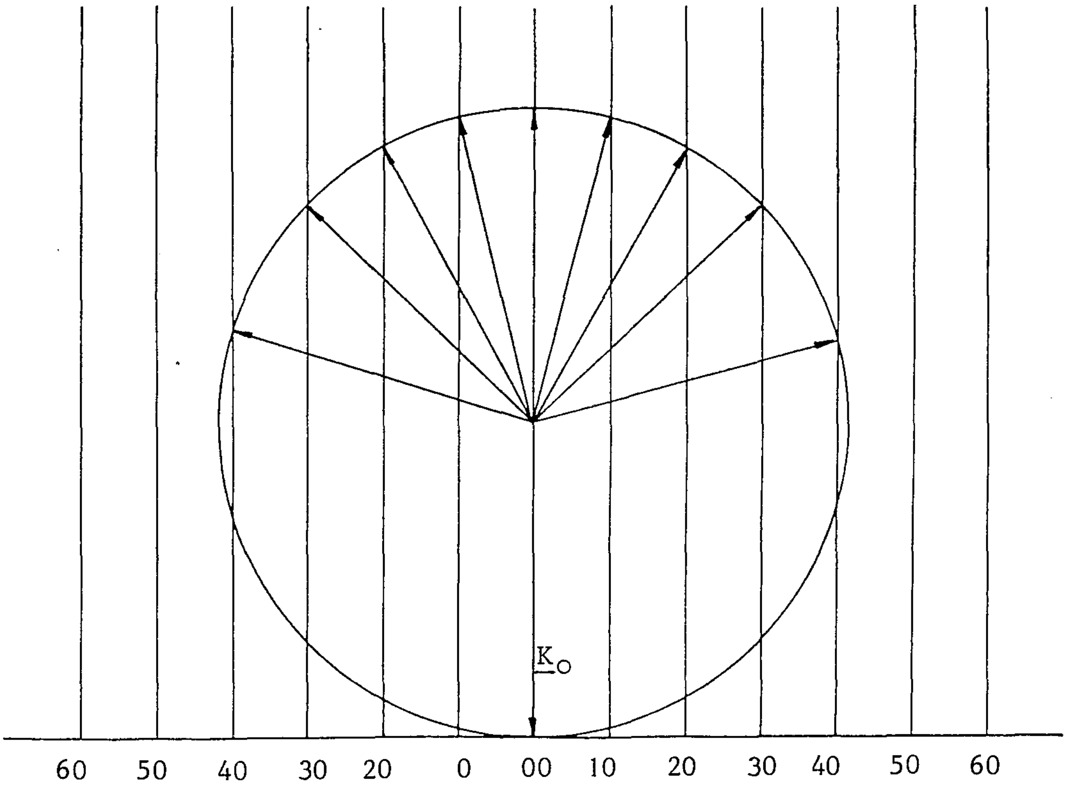

Fig. 3.4 The Ewald sphere construction for L.E.E.D. from a perfect crystal surface.

The total wavefield ($\Psi(\underline{r})$) is a superposition of the incident wavefield ($\psi_i(\underline{r})$) and the scattered wavefield $\Psi_s(\underline{r})$:

$$\Psi(\underline{r}) = \Psi_i(\underline{r}) + \Psi_s(\underline{r}) \tag{3.14}$$

From (3.8)

$$\Psi_i(\underline{r} + \underline{R}) = A \exp(i\underline{K}_o \cdot \underline{r}) \exp(i\underline{K}_{\parallel o} \cdot \underline{R})$$

$$= \Psi_i(\underline{r}) \exp(i\underline{K}_{\parallel o} \cdot R) \tag{3.15}$$

where $\underline{K}_{\parallel o}$ is the component of $\underline{K}_o$ on the surface plane.

Similarly:

$$\Psi_s(\underline{r} + \underline{R}) = \Psi_s(\underline{r}) \exp(i\underline{K}_{\parallel o} \cdot \underline{R}) \tag{3.16}$$

Ψ_s does not have the periodicity of the surface, but by writing

$$\Psi_s(\underline{r}) = \phi_s(\underline{r}) \exp(i\underline{K}_{\parallel o} \cdot \underline{r}_{\parallel}) \tag{3.17}$$

and substituting (3.17) into (3.16) it can be shown that:

$$\phi_s(\underline{r}+\underline{R}) = \phi_s(\underline{r}) \tag{3.18}$$

$\phi_s(\underline{r})$ is a two-dimensional Bloch function with the periodicity of the surface. It can be written as a Fourier expansion

$$\Phi_s(\underline{r}) \quad = \quad \sum_G \alpha_G(z) \exp(i\underline{G}\cdot\underline{r}_\parallel) \qquad (3.19)$$

In order for (3.19) to satisfy (3.18)

$$\underline{G}\cdot\underline{R} = 2n\pi \qquad (3.20)$$

Hence vector $\underline{G}$ can be expressed as

$$\underline{G}_{hk} \quad = \quad h\underline{a}^* + k\underline{b}^* \qquad (3.21)$$

By applying the conditions:

$$\begin{aligned} \underline{a}^*\cdot\underline{a} \quad &= \quad \underline{b}^*\cdot\underline{b} \quad = \quad 2\pi \\ \underline{a}^*\cdot\underline{b} \quad &= \quad \underline{b}^*\cdot\underline{a} \quad = \quad 0 \end{aligned} \qquad (3.22)$$

the basis vectors of $\underline{G}$ can be represented by

$$\underline{a}^* = 2\pi(\underline{b} \times \underline{c}) / (\underline{a}\cdot\underline{b}\times\underline{c}), \quad \underline{b}^* = 2\pi(\underline{c} \times \underline{a}) / (\underline{b}\cdot\underline{c}\times\underline{a}) \qquad (3.23)$$

where $\underline{c}$ is a unit vector of the bulk crystal structure normal to the surface.

The vectors $\underline{G}_{hk}$ define the reciprocal lattice of the crystal surface.

By substituting (3.19) into (3.17) the scattered wavefunction becomes

$$\Psi_s(\underline{r}) = \sum_G \alpha_G(z) \exp\{i(\underline{K}_{o\parallel} + \underline{G}).\underline{r}_\parallel\} \tag{3.24}$$

In LEED the effects of the scattered electrons are observed outside the crystal for which $V(\underline{r}) = 0$.

Hence by solving the Schrödinger equation for the total wavefunction outside the crystal, the expression

$$\alpha_G(z) = \beta_G \exp\{-i({}^{2M_e E}/\hbar^2 - (\underline{K}_{o\parallel} + \underline{G})^2)^{\frac{1}{2}}z\} \tag{3.25}$$

is obtained, where β_G is a constant for each value of $\underline{G}$.

The scattered wave outside the crystal now becomes

$$\Psi_s(\underline{r}) = \sum_G \beta_G \exp i(\underline{K}_s.\underline{r}) \tag{3.26}$$

The scattered wavevector satisfies

$$\underline{K}_s = \underline{K}_o + G_{hk}, \quad (\underline{G} = \Delta\underline{K}) \tag{3.27}$$

$$\underline{K}_s = (K_{ox} + G_x, K_{oy} + G_y, (-2M_e e/\hbar^2 - (\underline{K}_{o\parallel} + \underline{G})^2)^{\frac{1}{2}}) \tag{3.28}$$

Hence the diffracted wavefield from a perfect crystal forms a series of beams, the directions of which are denoted by $\underline{K}_s$. Each beam has a different component of momentum parallel to the surface (equation 3.27).

The diffraction conditions can be represented in reciprocal space by the Ewald construction (fig. 3.4). A series of parallel rods are drawn normal to each point of the reciprocal surface net. The rods are denoted by the indices h, k of the vector $\underline{G}_{hk}$ originating at O. The incident beam is denoted by the vector $\underline{K}_o$. Energy conservation is represented by drawing a sphere centred at X, radius $|\underline{K}_o|$, with each scattered beam originating at X and lying on the sphere. By applying the condition of equation 3.27 the scattered wavevectors also lie on the reciprocal lattice rods. Hence the diffracted beams may also be labelled by the indices h, k.

(c) DYNAMIC THEORY

In the kinematic theory single scattering of the primary electrons was assumed. In practice the high atomic scattering factors for low energy electrons from atoms invalidates this assumption and multiple scattering events in fact occur. Multiple scattering becomes evident when the two outermost layers of a surface have different periodicities (e.g. the 7 x 4 pattern for the oxidation of Sn(101) at 390 K, chapter 6). I/V curves exhibit secondary maxima apart from the primary Bragg peaks.

If the primary beam is scattered within the three-dimensional single crystal lattice, the condition for diffraction will be

$$\underline{K}_s = \underline{G}_B + \underline{K}_o \tag{3.29}$$

where $\underline{G}_B$ represents a reciprocal lattice point of the bulk crystal; $\underline{K}_o$ and $\underline{K}_s$ are the incident and scattered vectors respectively. If the diffracted electron undergoes a further scattering event (e.g. at the surface) then the wavevector of the emitted electron ($\underline{K}_s'$) will be

$$\underline{K}_s' = \underline{G}_s + \underline{K}_s \tag{3.30}$$

$$= \underline{G}_s + \underline{G}_B + \underline{K}_o \tag{3.31}$$

(d) LEED FROM DISORDERED SURFACES

A number of defect structures have been identified in the present and previous (Rider, 1981) studies on single crystal tin. In the present case a complex arrangement of steps and terraces has been identified on the clean Sn(001) surface (chapter 6). The characteristics of the resulting L.E.E.D. patterns from surfaces with defects has been reviewed by Henzler (1977).

The origins of the features observed in the L.E.E.D. patterns from stepped surfaces become evident on considering the simple case of a stepped surface with constant terrace width and step height, and with steps along only one direction of the surface (fig. 3.5).

If $W\underline{a}$ is the width of M terraces with edge atoms of adjacent terraces separated by vector

$$\underline{g} = \underline{g}_1 + \underline{g}_2 \qquad (3.32)$$

then if A is the scattering factor for 1 terrace , the scattering factor for M terraces (A_T) is given by

$$A_T = A \sum_{o}^{M-1} (\exp\{i(\underline{K}_s - \underline{K}_o).t(W\underline{a} + \underline{g})\}) \qquad (3.33)$$

The scattered intensity I_T is given by

$$I_T = |A|^2 \{\mathrm{Sin}\{\tfrac{1}{2}M(\underline{K}_s - \underline{K}_o).\underline{g}\}/\mathrm{Sin}\{\tfrac{1}{2}(\underline{K}_s - K_o).\underline{g}\}\}^2 \qquad (3.34)$$

The intensity $|A|^2$ from a single terrace has maxima given by the Ewald construction for a perfect surface (fig. 3.4). The positions of maxima are now modulated by the second term in equation 3.34 for the stepped surface. Fig. 3.5d shows the resulting intensity distribution (assuming single scattering) for the case of a stepped surface of 6 terraces with 5 atoms per terrace (after Henzler, 1977).

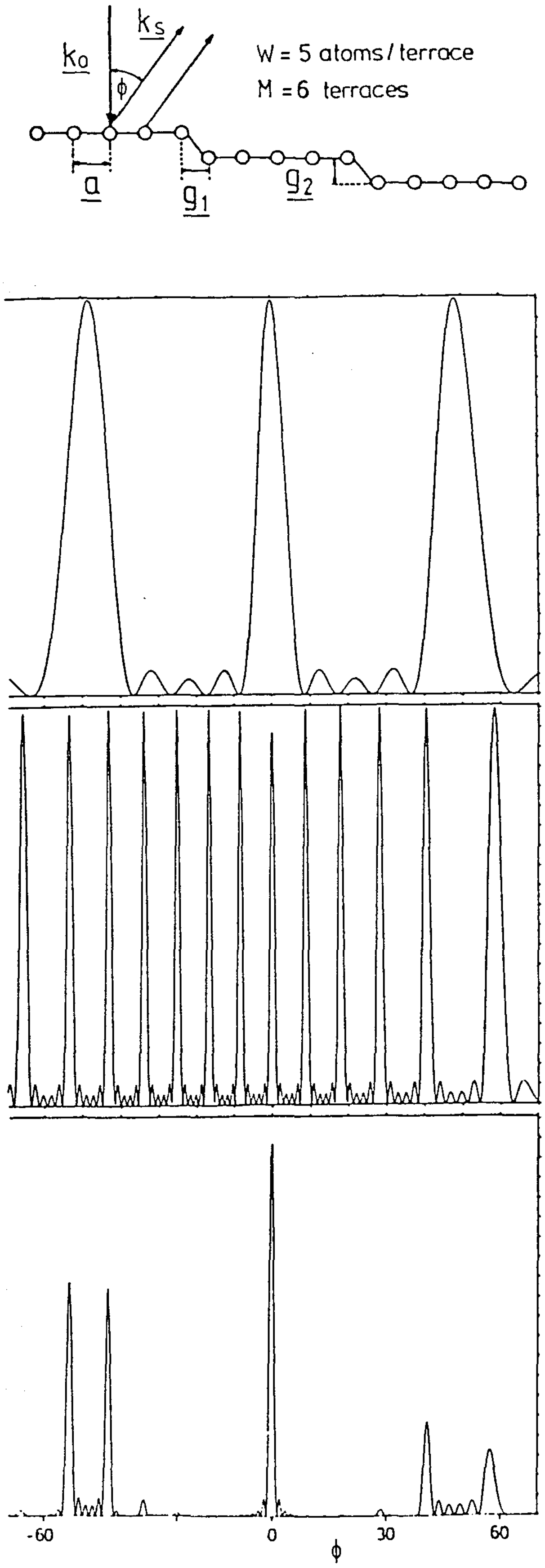

a) The stepped surface.

b) Angular variation of the intensity distribution function from a single terrace of 5 atoms.

c) Intensity distribution function for a step array of 6 terraces.

d) Product of (b) and (c).

Fig. 3.5 Low energy electron diffraction from a regular stepped surface (after Wagner, 1979).

Here the (10) beam is now split into two beams of approximately equal intensity for the primary beam energy considered, whereas a perfect surface only produces one beam. A single beam will be produced for any (hk) reflection whenever all of the atoms of all the terraces scatter in phase such that

$$\underline{g} \cdot (\underline{K}_{hk} - \underline{K}_o) = 2n\pi \tag{3.35}$$

Conversely antiphase scattering occurs when

$$\underline{g} \cdot (\underline{K}_{hk} - \underline{K}_o) = (2n+1)\pi \tag{3.36}$$

The energy (E) of an electron incident on the surface is:

$$E = Ve = \hbar^2 \, |\underline{K}_o|^2 / 2M_e \tag{3.37}$$

$$\text{Thus } |\underline{K}_o| = 2\pi \sqrt{V/150} \qquad (\text{units } \text{Å}^{-1}) \tag{3.38}$$

Hence from (3.35) and (3.36) the characteristic voltages at which single or double spots are observed for the (hk) reflection with the primary beam at normal incidence is:

$$V_{hk} = \frac{150}{4|\underline{g}_2|^2} \left[S - hx + \frac{ha^* |\underline{g}_2|^2}{4\pi^2 (S-hx)} \right]^2 \tag{3.39}$$

For single spots S is integer, and for double spots (antiphase scattering) S is half-integer.

Fig. 3.6 shows how the terrace width ($W\underline{a}$) may be determined. The reciprocal lattice of the terrace structure has been superimposed on that of a single terrace. The antiphase condition for splitting of the (10) beam has been shown. The separation between the reciprocal lattice rods of the terrace structure is given by:

$$(2\pi/|\underline{g}_2|)\ \sin\alpha \quad = \quad 2\pi/L \tag{3.40}$$

where

$$L \quad = \quad W|\underline{a}|/\cos\theta \tag{3.41}$$

In fig. 3.6 the angular separation (ϕ) between the two positions of constructive interference for the (10) beam at the antiphase condition is given (Wagner, 1979) by

$$\Delta\phi \quad = \quad \frac{\lambda}{W|\underline{a}|\cos\phi + |\underline{g}_2|\ \sin\phi} \tag{3.42}$$

The reciprocal lattices of a regular monotonic step array (fig. 3.7a), and a regular two-layered step array (fig. 3.7b), have been determined by Henzler (1977). In the case of the two-layered step array three spots are formed for a (hk) beam in the antiphase condition, and two spots under conditions intermediate between in-phase and antiphase scattering.

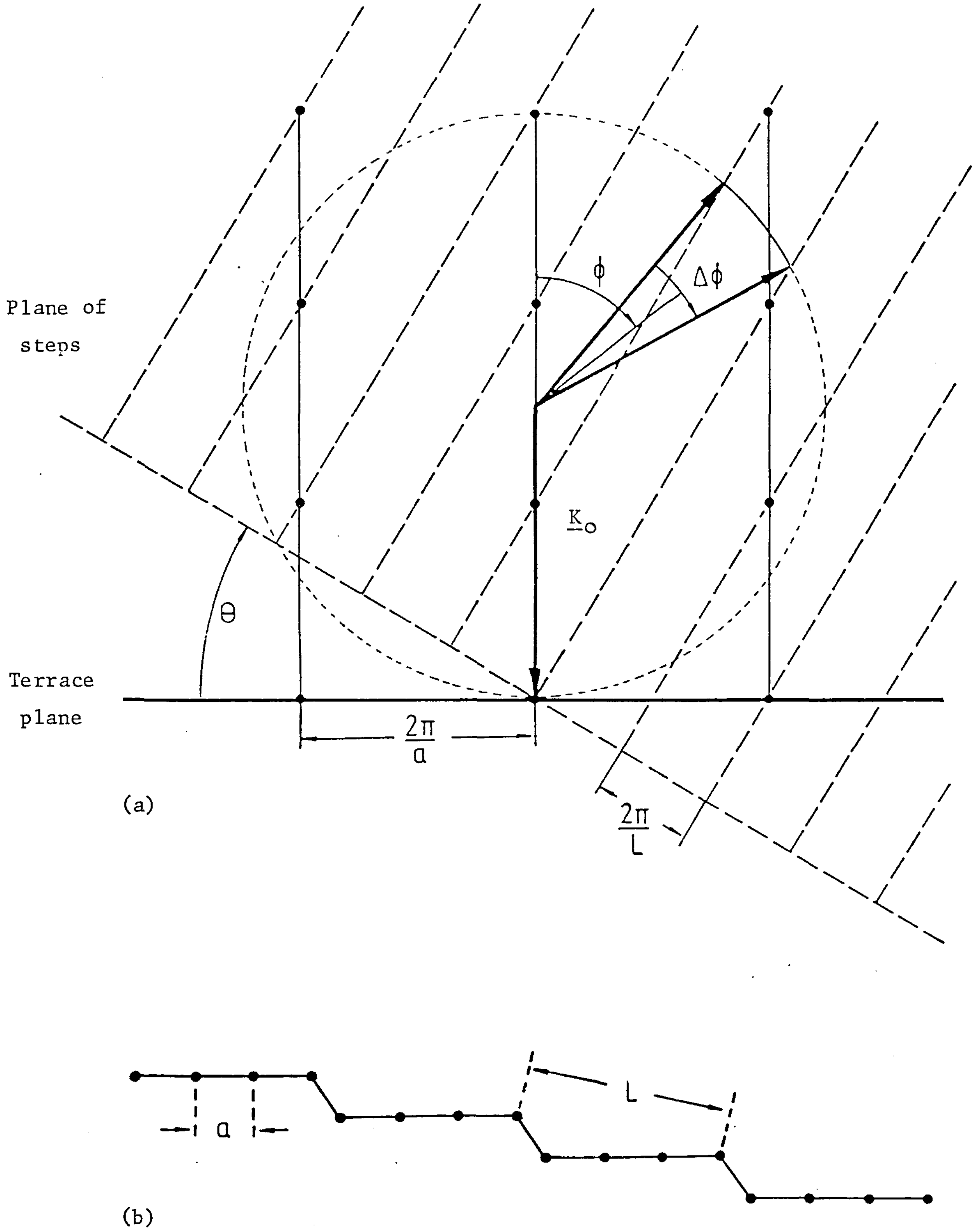

Fig. 3.6 (a) Superimposed reciprocal lattices of terrace structure (solid lines) and step array (dashed lines) for a monotonic step array (b) in the determination of the terrace width. The condition for splitting of the (10) beam is shown at normal incidence.

(a) Regular step array
(monotonic)

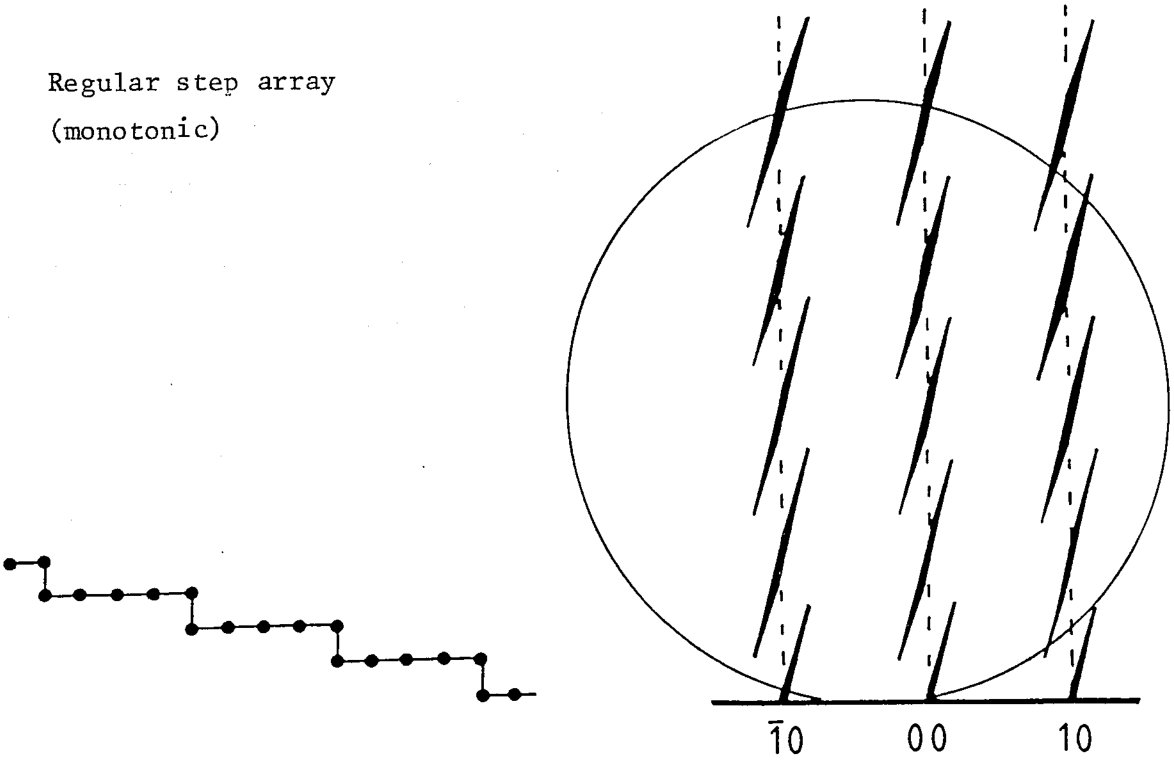

(b) Two-layered step array
(.e.g the oxide structure
on Sn (101) after 500L
exposure at 390K).

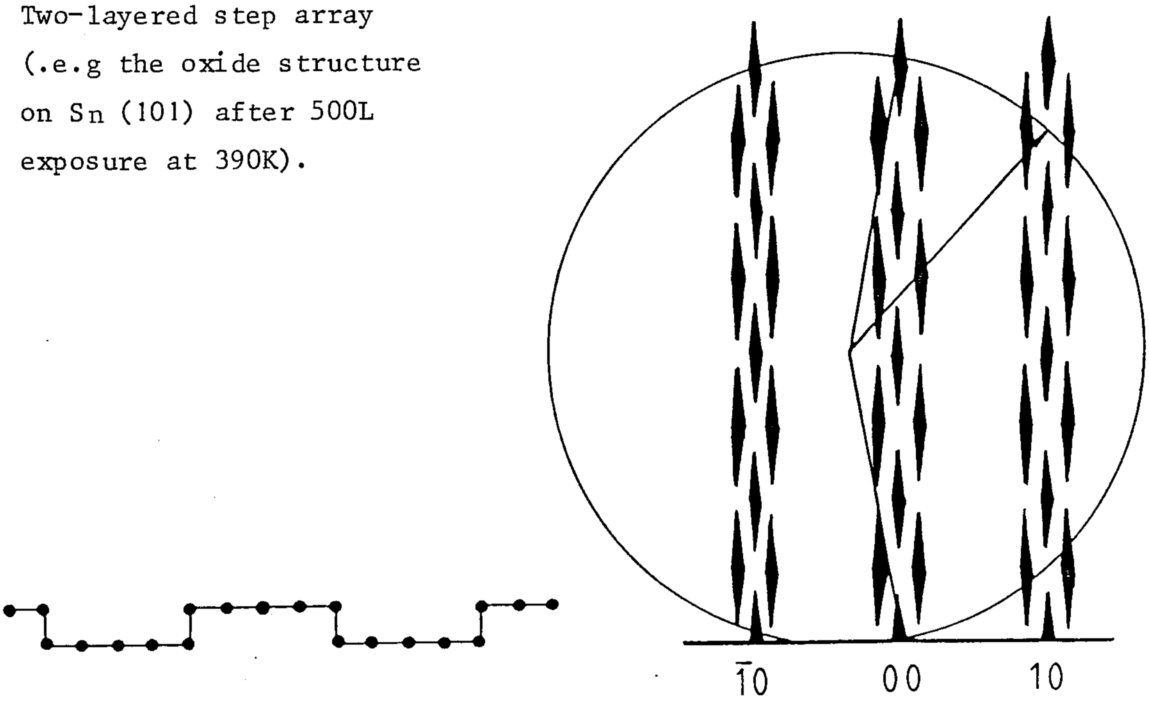

Fig. 3.7 Reciprocal lattices for two types of stepped structures. (after Henzler, 1977).

(e) COHERENCE ZONE

A consideration of equation 3.34 suggests that for a perfect surface the L.E.E.D. spots should be infinitely sharp. The experimental conditions in fact lead to a finite spot size. The finite size of the electron source, angular deviation (θ) and finite energy spread (ΔE), limits the diameter of the zone in which the primary beam may be considered coherent to the order of 50 - 100Å. Heinreich (1964) has determined an expression for the coherence width (L) at energy E

$$L \approx \lambda/2\theta(1 + {}^{\Delta E}/E) \tag{3.43}$$

where λ is the wavelength of the primary electrons.

CHAPTER 4

EXPERIMENTAL TECHNIQUES

4.1 THE U.H.V. SYSTEM

The stainless steel ultra-high vacuum chamber and attachments (fig. 4.1) was essentially the same as that used by G C Rider (1981). The main differences were the replacement of the 3-grid L.E.E.D-Auger optics by a Varian 4-grid L.E.E.D.-Auger optics model 981-027 with an off-axis electron gun; a second (back-up)V.G Micromass Anavac -2 mass spectrometer; and two crystal cooling devices with crystal mounts.

The ultimate base pressure of the system was 3×10^{-10} torr. This was attained from atmosphere by initially pumping the stainless steel chamber with the rotary and diffusion pump backing line (fig. 4.2) to a pressure of $\approx 5 \times 10^{-10}$ torr, followed by further pumping by the 60 l/s triode ion pump to $\approx 3 \times 10^{-7}$ torr and baking the chamber at 200^{o}C for two days to attain u.h.v.

4.2 PRESSURE MEASUREMENTS

The available pressure measuring devices were: a Varian model UHV-14 nude ionization gauge; a V.G. VIG 10 nude ionization gauge; and two Anavac-2 quadrupole mass spectrometers. The total pressure readings of the quadrupole mass spectrometers were found to vary by up to an order of magnitude after filament replacement compared with an ionization gauge.

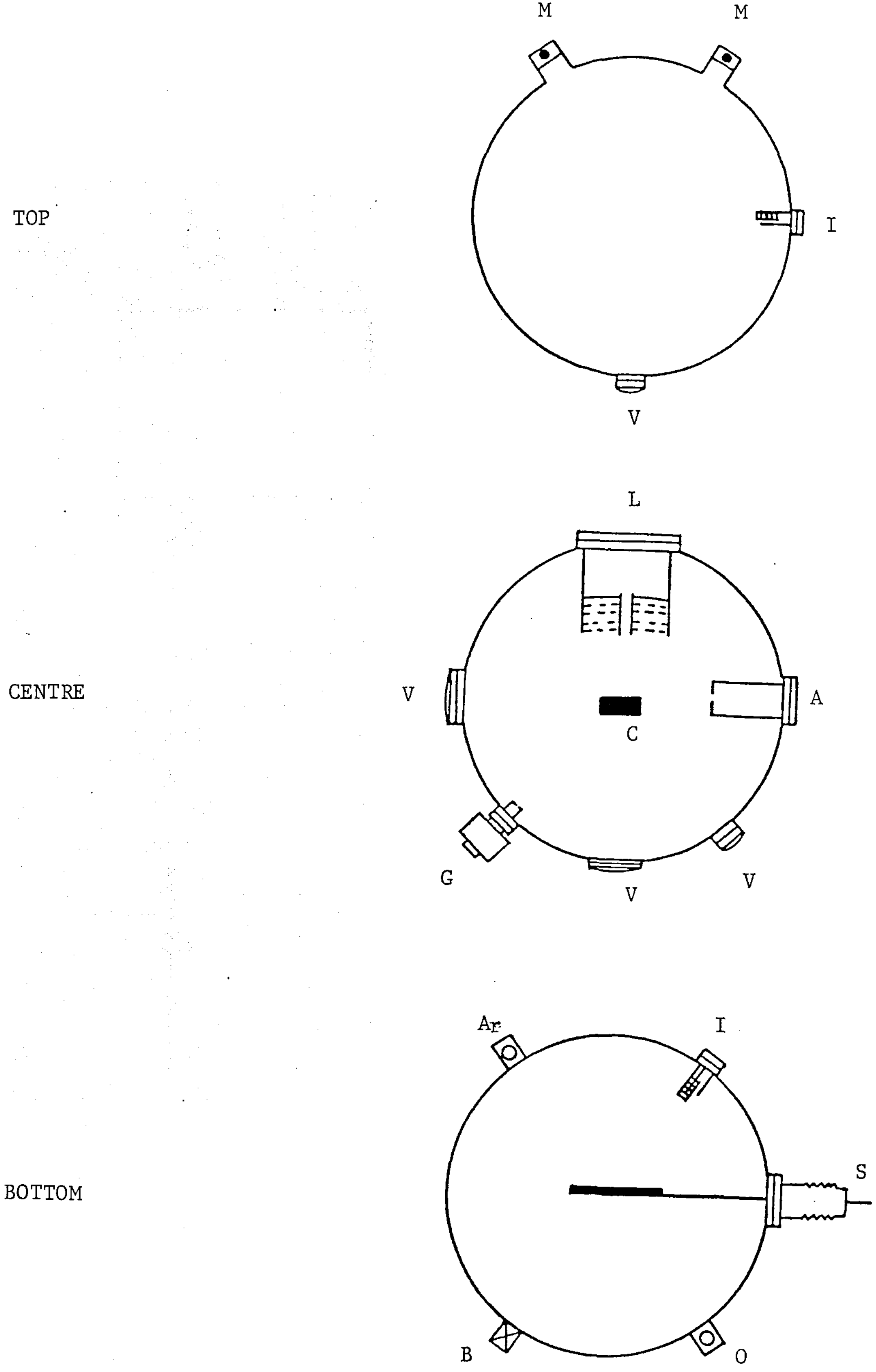

FIG. 4.1 The arrangement of the attachments to the vacuum chamber in three layers.

Key:- A: Argon Ion Gun; Ar: Argon inlet valve; B: Isolation Valve To Backing Line;C: Crystal; G: Argon Ion Gun; I: Ionization Gauge; L: Leed-Auger Optics; M: Mass Spectrometer; O: Oxygen Inlet Valve; S: Optics Shield; V: Viewport.

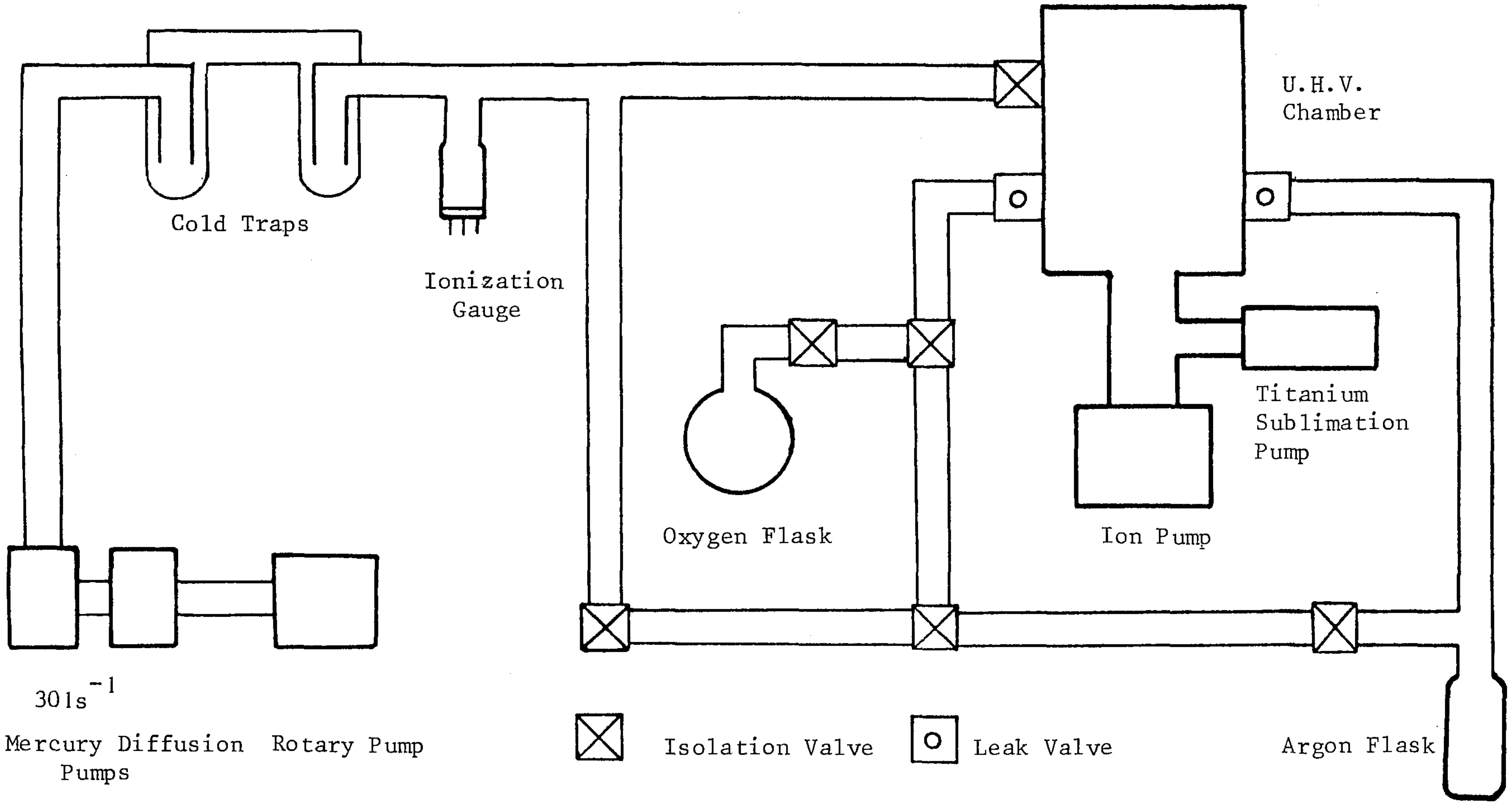

FIG. 4.2 The backing line and gas line to the u.h.v. chamber.

Thus, they were not used for total pressure measurements. Varying leakage currents also made the ion pump current measurement unsuitable for pressure readings. Hence, the Varian ion gauge was used for total pressure measurements and a mass spectrometer for partial pressure measurements.

4.3 OXIDATION

In order to make the conditions of this series of experiments as consistent as possible with those of Rider, both crystal surfaces studied were oxidised at 5×10^{-7} torr with BOC research grade oxygen, the chamber being pumped continuously. The oxygen purity decreased typically by 15 - 25% from an initial purity of 80% to > 90% during any particular experiment. This was mainly due to a build-up of CO, with some CO_2. There was also always a small percentage ($\approx$ 5 - 10%) of argon present. No trace of carbon or argon was ever found in the Auger spectra during oxygen adsorption suggesting that no adsorption of these contaminants took place under the experimental conditions used. The argon was presumed to have been emitted from the ion pump by a memory effect and originated from the argon used in ion bombardment of the surfaces.

4.4 CRYSTAL MANIPULATOR ASSEMBLY

The crystal support, cooler, and electrical connections were mounted on a Torvac manipulator which allowed rotation about a vertical axis. The presence of a bellows between the manipulator and the vacuum chamber enabled adjustments to be made to the horizontal and vertical positions of the samples.

Two arrangements of crystal supports and cooling devices were used in this study. The first (fig. 4.3) consisted of the support used by Rider combined with a new cooling device. Initially, it had been hoped to have a reservoir for the liquid nitrogen, but the available construction techniques necessitated the use of an O.F.H.C. copper heat sink mounted on a tube through which liquid nitrogen was continuously supplied. The heat sink was connected to the crystal support via a copper braid. This arrangement enabled the crystal temperature to be reduced to 215K, which was adequate for previously observed reconstructions on tin single crystals (G C Rider, 1981), and for improving the relative intensity of the L.E.E.D. spot pattern to that of the background. A blockage created in the liquid nitrogen line in attempting to seal a leak necessitated the use of the second system in later studies. This was based on a Leisk cooler, the samples being mounted on a tantalum plate attached to the cooler (fig. 4.4). Initially, only the Sn (101) crystal was mounted and it was possible to reach temperatures of 90K. As it was found that the assembly could rotate by $\pm$ 180^o, an Sn(001) crystal was also mounted. The lowest attainable temperature with the two crystals mounted was 140K (fig. 4.5). For both assemblies the surfaces of the supports in the vicinity of the samples was covered in tin foil to prevent sputtering of support material onto the crystals during argon ion bombardment. Temperature measurements were made using chromel-alumel thermocouples.

4.5 SAMPLE PREPARATION

The Sn(001) and Sn(101) single crystals were in the form of slices taken from a cylindrical single crystal rod of purity 99.9995%. The slices were cut by spark erosion after approximate orientation by Laue X-ray back reflection.

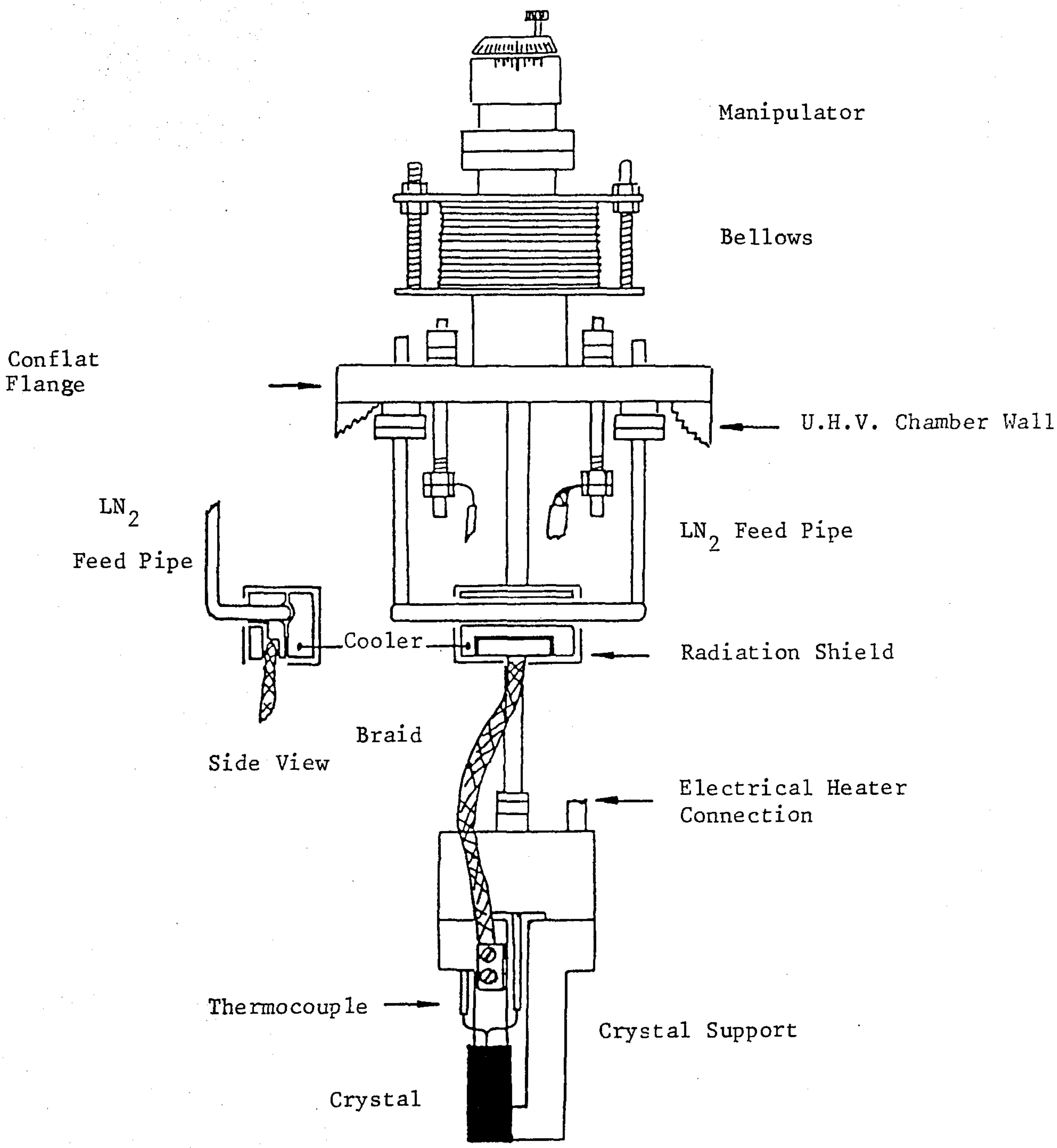

FIG. 4.3 Crystal manipulator assembly with the first crystal cooling device.

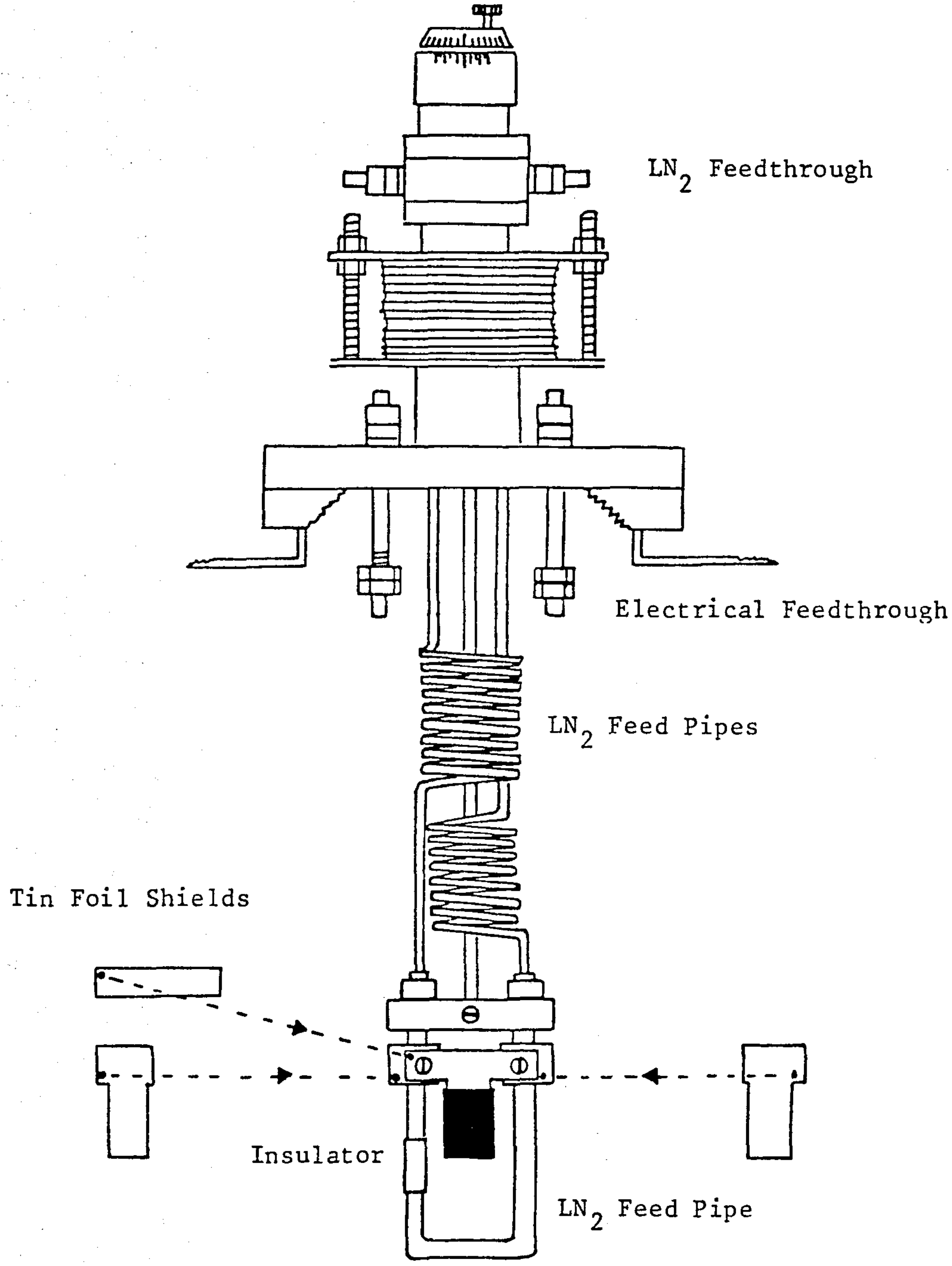

FIG. 4.4 Crystal manipulator with the second (Leisk) cooling device.

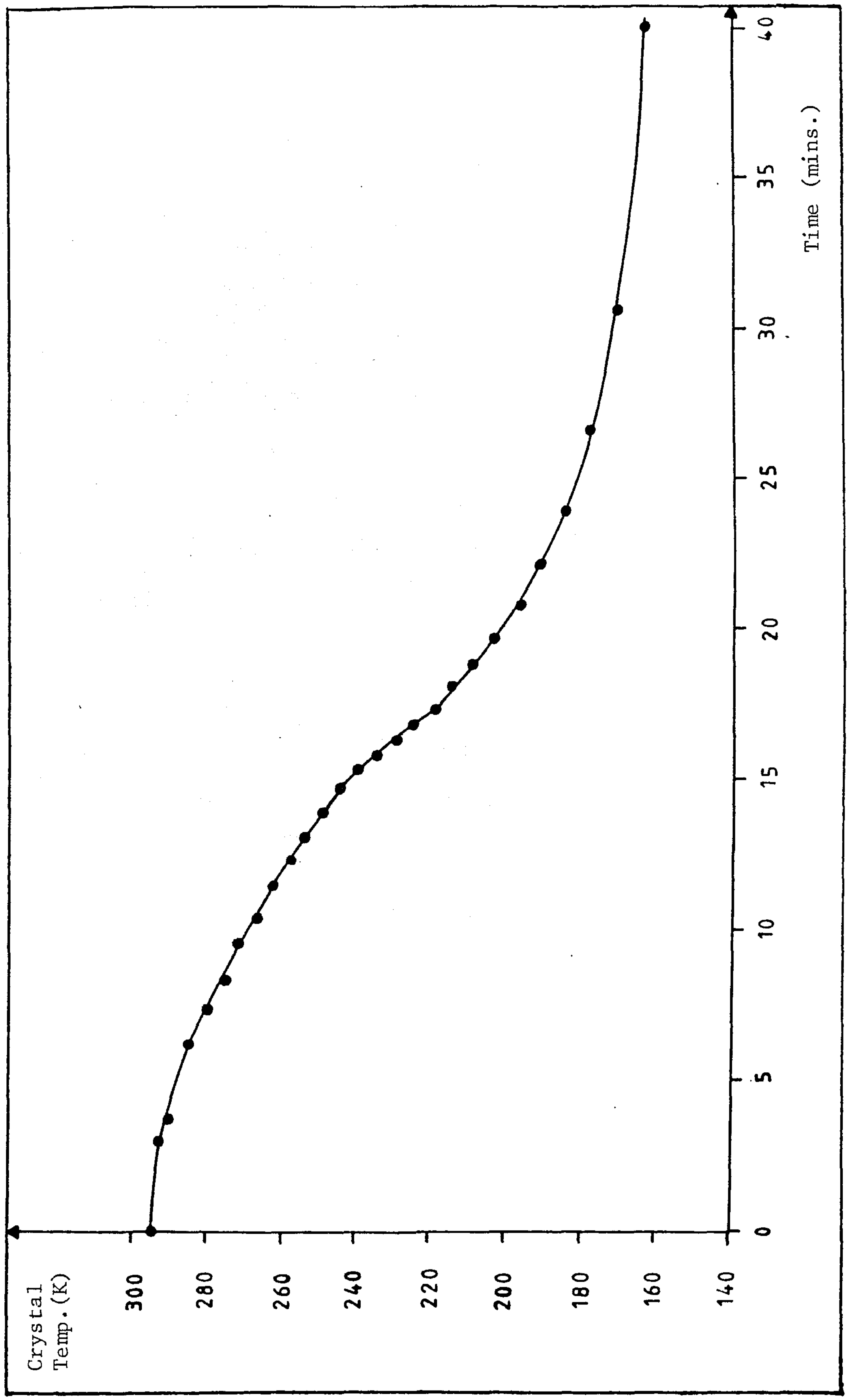

FIG. 4.5 Typical cooling curve for the single crystal samples when two crystals were mounted on the second (Leisk) cooling device.

After accurate orientation to within half of a degree of that required, the crystals were spark planed to obtain the (001) and (101) surfaces. The Laue X-ray diffraction photographs from the oriented Sn(001) and Sn(101) single crystals are shown in figs. 4.6,7, together with an explanation of the observed patterns.

Polished surfaces were obtained by lapping with successively finer grades of diamond paste (2μ, $\frac{3}{4}\mu$, and $\frac{1}{4}\mu$ respectively). The etch and polish used by Rider on his (101) crystal to remove the damaged layers created during lapping was not used on the single crystals of this study as the etch preferentially attacks defect sites to form etch hillocks (K Honda et al, 1972).

It was found that several hours of argon ion bombardment of the crystals was sufficient to obtain clean ordered surfaces. Kikuchi patterns obtained from the surfaces using the Auger gun are shown in fig. 4.8. After undergoing the bombardment, the surfaces, which were initially polished, were seen to become matt. Scanning electron micrographs of the (001) surface (fig. 4.9) taken before and after placing in the u.h.v. chamber, show extensive damage created by the ion bombardment in the course of the study. Fig. 4.10 shows the (101) surface after polishing. Even after extensive polishing the surface appears rough and pitted on a microscopic scale. It was not possible to take scanning electron micrographs of the (101) surface after ion bombardment as the crystal was accidentally melted during the course of the u.h.v. studies.

The formation of clean surfaces before each experiment required approximately 10 minutes argon ion bombardment using a Vacuum Generators AG2 ion gun with a beam energy of 2.5keV at 5 x 10^{-4} torr. After bombardment the system was pumped to 2 x 10^{-7} torr with the backing line using the ion pump to return the system to u.h.v.

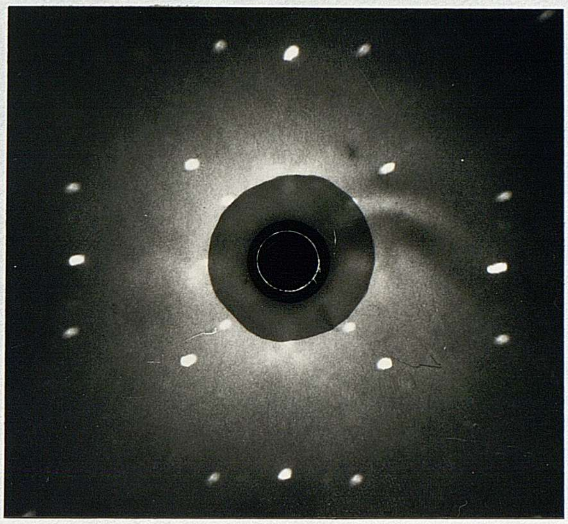

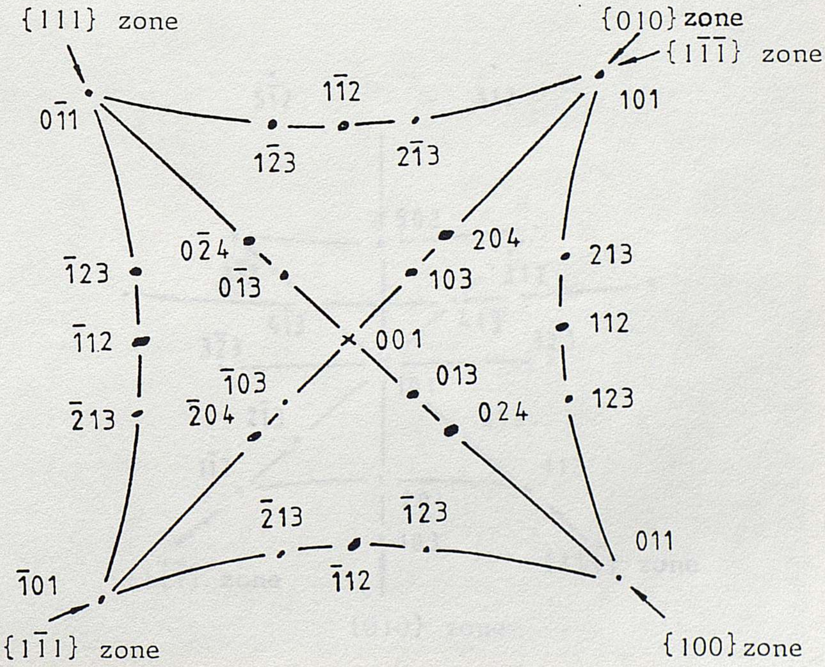

FIG. 4.6 Laue back-reflection photograph and key for the Sn(001) single crystal surface.

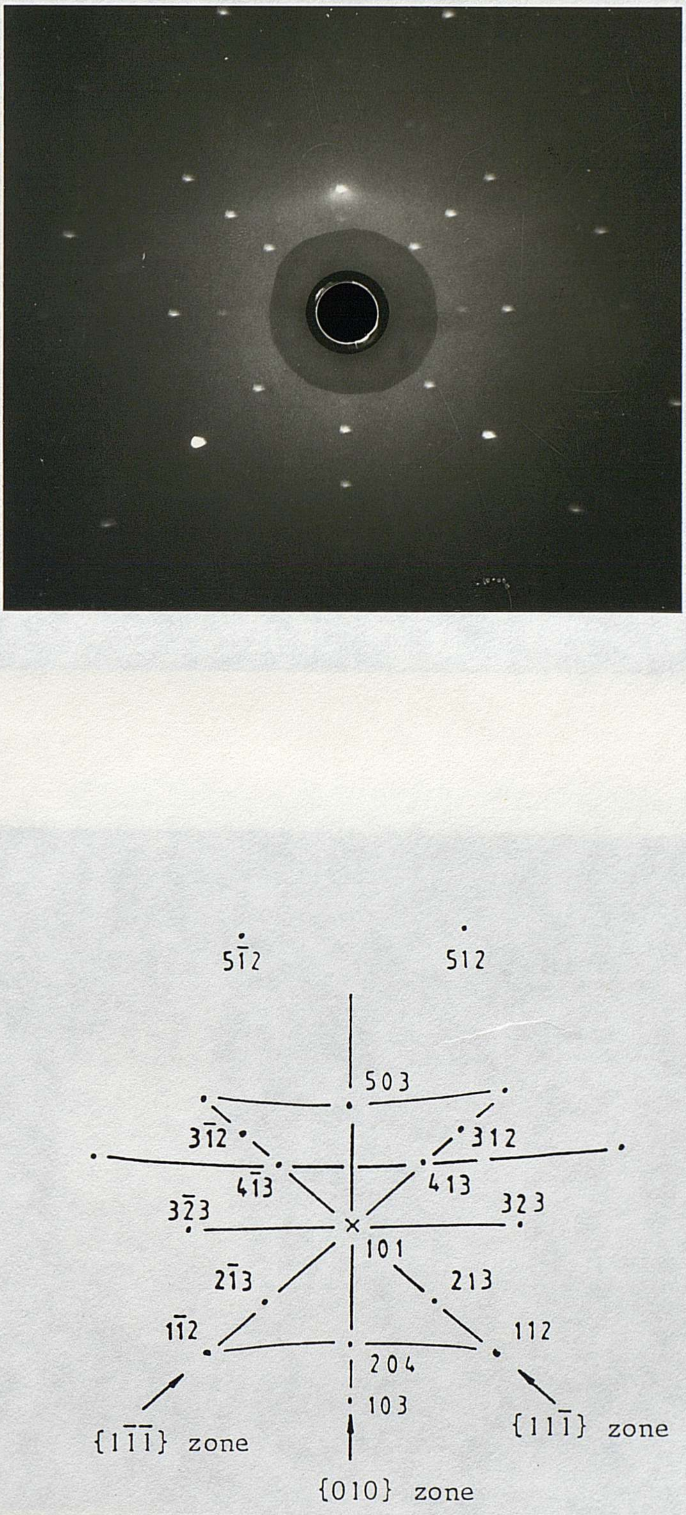

FIG. 4.7 Laue x-ray diffraction photograph and key from the Sn(101) single crystal.

(a)

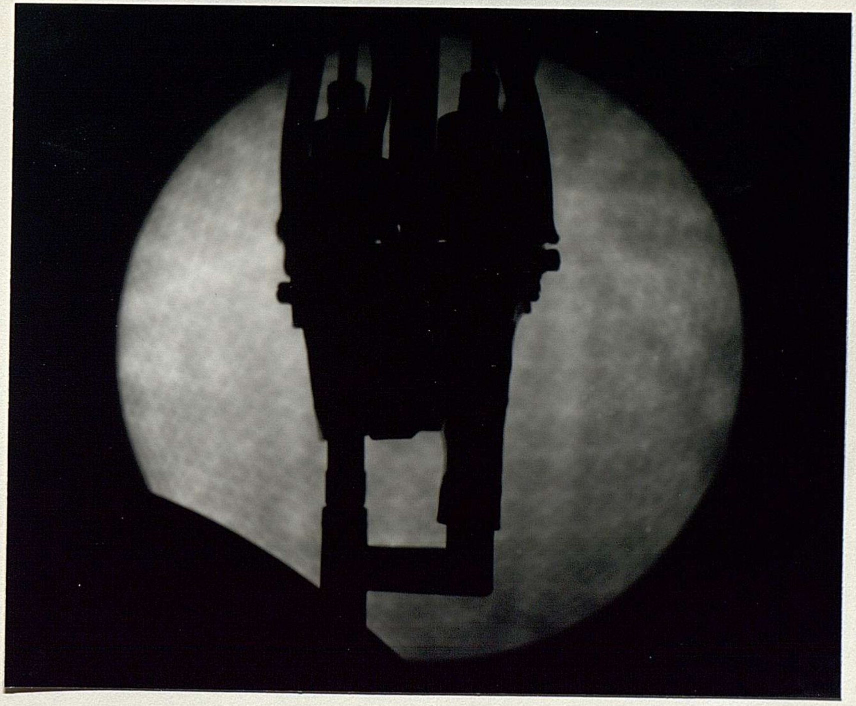

(b)

FIG. 4.8 Kikuchi patterns from (a) the (001) surface (b) the (101) surface, using the Auger gun at 20° angle of incidence to the surface planes.

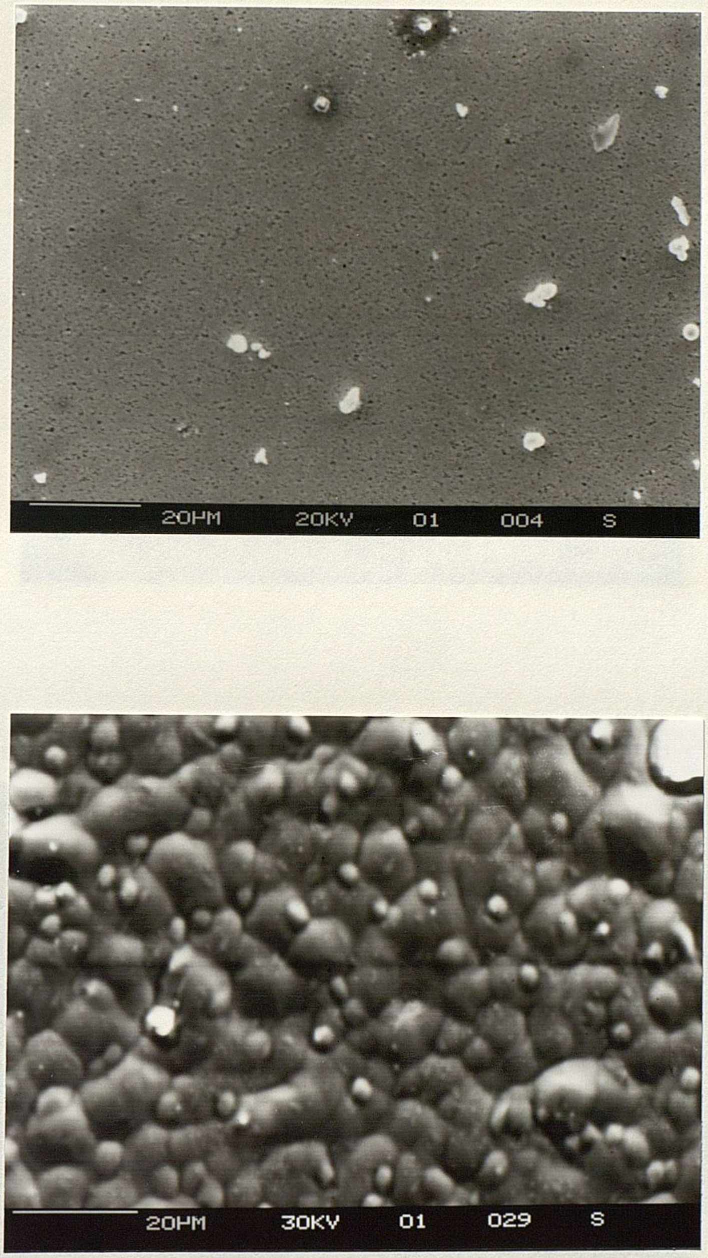

FIG. 4.9 Scanning electron micrographs from the Sn(001) single crystal surface after:

(a) Polishing, and before experimentation under UHV.

(b) Extensive argon ion bombardment and experimentation under UHV.

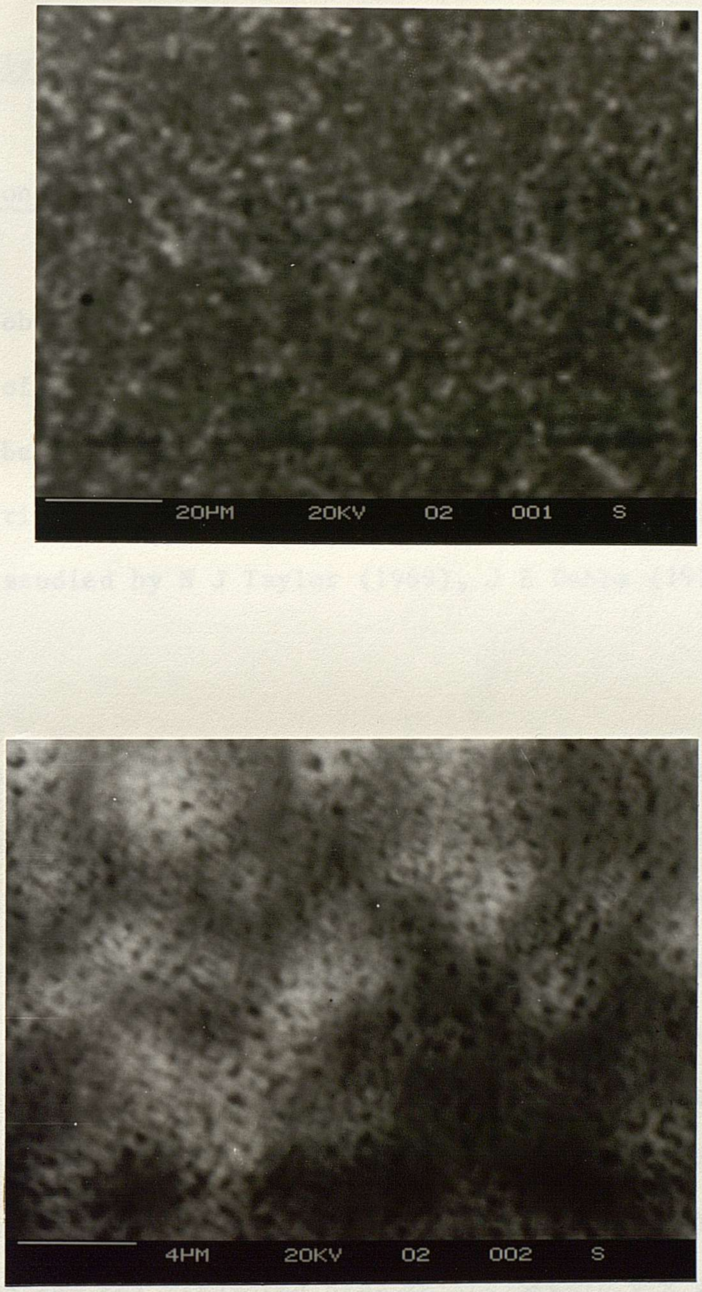

FIG. 4.10 Scanning electron micrographs of Sn(101) after extensive polishing with successive size diamond pastes, and before placing in the vacuum chamber.

4.6 SURFACE EXAMINATION TECHNIQUES

(a) Chemical Analysis

(i) Auger electron spectroscopy (A.E.S.)

Auger spectra were obtained using the four-grid retarding field analyser (R.F.A.). The use of a L.E.E.D optics for studying Auger spectra was first mentioned by R E Weber et al (1967). The experimental operating conditions and design characteristics affecting the resolution and sensitivity of such analysers has been studied by N J Taylor (1969), J E Dabbs (1973), and G P Hopkins (1976).

A schematic diagram of the arrangement used in obtaining spectra is shown in fig. 4.11. Initial ionization of the atoms of the sample surface was accomplished by the use of a beam of energy 2.5 keV, and current 7.5 - 15μA, at an angle of 20° incidence to the surface plane for maximum signal (L A Harris, 1969). A first order differential energy distribution of the emitted secondary electrons could be obtained by applying a retarding ramp to the grids of the R.F.A., which thus acted as a high pass filter allowing only electrons of energy $E \geqslant eV$ (V being the retarding potential) to be detected. The use of two grids for the retarding bias in the 4-grid R.F.A. improves the resolution by up to an order of magnitude over that of a 3-grid R.F.A. for which only one grid is used (N J Taylor, 1969). In the case of the 3-grid R.F.A., potential variations in the holes of the mesh lead to reduced resolution.

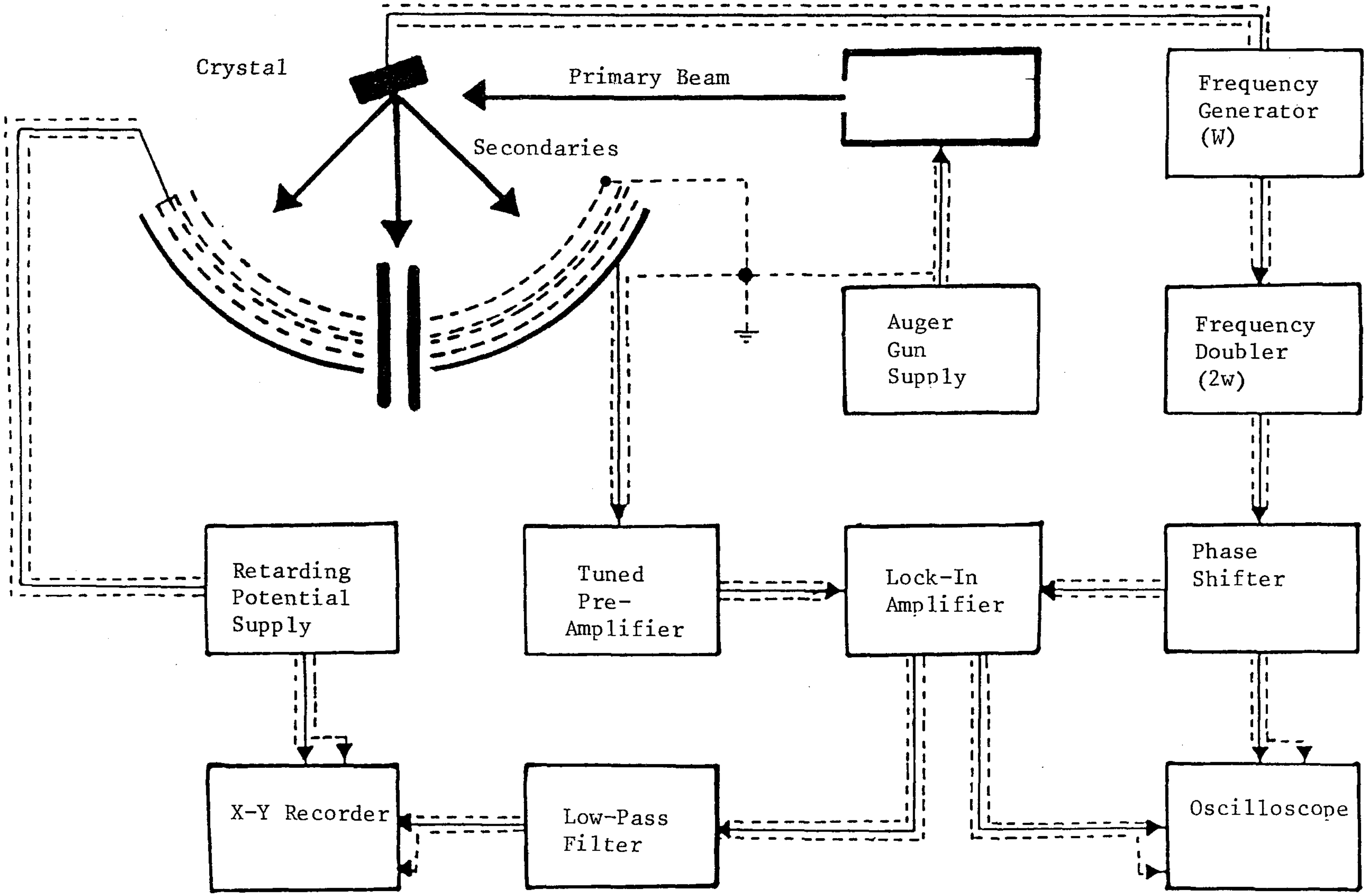

FIG. 4.11 Experimental arrangement for Auger electron spectroscopy. Crystal modulation is depicted in this case.

Signal modulation and phase-sensitive detection were used to distinguish the Auger peaks from the slowly varying secondary electron background, and reduce the noise levels.

Various short-circuits which occurred on different occasions necessitated the use of two modes of operation of the analyser: either the crystal could be earthed with the retarding ramp and modulation being applied to the centre two grids, the remaining two grids being earthed; or the crystal could be modulated about earth with the first grid at earth, and the retarding bias being applied to the remaining three grids. In the former mode the earthed fourth grid acted as a shield reducing the capacative coupling between the modulated grids and the collector. It was also necessary to apply a 67V positive bias to the collector to ensure that most of the secondaries emitted by the collector were returned to it, whereas in the latter case this was not necessary as the retarding potential on the fourth grid effectively applied a retarding field between the fourth grid and the collector. There was also no noticeable coupling between the crystal and the collector.

As retarding field analysers operate as high pass filters, the detected current I(V) for an applied retarding potential V is given by:

$$I(V) = \int_{V}^{\infty} N(V)\, dV \qquad (4.1)$$

where N(V) is the number of electrons with energy eV. In order to obtain an energy distribution, equation 4.1 must be differentiated. Experimentally this is done by applying the modulation voltage $\Delta V = Vo \sin wt$ onto the retarding voltage V. The detected current can be written as a Taylor expansion about the retarding voltage V:

$$\begin{aligned} I(V + \Delta V) &= I(V) + dI/dV\,\Delta V + \tfrac{1}{2}!\ d^2I/dV^2\,(\Delta V)^2 \\ &+ 1/3!\ d^3I/dV^3\,(\Delta V)^3 + \tfrac{1}{4}!\ d^4I/dV^4\,(\Delta V)^4 + \ldots \\ &= I(V) + \{Vo\ dI/dV + (Vo^3/8)\ d^3I/dV^3 + \ldots\}\ \sin wt \\ &- \{(Vo^2/4)\ d^2I/dV^2 + (Vo^4/48)\ d^4I/dV^4 + \ldots\}\ \sin 2wt \end{aligned} \tag{4.2}$$

For small modulation amplitudes (Vo) the fundamental frequency component of the detected current is proportional to dI/dV (N(V)), and the first harmonic component to d^2I/dV^2 (N'(V)). In the experiments a low modulation voltage (3V peak-to-peak) was used in the low energy (35eV-120eV) region of the secondary distribution with a rapidly varying background, and a higher modulation (8V peak-to-peak) at higher energies than this where the background is slowly varying. When the modulation was applied to the grids there was a capacitively-coupled signal at frequency w which had to be annulled by applying a sinusoidal signal, frequency w, which was 180° out of phase with the detected signal.

A plot of the energy distribution results in small Auger peaks on a high secondary background. In practice the derivative of the energy distribution (N'(V) vs. eV) was measured so that the Auger peaks were accentuated and the slowly-varying background of secondaries was diminished. This was accomplished by passing the signal from the collector through a tuned amplifier with a resonant frequency of 2w. Hence the detected current was $I \,\alpha N'(eV)$.

The resonant frequency of 2w = 4.6kHz was in a region in which the noise level was low, and the frequency response good for the amplifier (R Nathan et al, 1973). By using standard phase sensitive detection techniques a low noise d.c. signal could be measured on a chart recorder at any particular retarding voltage. Spectra were obtained by scanning over a range of retarding voltages.

(ii) Electron energy loss spectroscopy (E.L.S. or E.E.L.S)

The mean free path of electrons in most solids is a minimum for electrons with energies less than 100eV (fig. 4.12). Thus for maximum surface sensitivity a beam of energy 67 - 70eV and current $\leqslant$ 0.5μA was used. The beam was supplied by the L.E.E.D gun and aligned on the sample at normal incidence by L.E.E.D. The detection system for E.L.S. (fig. 4.13) was the same as for A.E.S. except that in E.L.S. the modulation voltage was applied to the grids throughout. A modulation voltage of 3V peak-to-peak was used.

The loss spectra obtained after oxidation of the Sn(001) and Sn(101) single crystal surfaces were compared with those obtained in previous studies in order to be able to identify the oxidation state of the observed oxides.

(b) Structural analysis by low energy electron diffraction (L.E.E.D)

Diffraction patterns were observed in the range 20 - 250eV. The beam current from the Varian model 981-2125 off-axis electron gun (with a hot tungsten filament) was typically 0.2 - 0.5μA.

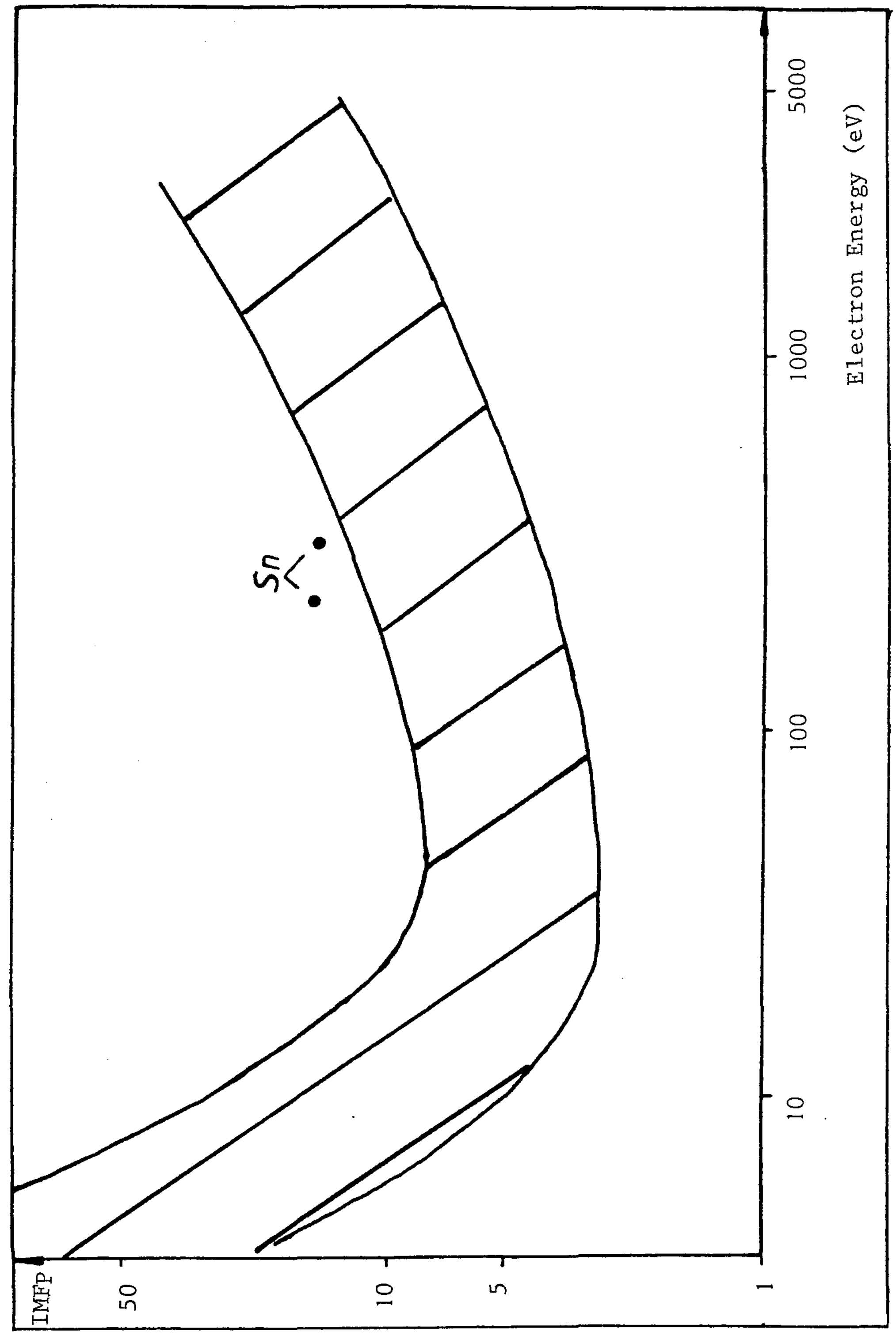

FIG. 4.12 Inelastic mean free paths (I.M.F.P) as a function of electron energy above the Fermi level.
(C R Brundle, 1977; C J Powell, 1974 (tin values)).

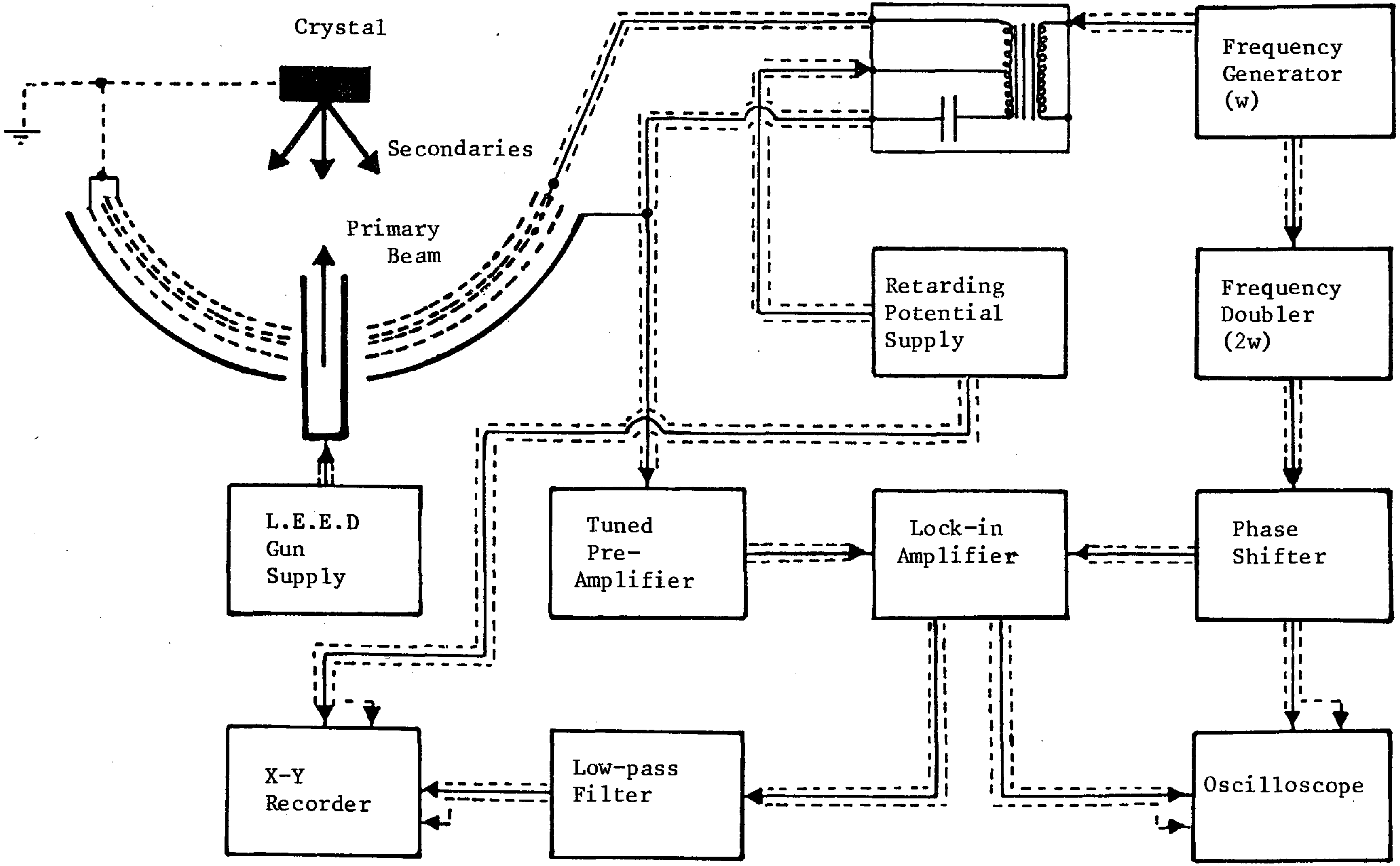

FIG. 4.13 Experimental arrangement for electron energy loss spectroscopy (ELS).

The L.E.E.D optics had an acceptance angle of 120°. The sample surface was positioned at the centre of curvature of the optics by using the Auger gun and observing the shadow cast on the viewport on the opposite side of the chamber. The manipulator was moved until the crystal shadow lined up with a marker at the centre of the viewport. The crystal and first grid of the optics were at earth potential and the diffracted electrons initially passed through a field- free region. A potential which could be varied within 0 to -9V of the primary beam potential was applied to the remaining grids in order to suppress the inelastic secondaries. The electrons were then accelerated by a + 7kV potential onto the fluorescent screen.

Measurements from photographs of the observed patterns indicated a small amount of distortion possibly due to magnetic fields. Very little intensity analysis was undertaken as the beam current from the electron gun would increase with energy, and there was no correction for magnetic field effects.

CHAPTER 5

ELECTRON SPECTROSCOPIC RESULTS

5.1 INTRODUCTION

In order to be able to compare the results of the present study with those of Rider (1981), the experimental conditions and the presentation of the results in this chapter have been kept as close as possible to that study. The main difference lies in presentation of the oxygen uptake curves. In the present study the more usual style of presentation of the ratio adsorbate/substrate Auger signals has been adopted. For a short period after bakeout adsorption of mercury (originating from the diffusion pumps) was found to occur at low temperatures. Although the experimental set-up did not facilitate detailed study, those results which could be taken have been discussed in section 5.6.

5.2 THE CLEAN SURFACE

The Auger spectra taken after pumpdown from atmosphere to u.h.v. revealed identical contaminants on all the tin surfaces studied to date: carbon, sulphur, chlorine, and oxygen have always been present in varying concentrations (fig. 5.1), the chlorine having been found to desorb under the primary electron beam of the Auger gun whereas little change occurred in the signals of the other contaminants (fig. 5.2 and Rider, 1981). The main tin Auger peaks were also always present.

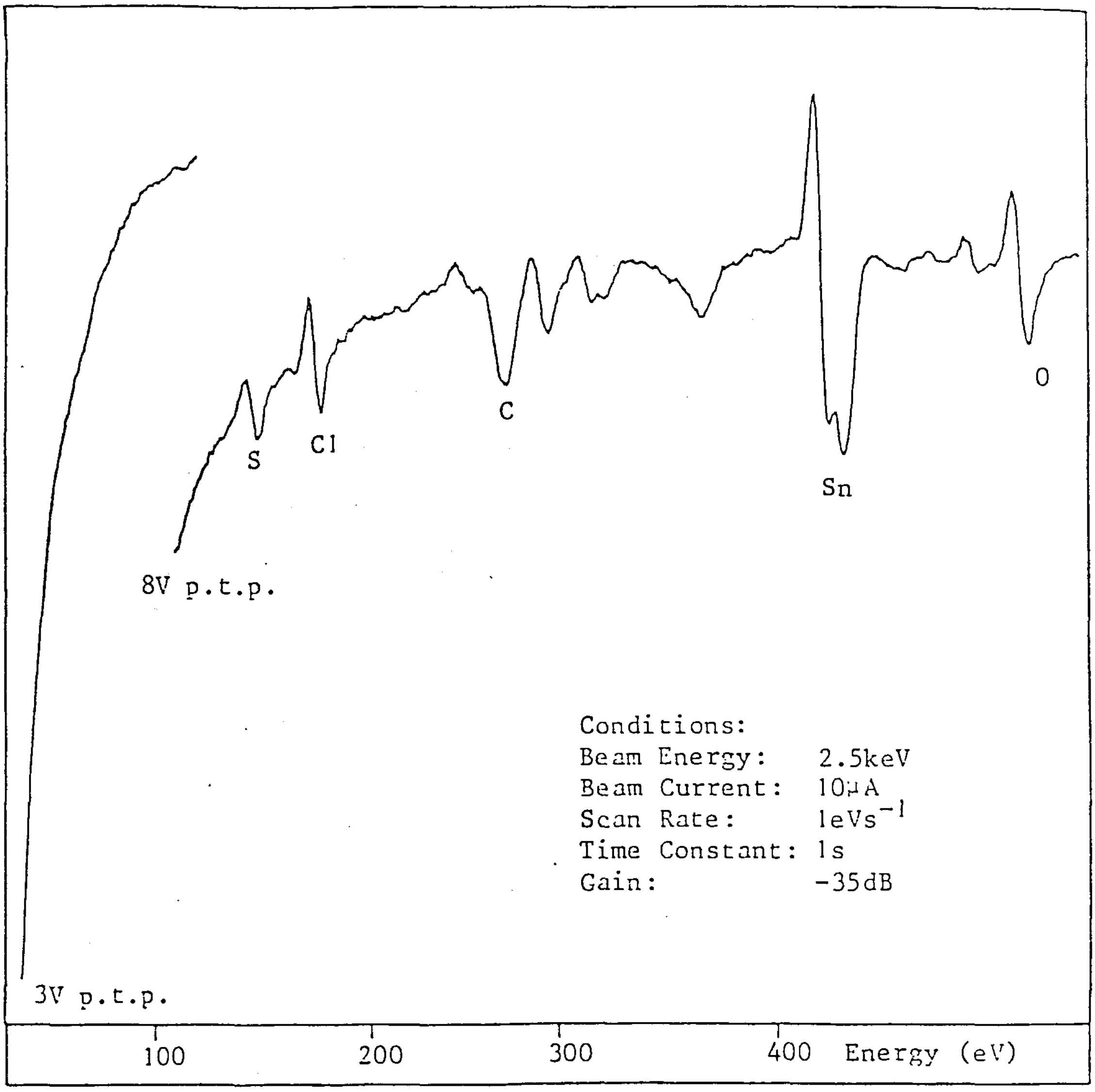

FIG. 5.1 Auger spectrum of tin after bakeout.

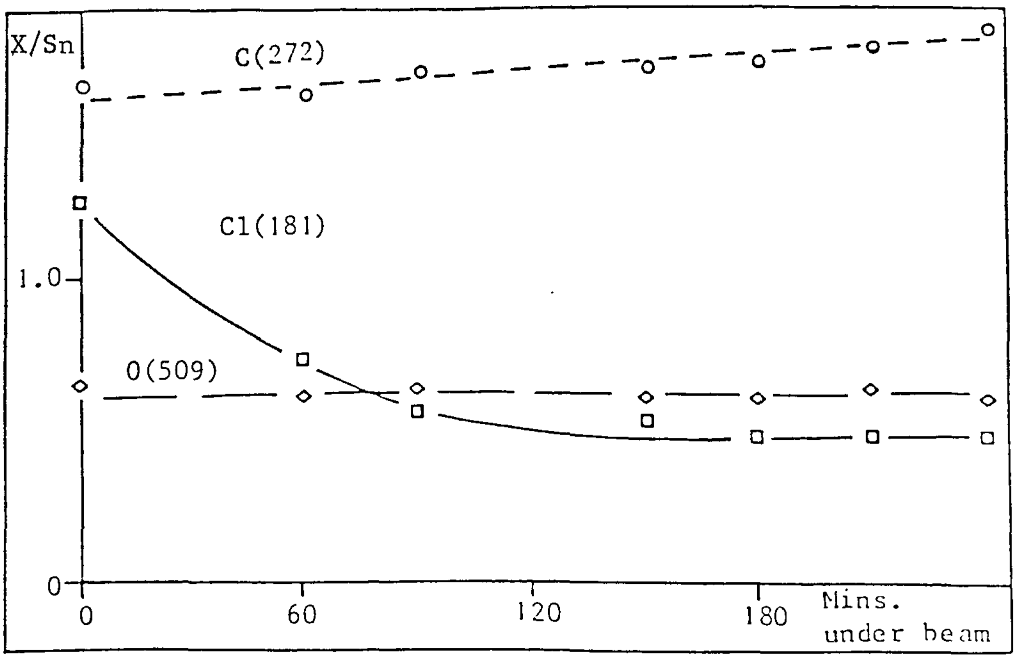

FIG. 5.2 Desorption of chlorine under 15μA, 2.5 keV electron beam.

A typical first order differentiated Auger spectrum obtained from the clean surface is shown in fig. 5.3. The principal Auger transitions (300-500V) are well documented in the literature. Peaks seen at 413eV and 421eV in the present study have been attributed to bulk plasmon losses from the $M_{4,5}$ $N_{4,5}$ $N_{4,5}$ Auger transitions by R A Powell (1979). Minor peaks in the range 0 - 300 V were assigned by Rider (1981). The minor peak seen by Rider at 130V was not seen in the present study, and the peak at 108V was rarely seen in both studies. Fig. 5.9 lists all the Auger transitions detected in the present study.

The electron energy loss spectrum of clean tin (fig. 5.4) showed losses at 10V and 14V as well as at multiples of these voltages. Previous studies (e.g. Bayat-Mokhtari et al, 1979)have assigned the 10V loss to a surface plasmon excitation, and the 14V loss to a bulk plasmon excitation. Further losses were also seen at 5V and 63V in the present study. The loss at 5V was considered by Bayat-Mokhtari et al to be either the $\Gamma_5^+ - \Gamma_4^-$ interband transition identified by R A Macrae et al (1967), and by Rasigni et al (1966), or the presence of a small amount of oxide below the detection limit of Auger electron spectroscopy. Rider (1981) suggested the possibility of the presence of a small amount of SnO after consideration of the E.L.S. spectra by C J Powell (1960). In a recent study by A J Bevolo et al (1982) this loss was suggested to be caused by an intraband transition. The loss at ≃ 25V in the present study was identified as an interband transition by R A MacRae et al. A J Bevelo et al noted a doublet with losses at 24.0V and 25.0V and labelled them as 4d Sn interband transitions.

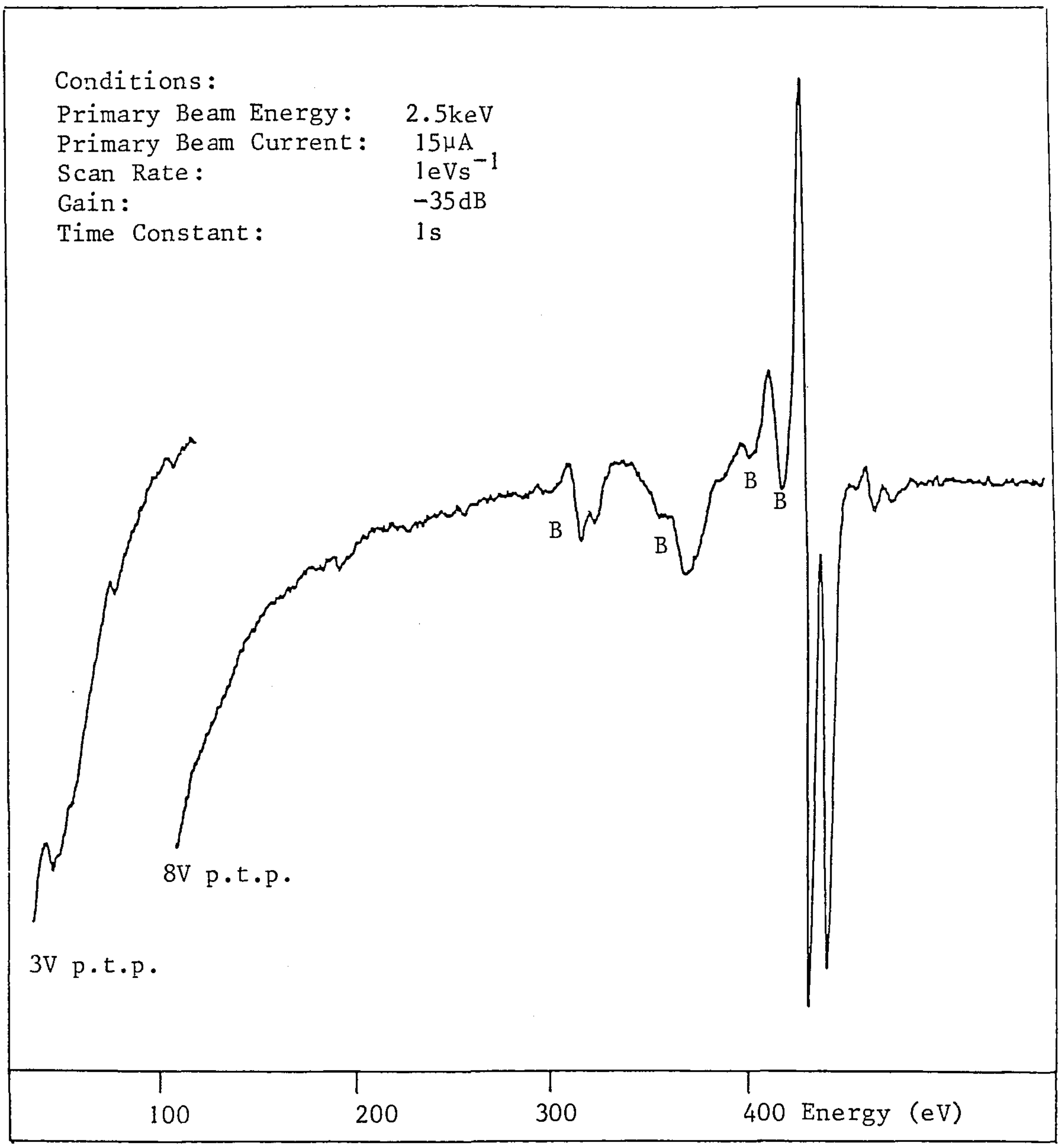

FIG. 5.3 The clean tin Auger spectrum.
Labels 'B' denote bulk plasmon losses.

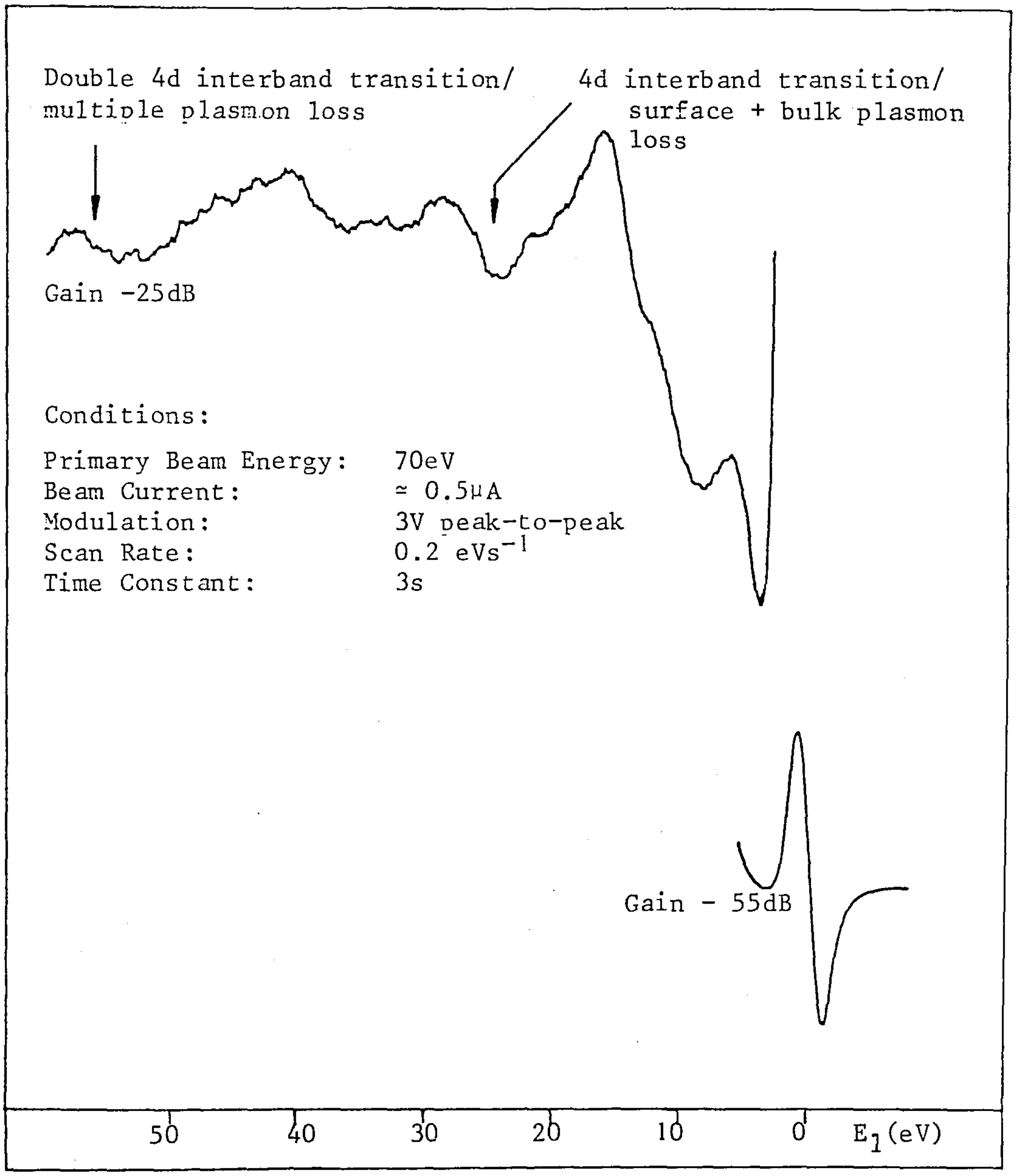

Conditions:

Primary Beam Energy:	70eV
Beam Current:	≃ 0.5μA
Modulation:	3V peak-to-peak
Scan Rate:	0.2 eVs^{-1}
Time Constant:	3s

FIG. 5.4 Electron energy loss spectrum of tin after cleaning by ion bombardment.

Other previous studies have also labelled these losses as multiple plasmon excitations. Both losses may contribute to the observed features. The loss at ≃ 63V seen in the present study has been labelled as a double 4d interband transition.

5.3 THE OXIDISED SURFACES

Oxidation to saturation of both the (001) and (101) surfaces at 5×10^{-7} torr led to the attenuation of all the tin Auger transitions (fig. 5.5). In particular those transitions involving valence electrons were greatly attenuated or disappeared (figs. 5.5,6). The width of the major Auger transitions was unaltered after oxidation of Sn(101) under all conditions; or for Sn(001) at 293K and 440K. There were also no shifts in the positions of the main Auger transitions after oxidation under these conditions. No shifts were noted by Rider after his oxidation studies under similar conditions on other tin single crystal surfaces. The relative sizes of the $M_4 N_{4,5} N_{4,5}$ and $M_5 N_{4,5} N_{4,5}$ transitions were notably different before and after oxidation. Although attenuated, the presence of the bulk plasmon loss after oxidation indicates that only a thin oxide layer was formed and that the $M_{4,5} N_{4,5} N_{4,5}$ transitions contained a component from the underlying bulk metallic tin.

Oxidation of Sn(001) at 135K led to the attenuation of all the major tin Auger transitions and the disappearance of all the minor peaks apart from the $M_3 M_4 N_{4,5}$ transition (fig. 5.7). Shifts were observed in the positions of all the Auger peaks remaining after oxidation.

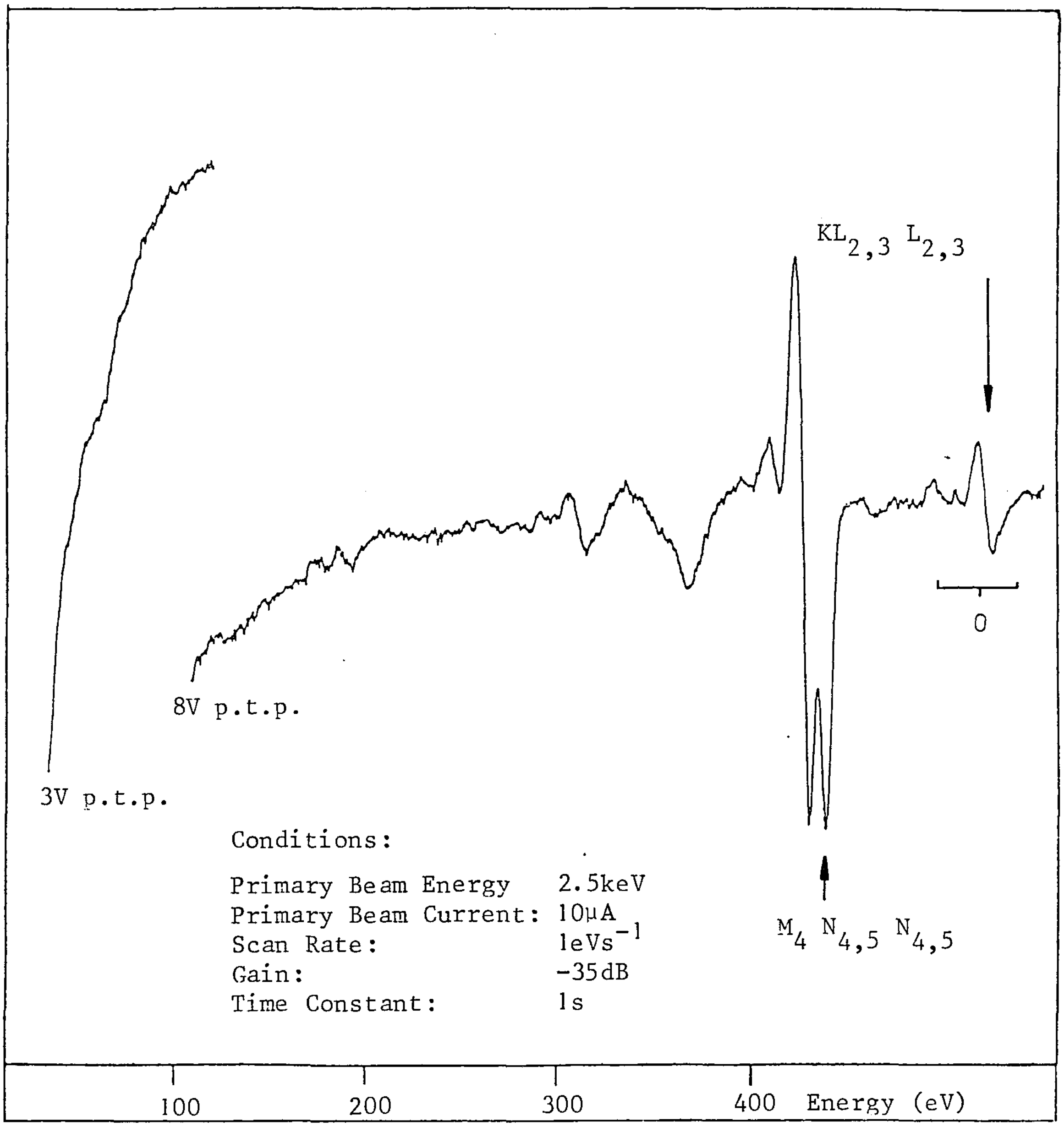

FIG. 5.5 Auger spectrum after oxidation of Sn(001) (except 135K) and Sn(101).

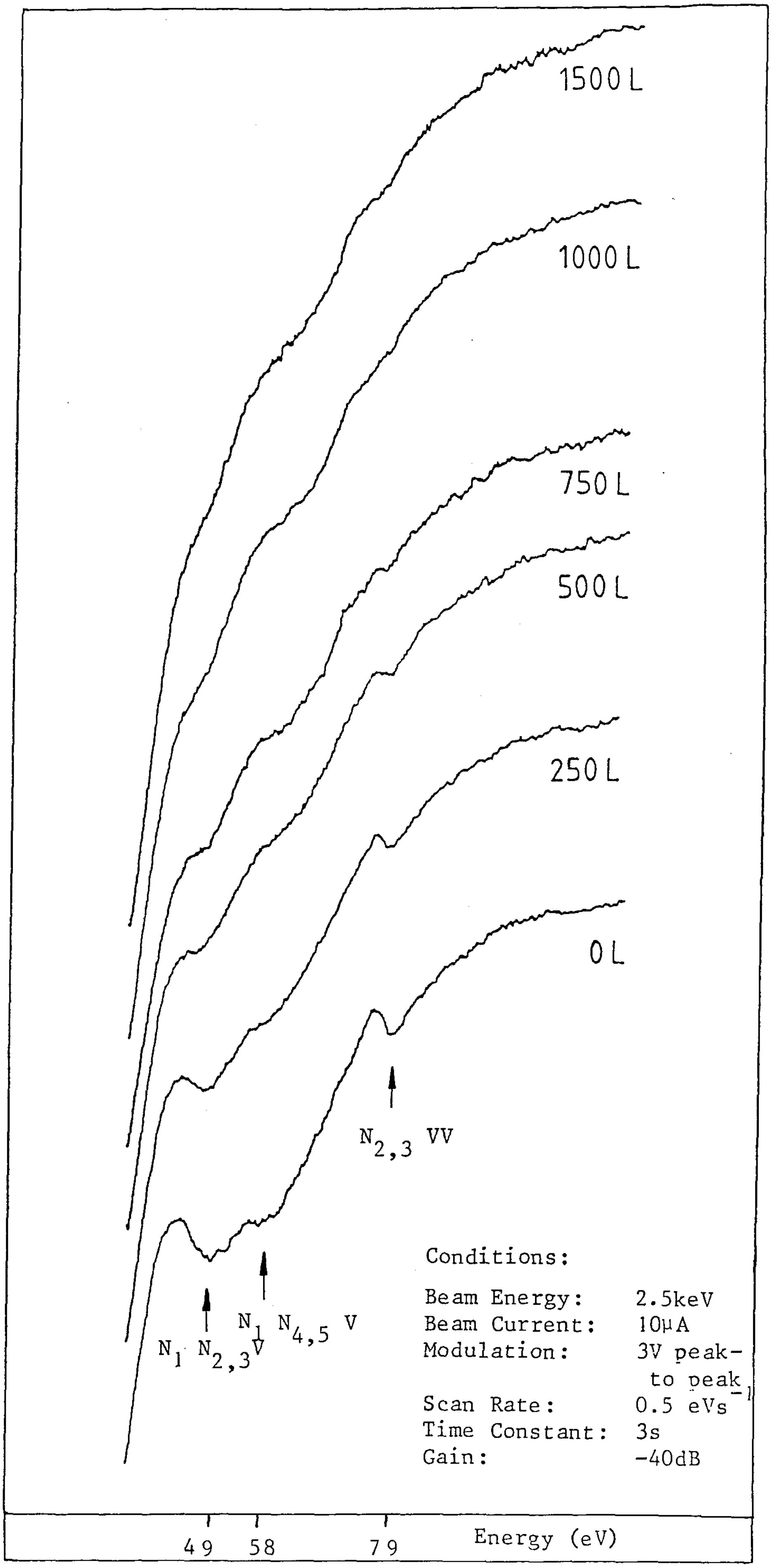

FIG. 5.6 Attenuation of the low energy Auger transitions of tin involving valence electrons during the oxidation of Sn(001) at 293K.

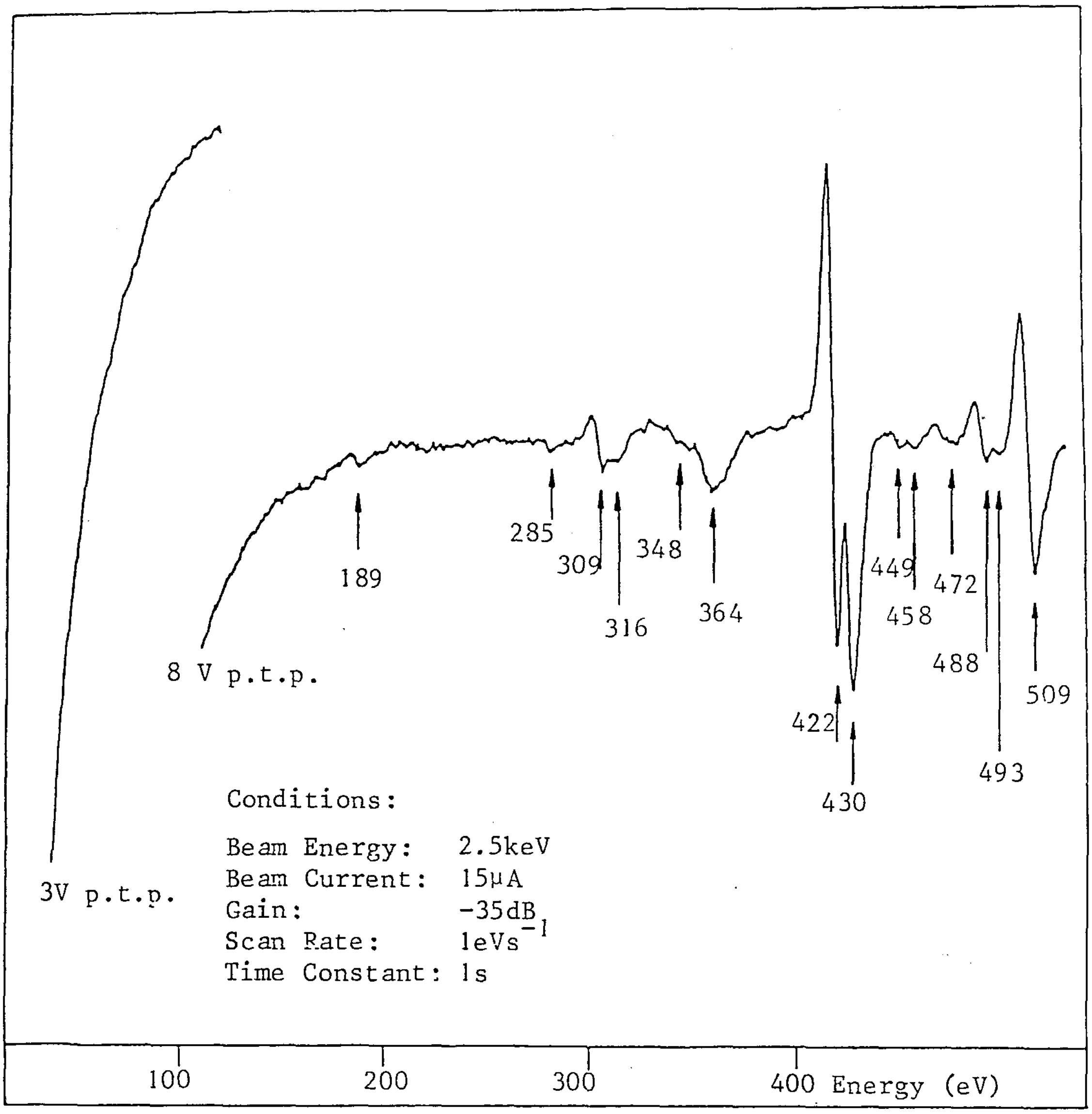

FIG. 5.7 Auger spectrum after 10,000L oxidation of Sn(001) at 135K.

In some of the experiments there was a marked period (figs. 5.8 b,c) during which the major shift in the $M_4\ N_{4,5}$ and $M_5\ M_{4,5}\ N_{4,5}$ transitions was seen to take place. Before this period (fig.5.8a) there was mainly attenuation of these peaks apart from a 1eV shift in their energies. The total shift of 5eV was completed by 8000L exposure. A summary of all the Auger peak shifts observed is given in fig. 5.9.

The bulk plasmon peaks had also disappeared after oxidation at 135K suggesting that a thicker oxide had formed on the (001) surface at this temperature than was present after oxidation at 293K or 440K. The disappearance of the bulk plasmon peaks also implies that the tin Auger peaks had no component from the underlying bulk tin but resulted from the oxide layer.

Previous studies on SnO and SnO_2 give conflicting values for the shifts of their $M_4\ N_{4,5}\ N_{4,5}$ and $M_5\ N_{4,5}\ N_{4,5}$ Auger transitions compared with clean tin values. Sen (1981) gives values of 7 ± 1 eV for SnO_2 and 3 ± 1 eV for SnO, whereas Wagner et al and R Powell have stated that both oxides exhibit a shift of 5eV.

The E.L.S. spectrum taken after oxidation of Sn(001) at 135K was identical to those taken after oxidation of both Sn(001) and Sn(101) under all other conditions considered (figs. 5.10,11).

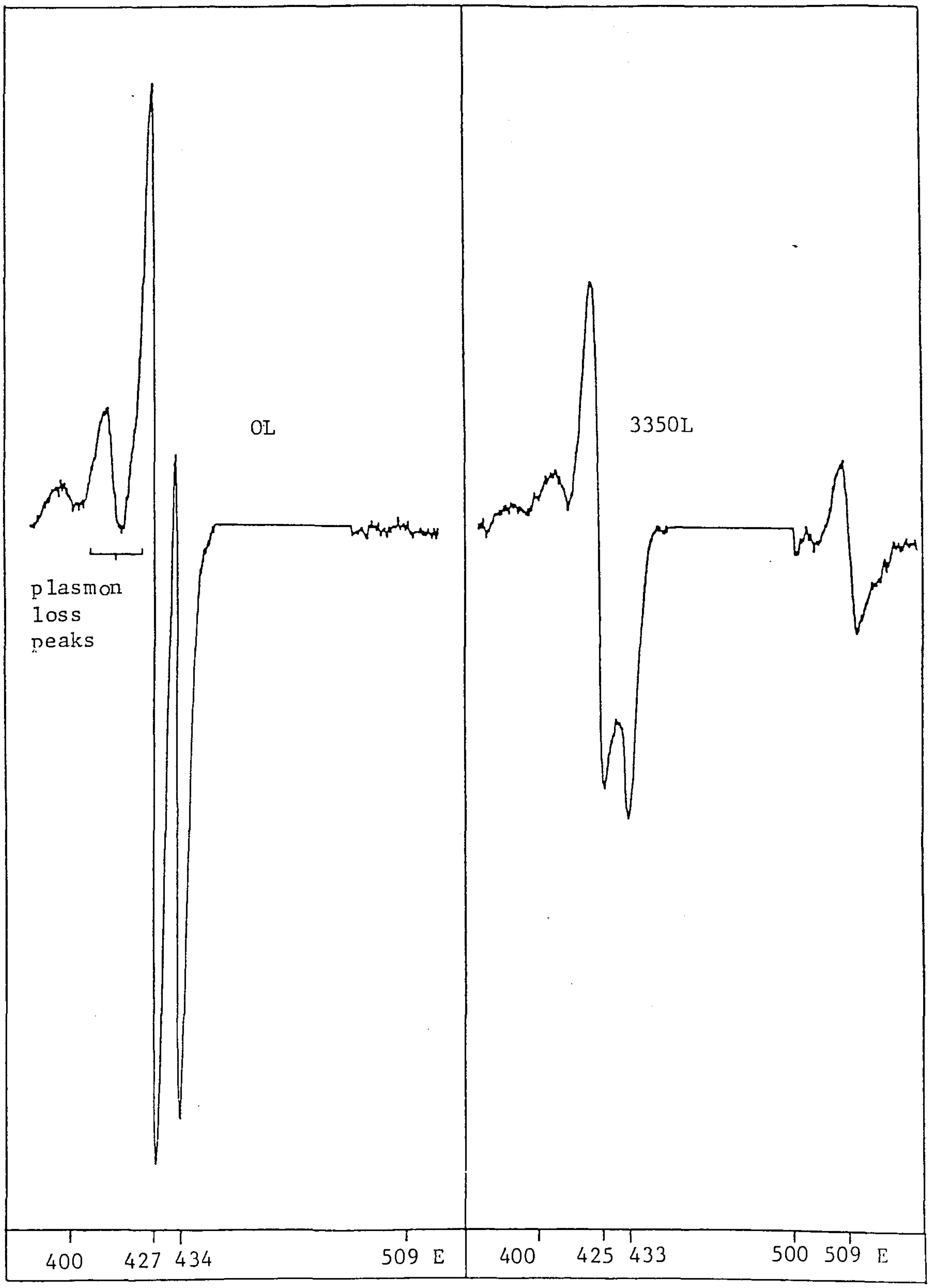

FIG. 5.8a The tin $M_{4,5}N_{4,5}N_{4,5}$ and oxygen $KL_{2,3}L_{2,3}$ Auger transitions during the oxidation of Sn(001) at 135K. The oxygen pressure was 5.0×10^{-7} torr.

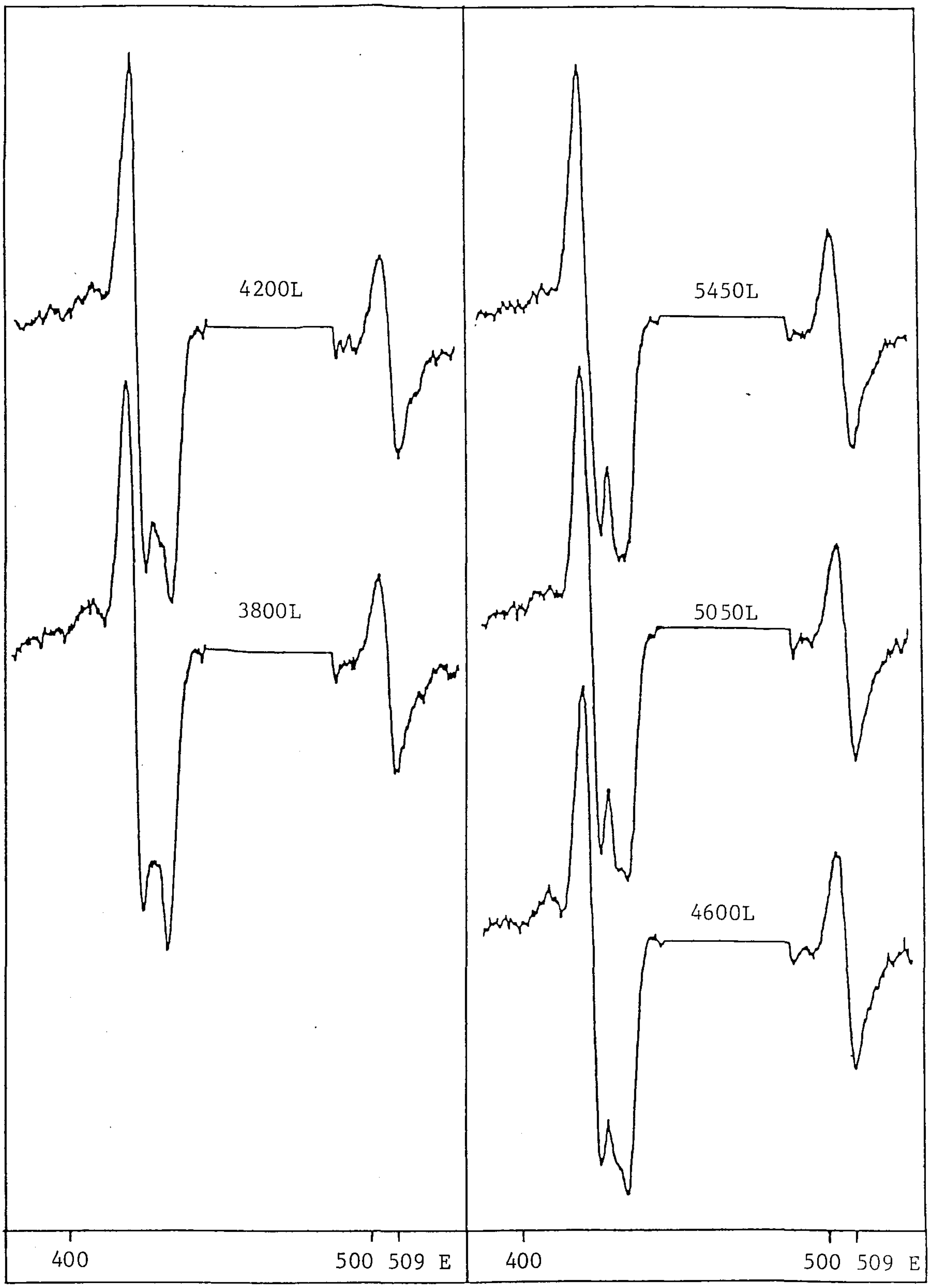

FIG. 5.8b The tin $M_{4,5}$ $N_{4,5}$ $N_{4,5}$ and oxygen $KL_{2,3}$ $L_{2,3}$ Auger transitions during the oxidation of Sn(001) at 135K.

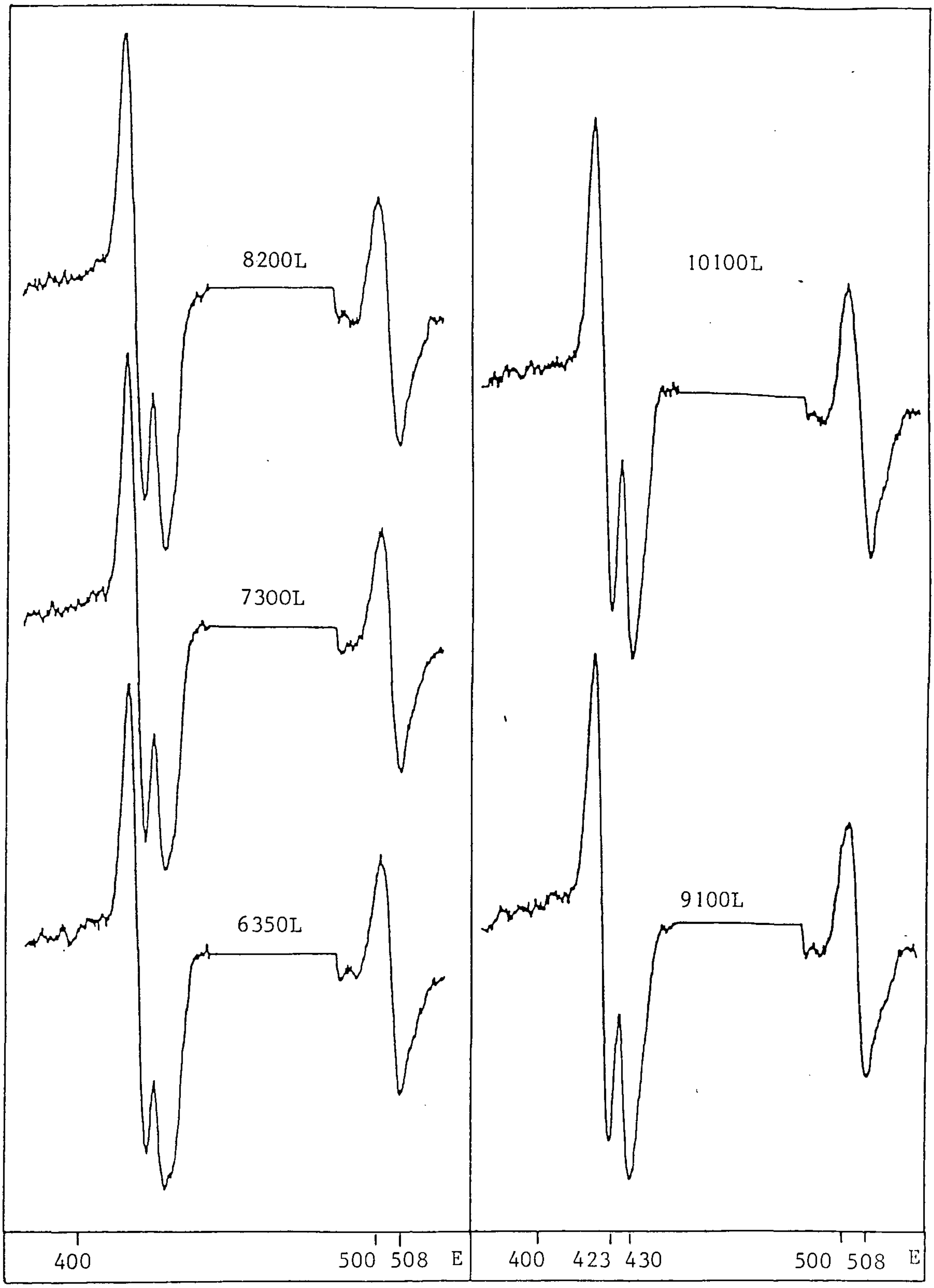

FIG. 5.8c The tin $M_{4,5}$ $N_{4,5}$ $N_{4,5}$ and oxygen $KL_{2,3}$ $L_{2,3}$ Auger transitions during the oxidation of Sn(001) at 135K. The oxygen pressure was increased from 5.0×10^{-7} torr to 1.0×10^{-6} torr after 5450 L exposure.

TRANSITION	ENERGY FOR CLEAN SURFACE/eV	ENERGY SHIFT AFTER 10,000L OXIDATION OF Sn(001) AT 135K (WHERE OBSERVED)/eV	
$N_1\ N_{2,3}\ V$	48/49		
$N_{2,3}\ N_{4,5}\ V$	58		
$N_{2,3}\ V\ V$	79		
$N_1\ N_{4,5}\ V$	108		
$M_2\ M_5\ N_{2,3}$	181 - 183		
$M_3\ M_4\ N_{4,5}$	194/195		
$M_2\ M_4\ N_{4,5}$	226/227		
$M_5\ N_1\ N_{4,5}$	315	-3 to -5	poorly resolved
$M_4\ N_1\ N_{4,5}$	321	-3 to -5	
$M_5\ N_{2,3}\ N_{4,5}$	364 - 366	-3	
$M_5\ N_{4,5}\ N_{4,5}$	427	-5	
$M_4\ N_{4,5}\ N_{4,5}$	435	-5	
$M_5\ N_{4,5}\ V$	455/456		
$M_4\ N_{4,5}\ V$	464/465	-5	

FIG. 5.9 Summary of the observed Auger transition for tin, and the shifts observed on oxidation of Sn(001) at 135K.

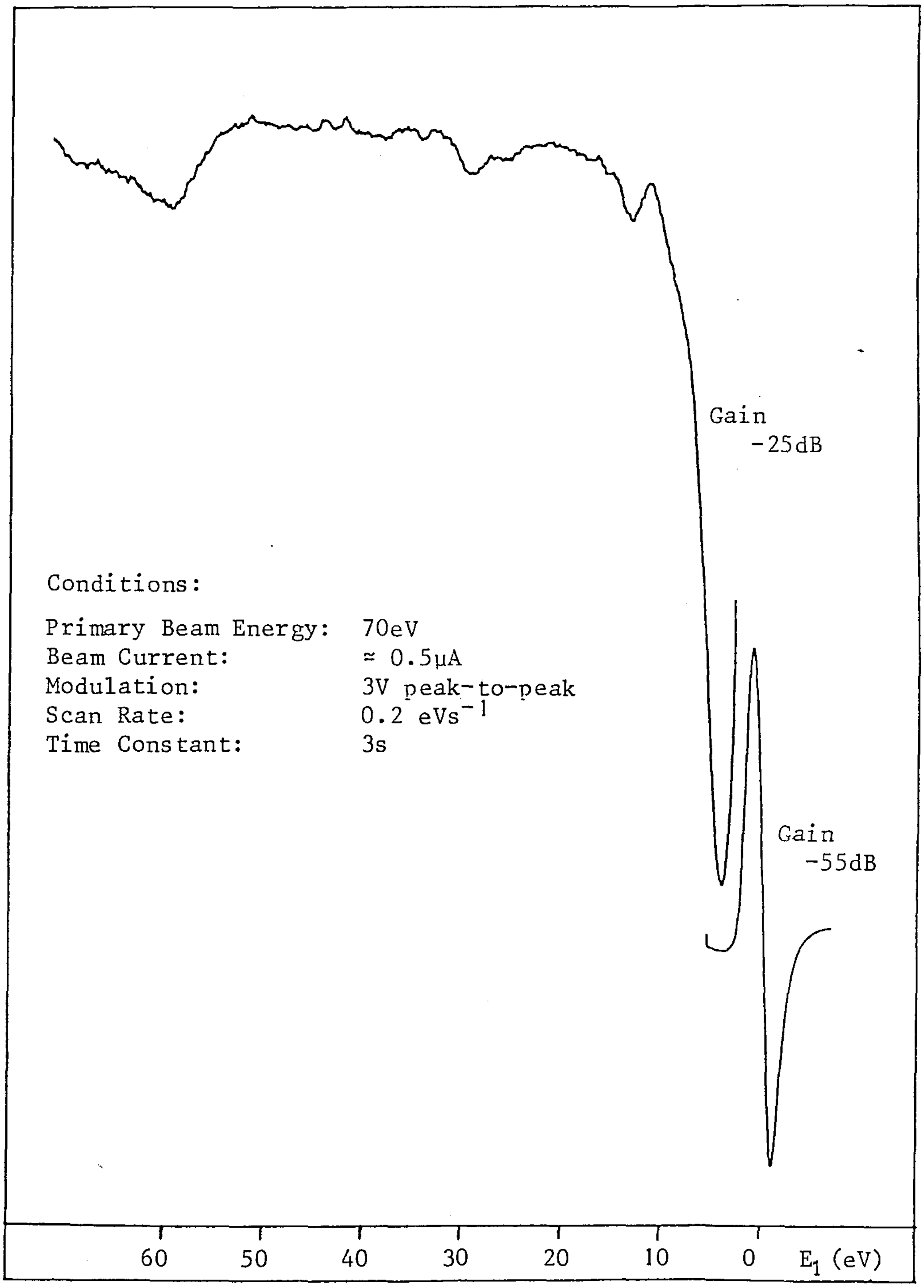

Conditions:

Primary Beam Energy: 70eV
Beam Current: ≈ 0.5μA
Modulation: 3V peak-to-peak
Scan Rate: 0.2 eVs^{-1}
Time Constant: 3s

FIG. 5.10 Electron energy loss spectrum of oxidised tin.

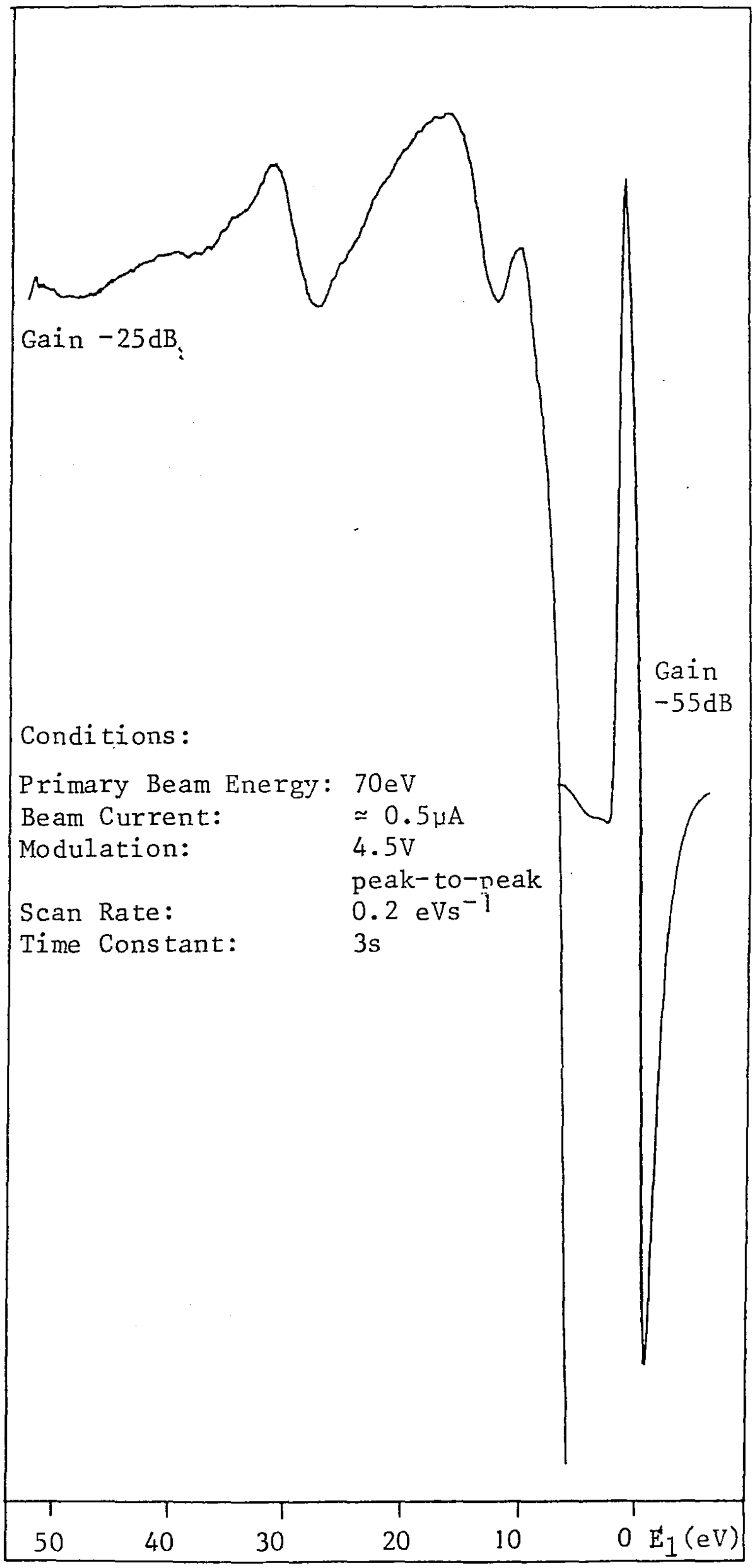

FIG. 5.11 Expanded electron energy loss spectrum after the oxidation of tin.

After oxidation, the ratio of the oxygen to tin Auger peaks was measured as the angle of incidence of the primary electron beam was varied (figs. 5.12-14). This measurement was taken in order to be able to determine the relative positions of the oxygen and tin atoms with respect to the surface. Christmann et al (1972) have stated that the Auger electrons originate from a layer of thickness $d = \ell \sin\theta$, where θ is the angle of incidence (fig. 5.12) and ℓ is the mean free path of the primary electrons. Thus as θ is reduced a higher proportion of the detected Auger signal will originate from the surface layer.

Care has to be taken in interpreting such angular distribution curves, in particular for single crystal substrates. Rusch et al (1973) have found maxima occurring in Auger electron signal intensities when the primary beam axis is parallel to the directions of intensity maxima in the Kikuchi pattern. Diffraction effects in the angular distribution of Auger electrons have been further considered by Anderson et al (1975). Although the retarding field analyser accepts electrons over a wide acceptance angle, the range of emission angles accepted from the sample surface changes as the excitation angle (θ) is varied. Any changes in the emission angle dependence, or the excitation angle dependence, of the overlayer and substrate Auger signals could affect the O/Sn peak height ratios.

A study by Rawlings et al (1976) of oxygen, sulphur, and lead on single crystal silver, found that the adsorbate/adsorbent peak height ratios followed the trends expected for their respective distributions on the surface.

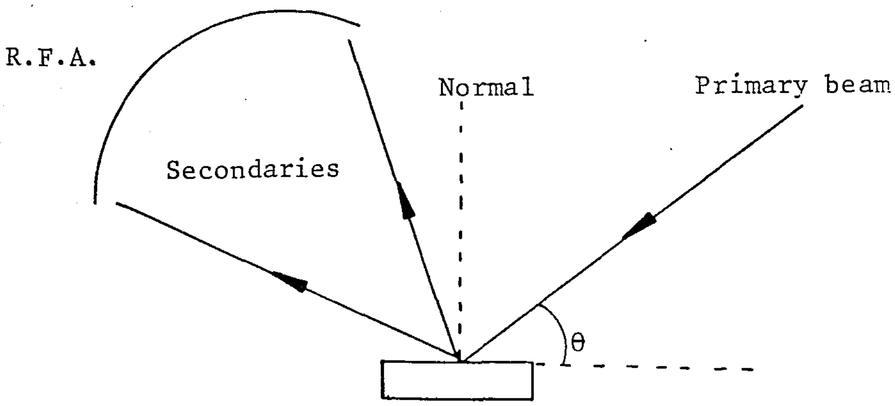

FIG. 5.12 Experimental arrangement for the performance of angular Auger studies after oxidation.

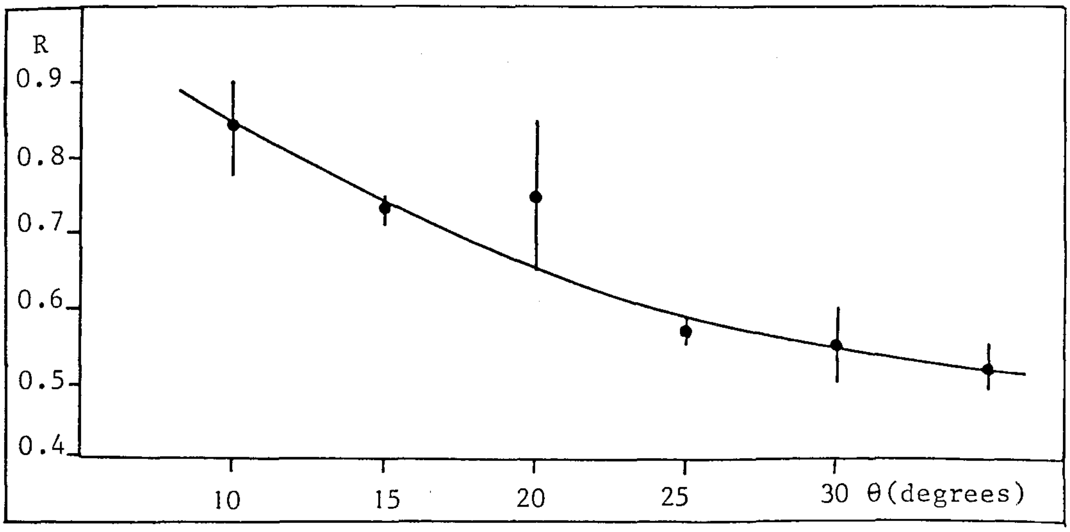

FIG. 5.13 Ratio (R) of the oxygen to tin Auger peaks at various primary beam incidence values after oxidation of Sn(001) at 293K.

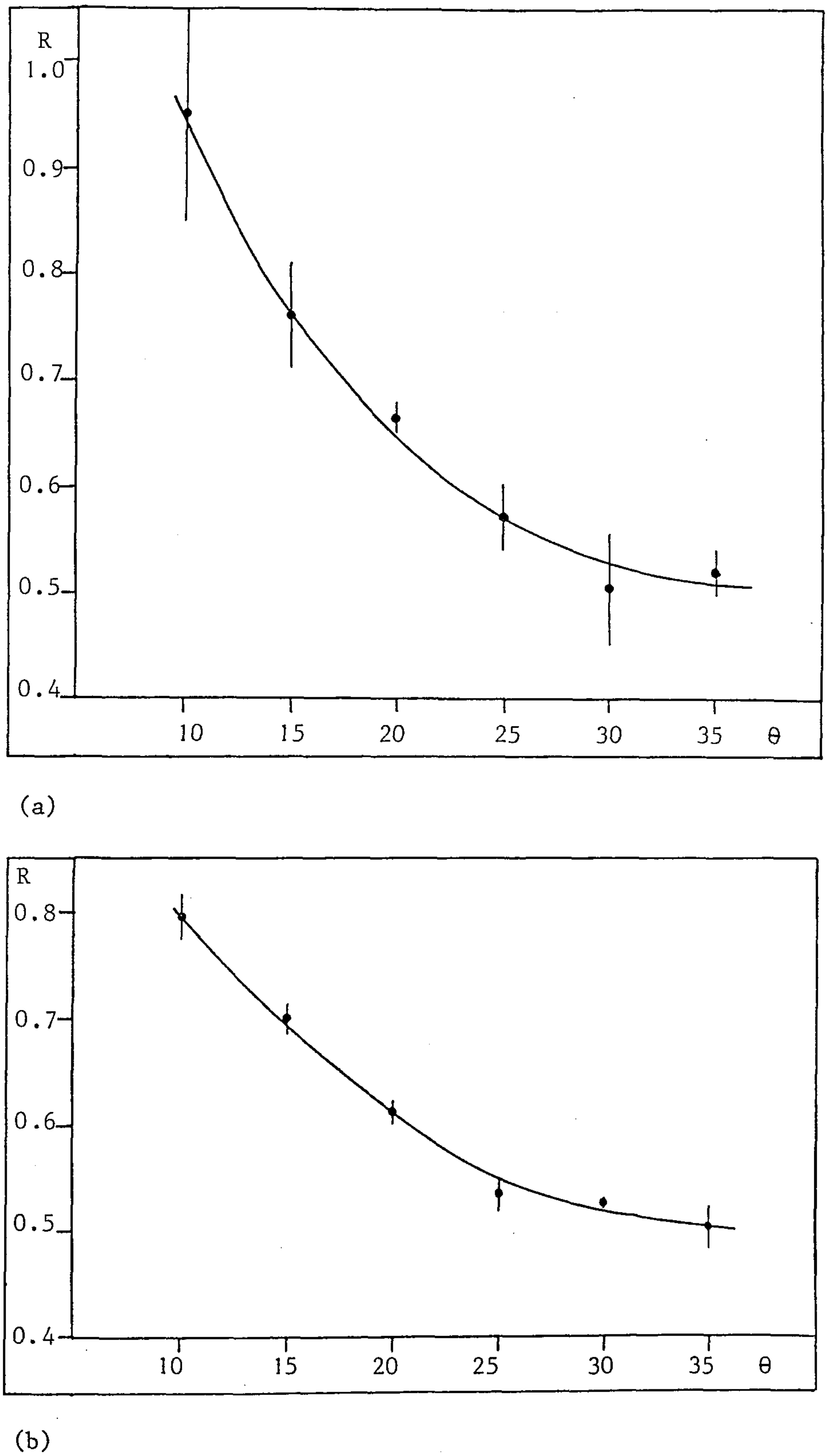

FIG. 5.14 Ratio(R) of the oxygen to tin Auger peaks at varying beam incidence values after oxidation of Sn(101) at (a) 293K (b) 390K.

The crystallographic variations mentioned above were considered to have only minor effect on the general trends. This also appears to be the case in the present study. Both the room temperature (293K) oxidised Sn(001) surface, and the room and high temperature (415K) oxidised Sn(101) surface showed an increase in the O/Sn ratio as the angle of incidence was reduced. This is consistent with an oxygen-rich surface on both the amorphous room temperature oxidised (001) and (101) surfaces, and the ordered high temperature oxidised Sn(101) surface.

Under all conditions of oxidation the electron energy loss spectra (figs. 5, 10, 11) were identical with those predominantly observed by Rider (1981). After oxidation the bulk plasmon feature at a loss (E_1) of 14V was reduced in magnitude, the clean tin surface plasmon had disappeared, and the feature adjacent to the elastic peak was greatly enlarged.

Standard E.L.S. spectra of polycrystalline Sn, SnO, and SnO_2, have been published by R A Powell (1979), and A J Bevolo et al (1982). Bevolo's spectra were in first order differential form like those in this study. Powell's spectra have been reduced to first order differential form by Rider (1981).

According to Bevolo, the main difference between the E.L.S. spectra of SnO and SnO_2 was the presence of an additional loss at 17eV in SnO_2. This loss was not present in the E.L.S. spectra of the present study. Comparing the present spectra with the standard spectra suggests that the spectra of the present study strongly resemble the SnO spectrum.

5.4 OXIDE GROWTH

(a) Models for adsorbate growth

Several authors (D C Jackson et al, 1973; G E Rhead et al, 1981; T Gallon, 1969; M P Seah, 1972; J P Biberian et al, 1979) have discussed the variation of Auger signals during adsorption. Jackson et al determined expressions for the substrate and adsorbate Auger currents during layer growth of an adsorbate.

Assuming a coverage-independant sticking coefficient of S_1 for the adsorbate on the substrate, and S_2 for the adsorbate on the adsorbate (should growth beyond one monolayer occur), the Auger current at time t during the growth of the first monolayer is

$$I_A = R\,S_1\,I_1\,t \qquad (5.1)$$

where R is the rate of arrival of adsorbate and I_1 is the current from a monolayer of A.

For the case of multiple layers adsorbing (e.g. oxygen on aluminium (R Michel et al, 1980) the adsorbate current for n layers is given by

$$I_n = I_{oo}\left[1 - \left[1 - I_{1}/I_{oo}\right]\right] \qquad (5.2)$$

(Gallon, 1969) where I_{oo} is the current from the bulk substrate. Jackson et al obtained similar expressions for the decay of the substrate Auger signal.

Typical intensity plots for the case of monolayer adsorption (in the formation of a surface compound), and multilayer adsorption, are shown in fig. 5.15 (after G E Rhead et al, 1981). For the case of multiple-layered adsorption there is a change in slope at the onset of each new layer as each adsorbate layer attenuates the signal from underlying layers. The assumption has been made that the (n + 1)th layer has not started to form before the nth is completed.

Rhead has considered the effects of sticking probability, diffusion, and other effects on the intensity curves for these growth modes, and growth modes seen in thin film growth. The applicability of these effects in the present study are considered in section 5.4b.

(b) Growth of the oxides on the Sn(001) and Sn(101) surfaces

Experimentally the oxidation of the Sn(001) and Sn(101) surfaces was studied by monitoring the first order differentiated tin $M_4 N_{4,5} N_{4,5}$ and oxygen $KL_{2,3} L_{2,3}$ peaks and plotting the O/Sn peak-to-peak height ratio against oxygen exposure. The features of the ideal growth conditions mentioned in section 5.4a and exhibited in fig.5.15 would be reproduced in this form of plot.

Each of the uptake curves (figs. 5.16-20) showed an initial linear increase in O/Sn ratio with exposure. The uptake curve for oxygen adsorption onto Sn(101) at 135K (fig. 5.16) reached an abrupt plateau after 1200L exposure (of oxygen atoms). There was very little change after this.

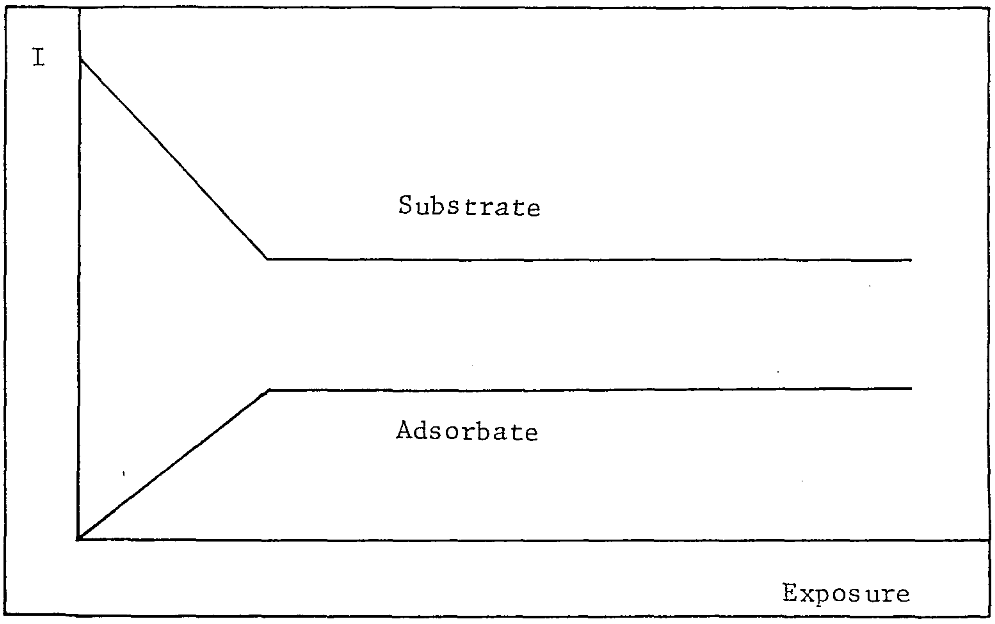

(a)

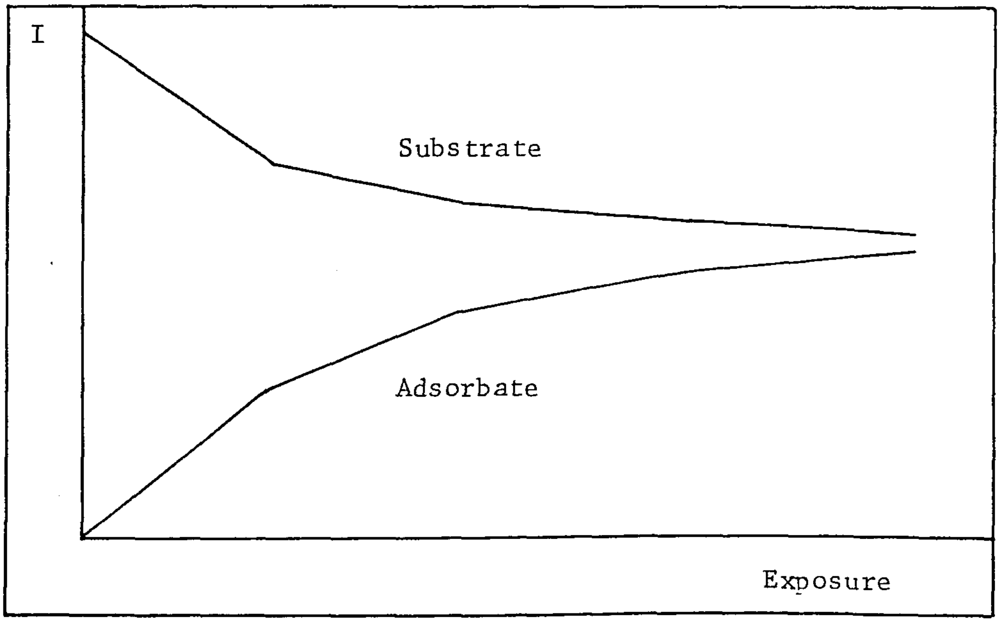

(b)

FIG. 5.15 Ideal Auger signal intensities (I) for
(a) Monolayer adsorption
(b) Multilayer adsorption
with constant sticking coefficients.

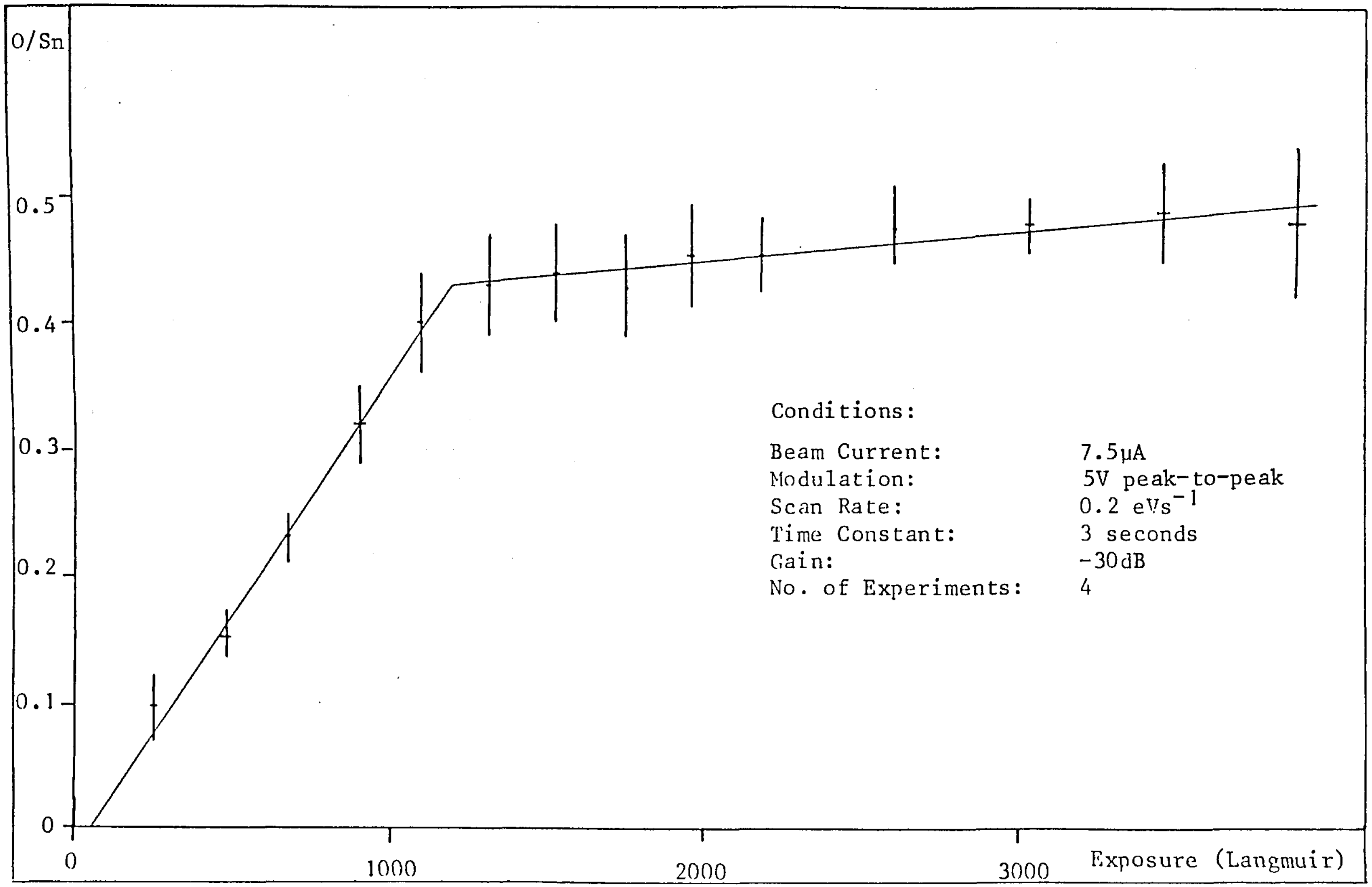

Conditions:

Beam Current: 7.5μA
Modulation: 5V peak-to-peak
Scan Rate: 0.2 eVs^{-1}
Time Constant: 3 seconds
Gain: -30dB
No. of Experiments: 4

FIG. 5.16 Uptake curve for the oxidation of Sn(101) at 135K.

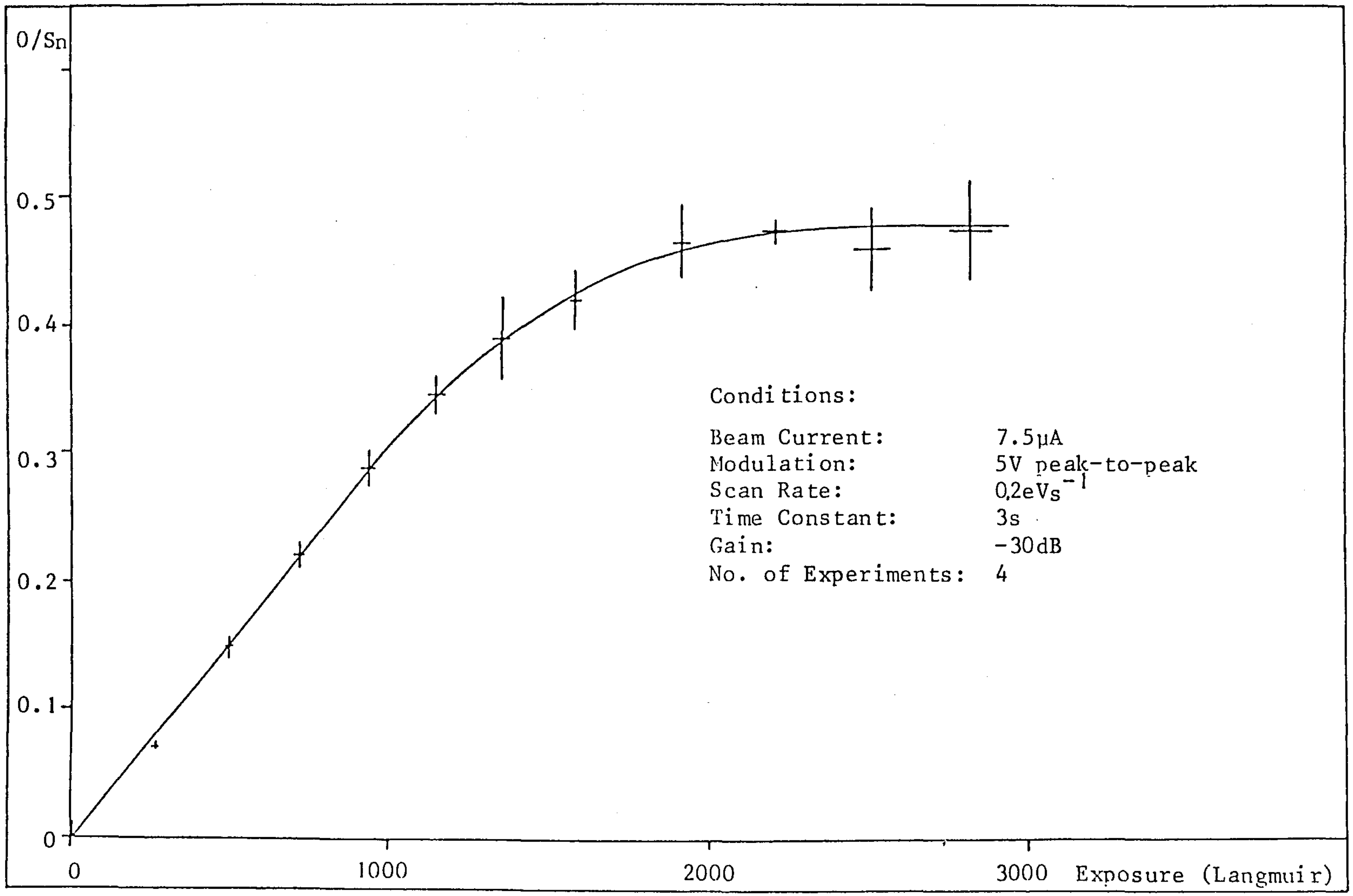

FIG. 5.17 Uptake curve for the oxidation of Sn(101) at 293K.

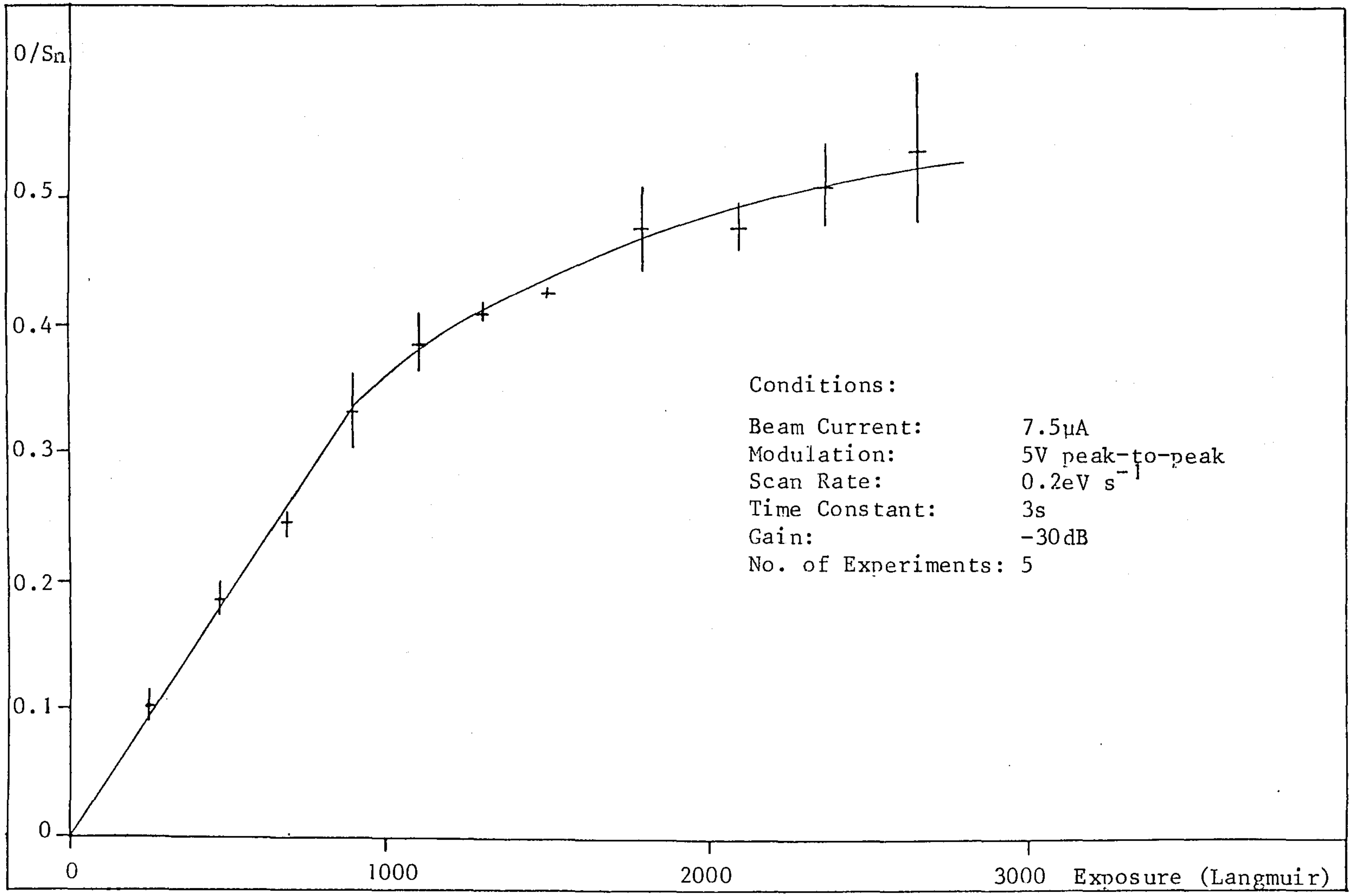

Conditions:

Beam Current: 7.5μA
Modulation: 5V peak-to-peak
Scan Rate: 0.2eV s^{-1}
Time Constant: 3s
Gain: -30dB
No. of Experiments: 5

FIG. 5.18 Uptake curve for the oxidation of Sn(101) at 390K.

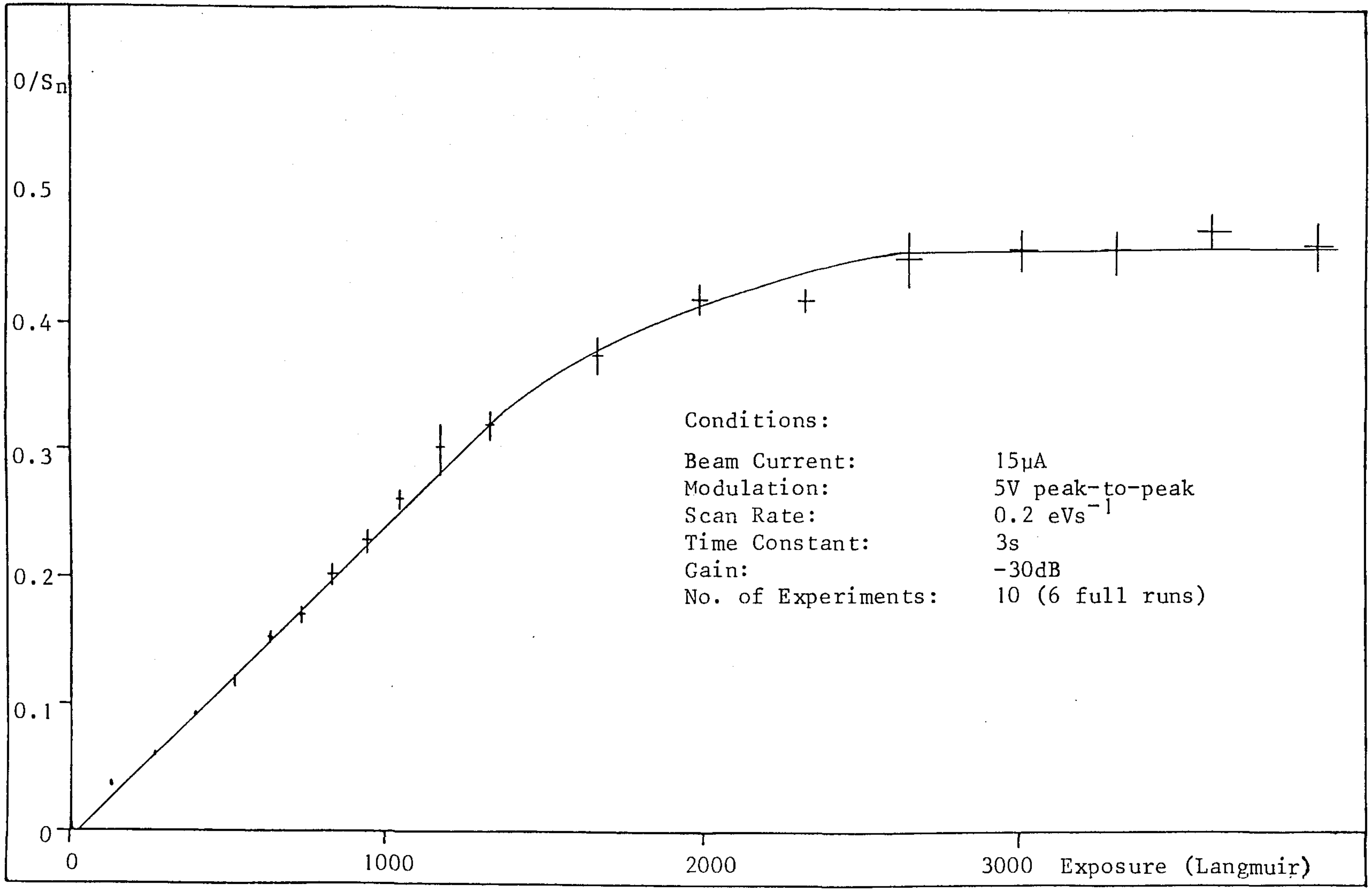

FIG. 5.19 Uptake curve for the oxidation of Sn(001) at 293K.

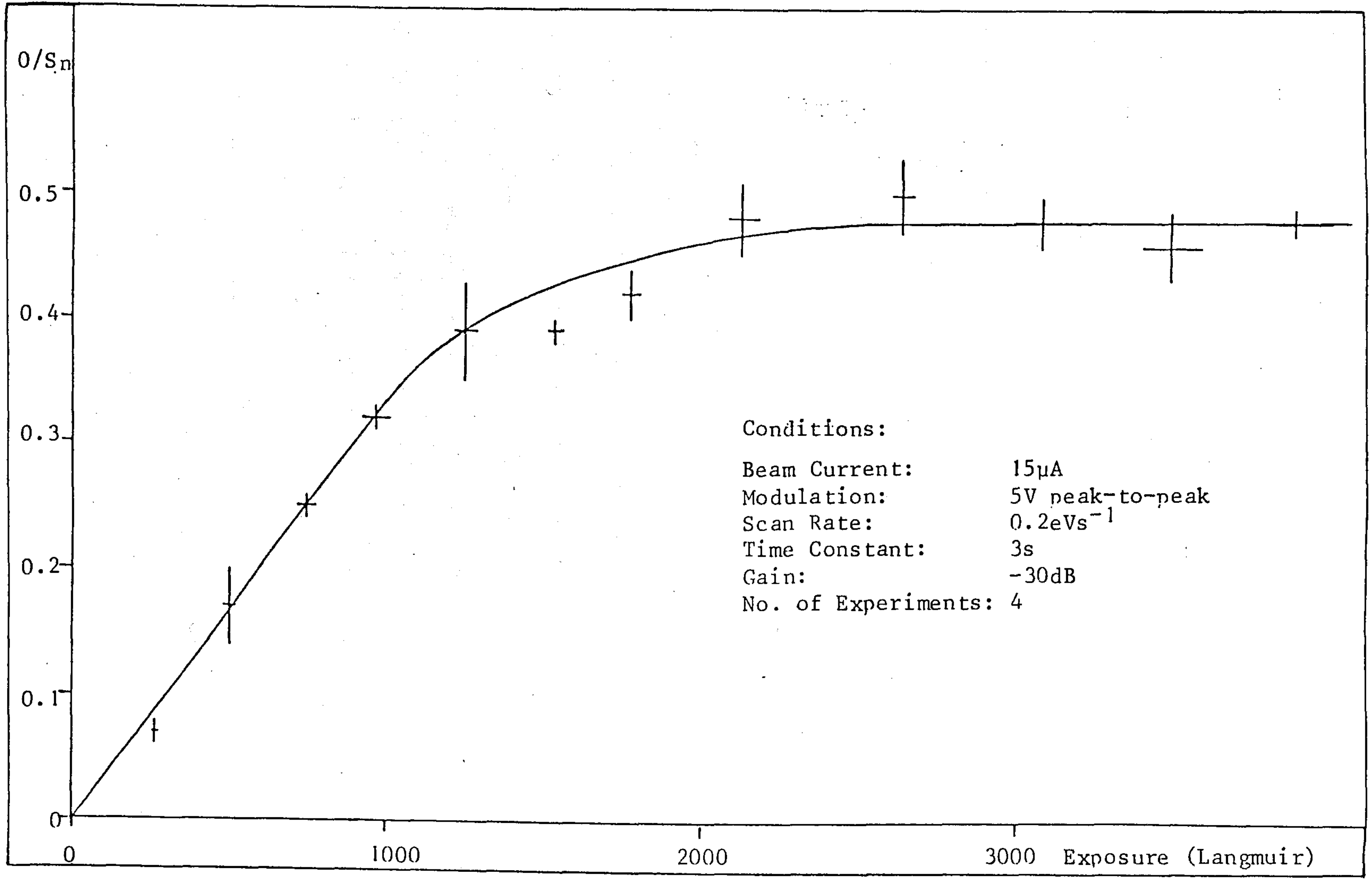

Conditions:

Beam Current: 15μA
Modulation: 5V peak-to-peak
Scan Rate: 0.2eVs^{-1}
Time Constant: 3s
Gain: -30dB
No. of Experiments: 4

FIG. 5.20 Uptake curve for the oxidation of Sn(001) at 415K.

This is characteristic of a single oxide state being formed, there being no changes of sticking probability, and no noticeable desorption to saturation. From the arguments in section 5.4a of adsorbate growth mechanisms, one may conclude that the levelling off of the curve coincides with the formation of a monolayer of oxide. From fig. 5.16 very little further oxidation or diffusion into the bulk may be interpreted above 1200L exposure for the exposure range considered.

The uptake curves for the oxidation of Sn(101) at 293K and 390K (figs. 5.17,18) each began to curve after the initial linear rise. At 293K saturation appeared to occur after 2000L exposure, whereas at 390K there appears to be no saturation up to 2600L exposure (although there is quite a large scatter in some of the readings). The levelling off of the curve at 293K occurs at approximately the same value of O/Sn ratio as at 135K, and it appears that the curvature in the uptake curves is related to changes in sticking probability. Melting of the Sn(101) crystal prevented further investigation of the uptake curve at 390K to higher exposures, although Auger spectra taken after 30,000L exposure still showed the presence of the bulk plasmon losses to the $M_{4,5}$ $N_{4,5}$ $N_{4,5}$ transitions, suggesting that no thick oxide layer had formed up to that point.

The uptake curves for oxygen adsorption onto Sn(001) at 293K and 415K (figs. 5.19,20) also show curvature near saturation. The initial rate of oxidation at 415K was 1.4 ± 0.2 times faster than that at 293K.

In order to check for beam effects during adsorption, the primary electron beam was kept on continuously during some of the experiments undertaken to formulate the uptake curves, whereas normally the primary beam was only turned on after each exposure period while taking readings. No measurable differences were observed.

It is difficult to determine whether there was any trend in the changes in the O/Sn Auger peak height ratio measured after oxidation of the Sn(101) surface (fig. 5.21a). The O/Sn Auger peak height ratio from the Sn(001) surface always increased to some extent with time (fig. 5.21b). Also in the angular Auger experiments taken after oxidation (figs. 5.13,14) the O/Sn ratios measured at $\theta = 20^{\circ}$ were higher than the saturation values of the uptake curves. This did not appear to be caused by backlash in the manipulator.

5.5 MERCURY ADSORPTION

On a small number of occasions mercury was found to have adsorbed onto the (001) and (101) surfaces when cooled below room temperature. Mercury is not detectable on the Anavac-2 mass spectrometer and it was not possible to undertake controlled adsorption or desorption experiments. The adsorption was found to be reversible, there being no trace of mercury on the surfaces on returning to room temperature. Preliminary experiments carried out before contamination by mercury ceased to occur indicated that desorption from the (001) surface occurred between 215K and 240K on heating from a base temperature of 170K (fig. 5.22).

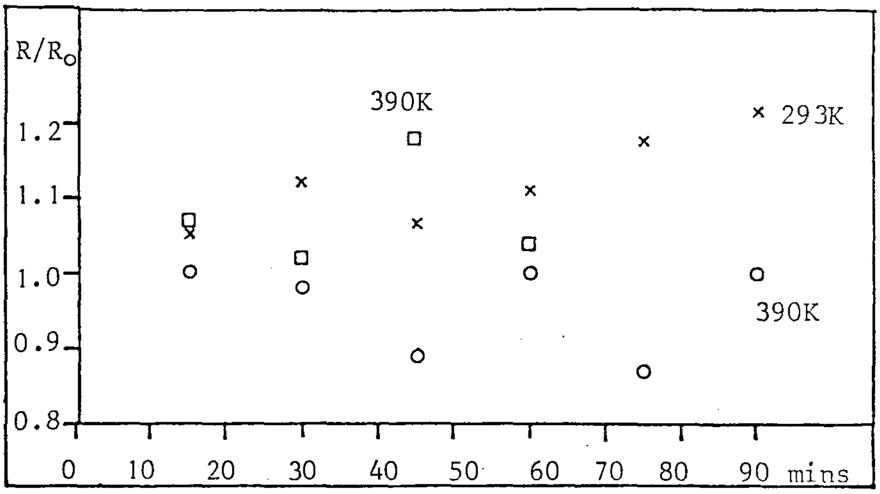

(a) Sn(101)

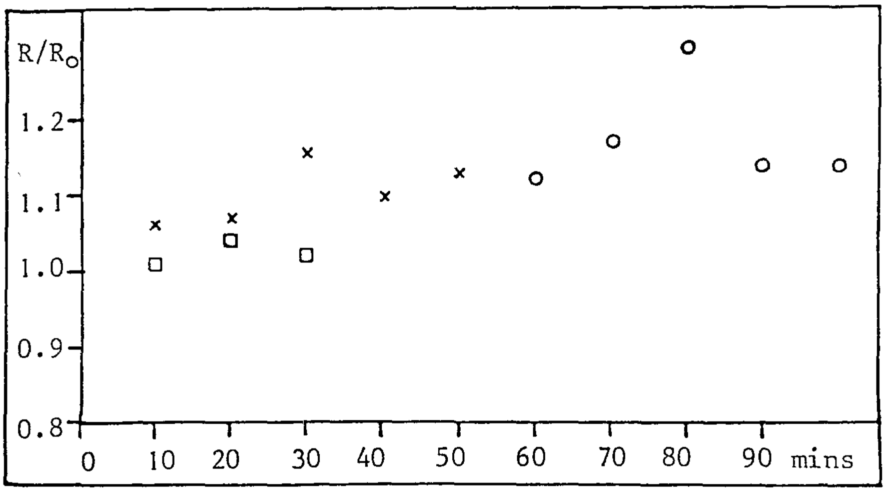

(b) Sn(001) at 293K

FIG. 5.21 Changes in the O/Sn peak-to-peak height ratios (R) after pumpout after oxidation. The ratios are normalised with respect to the O/Sn ratios (R_o) on completion of each oxidation experiment. Different symbols represent different experiments.

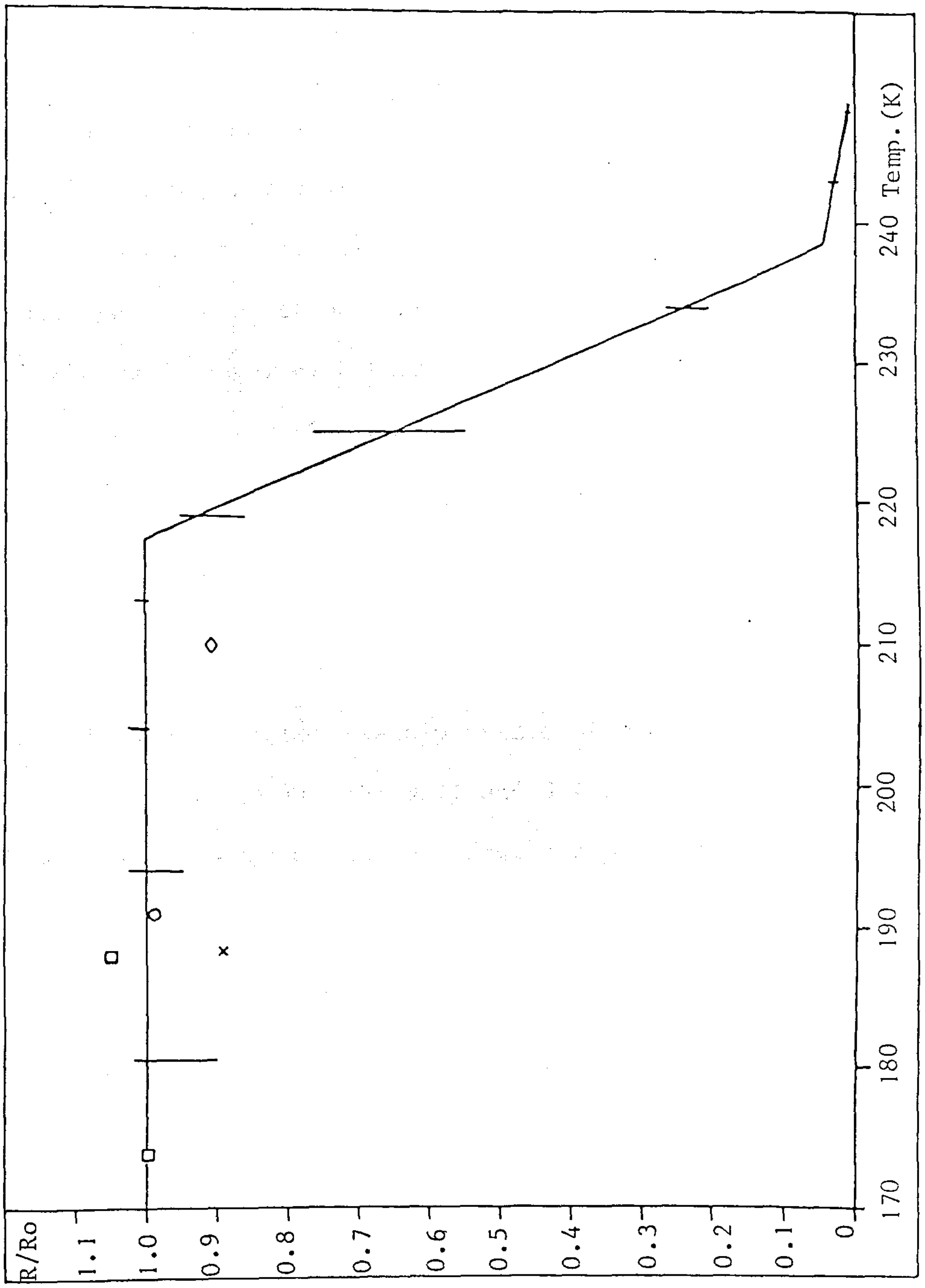

FIG. 5.22 Desorption of Hg from Sn(001) after adsorption at 170K. The Hg/Sn peak-to-peak height ratios, R, have been normalised with respect to the initial ratio R_o.

Fig. 5.24 shows the electron energy loss spectrum corresponding to the Auger spectrum of fig. 5.23 for the Sn (001) surface with the highest measured mercury contamination. Losses of approximately 4V, 7V, and 12V are present. Fig. 5.25 shows an electron energy loss spectrum from an Sn(101) surface for which the Hg/Sn Auger peak height ratio was one fortieth of that in fig. 5.23. The loss at ≃ 4V seen in the present study was not seen on the mercury-contaminated(101) surface studied by Rider.

5.6 SUMMARY

i) Auger and E.L.S. spectra have been presented for clean, oxidised, mercury-contaminated, and as-prepared Sn(001) and Sn(101) surfaces. E.L.S. spectra taken from the oxidised surfaces had features in identical positions to standard SnO E.L.S. spectra.

ii) Oxygen uptake curves for Sn(001) and Sn(101) indicate the formation of a single chemisorbed layer in most cases. Such a conclusion cannot be clearly stated for the oxidation of Sn(101) at 440K.

iii) Oxidation of Sn(001) at 135K led to the lowering in energy of the remaining tin Auger transitions and the formation of a thicker oxide layer than was present under the other conditions considered.

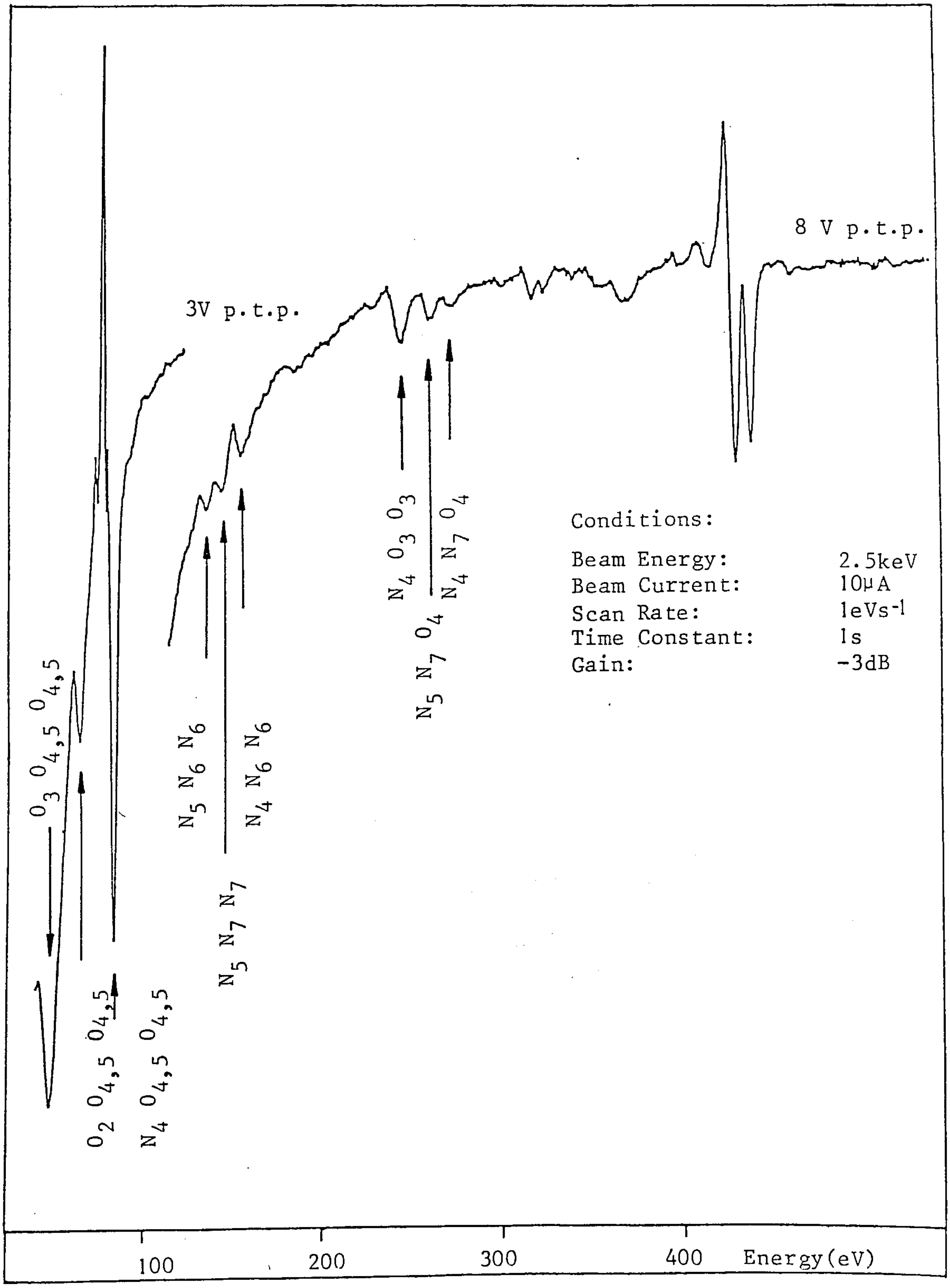

FIG. 5.23 Auger spectrum from mercury adsorbed onto Sn(001) at 170K.

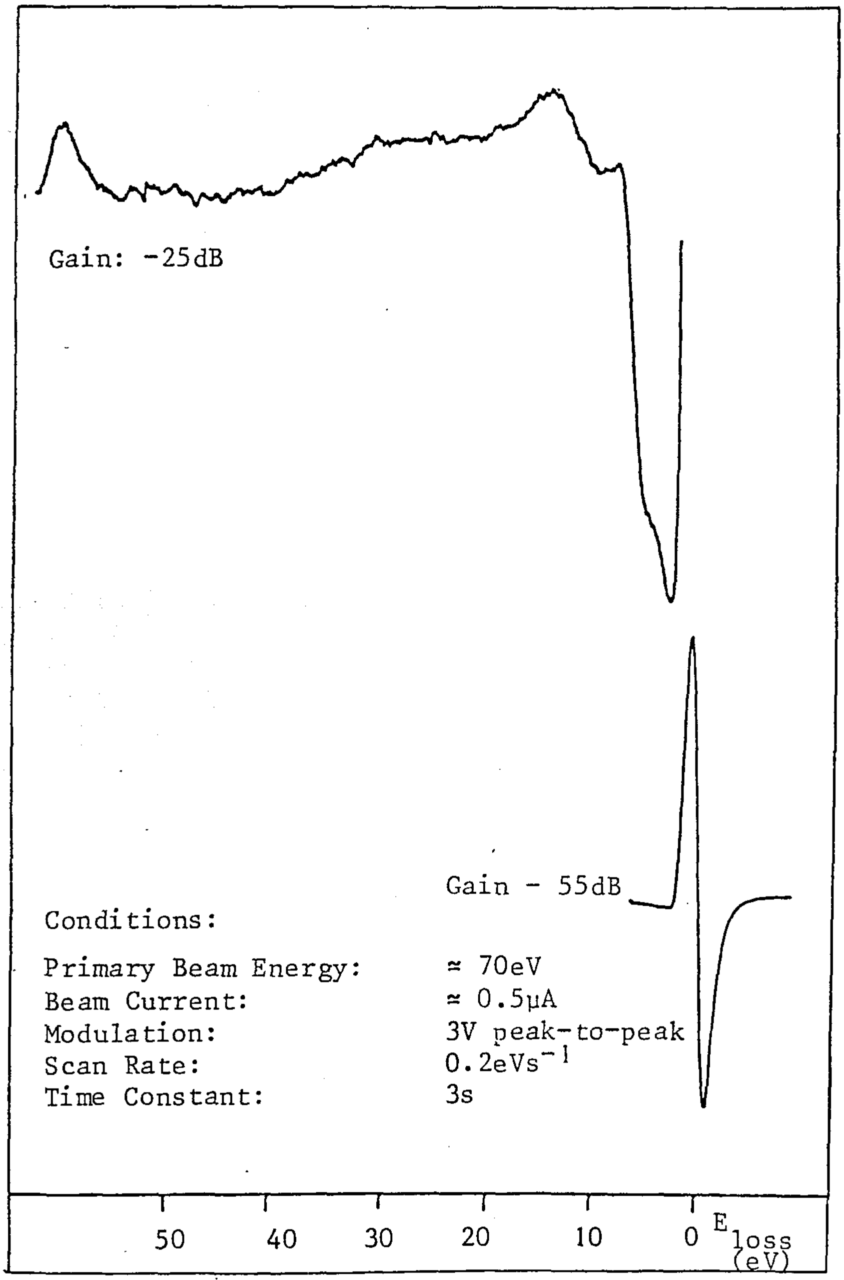

Conditions:

Primary Beam Energy: ≃ 70eV
Beam Current: ≃ 0.5μA
Modulation: 3V peak-to-peak
Scan Rate: 0.2eVs^{-1}
Time Constant: 3s

FIG. 5.24 E.L.S. spectrum from mercury contaminated on Sn(001) at 170K (corresponding to the Auger spectrum of Fig. 5.23).

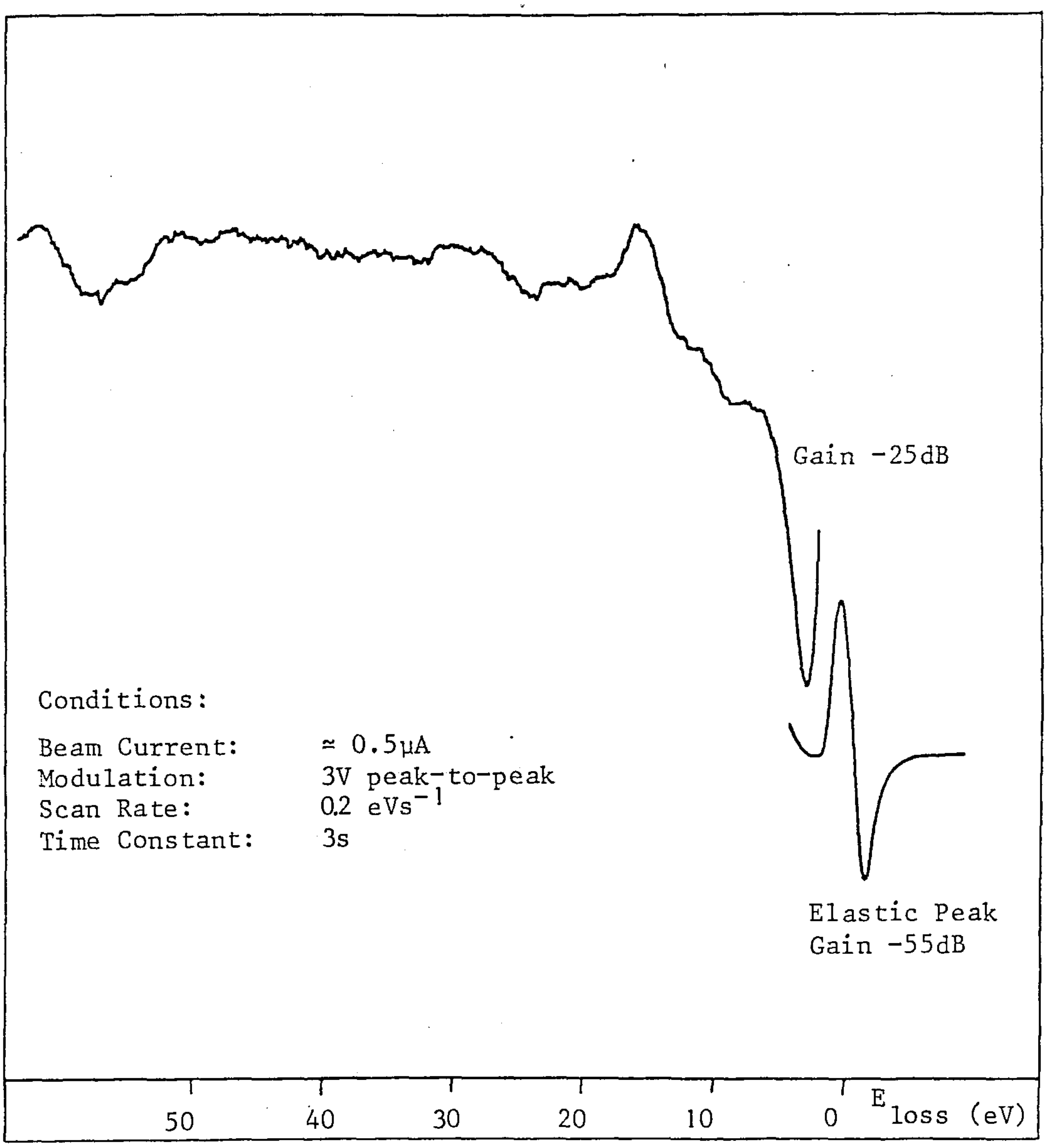

Conditions:

Beam Current: ≈ 0.5μA
Modulation: 3V peak-to-peak
Scan Rate: 0.2 eVs^{-1}
Time Constant: 3s

FIG. 5.25 E.L.S. spectrum from a mercury contaminated Sn(101) surface at ≈ 95K.

CHAPTER 6

L.E.E.D. RESULTS FROM THE Sn(001) SURFACE

6.1 THE CLEAN Sn(001) SURFACE RESULTS

The L.E.E.D. pattern expected from a perfect Sn(001) surface with unit cell dimensions corresponding to those of the bulk plane would have a square reciprocal net. The pattern obtained from a clean Sn (001) surface is shown in Figs. 6.1-7. Calculations from the observed patterns gave a value of 5.6 ± 0.3Å for the dimensions of the square surface unit net, the bulk value from x-ray data being 5.83Å. No changes were observed in the patterns on annealing the crystal to 473K, or cooling to 115K, apart from the expected reduction in background and increase in intensity of the spots the lower the temperature.

Each reciprocal lattice point of the observed pattern alternated between a single spot and multiple spots. Single spots were observed to occur for the (00), {10}, {11},{20}, {21}, {22}, {30}, and {31} positions. Splitting was most easily identified for the {10} and {11} spots at low primary beam energies (20-35eV). The patterns were photographed at 115K in order to be able to distinguish the constituent features.

At 20.0V, and with the primary electron beam at normal incidence, the {11} spots were sharp and single (Fig. 6.1a). The {10} reflections were split along [10] and [01] directions. By 22.0V (Fig. 6.1b) the split $(\bar{1}0)$ position could be seen to consist of a central cross-shaped feature with a further two spots between the cross and each of the $(\bar{1}1)$ and $(\bar{1}\bar{1})$ spots. Further splitting could also be seen along the [01] direction between the $(\bar{1}0)$ and (00) reflections. Faint splitting of the (11) spot occurred at 24.0V (Fig. 6.1c). Occasionally, (Figs.6.3a,b) the splitting around the cross-shaped features of the {10} reflections appeared more extensive. The splitting between the {10} and {11} positions was clearest at 26.0V (Fig. 6.2a). Each of the {11} reciprocal lattice positions consisted of features about the normal reciprocal lattice points with a further spot between each of these features and the adjacent {10} positions. At this voltage the split spots of the {10} reflections had coallesced to form a diffuse region about the central cross-shaped features. Between 28.0V and 35.5V (Figs. 6.2 b-d) the {11} features became diffuse, and the {10} features coallesced to form single sharp spots at 35.5V.

Figs. 6.4,5 show a further sequence of L.E.E.D. photographs from 48.6V to 142.5V showing the voltages for which the {11}, {20}, {21}, {22}, {30}, and {31} positions formed sharp single spots. Note that the spots became diffuse and disappear beyond the voltages at which sharp spots occur.

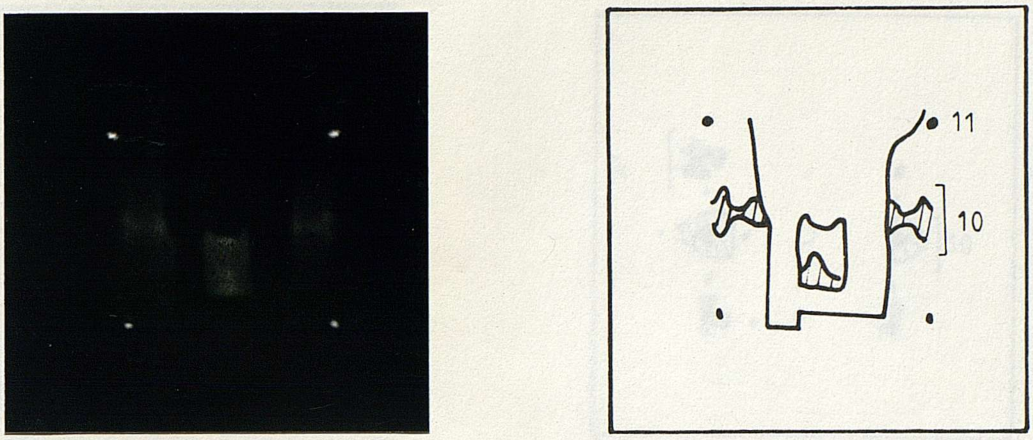

(a) 20.0V Single sharp {11} spots and diffuse, split {10} reflections.

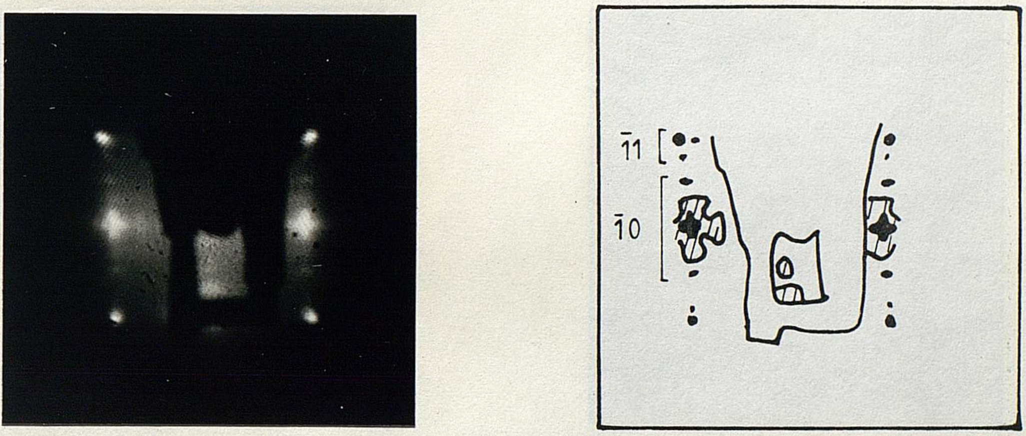

(b) 22.0V Multiple splitting of the {10} reflections and initial splitting of the {11} reflections.

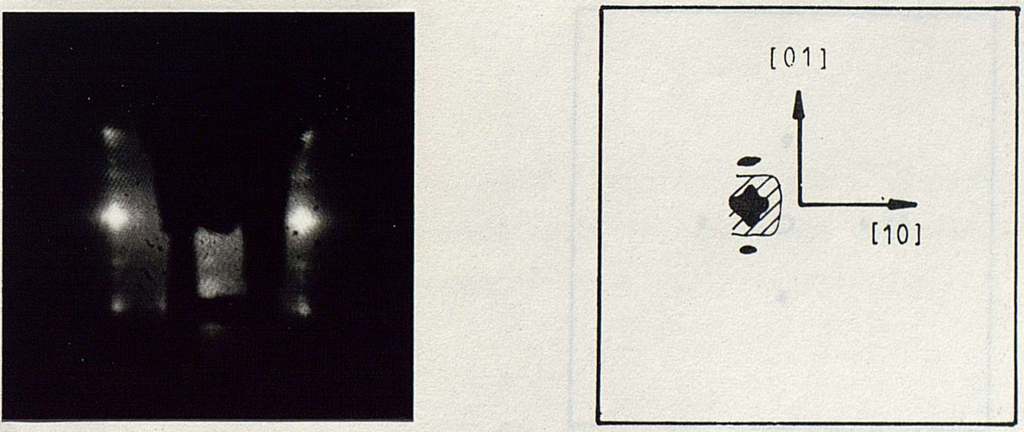

(c) 24.0V

FIG. 6.1 L.E.E.D. from the clean Sn(001) surface at normal incidence.

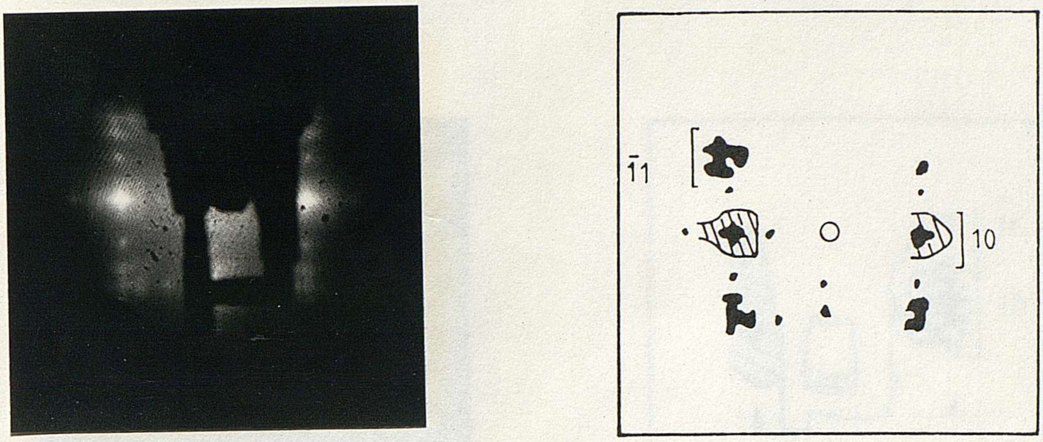

(a) 26.0V Extensive splitting of both the {10} reflections and the {11} reflections

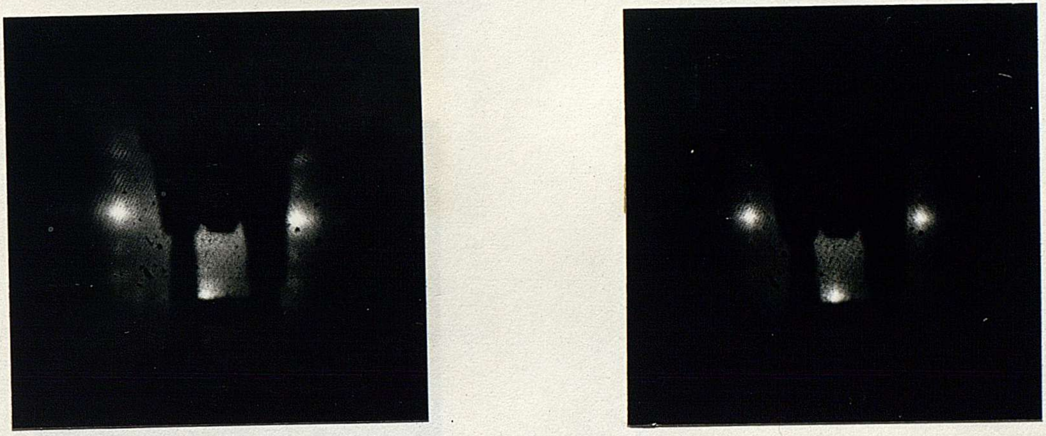

(b) 28.0V (c) 30.0V

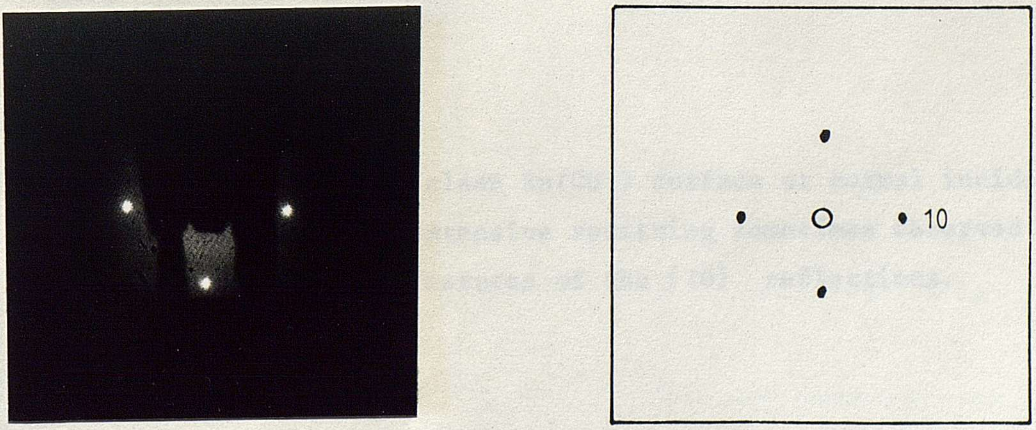

(d) 35.5V Single sharp {10} spots, no visible {11} reflections.

FIG. 6.2 L.E.E.D. from the clean Sn(001) surface at normal incidence.

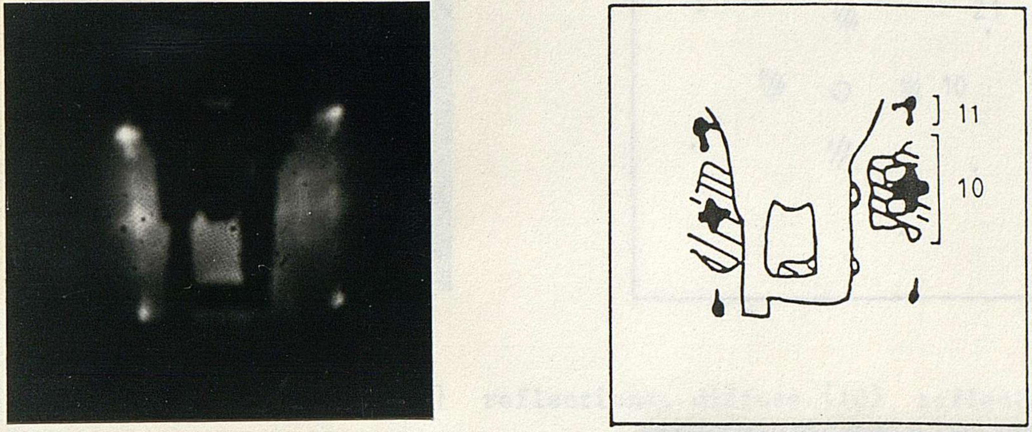

(a) 22.0V

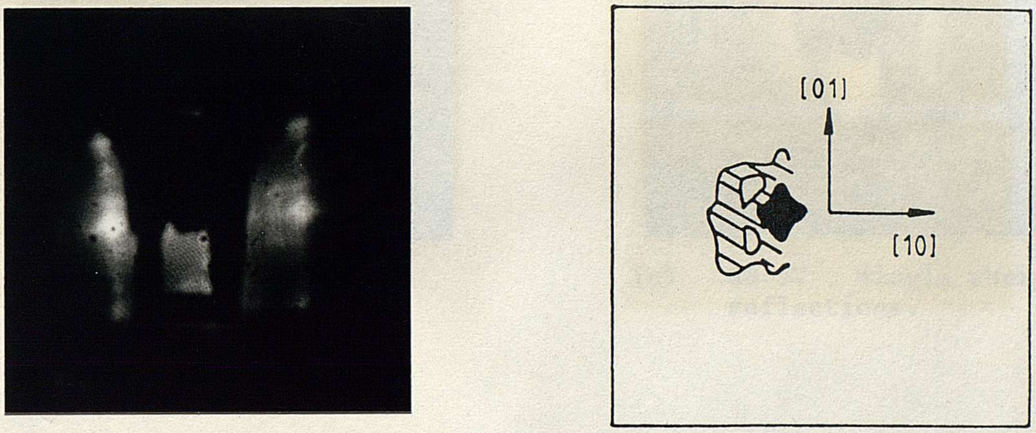

(b) 24.0

FIG. 6.3 L.E.E.D. from the clean Sn(001) surface at normal incidence showing the more extensive splitting sometimes observed around the cross-shaped features of the {10} reflections.

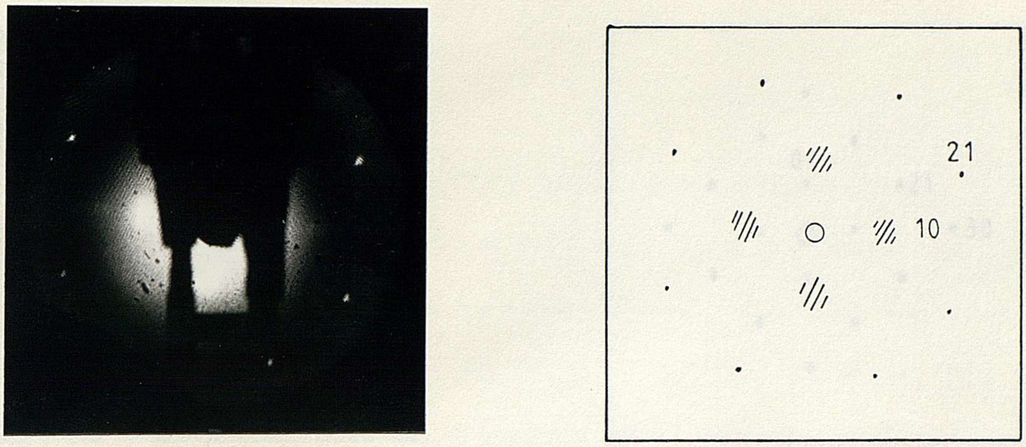

(a) 46.8V Single sharp {21} reflections, diffuse {10} reflections.

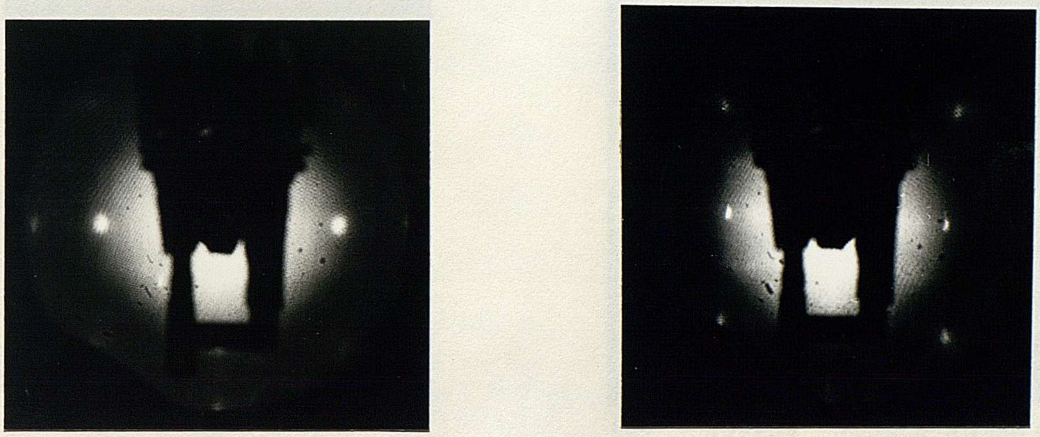

(b) 65.0V No {21} reflections visible; {20}, and {22} reflections diffuse.

(c) 68.5V Single sharp {20} reflections.

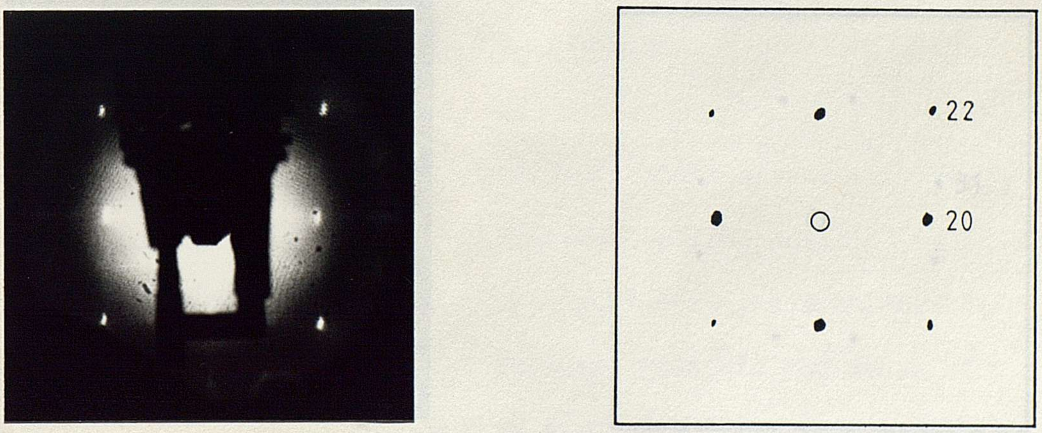

(d) 80.0V Single sharp {22} reflections, {20} reflections becoming diffuse.

FIG. 6.4 Formation of single sharp spots by the {21}, {20}, and {22} reflections at normal incidence.

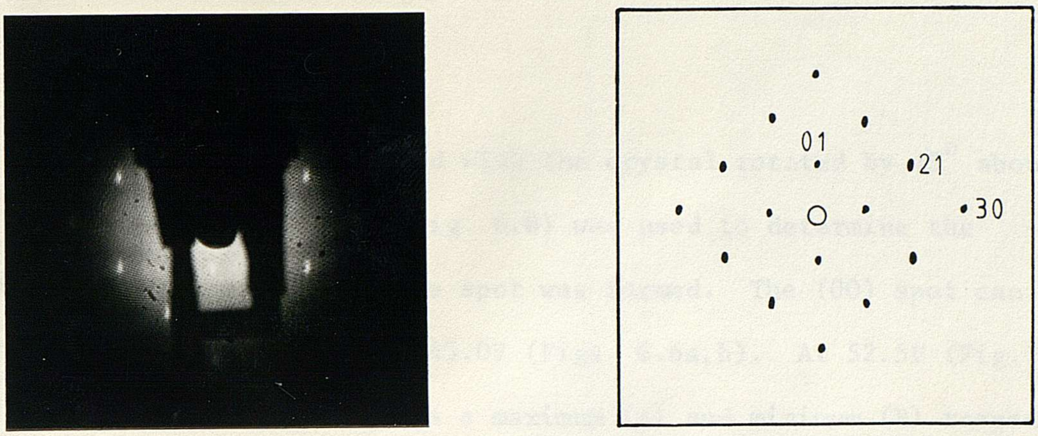

(a) 101.0V Single sharp {21} spots, faint {30} spots.

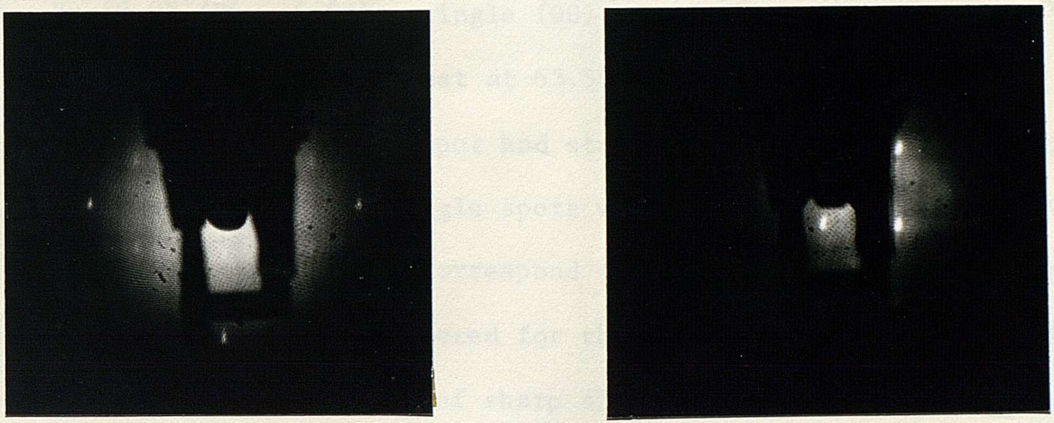

(b) 112.5V Single sharp {30} spots, faint {21} spots.

(c) 137.5V Single sharp {11} spots.

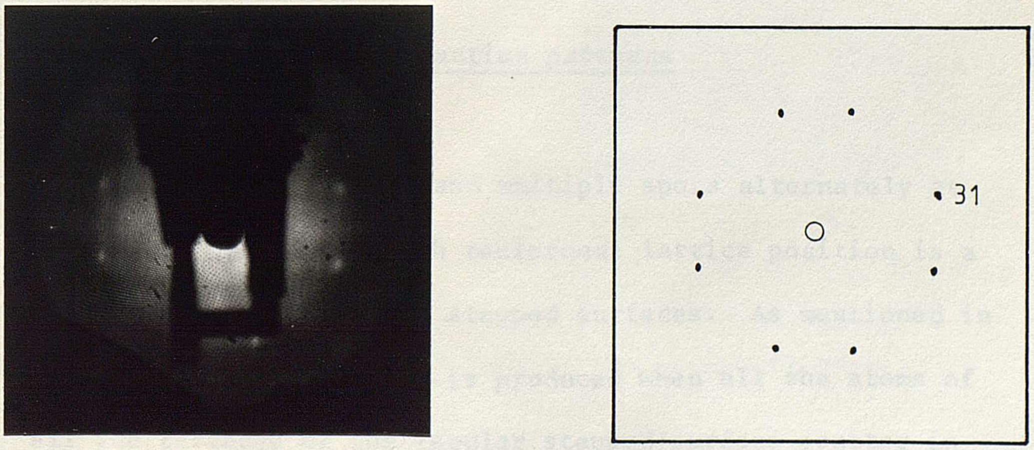

(d) 142.5V Single {31} spots.

FIG. 6.5 Formation of single sharp spots for the {21} , {30}, {11} and {31} reflections at normal incidence.

The (00) features were observed with the crystal rotated by 15^{o} about the [01] axis. An I/V plot (Fig. 6.8) was used to determine the voltage at which a sharp single spot was formed. The (00) spot can be seen to be split at 35.7V and 45.0V (Figs. 6.6a,b). At 52.5V (Fig. 6.6c) and 56.5V (Fig. 6.6d) there was a maximum (A) and minimum (B) respectively on the I/V curve. The maximum did not correspond to a single sharp spot. By 59.0V (Fig. 6.6e) a single (00) spot had become apparent. It was at its sharpest and brightest at 63.5V (Fig. 6.7a), corresponding to C on the I/V curve. The (00) spot had started to become diffuse by 75.0V (Fig. 6.7b). Further sharp single spots were observed at 137V and 249V (Figs. 6.7d,f). Figs. 6.7c,e correspond to the positions of out-of-phase scattering from the model predicted for the surface in Section 6.2. The conditions for the observation of sharp single spots have been summarised in Figs. 6.9a, and 6.10a.

6.2 ANALYSIS

(a) Deductions from the diffraction patterns

The appearance of single and multiple spots alternately at specific voltages for each reciprocal lattice position is a characteristic of regular stepped surfaces. As mentioned in Section 3.4 a single spot is produced when all the atoms of all the terraces of the regular stepped surface scatter in phase. Multiple spots are produced otherwise.

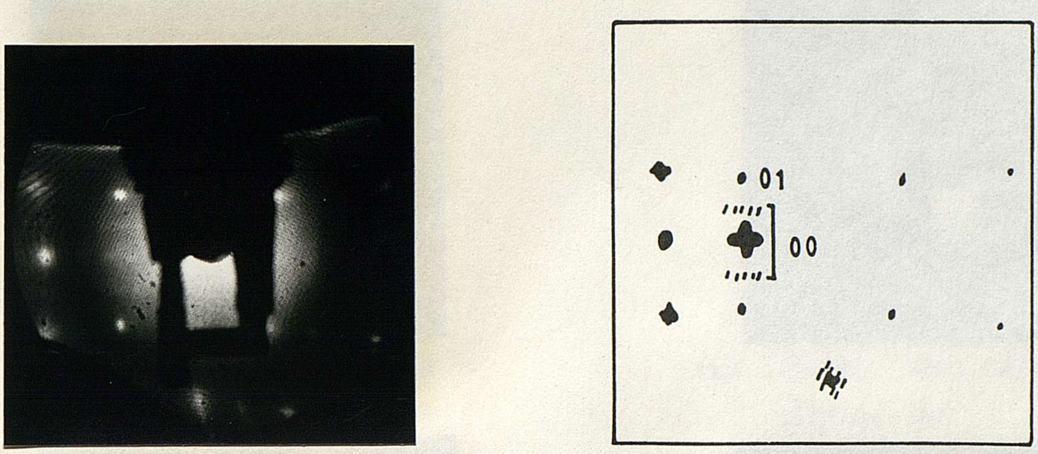

(a) 35.7V. The (00) reflection split at the position of antiphase scattering.

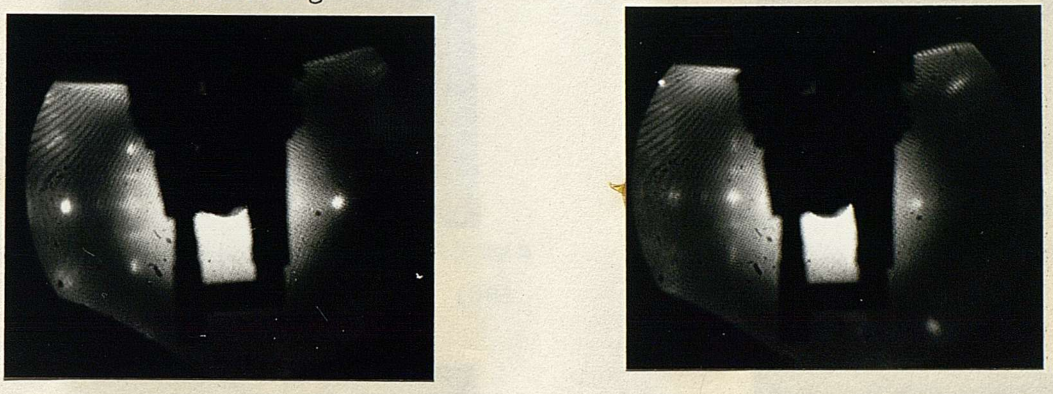

(b) 45.0V.

(c) 52.5V. (A)

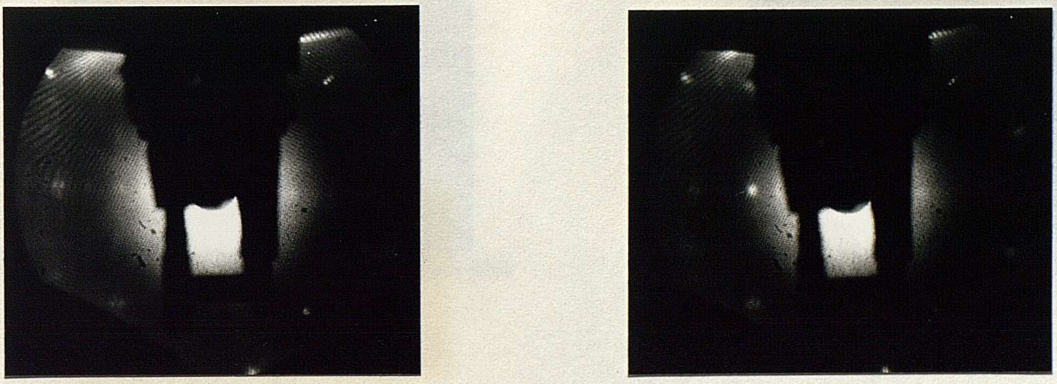

(d) 56.5V (B)

(e) 59.0V The (00) reflection becoming brighter, and a single spot.

FIG. 6.6 The (00) reflection observed at an incidence angle of 15°. Letters in brackets denote positions on the I/V curve (Fig. 6.8).

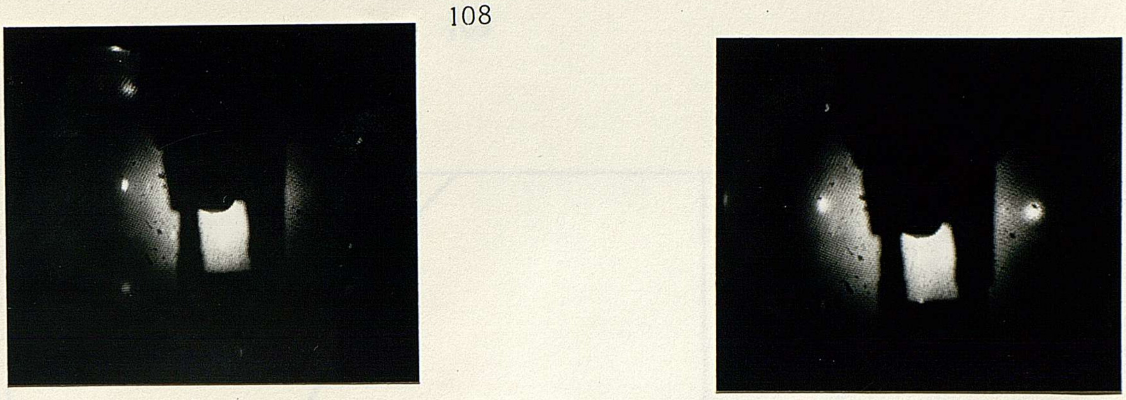

(a) 63.5V. (00) sharp and single (C)

(b) 75.0V. (00) becoming diffuse (D)

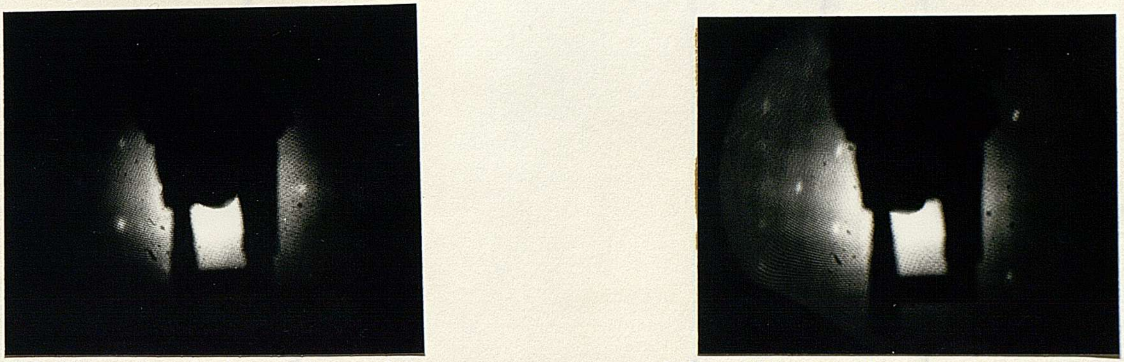

(c) 92.5V. Position of antiphase scattering. No visible (00) reflection.

(d) 137V. Single sharp (00) spot.

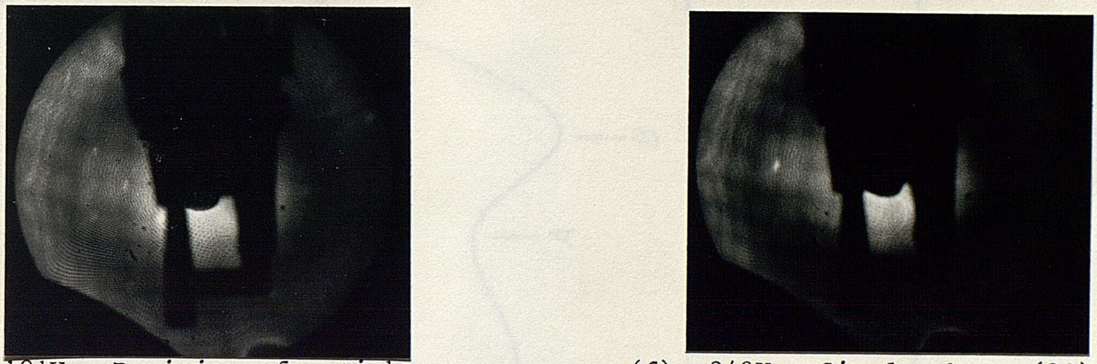

(e) 181V. Position of antiphase scattering.

(f) 249V. Single sharp (00) spot.

FIG. 6.7 The (00) at a 15^o incidence angle for a number of positions of in-phase and antiphase scattering. Letters in brackets refer to positions in the I/V curve (Fig. 6.8).

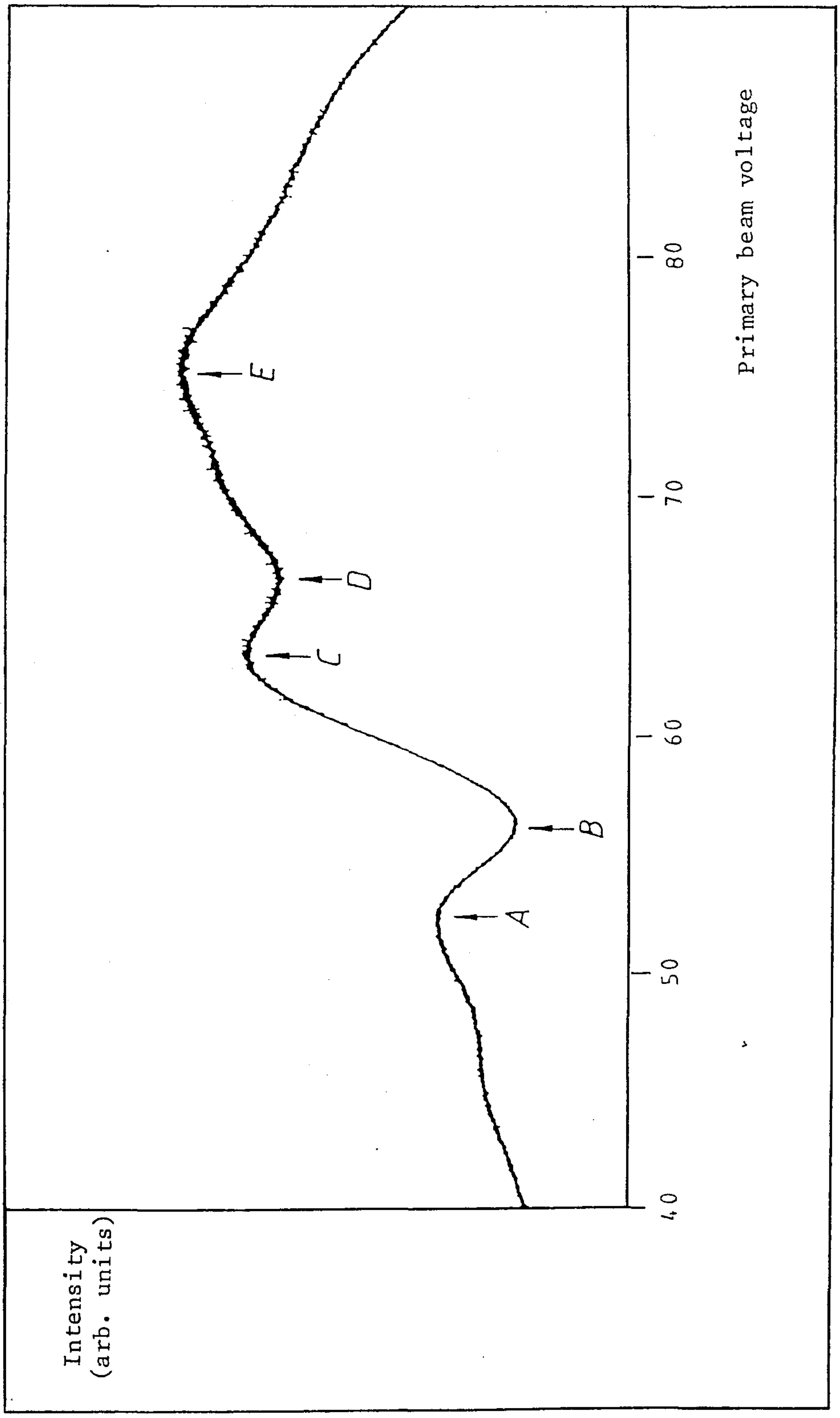

FIG. 6.8 I/V curve for the (00) reflection at a 15° angle of incidence/beam current ≃ $\frac{1}{2}$μA at 40V, 1μA at 90V).

S	(1)d= $\underline{c}$ /4 (0.80A)	(2)d= $\lvert\underline{c}\rvert/2$ (1.59Å)	(3)d=3 $\lvert\underline{c}\rvert/4$ (2.39Å)	(4)d= $\lvert\underline{c}\rvert$ (3.18Å)	Experimental values of V_{oo} (volts)
1	63.6	15.9	7.1	4.0	-
2	254	63.6	28.3	15.9	63.5
3		143	63.6	35.8	137
4		254	113	63.6	249

(a)

S	V_{oo} (theory) (volts)
3/2	35.7
5/2	92.5
7/2	181.3

(b)

FIG. 6.9a Comparison of experimental values of V_{oo} with those calculated using equation 6.1 for step heights of multiple values of $\lvert\underline{c}\rvert/4$, and the primary beam at 15° incidence.

6.9b Theoretical antiphase conditions for the (00) spot with the primary beam at 15° incidence.

{hk}	S	V_{hk} theory (volts)	V_{hk} expt. (volts)
{10}	1	35.5	35.5
{11}	2	19.5	20.0
	3	63.7	
	4	137.6	137.5
{20}	3	68.3	68.5
{21}	3	45.2	46.8
	4	103.8	101.0
{22}	4	78.1	80.0
{30}	4	113.4	112.5
{31}	5	156.1	142.5

FIG. 6.10a Theoretical and experimental values of V_{hk} for the formation of single spots for the {hk} reflections at normal incidence.

{hk}	S	V_{hk} theory (volts)
{10}	3/2	17.1
{11}	5/2	37.9
	7/2	97.0
{20}	5/2	42.7
{21}	7/2	70.7
{22}	9/2	111.0
{30}	7/2	80.7
{31}	9/2	115.8

FIG. 6.10b Theoretical antiphase conditions for the {hk} reflections at normal incidence.

The splitting of the {10} and {11} spots (Figs. 6.1-3) along all the <10> directions suggests the presence of regular arrays of steps both up and down along the [01] and [10] directions of the (001) surface (M Henzler, 1977). This assumption is supported by the symmetry of all the L.E.E.D. patterns at normal incidence (Figs. 6.1-5) about mirror planes along the [10] and [01] directions of the reciprocal lattice.

Henzler has determined the reciprocal lattice for a regular array of steps both up and down along a single axis. Four spots would be expected for a particular (hk) reflection at primary beam energies intermediate between those required for in-phase and out-of-phase scattering. The patterns observed on the Sn(001) surface would appear to be more complex than that expected by simply extending Henzler's one-dimensional model to two dimensions.

Apart from the extensive splitting sometimes observed around the central cross-shaped feature of the {10} reciprocal lattice positions (Fig. 6.3), no other splitting was observed apart from that along the <10> directions. Kinematic intensity distributions have been calculated for models of the surface in order to try to replicate the observed L.E.E.D. patterns and estimate the average terrace size of the surface.

(b) Derivation of the step height, terrace separation and atomic arrangement

A terraced surface with regular steps produces a single (00) spot at voltages (V_{oo}) dependant only on the step height, d, and the angle of incidence, Θ, of the primary beam to the surface terraces (M Henzler, 1977). The characteristic voltages are given by

$$V_{oo} = \frac{150\ S^2}{4d^2 \cos^2\Theta} \qquad (6.1)$$

In the bulk unit cell (Fig. 2.1) there are tin atoms in multiples of 1/4 $|\underline{c}|$, where $\underline{c}$ is the unit vector normal to the (001) plane, and $|\underline{c}|$ = 3.18Å. Using these bulk atomic positions as a basis for the step height, and with the experimental incidence angle of 15° for observation of the (00) spot, values of V_{oo} were calculated for a number of integer S values for the in-phase, single spot condition. These values are listed in Fig. 6.9. Comparing the calculated and experimental values it is clear that the step height, $d \approx |\underline{c}|/2$ = 1.59Å for the surface. The bulk unit cell atomic positions corresponding to this value are (0, 0,0) and($\frac{1}{2}$, $\frac{1}{2}$, $\frac{1}{2}$) (Fig. 2.1). These atomic positions were the basis of the model to obtain a general expression for the characteristic primary beam potentials, V_{hk}, for the (hk) beam at the in-phase and out-of-phase conditions.

In the model it is assumed that the atoms of any terrace lie in positions corresponding to those of a bulk (001) plane with unit vectors $\underline{a}_1$, $\underline{a}_2$ ($|\underline{a}_1| = |\underline{a}_2| = a$) along x and y axes respectively. From the argument of the preceding paragraph it is assumed that if the atoms of one terrace lie in (0, 0, 0) positions, then the atoms of a neighbouring terrace lie in ($\frac{1}{2}$, $\frac{1}{2}$, $\frac{1}{2}$) positions. Between adjacent terraces there are steps both up and down along the [01] and [10] directions (Fig. 6.11). The separation between neighbouring atoms of adjacent terraces is given by a vector of modulus

$$|\underline{g}| = \frac{1}{2}\left(|\underline{a}_1|^2 + |\underline{a}_2|^2 + c^2\right)^{\frac{1}{2}} \tag{6.2}$$

where c/2 is the step height and $^{a_1}/2$, $^{a_2}/2$ are the separations between adjacent terraces in the [10] and [01] directions respectively.

If $\underline{a}_1^*$, $\underline{a}_2^*$, $\underline{c}^*$ are the reciprocal space vectors of a perfect tin crystal then if an incident electron beam of wavevector $\underline{K}_o$ is incident on the surface, the scattered wavevector with indices h, k, is

$$\underline{K}_s = \underline{K}_o + h\underline{a}_1^* + k\underline{a}_2^* + L\underline{c}^* \tag{6.3}$$

For normal incidence

$$L\,|\underline{c}^*| = |\underline{K}_o| + [\,\underline{K}_o^2 - 4\pi^2((h^2+k^2)/a^2)\,]^{\frac{1}{2}}$$

The condition for in-phase scattering from all atoms of the terraced surface is

$$\underline{g}\cdot(|h|\underline{a}_1^* + |k|\underline{a}_2^* + L\underline{c}^*) = 2n\pi \qquad (6.5)$$

and the antiphase condition for multiple spots is

$$\underline{g}\cdot(|h|\,\underline{a}_1^* + |k|\,\underline{a}_2^* + L\underline{c}^*) = (2n+1)\pi \qquad (6.6)$$

From equation 3.38:

$$|\underline{K}_0| = 2\pi(V/150)^{\frac{1}{2}} \qquad (6.7)$$

when a and c are measured in Angströms.

By expanding eqn. 6.5 one obtains for normal incidence the expression

$$V_{hk} = \frac{150}{c^2}\left[S - \frac{(|h| + |k|)}{2} + \frac{c^2(h^2 + k^2)}{4a^2(S-\frac{1}{2}(|h| + |k|))}\right]^2 \qquad (6.8)$$

for the characteristic voltages for single and split spots for the (hk) beam, where S = n for in-phase scattering and single spots; and $S = n + \frac{1}{2}$ for antiphase scattering and split spots. The values of S are such that

$$S \geq \frac{(|h| + |k|)}{2} - \frac{c(h^2 + k^2)^{\frac{1}{2}}}{2a} \qquad (6.9)$$

that the characteristic voltages are independant of the size of the terraces, although for the model to be applicable there must be more than one terrace within any one coherence zone.

Values of V_{hk} have been determined using eqn. 6.8 for a number of observed {hk} reflections at the single spot condition. They have been listed in Figs. 6.9a, and 6.10a. A comparison with the experimental values of the primary beam potentials for single spots shows that this model gives close agreement between theory and experiment. The theoretical antiphase conditions have been listed in Figs. 6.9b, and 6.10b.

6.3 MODEL FOR THE Sn(001) SURFACE

In this section the intensity distribution has been calculated for a model of the Sn(001) surface using kinematic techniques. By altering the parameters of the model an attempt has been made to replicate the experimental patterns and thus gain some understanding as to the approximate mean dimensions of the terraces.

The model has been based on the dimensions of the surface determined in the previous section. This kinematic technique has been successfully applied by W. P. Ellis et al (1968) in the analysis of a stepped UO_2 surface. Although kinematic theory correctly predicts the positions of spots, dynamic theories are required to give intensity values in closer agreement with experiment.

Referring to Fig. 6.11, the conditions defining the model of the Sn(001) surface are:

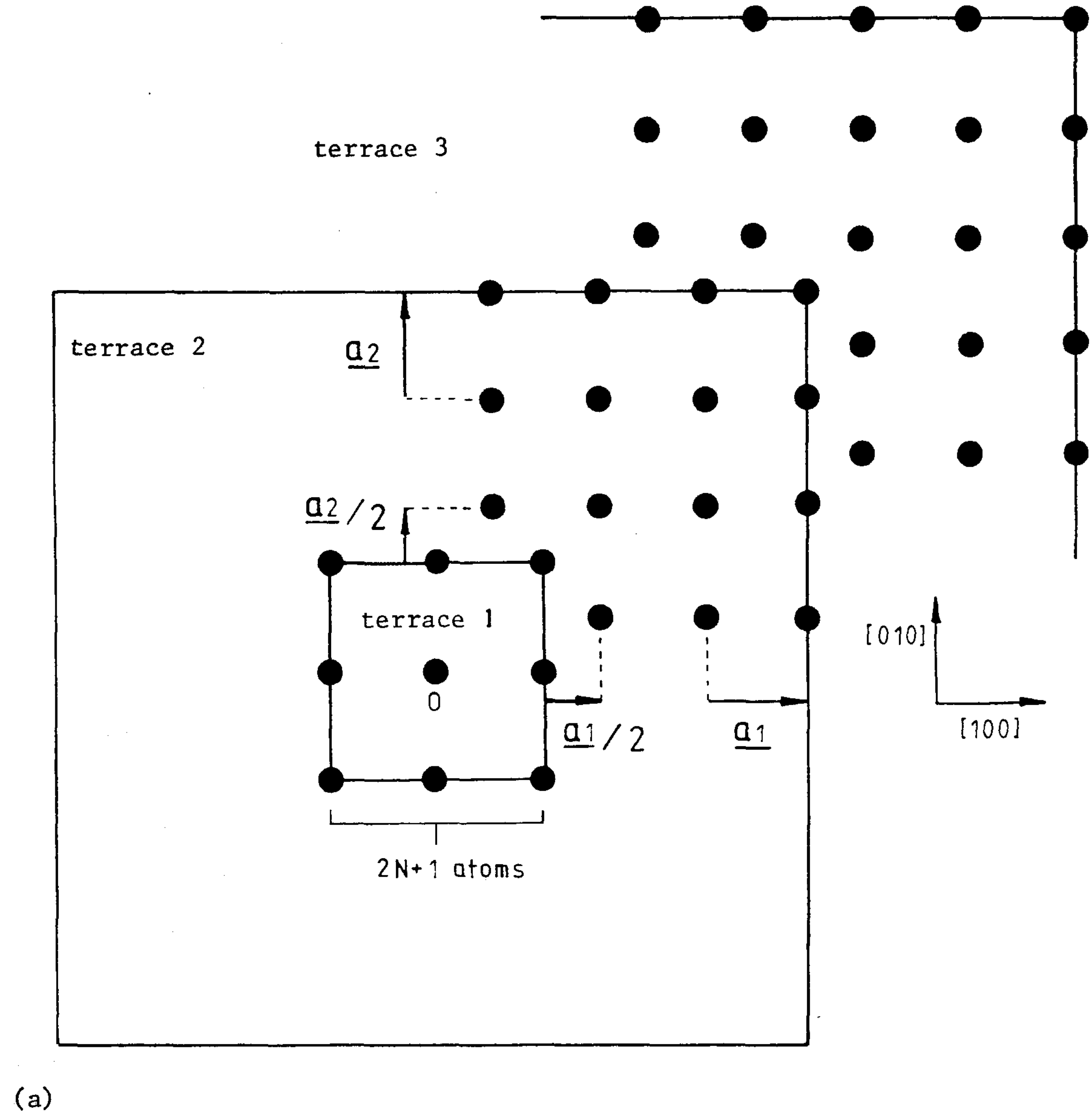

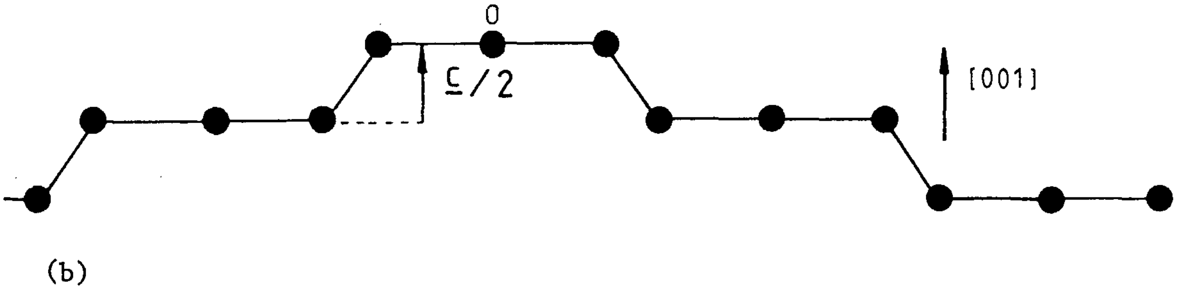

FIG. 6.11 A model of the terraced Sn(001) surfaced used in the kinematic intensity calculations:
(a) View along $[00\bar{1}]$ direction,
(b) Cross-section of surface.
The model is shown for the case N = 1.

i. The model is based on alternate square terraces of Sn(001) bulk planes, the atoms being at (0, 0, 0) and ($\frac{1}{2}$, $\frac{1}{2}$, $\frac{1}{2}$) positions of the bulk unit cell for alternate terraces.

ii. A single coherence zone is considered. Within the coherence zone are n square terraces (n even) with steps between the terraces along the [01] and [10] directions.

iii. The atomic positions within any terrace are defined by the vectors $\underline{a}_1$, $\underline{a}_2$ of the (001) plane of the bulk unit cell.

iv. The displacement of adjacent terraces is given by a vector of modulus $|\underline{g}| = \frac{1}{2}(a_1^2 + a_2^2 + c^2)^{\frac{1}{2}}$.

v. The first terrace is a square with 2N+1 atoms along each side. The position of each atom with respect to the origin 0 is denoted by integral quantities of the vectors $\underline{a}_1$ and $\underline{a}_2$.

vi. All the terraces are of width (2N + 1) atoms.

As all the atoms of odd numbered terraces lie in equivalent positions along [01] and [10] axes (as do all those of even terraces), the total scattering amplitude, A_{Tot}, was determined by considering separately the set of u = 1 to n/2 even and odd terraces.

The scattering amplitude for the first terrace is:

$$A_1 = f \sum_{r=-N}^{N} \sum_{s=-N}^{N} \exp [i\underline{\Delta K} \cdot (r\underline{a}_1 + s\underline{a}_2)]$$

$$= f \sum_{r,s=0}^{N} \cos [\underline{\Delta K}.(r\underline{a}_1 + s\underline{a}_2)] \qquad (6.10)$$

where f is the atomic scattering factor, and $\underline{\Delta K}$ is the scattering vector.

The scattering factor for the second terrace is:

$$A_2 = \exp[-i\underline{\Delta K}.\underline{g}_3](\sum_{r,s=0}^{4N-1} - \sum_{r,s=0}^{N}) \cos [\underline{\Delta K}.(r+\tfrac{1}{2})\underline{a}_1] \cos [\underline{\Delta K}.(s+\tfrac{1}{2})\underline{a}_2]$$

$$(6.11)$$

The first summation refers to the whole area covered by the second terrace, and the second summation subtracts the scattering amplitude for the area which is overlapped by the first terrace. Thus the scattering amplitude for the whole coherence zone is:

$$A_{Tot} = f \Bigg[\Bigg[\sum_{u=1}^{n/2} \exp [-i\underline{\Delta K}.(2u-1)\underline{g}_3]$$

$$\times \left(\sum_{r,s=0}^{5Nu-N-1} - \sum_{r,s=0}^{5Nu-4N} \right) \cos[\underline{\Delta K}.(r+\tfrac{1}{2})\underline{a}_1] \cos [\underline{\Delta K}.(s+\tfrac{1}{2})\underline{a}_2] \Bigg]$$

$$+ \left[\sum_{u=1}^{n/2} \exp[-i\underline{\Delta K}.2(2u-2)\underline{g}_3] \right.$$

$$\left. \times \left(\sum_{r,s=0}^{5Nu-4N} - \sum_{r,s=0}^{5Nu-6N-1} \right) \cos[\underline{\Delta K}.r\underline{a}_1] \cos[\underline{\Delta K}.s\underline{a}_2] \right]\Bigg] \qquad (6.12)$$

The intensity distribution, I is given by

$$I = (A_{Tot})^* A_{Tot} \qquad (6.13)$$

Using spherical polar co-ordinates I can be expressed as $I(\Theta,\phi)$, where Θ is the angle between the surface normal and the scattering vector $\underline{\Delta K}$; and ϕ is the angle between a projection of $\underline{\Delta K}$ onto the (001) plane and the [100] direction (Fig. 6.12).

Thus for normal incidence

$$\underline{\Delta K}.\underline{a}_1 = ka_1 \sin\theta \cos\phi$$

$$\underline{\Delta K}.\underline{a}_2 = ka_2 \sin\theta \sin\phi$$

$$\underline{\Delta K}.\underline{g}_3 = kg_3 (1 + \cos\theta) \qquad (6.14)$$

where k is the modulus of the incident wavevector. As the L.E.E.D optics has an acceptance angle of 120°, the range of values of θ, and ϕ are:

$$0 \leqslant \theta \leqslant \pi/3$$

$$0 \leqslant \phi < 2\pi$$

The calculated intensity distributions have been plotted in two ways: firstly as L.E.E.D. patterns for a qualitative comparison of spot shapes and positions with those of the experimental results; and secondly in the form of graphical plots of intensities along specific axes in order to compare the theoretical and experimental positions of maxima, and to verify the predictions by Henzler for single and split spots.

Patterns and intensity distributions were derived for a perfect surface and for a range of possible terrace distributions assuming a coherence zone of between 300 - 400 Å. The terrace models considered were: 3 atoms per terrace, 12 terraces; 7 atoms per terrace, 6 terraces; and 11 atoms per terrace, 4 terraces, within the coherence zone. The patterns and intensity distributions were plotted at 19.5V, 26V, and 35.5V for each of these models as these voltages covered the range in which the {10} and {11} reflections underwent the transition between single and multiple spots. The intensity distributions were plotted along the [10] axis of the reciprocal lattice through the (00) and (10) spots, and the [01] axis through the (10) and (11) spots.

The theoretical pattern from a perfect single square terrace of 61 x 61 atoms at 26V (Fig. 6.13) has single spots (within an intensity range of two orders of magnitude) at each of the reciprocal lattice positions corresponding to the surface net of an (001) plane. The data for this perfect surface model was plotted at higher resolution ($\Delta\theta=\Delta\phi = 0.25^{o}$) than that for the terrace models for which $\Delta\theta=\Delta\phi = 0.5^{o}$. There is a rapid fluctuation of the intensity distribution within the envelope formed by each of the maxima in the intensity distribution of the perfect surface (Fig. 6.14). This fluctuation was not as well resolved in the intensity distributions of the terrace models. Only the envelopes formed by the major peaks were of importance for the purpose of comparison between the theoretical results, experimental results, and previous studies.

The real pattern at 26V (Fig. 6.15a) features a splitting of both the {10} and {11} reflections. The closest approximation to the real pattern is given by the model with 3 atoms per terrace (Fig. 6.15b). This model predicts a cross-shaped spot of approximately the right size for each of the {10} reflections, as well as a spot at the correct position between each of the {10} and {11} positions. It does not correctly predict the relative intensities of the {10} and {11} features (Figs. 6.15b, 17, 18); the size and shape of the {11} features; or the detail sometimes seen around the {10} features (Fig. 6.3). The other two models have reciprocal lattices with less resemblance to the real pattern at this voltage (Fig. 6.16a, b).

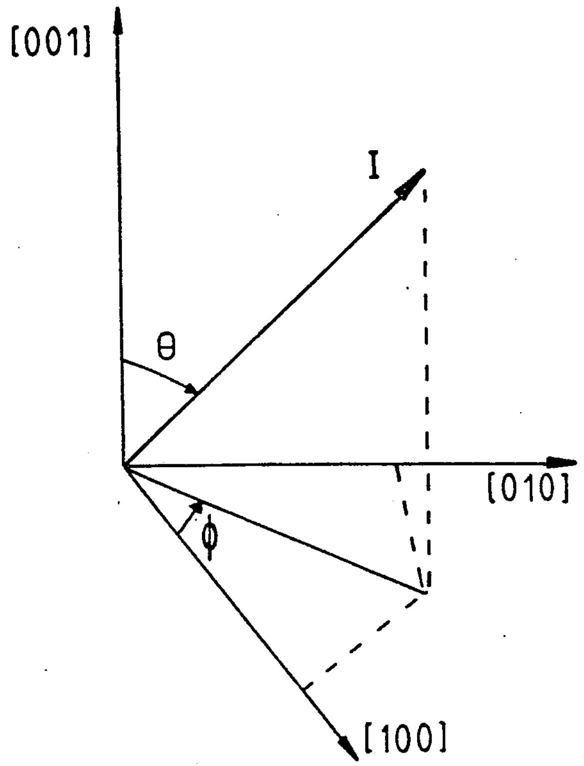

FIG. 6.12 Co-ordinate system for the kinematic model of the Sn(001) surface.

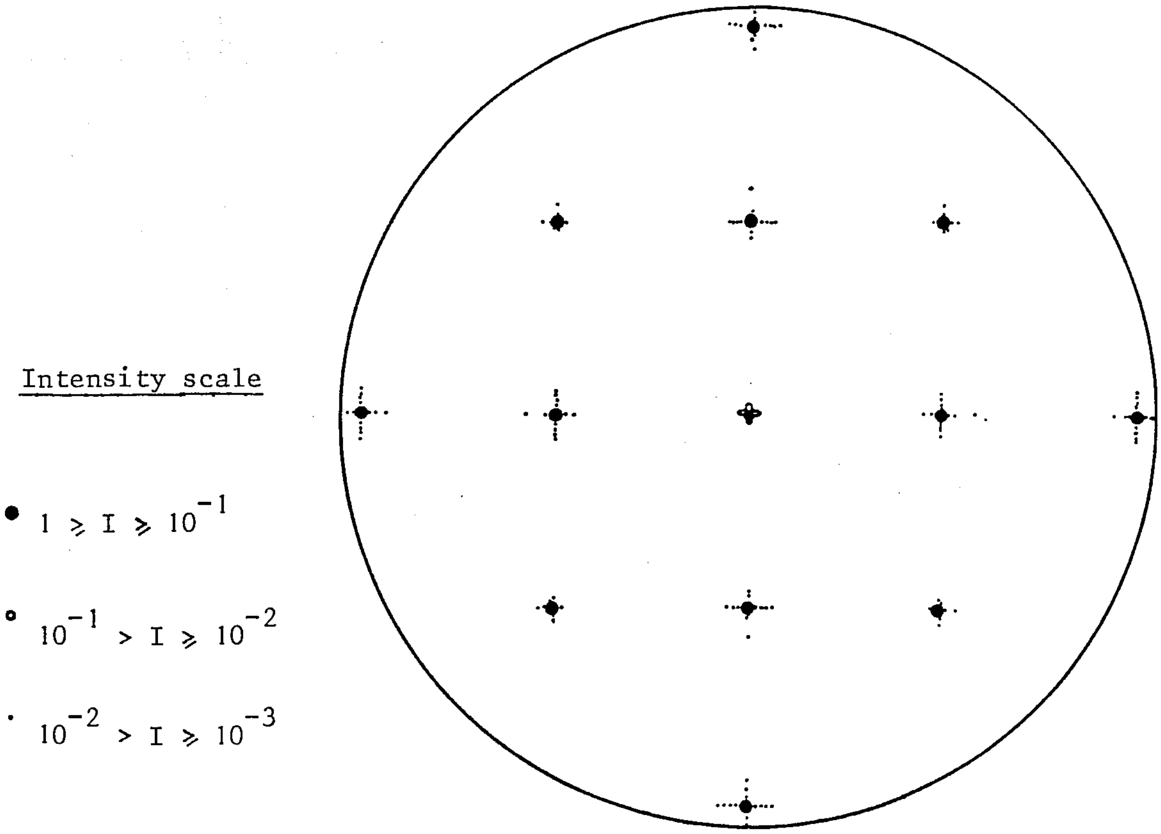

FIG. 6.13 Diffraction pattern calculated for one coherence zone (61 x 61 atoms) of a perfect Sn(001) surface at 26V, normal incidence.

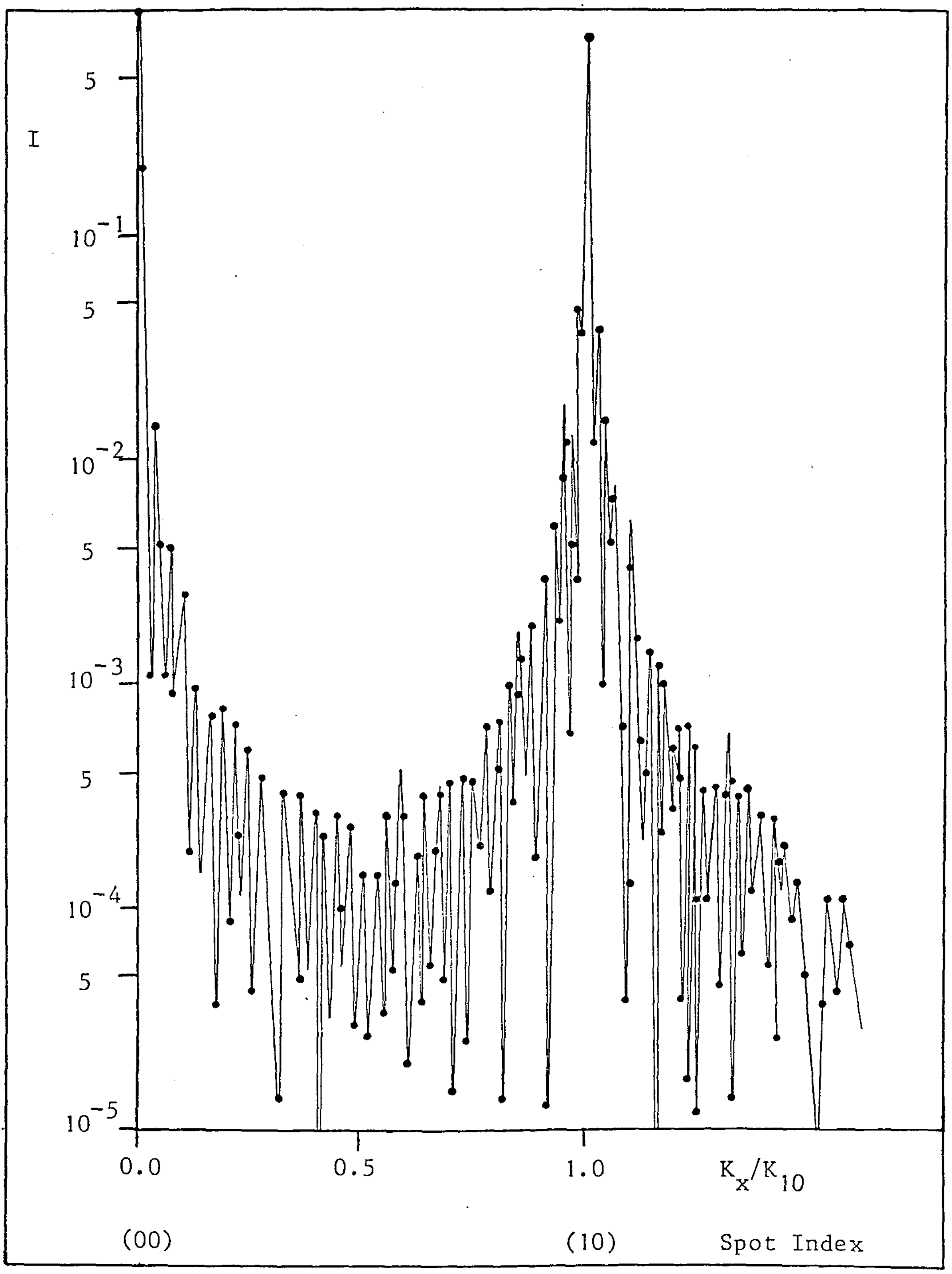

FIG. 6.14 Intensity distribution curve for a single Sn(001) terrace of 61 x 61 atoms along the [10] axis of the reciprocal lattice at 26V.

(a)

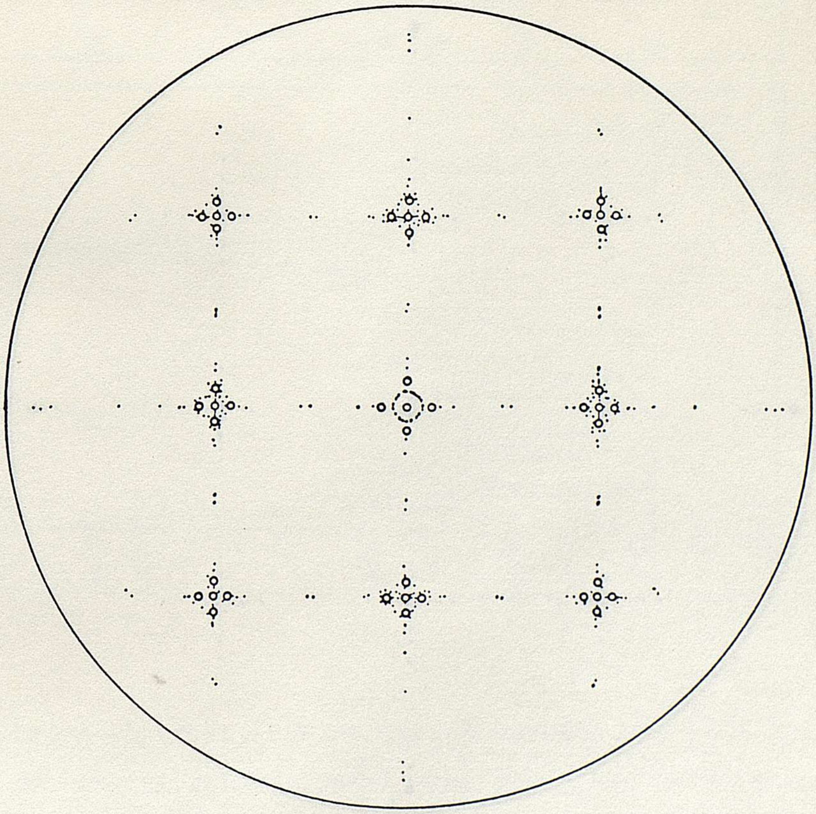

(b)

FIG. 6.15 (a) Real diffraction pattern at 26V.

(b) Theoretical pattern at 26V for a kinematic model with 3 atoms per terrace, 12 terraces.

(a)

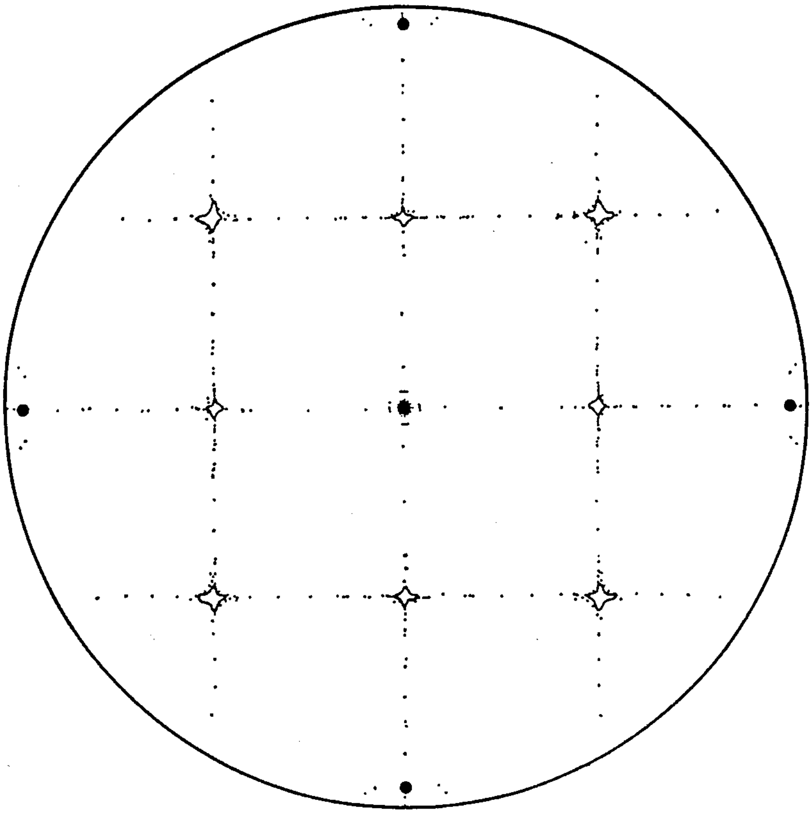

(b)

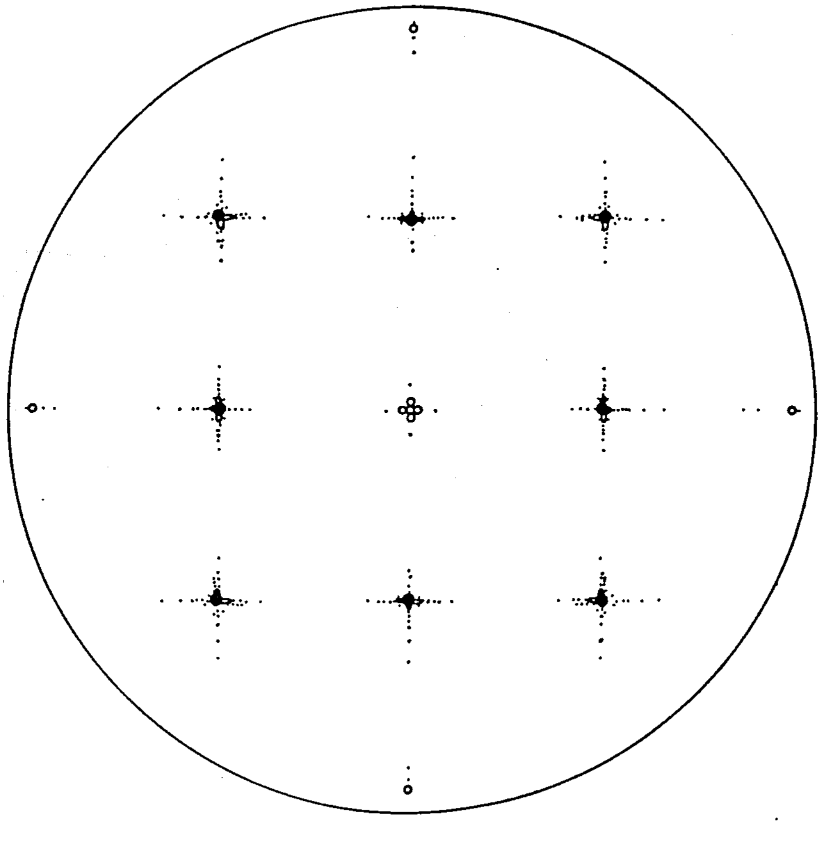

FIG. 6.16 Theoretical patterns at 26V for kinematic models with

(a) 7 atoms per terrace, 6 terraces

(b) 11 atoms per terrace, 4 terraces

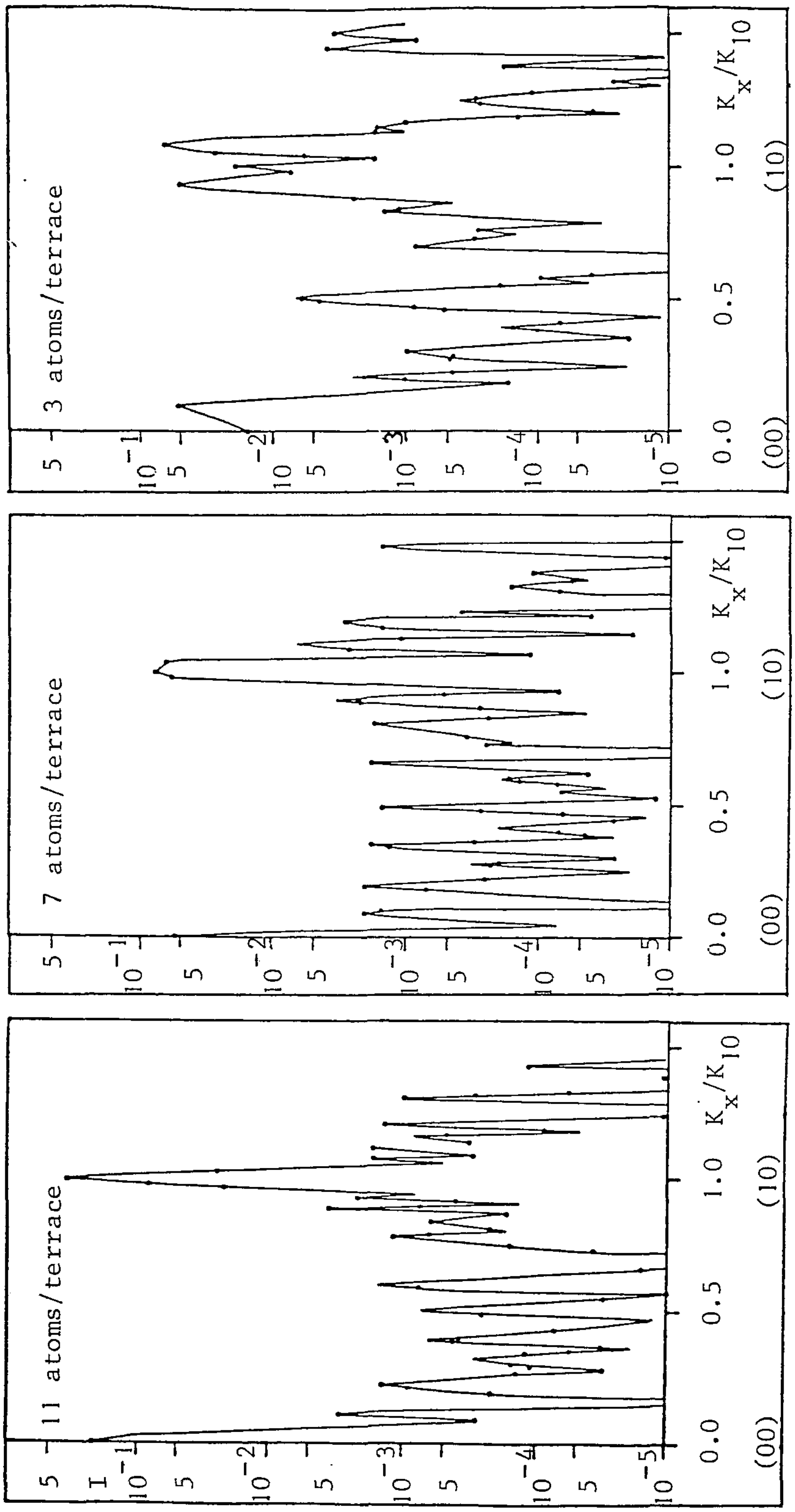

FIG. 6.17 Intensity distribution curves between the (00) and (10) reciprocal lattice points for the three terrace models at 26V.

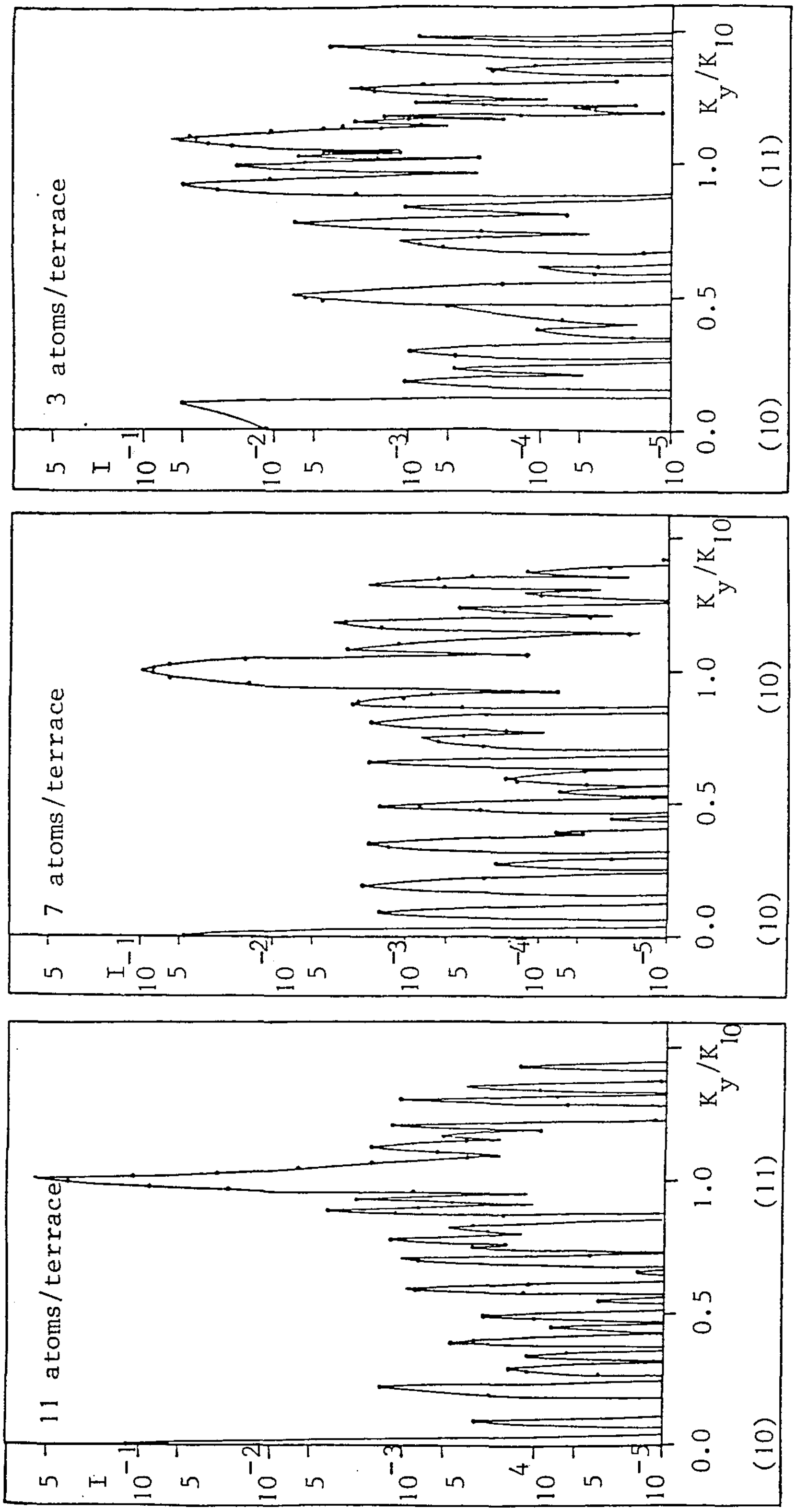

FIG. 6.18 Intensity distribution curves between the (10) and (11) reciprocal lattice points for the three terrace models at 26V.

Both the {10} and {11} reflections appear as single maxima for the model with 11 atoms per terrace (Figs. 6. 17,18). These reflections broaden in the model with 7 atoms per terrace and form multiple maxima in the model with 3 atoms per terrace. The (00) reflection also forms a single maximum (within an order of magnitude) in the models with 7 and 11 atoms per terrace but forms multiple maxima for the model with 3 atoms per terrace.

At 19.5V the {11} reflections form single spots (Fig. 6.19a), and the {10} reflections are faint and diffuse (being close to the antiphase condition of 17.1V for the {10} reflections). Each of the models predicts a splitting of the {10} reflections (Fig. 6.21) and a single maximum (within two orders of magnitude) for the {11} reflections (Fig. 6.22). The size of the splitting of the {10} reflections increases as the terrace width decreases. These reflections appear cross-shaped in the simulated diffraction patterns (Figs. 6.19b, 6.20a,b). Again the width of the {10} reflections is most closely approximated by the model with 3 atoms per terrace, although there appear to be more features present in the actual L.E.E.D. pattern. Most of the features with an intensity more than an order of magnitude below that of {11} spots are not visible in the real pattern.

(a)

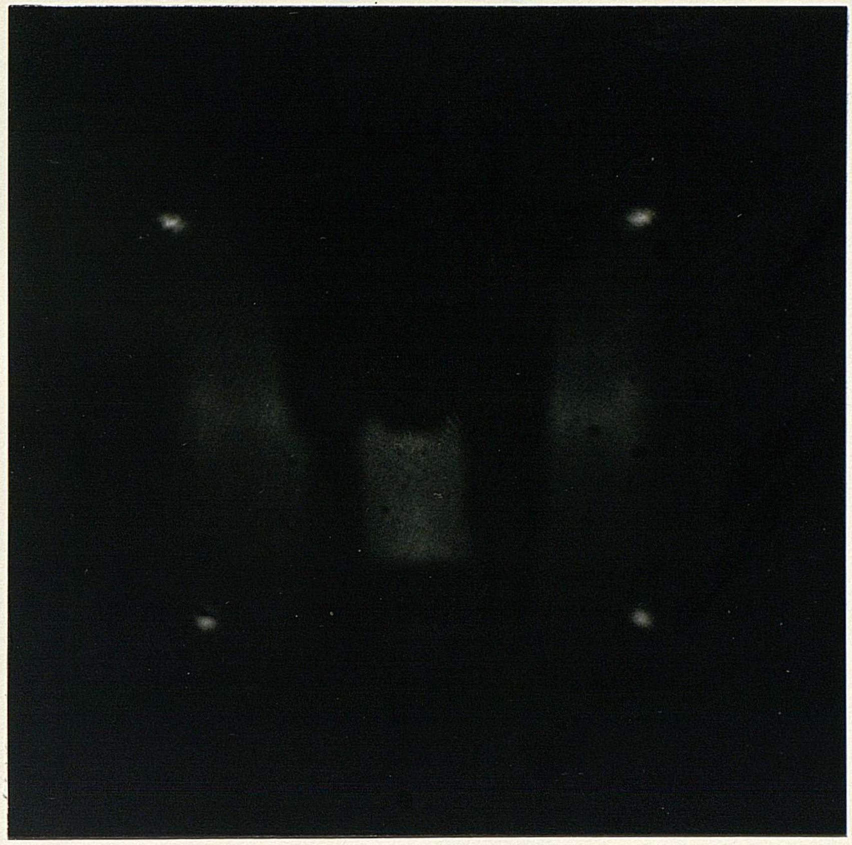

(b)

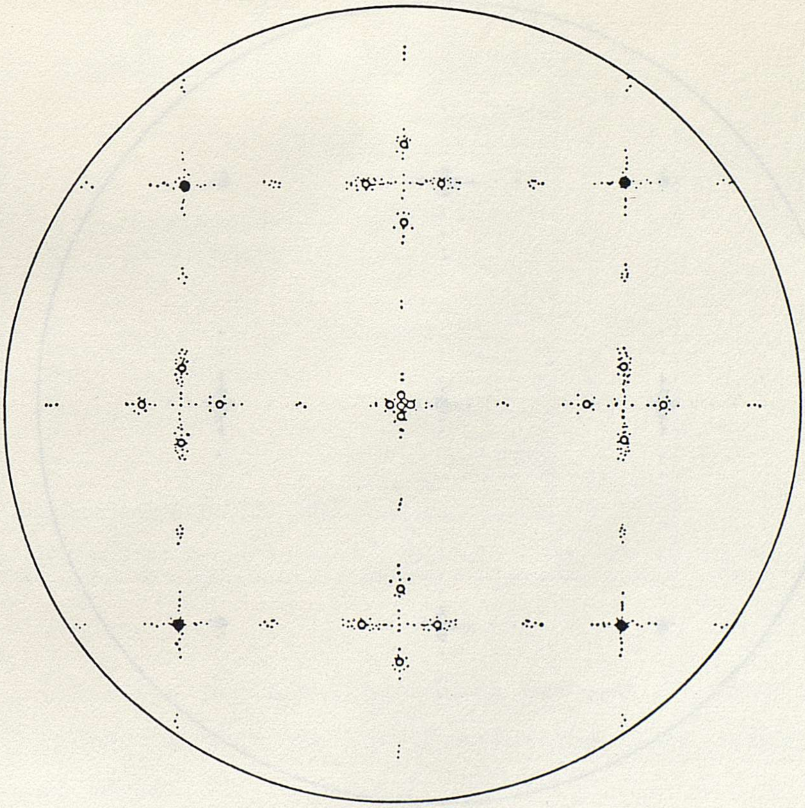

FIG. 6.19 (a) Real diffraction pattern at 19.5V

(b) Theoretical pattern at 19.5V for a kinematic model with 3 atoms per terrace, 12 terraces.

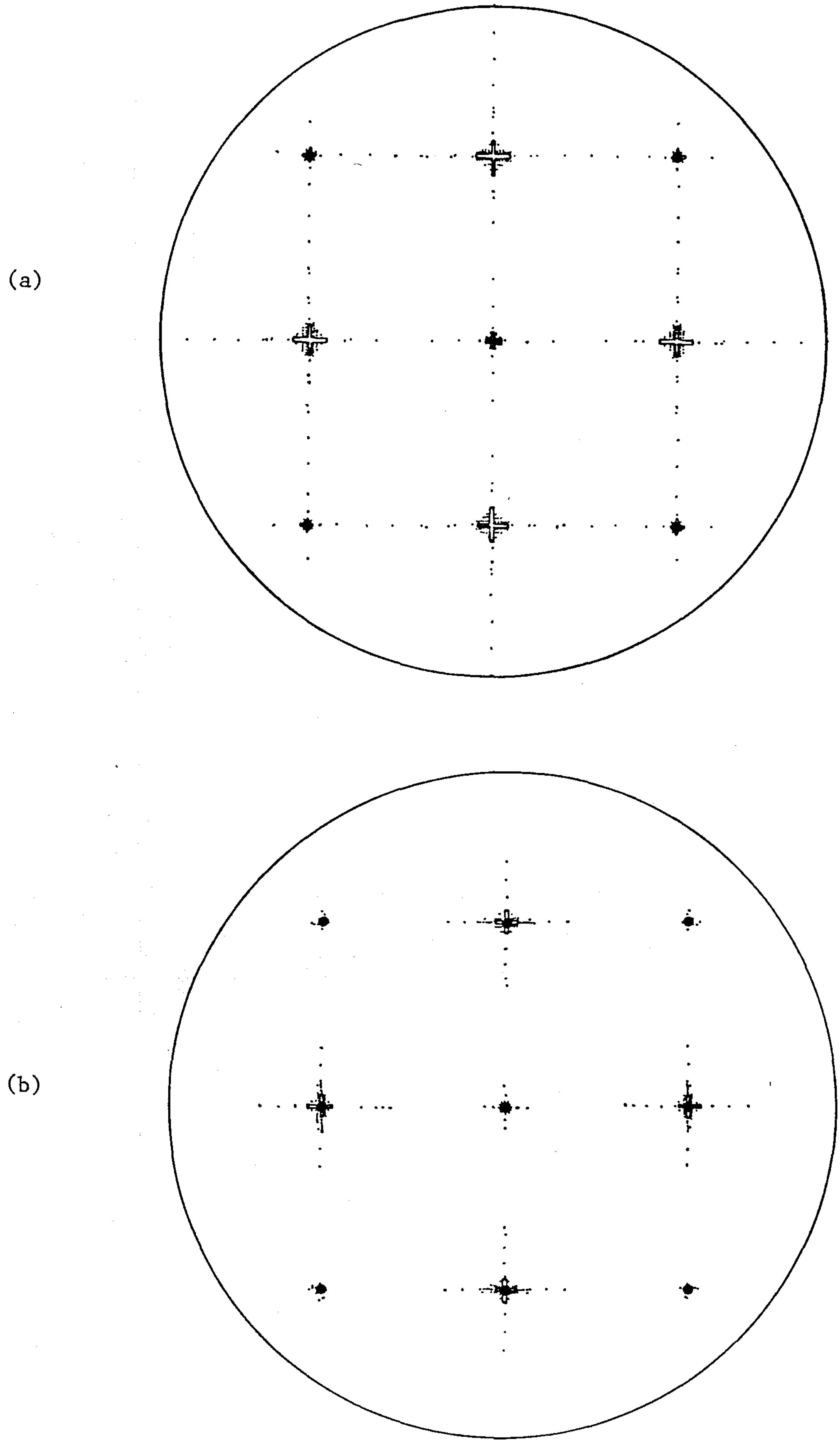

FIG. 6.20 Theoretical patterns at 19.5V for kinematic models
with (a) 7 atoms per terrace, 6 terraces.
(b) 11 atoms per terrace, 4 terraces.

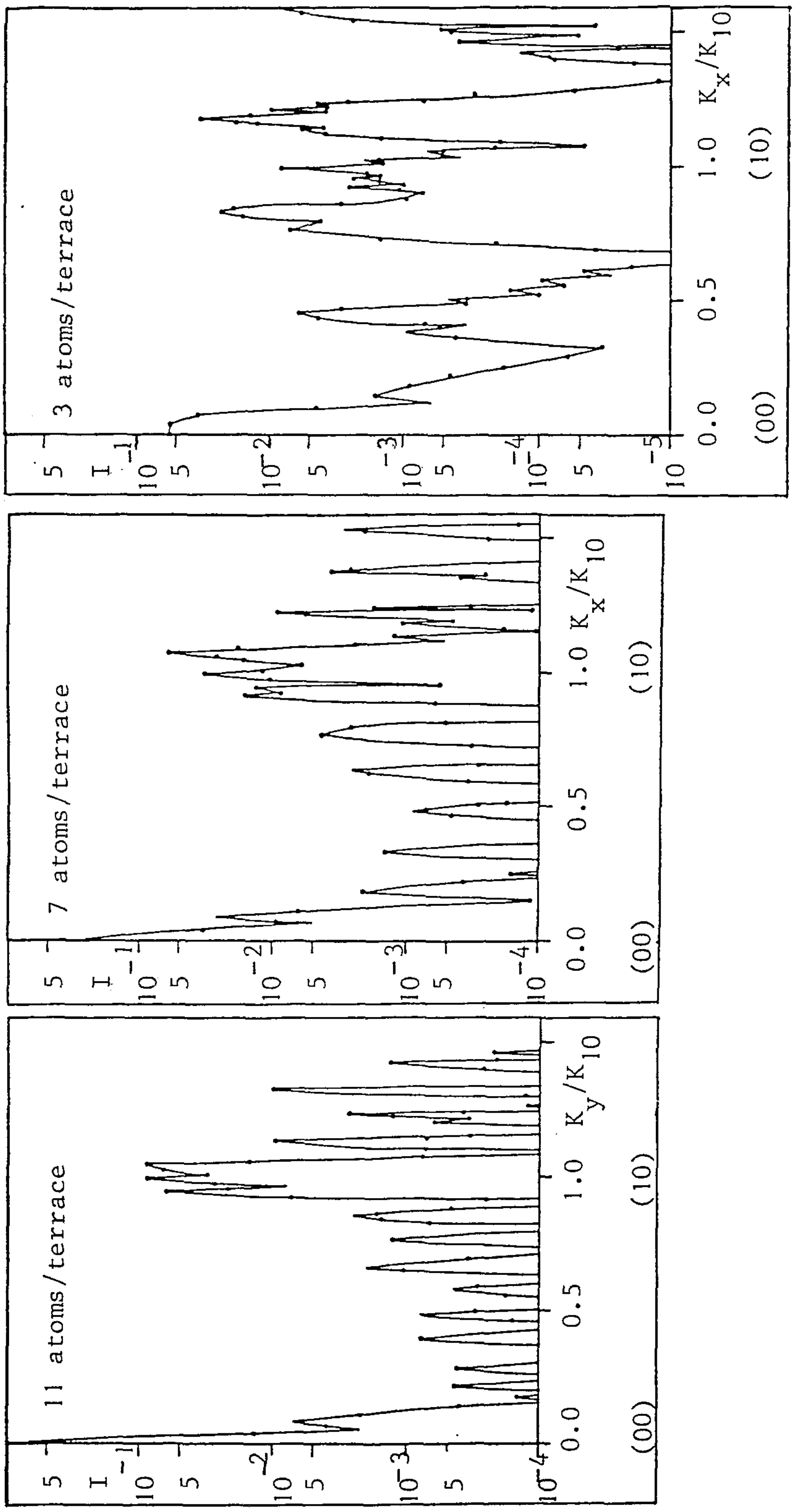

FIG. 6.21 Intensity distribution curves between the (00) and (10) reciprocal lattice positions for the three terrace models at 19.5V.

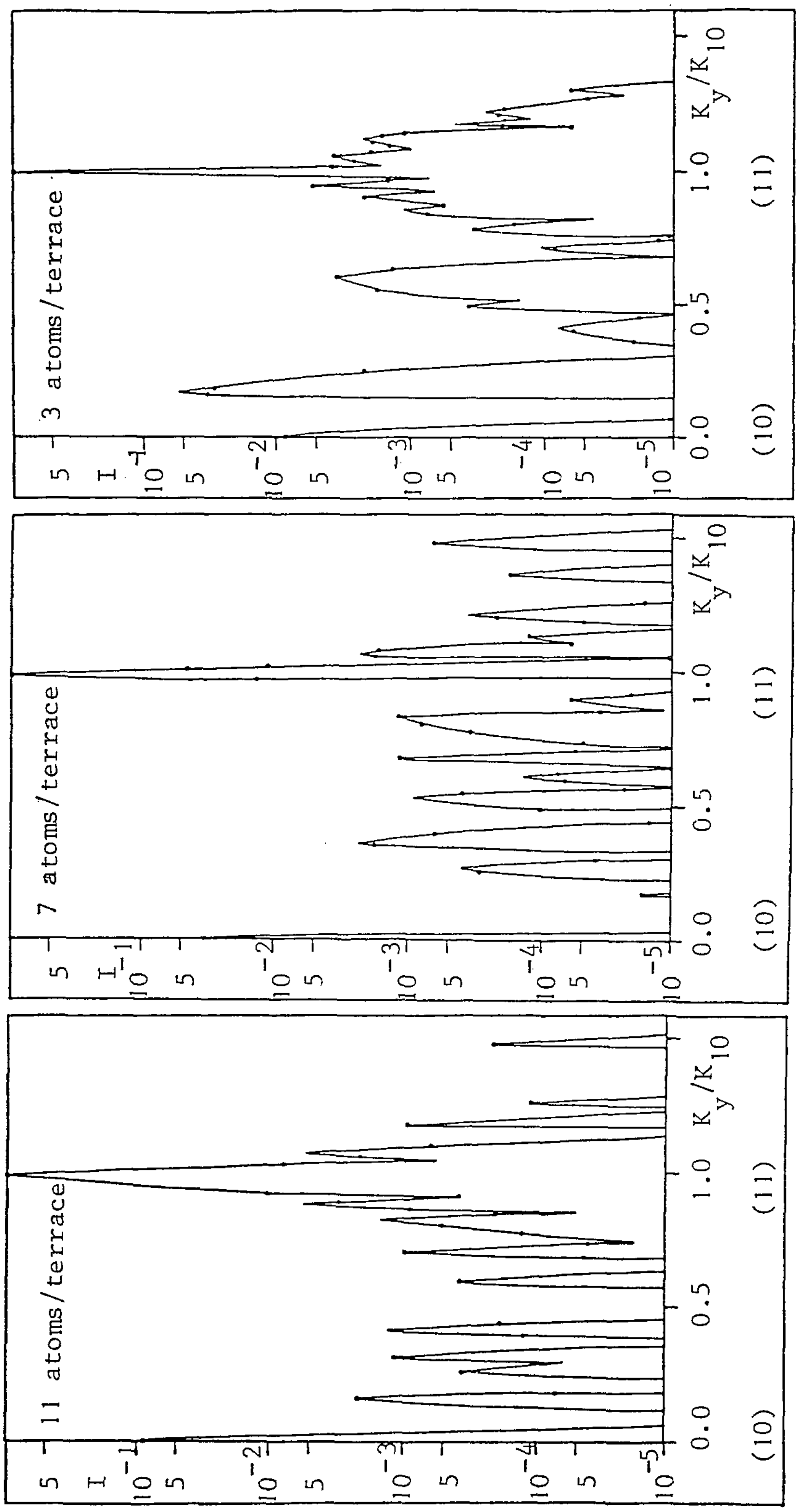

FIG. 6.22 Intensity distribution curves between the (10) and (11) reciprocal lattice positions for the three terrace models at 19.5V.

The situation at 35.5V is similar to that at 19.5V. Here, the real pattern (Fig. 6.23a) consists only of single {10} spots. The {10} reflections also appear as single spots in each of the theoretical patterns (Figs. 6.23b, 6.24a,b). The intensities of the features of the other reflections are an order of magnitude less than the {10} reflections (Figs. 6.25,26). The model with 3 atoms per terrace predicts splitting of all the reflections apart from the {10} reflections. Only the {11} reflections appear split in the model with 11 atoms per terrace while the model with 7 atoms per terrace shows splitting of most reflections.

Of the three models considered, the closest approximation to the real patterns is given by the model with 3 atoms per terrace, and 12 terraces within one coherence zone. This model does not give complete agreement between theory and experiment. These results have been further discussed in Chapter 8.

6.4 THE OXIDISED Sn(001) SURFACE

Oxidation of an initially clean Sn(001) surface at room temperature led to the gradual disappearance of the clean Sn(001) pattern (Fig. 6.27). After $\approx$ 1000L (corresponding to $\approx$ 3/4 monolayer by the uptake curve of Fig. 5.19) no spot pattern could be seen. Merely a background intensity was observable (Fig. 6.27c).

(a)

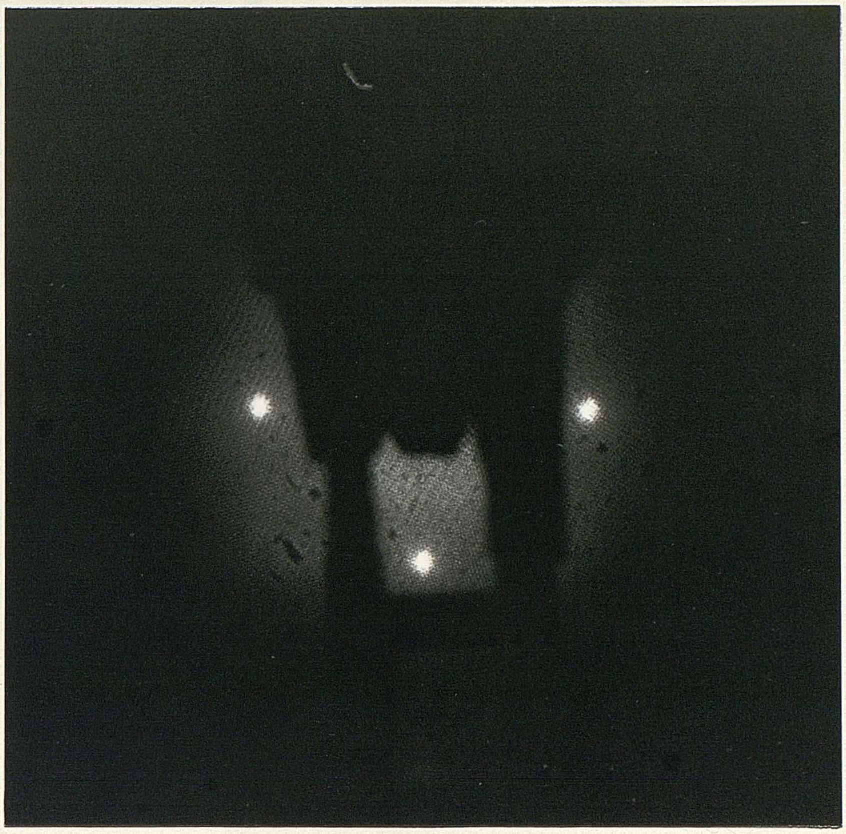

(b)

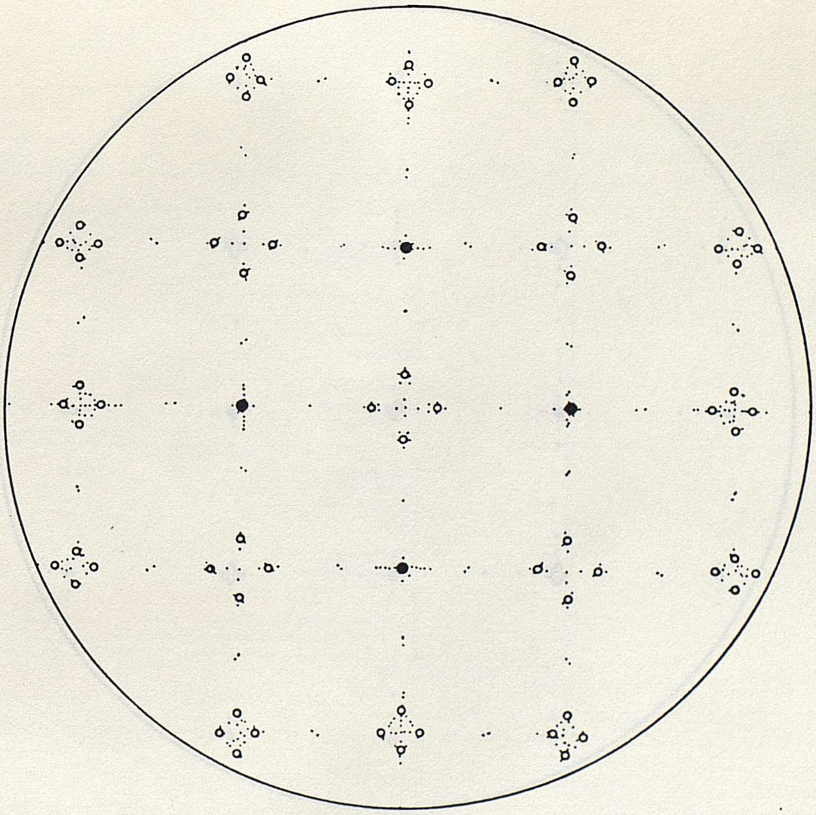

FIG. 6.23 (a) Real diffraction pattern at 35.5V.
(b) Theoretical pattern at 35.5V for a kinematic model with 3 atoms per terrace, 12 terraces.

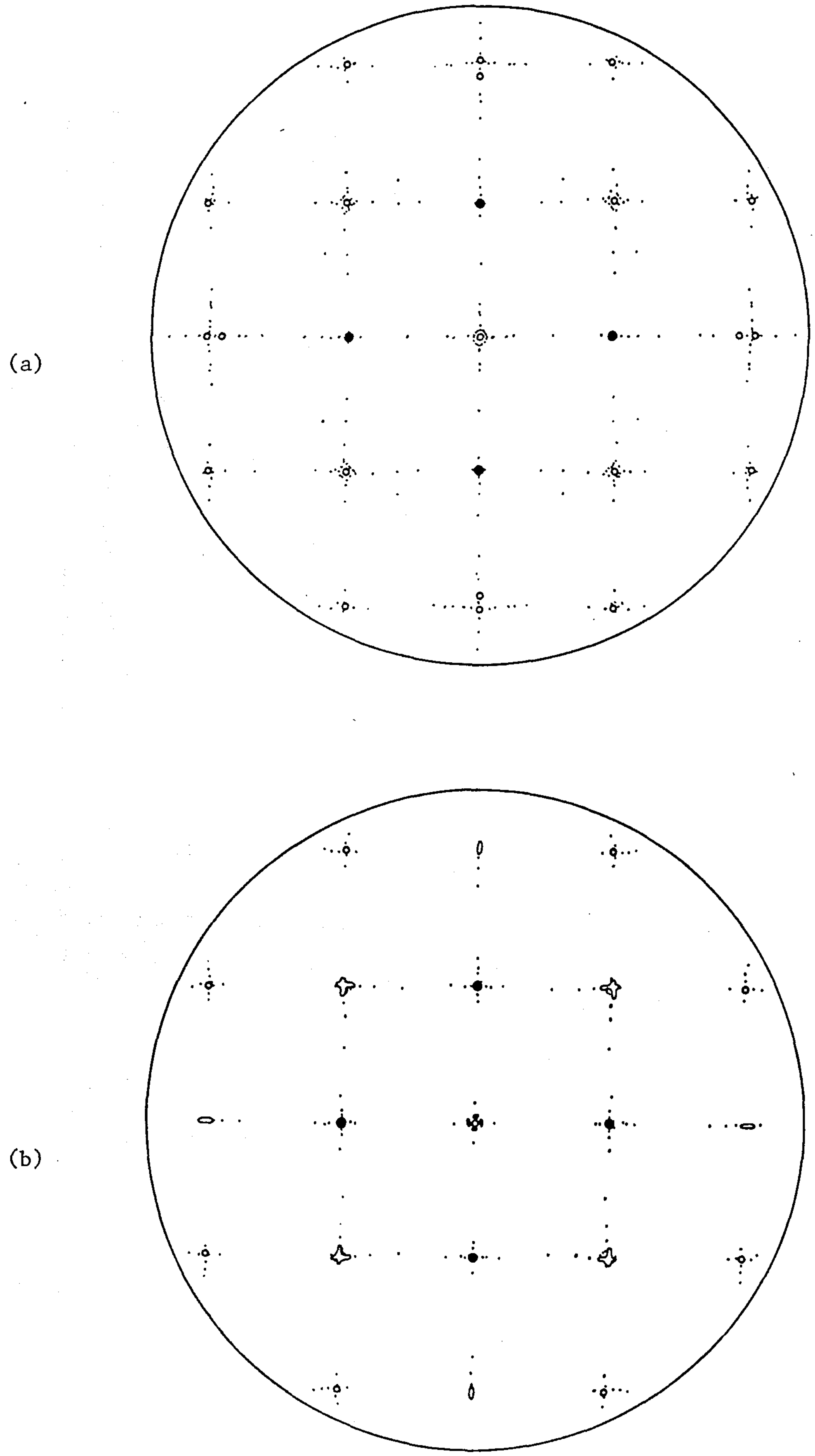

FIG. 6.24 Theoretical patterns at 35.5V for kinematic models with (a) 7 atoms per terrace, 6 terraces.
(b) 11 atoms per terrace, 4 terraces.

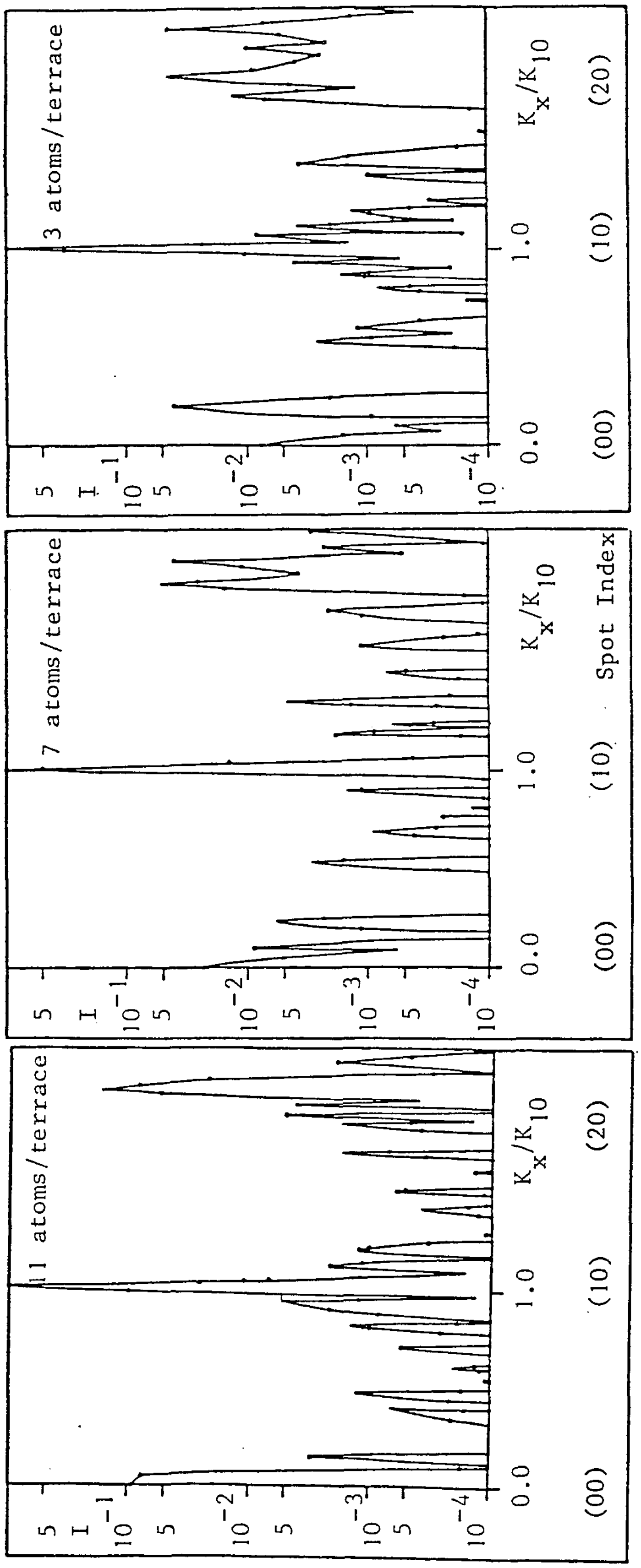

FIG. 6.25 Intensity distribution curves along the [10] axis of the reciprocal lattice for the terrace models at 35.5V.

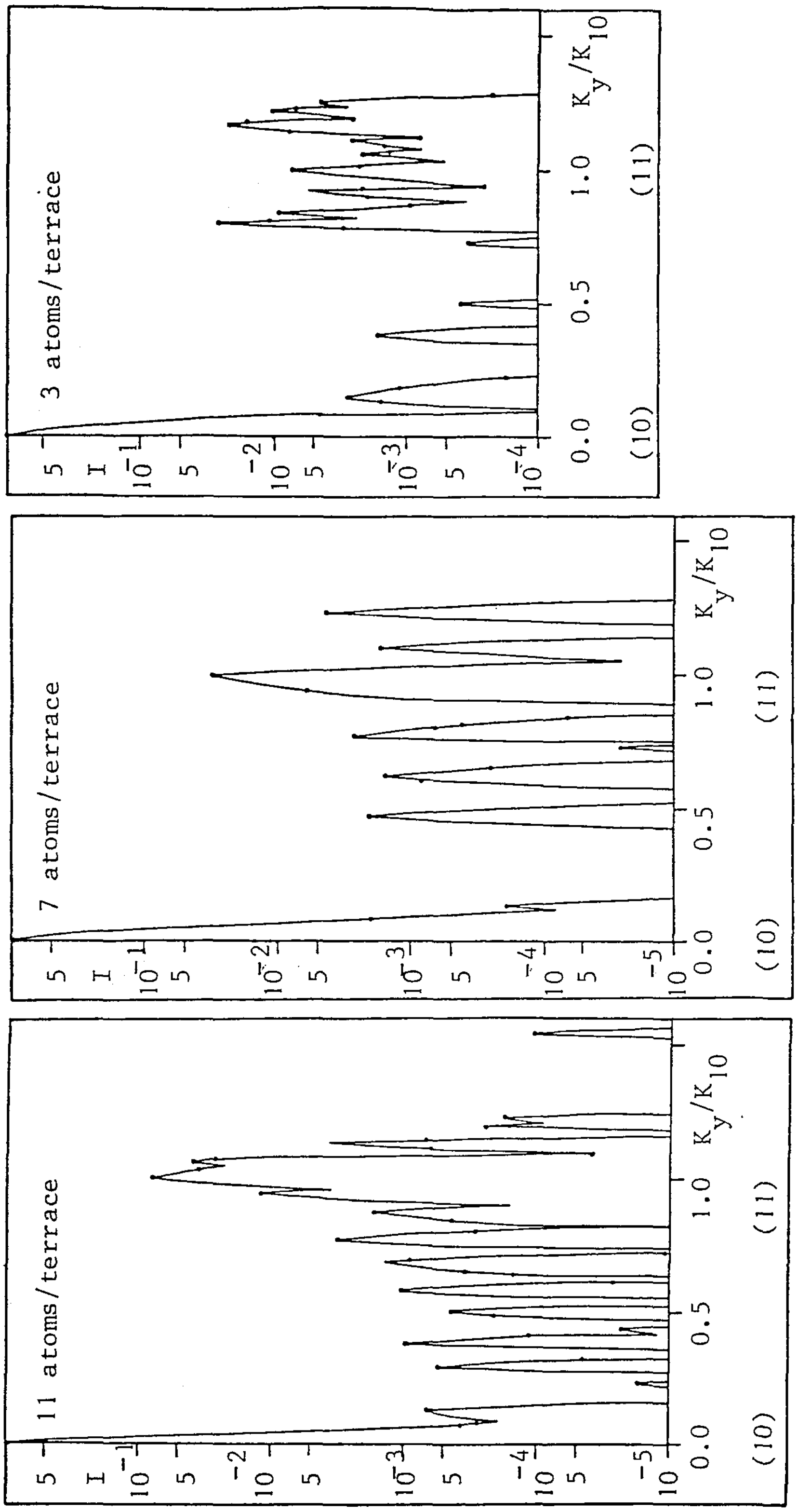

FIG. 6.26 Intensity distribution curves between the (10) and (11) reciprocal lattice points for the three terrace models at 35.5V.

(a) Clean surface

(b) After 500L

(c) After 1000L

FIG. 6.27 L.E.E.D. during room temperature oxidation of Sn(001)

A similar situation occurred on oxidation at 130K. Neither oxidation at 393K, nor annealing the room temperature grown oxide to 473K produced a spot pattern. Thus, one may conclude that the oxidation of the Sn(001) surface results in the formation of an amorphous overlayer under these experimental conditions.

6.5 SUMMARY

The clean Sn(001) surface formed after argon ion bombardment and annealing to 473K consisted of terraces of bulk (001) planes. The terraces were separated by steps of height 1.59Å, both up and down along the [01] and [10] directions of the surface net. The experimental L.E.E.D. patterns were compared with patterns and intensity distribution curves derived from model surfaces using kinematic theory. The closest agreement between theory and experiment was provided by a model with 3 atoms per terrace, and 12 terraces within one coherence zone.

The oxidised surface was amorphous over the temperature range 130K to 473K.

CHAPTER 7

L.E.E.D. RESULTS FROM THE Sn(101) SURFACE

7.1 THE CLEAN Sn(101) SURFACE

The bulk Sn(101) planes (fig. 7.1) may be considered in pairs, each pair being 2.10Å apart, and being displaced by 1.53Å from adjacent pairs along the [101] direction. Plane B of each pair is displaced from plane A by 0.70Å along the normal to the planes and by 3.70Å along the $[10\bar{1}]$ direction.

If the outermost layer of the surface is an A-type plane, the surface will also contain a partial exposure of a plane of type B. The formation of such a surface requires one partial covalent bond to be broken by each of the atoms of plane A. For the case of a B-type plane being outermost one may consider that no partial exposure of the adjacent underlying A-plane occurs. Each atom of the B-plane would be required to have three of its four bulk partial covalent bonds to be broken. In the latter case the kinematic structure factor for the surface is simply that of the centred-rectangular B-type plane and is

$$F(hk) = f \sum_{j=1}^{s} \exp\{i\underline{K}.\underline{r}_j\} \qquad (7.1)$$

where f is the atomic structure factor, and $\underline{r}_j = \underline{r}_1 \ldots\ldots \underline{r}_s$ are the atomic positions in the surface unit net which has dimensions $|\underline{a}_1| = 5.83$Å, $|\underline{a}_2| = 6.64$Å.

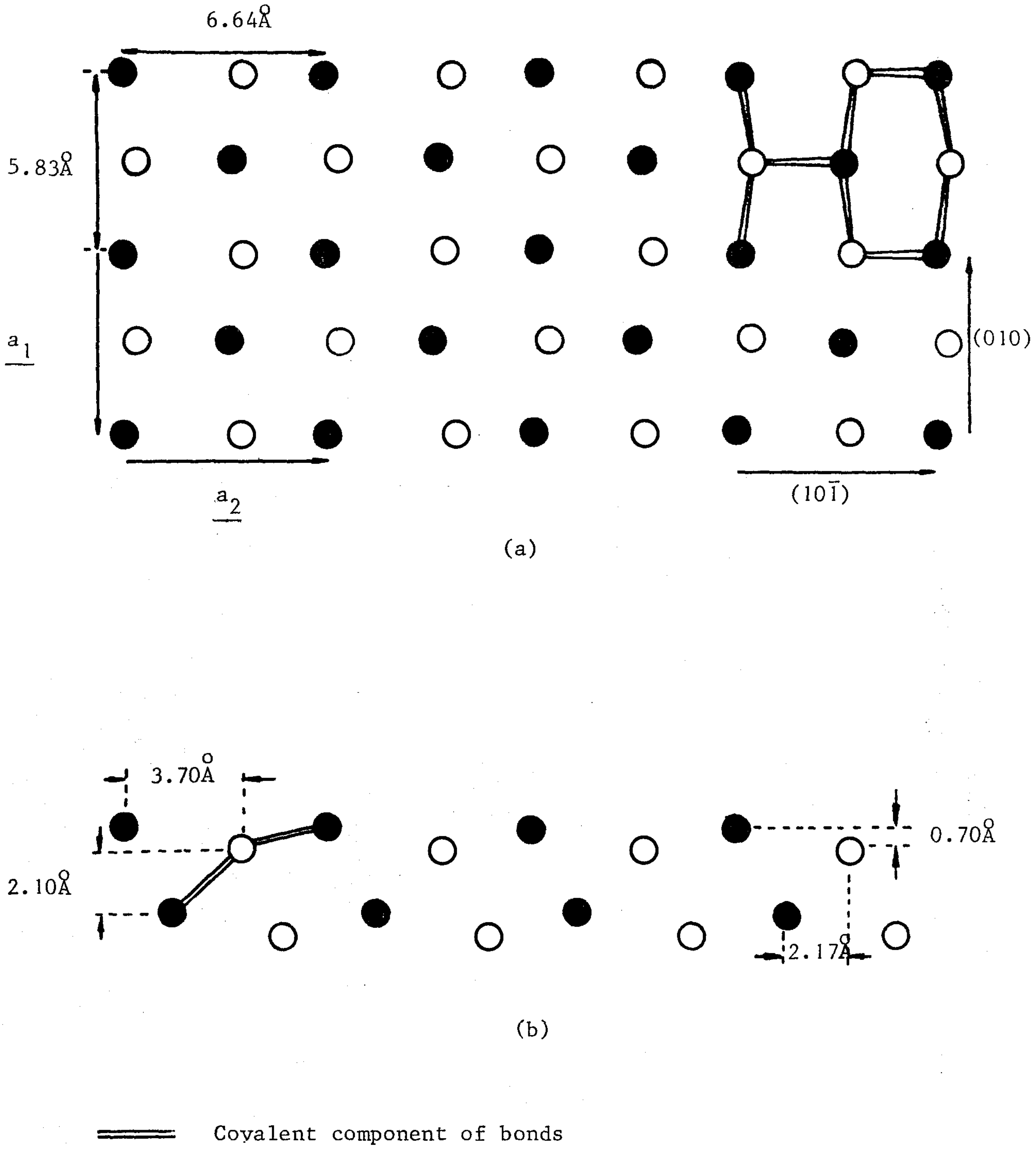

FIG. 7.1 The bulk (101) planes: 'A' planes are shaded, 'B' planes are unshaded.

(a) An 'A' plane outermost with partial exposure of a 'B' plane.

(b) Cross section of the (101) plane with an 'A' plane outermost.

In any one unit cell there are four atoms at (00) positions shared by four other unit cells, and one at a($\frac{1}{2}\frac{1}{2}$) position. Thus:

$$F(hk) = f(1 + \exp\{\pi i(h + k)\}). \tag{7.2}$$

Hence $F(hk) = 2f$ for $(h + k)$ even

0 for $(h + k)$ odd

Thus a centred-rectangular L.E.E.D. pattern would be expected in this case.

In the former case scattering occurs from the outermost A layer with a partially exposed B layer. Again, the basis vectors for the surface net are $\underline{a}_1$, $\underline{a}_2$. The surface net is no longer centred-rectangular. Qualitatively, one would expect the observed pattern for such a surface to be rectangular, the intensities of each of the (hk) reflections being affected by the relative displacements of the planes A, and B, both in and perpendicular to the (101) plane.

Apart from faint satellite spots, the observed diffraction spots (figs. 7.2,3) were centred-rectangular, the ratio of the basis vectors of the reciprocal net being 0.88 ± 0.01. The ratio of the unit vectors for a (101) plane is $|\underline{a}_1|/|\underline{a}_2| = 0.88$. This suggests a situation similar to the aforementioned case of a B-plane being outermost. The patterns appeared to be distorted by external (magnetic) fields which made interplanar measurements by I/V curves impossible.

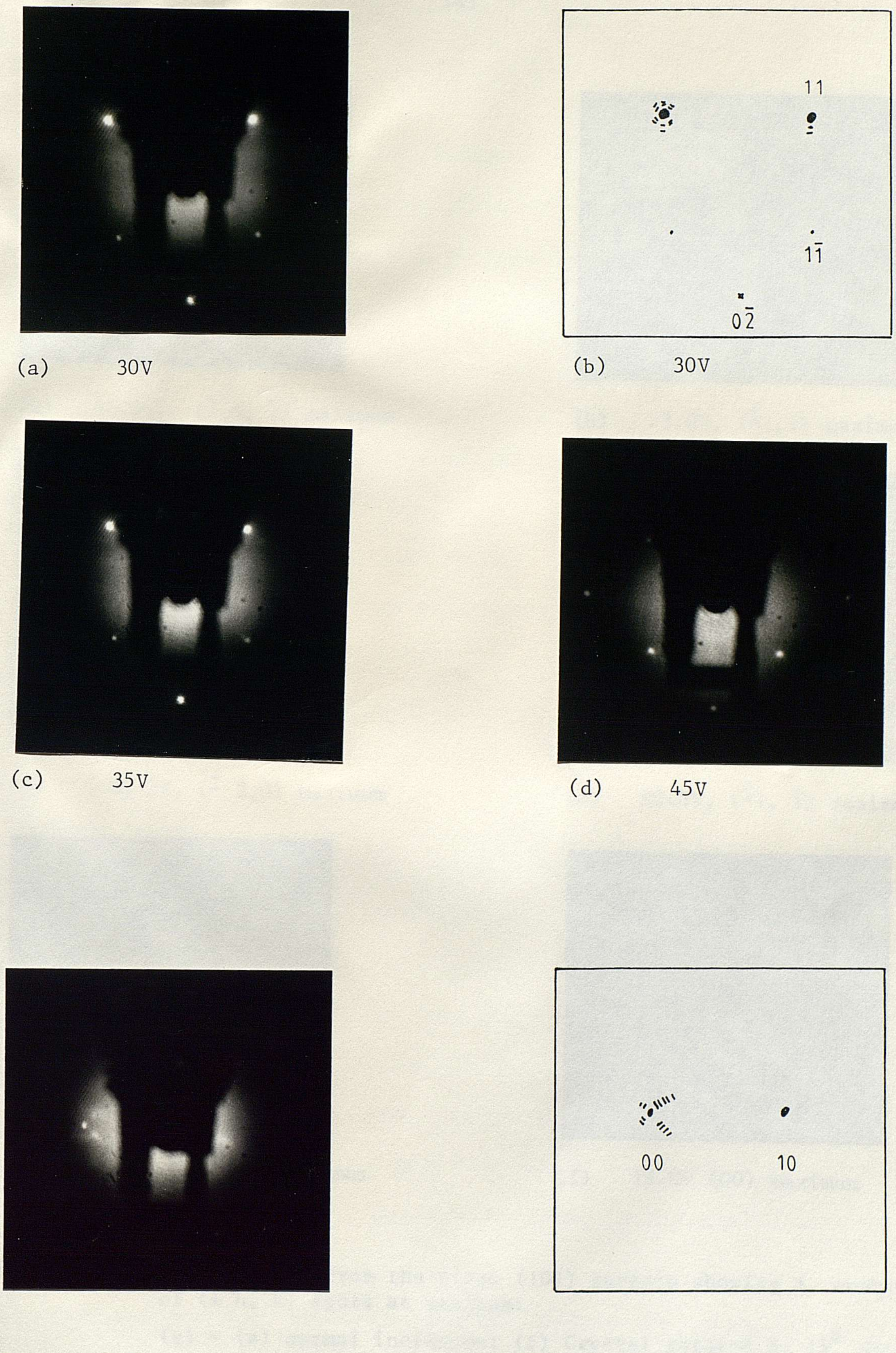

(a) 30V

(b) 30V

(c) 35V

(d) 45V

(e) 30V

(f) 30V

FIG. 7.2 Clean Sn(101): (a) - (d) normal incidence,
(e) - (f) 15° incidence.
Photos taken at 135K.

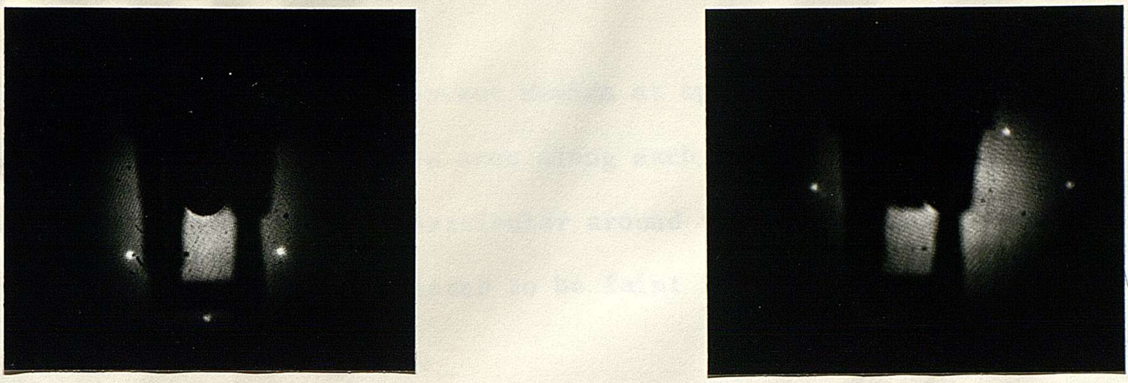

(a) 52.0V, $(\pm 1, \bar{1})$ maximum

(b) 73.0V, $(\pm 1, 1)$ maximum

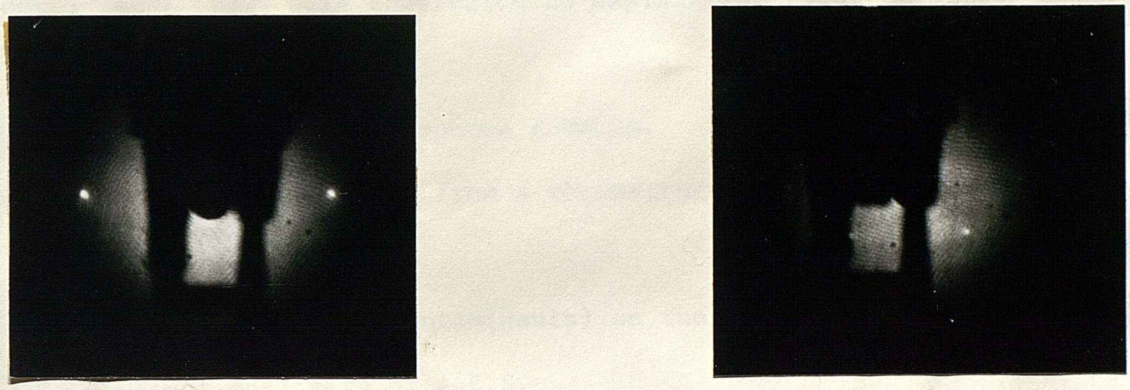

(c) 80.0V, $(\pm 2, 0)$ maximum

(d) 90.0V, $(\pm 1, \bar{1})$ maximum

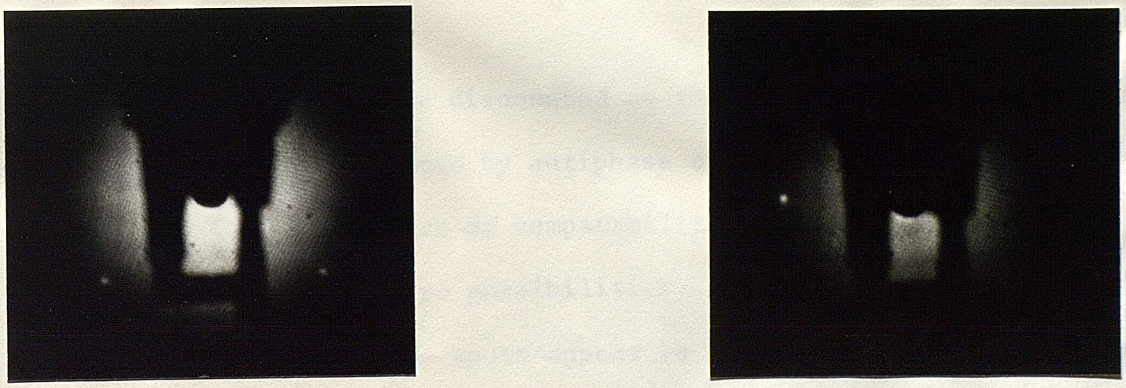

(e) 101.5V, $(\pm 2, \bar{2})$ maximum

(f) 79.0V (00) maximum

FIG. 7.3 LEED at 135K from the clean (101) surface showing a number of (± h, k) spots at maximum:
(a) - (e) normal incidence; (f) Crystal rotated by 15° about the $(10\bar{1})$ axis.

Each set of $(\pm hk)$ spots underwent maxima at specific voltages. Faint satellite spots could also be seen along each of the [11] directions of the reciprocal lattice, in particular around the (00) and (± 11) spots (fig. 7.2). There also appeared to be faint features between the (± 11) and $(\pm 1\bar{1})$ spots.

Four possibilities were considered to explain the faint satellite spots:

1) The presence of antiphase domains.
2) Multiple scattering from a reconstructed surface layer and the underlying bulk.
3) Oxygen (or other contaminants) on the surface below the detection limits of A.E.S.
4) Steps.

The first possibility may be discounted as there is splitting around the (00) spot which cannot be accounted by antiphase domains. The variation in the size of the splitting and the lack of compatability with the observed oxide excludes the second and third possibilities. Thus, as in the case of the Sn (001) surface, the satellite spots appear to be related to stepped structures. The main splitting of the spots into triplets along the [11] and $[1\bar{1}]$ directions is indicative of a two-layered surface structure (M. Henzler, 1977).

The aforementioned step structure does not explain the intensity variations observed in the L.E.E.D. patterns. The $(\pm hk)$ spots undergo maxima at one primary beam voltage whereas the $(\pm hk)$ spots undergo maxima at a different voltage (fig. 7.4). Two possibilities were considered to account for this:

Spot Index	Incidence angle/degrees	Position of maximum/volts
(00)	15	22.7 ± 0.5 78.4 ± 0.5 118.8 ± 0.7
(± 1 1)	0	29.1 ± 0.6 72 ± 1
(± 1 $\bar{1}$)	0	51.8 ± 0.5 88.5 ± 0.5
(20)	0	46.7 ± 0.7 79.9 ± 0.5
(02)	0	61.8 ± 0.2

FIG. 7.4 Positions of maximum intensity for the spots of the clean Sn(101) pattern.

a) either a monotonic step array was present along the $[10\bar{1}]$ direction with a constant step height, but random step width, as seen by M Henzler (1970) on an ion-bombarded GaAs surface; or

b) the surface layers, like those of the bulk, are displaced with respect to each other along the $[10\bar{1}]$ direction such that multiple scattering from the first few layers of the surface results in different positions of maxima for the $(\pm hk)$ and $(\pm h\bar{k})$ spots. The measured positions of maxima cannot be explained by the type of step structure considered in (a). Thus, multiple scattering seems a strong possibility to account for the intensity variations.

7.2 OXIDATION OF Sn(101)

(a) 135K and 293K

At room temperature (293K), and low temperature (135K), oxidation resulted in the disappearance of the L.E.E.D. patterns of the clean surface (fig. 7.5) leaving only a background intensity by 1000L (approximately corresponding to three quarters of the saturation levels of the corresponding uptake curves, figs. 5.16, 17). No further changes occurred on oxidation up to 5000L. Thus we may conclude that under these conditions an amorphous surface layer was formed.

(b) 393K

Oxidation at ∿ 393K, or annealing the room-temperature grown oxide to 393K led to the formation of an ordered surface layer which was observed by L.E.E.D. at 293K and 135K (figs. 7.6-9). The critical temperature for the formation of the ordered oxide lay between 383 - 393K.

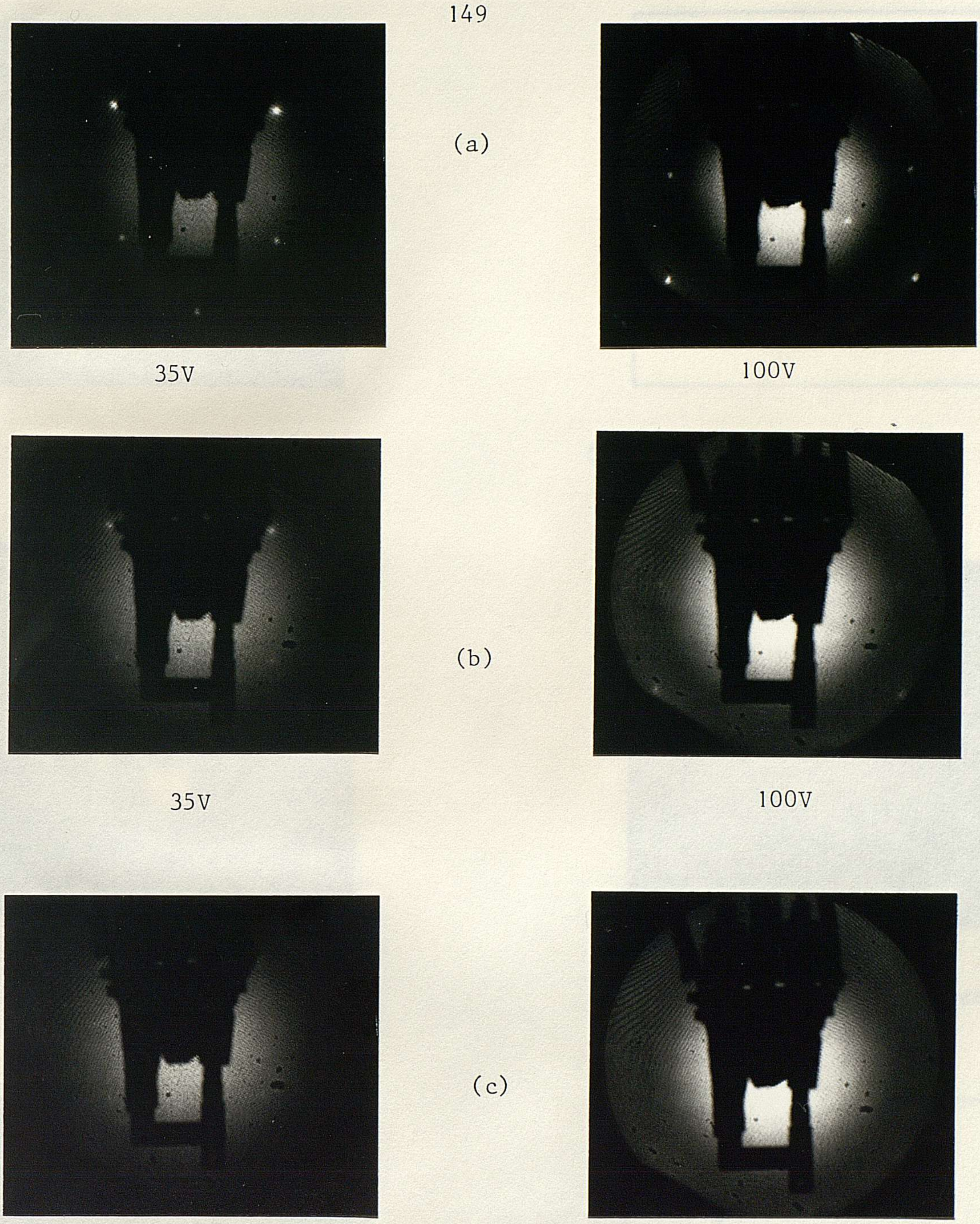

(a)

35V

100V

(b)

35V

100V

(c)

35V

100V

FIG. 7.5 Room temperature oxidation of Sn(101)
(a) clean surface, (b) after 500L, (c) after 1000L

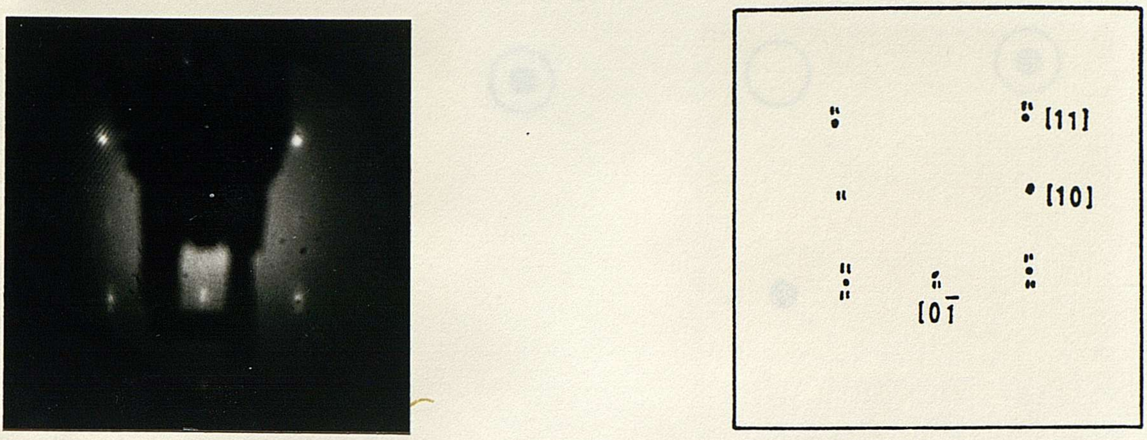

(a) 25V, normal incidence (b) 25V as (a)

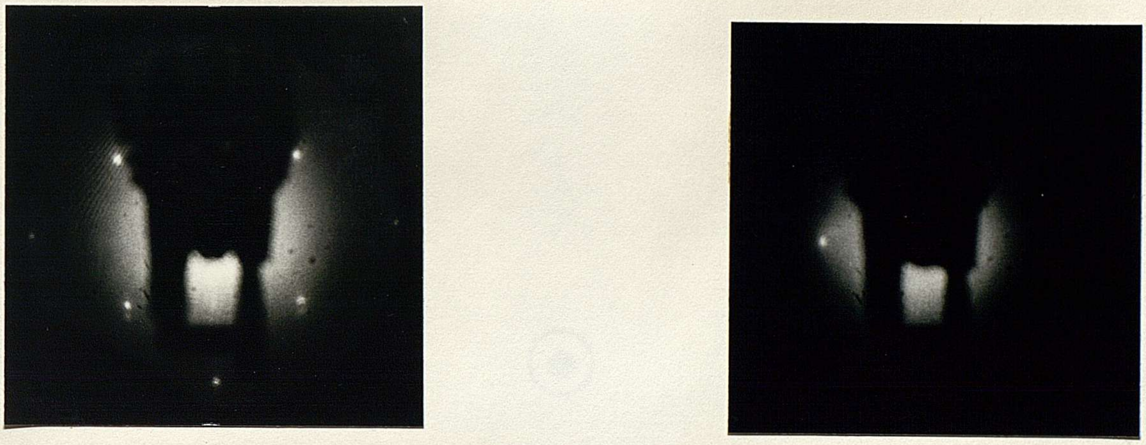

(c) 30V, normal incidence (d) 45V, (00) left of centre

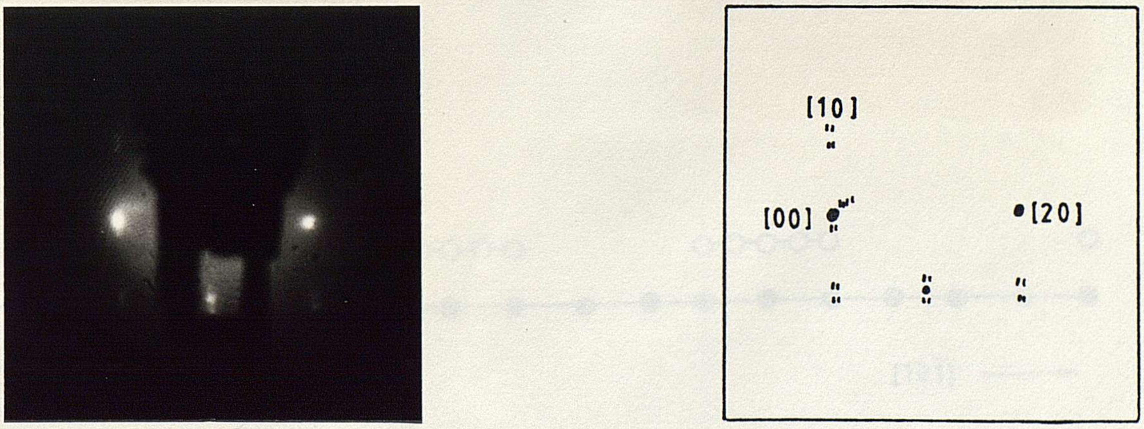

(e) 25V, 15° angle of incidence, (00) left of centre (f) 25V as (e)

FIG. 7.6 LEED of Sn(101) after 500L oxygen exposure at 390K. Photos taken at 130K

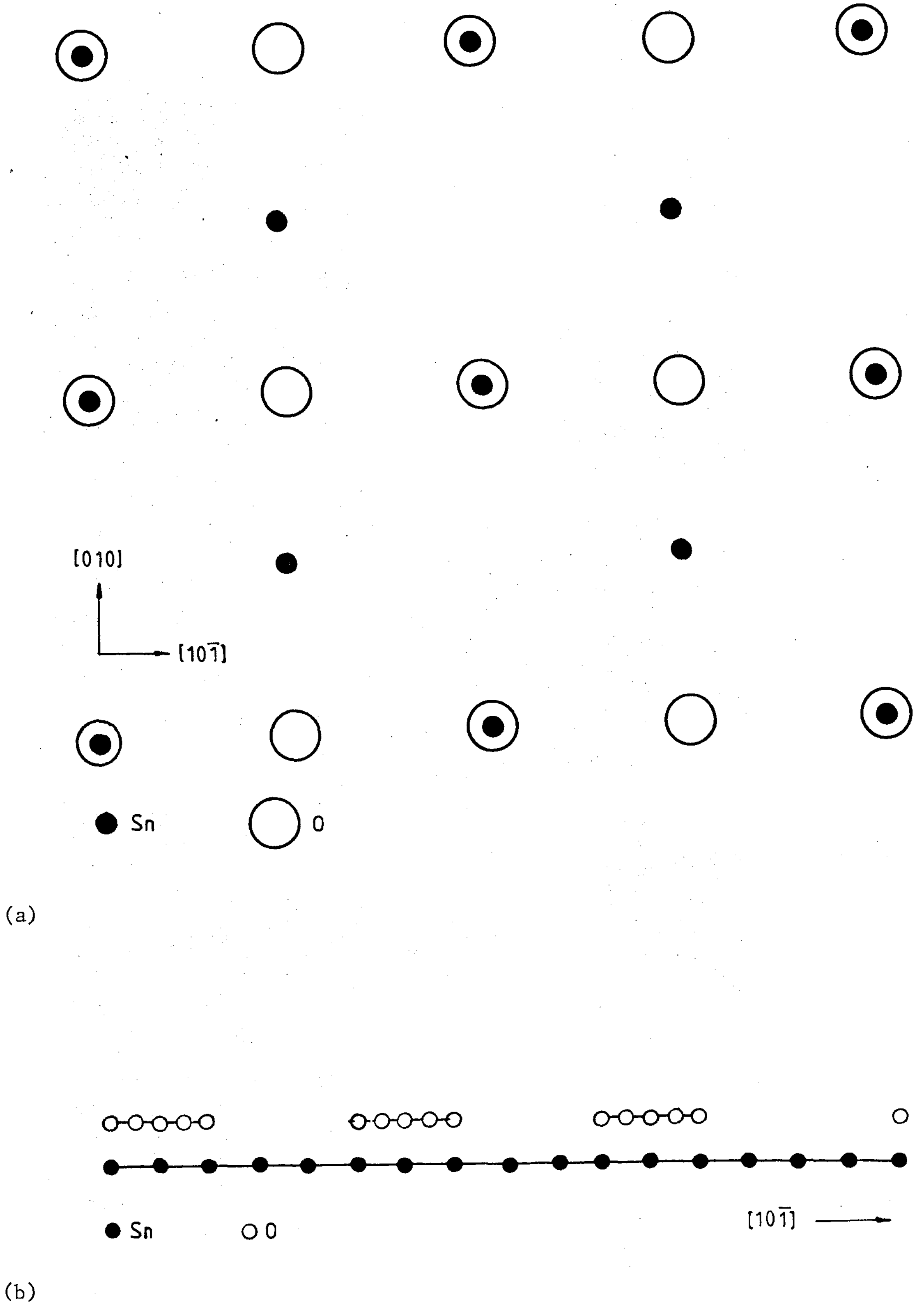

FIG. 7.7 Sn(101) p 1 x 2 - O structure formed after 500L oxygen exposure at 390K: (a) The Sn(101) plane; (b) Cross-section of the Sn(101) plane showing the two-layered structure formed. The relative positions of overlayer and substrate are shown as an example only.

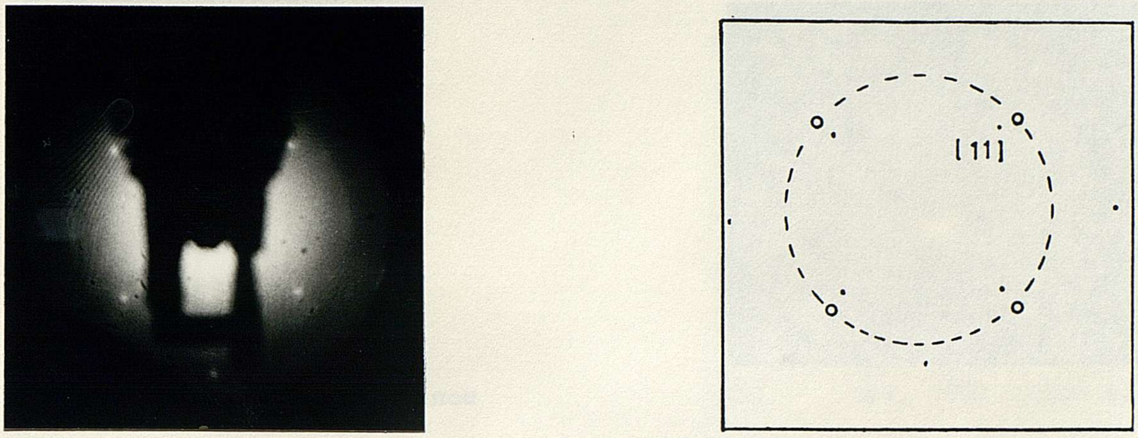

(a) 30V, normal incidence

(b) 30V, as (a)

(c) 35V, normal incidence

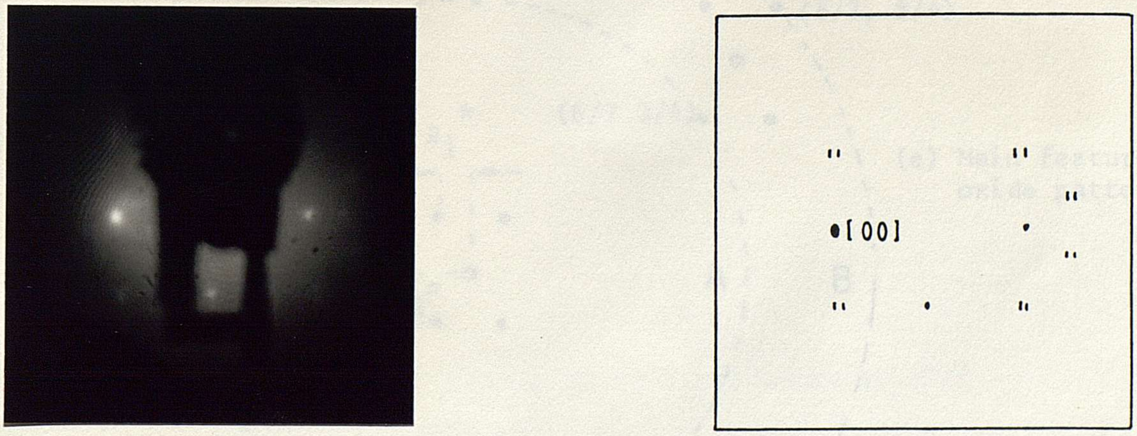

(d) 25V, 15° incidence angle

(e) 25V, as (d)

FIG. 7.8 LEED of S$_n$(101) after 1000L oxygen exposure at 390K. Photos taken at 130K.

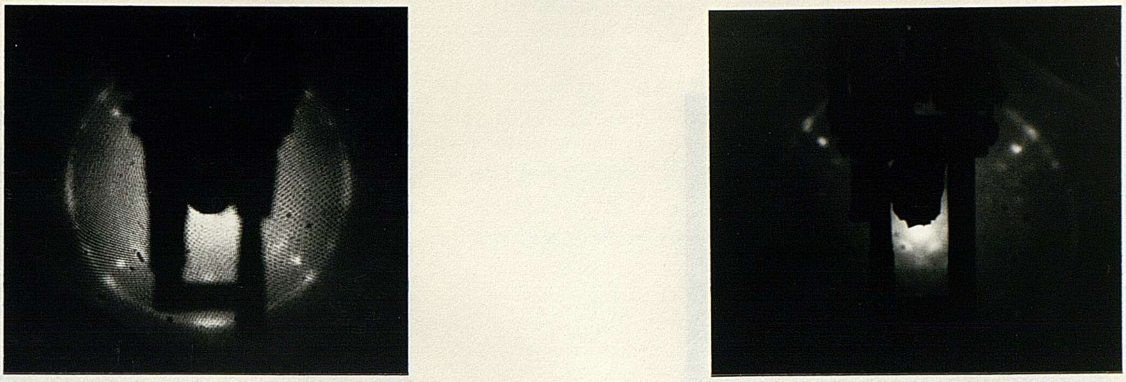

(a) 35V, normal incidence

(b) 30V, (00) below centre

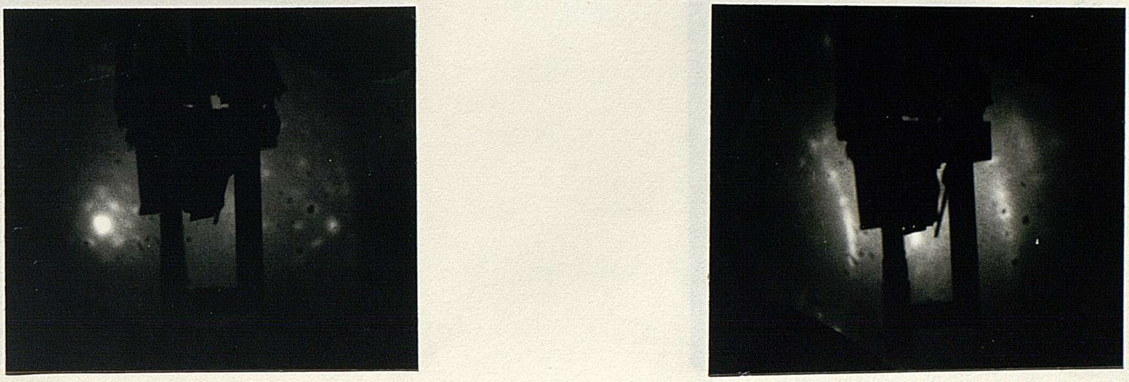

(c) 25V, (00) left of centre

(d) 30V, (00) far left off screen

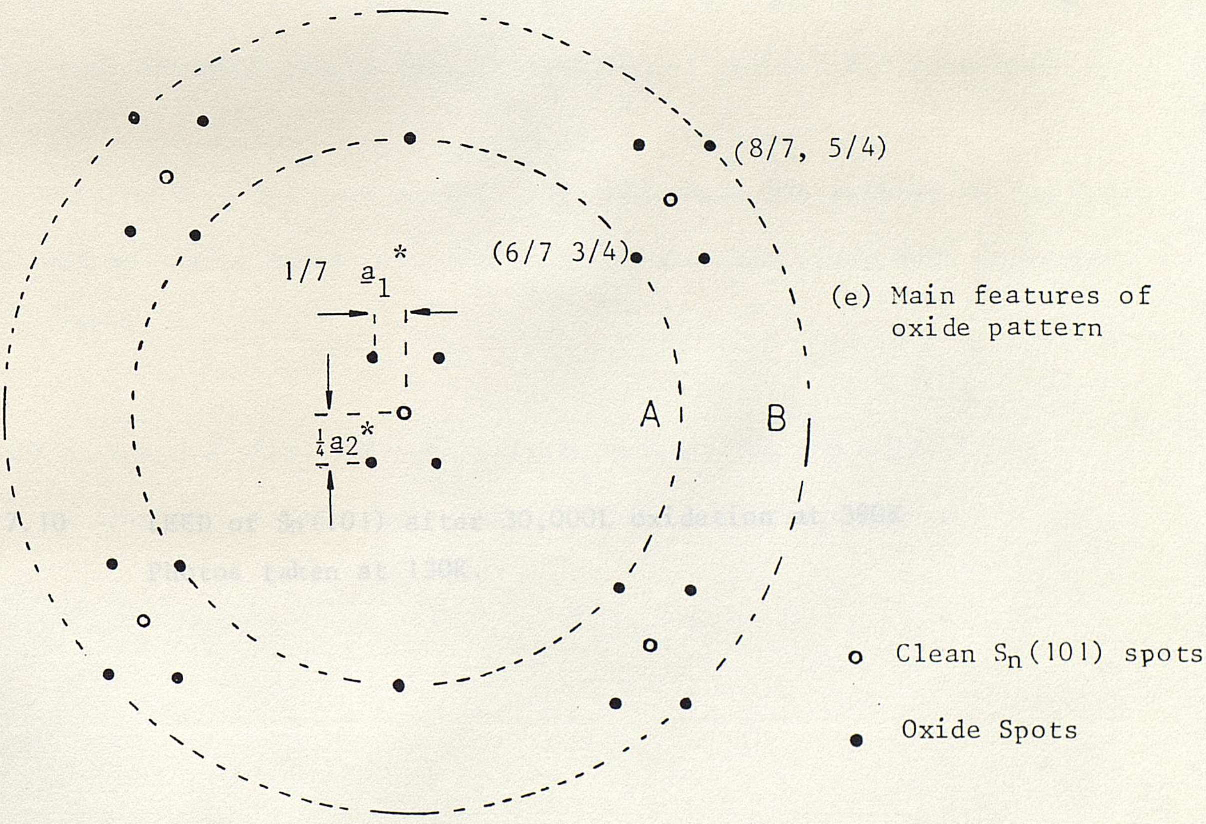

(e) Main features of oxide pattern

FIG. 7.9 LEED (at 130K) of Sn(101) after 4000L oxidation at 390K.

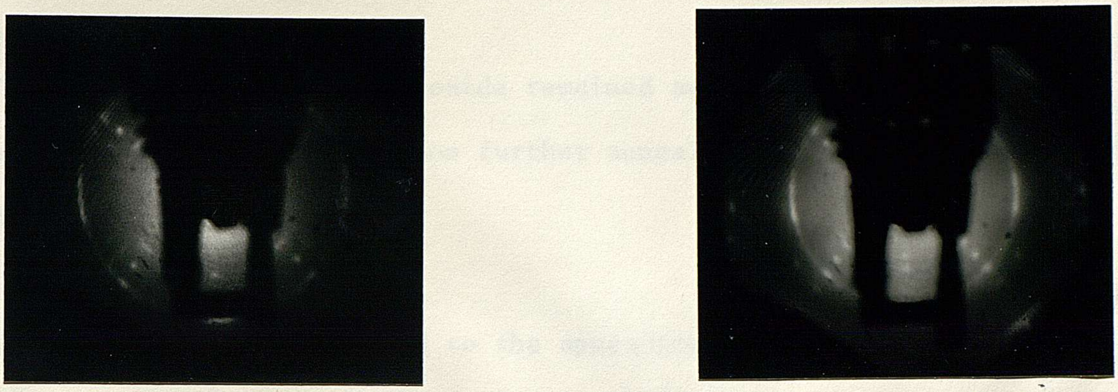

(a) 25V, normal incidence (b) 35V, normal incidence

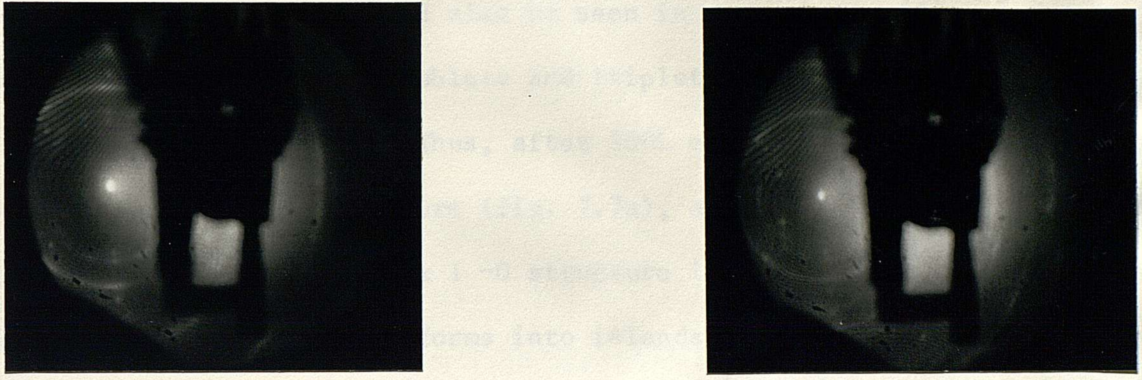

(c) 35V, (00) left of centre (d) 60V, (00) left of centre

FIG. 7.10 LEED of Sn(101) after 30,000L oxidation at 390K
Photos taken at 130K.

Below these temperatures the oxide remained amorphous. No changes were seen in the L.E.E.D. pattern on further annealing at 473K, or on further oxidation up to 30,000L.

Initial oxidation to 500L led to the appearance of spots corresponding to the missing (0 ± 1) reflections of the clean Sn(101) pattern (fig. 7.6). Very faint (± 10) spots could also be seen in some photos (fig. 7.6 a,b). The spots were split into doublets and triplets along the [01] direction of the reciprocal lattice. Thus, after 500L exposure Sn(101)p 1 x 2 -0 is the predominant oxide structure (fig. 7.7a), although the faint (± 10) spots suggest that the Sn(101) p1 x 1 -0 structure is also present. The splitting suggests that the overlayer forms into islands (M Henzler, 1977), there being steps between the islands and substrate along the [$10\bar{1}$] direction of the Sn(101) plane (7.7b). Although the oxygen atoms are shown above some of the tin atoms in fig. 7.7, it is not possible to determine the relative positions of the substrate and overlayer purely from observation of the L.E.E.D patterns.

By 1000L a faint ring and spot pattern appeared which was related to the 7 x 4 pattern seen at higher exposures. The pattern observed after 500L exposure was also present.

After 4000L exposure (fig. 7.9) the pattern seen at low exposures had been replaced by another ordered oxide pattern which contained three main features:

a) A spot pattern corresponding to the dimensions of the underlying tin substrate.

b) A spot pattern related to the oxide structure.

c) A ring pattern.

These patterns were observed up to 30,000L exposure (fig. 7.10).

The oxide pattern may be interpreted in terms of multiple scattering by both an overlayer and the underlying (101) plane of the tin substrate (E Bauer, 1967). Measurements from the oxidised tin patterns indicate that the reciprocal lattice vectors of the surface layer are given by

$$\begin{bmatrix} b_1^* \\ b_2^* \end{bmatrix} = \begin{bmatrix} 1/7 & 0 \\ 0 & \frac{1}{4} \end{bmatrix} \begin{bmatrix} a_1^* \\ a_2^* \end{bmatrix} \qquad (7.3)$$

Both the oxidised tin pattern and the clean Sn(101) pattern are centred-rectangular.

There are several possible explanations for the surface structure (figs. 7.11,12):

a) The oxidised surface could be considered to be a centred-rectangular superstructure of dimensions

$$\begin{bmatrix} b_1 \\ b_2 \end{bmatrix} = \begin{bmatrix} 7 & 0 \\ 0 & 4 \end{bmatrix} \begin{bmatrix} a_1 \\ a_2 \end{bmatrix}$$

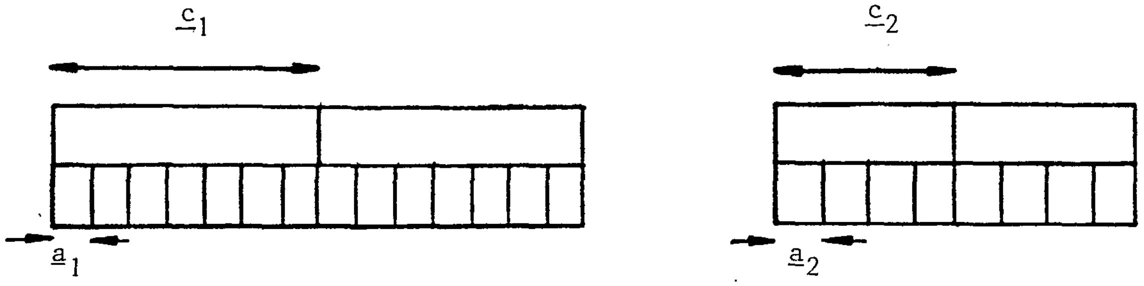

(a) Surface superstructure of dimensions $\underline{b}_1 = \underline{c}_1 = 7\underline{a}_1$, $\underline{b}_2 = \underline{c}_2 = 4\underline{a}_2$

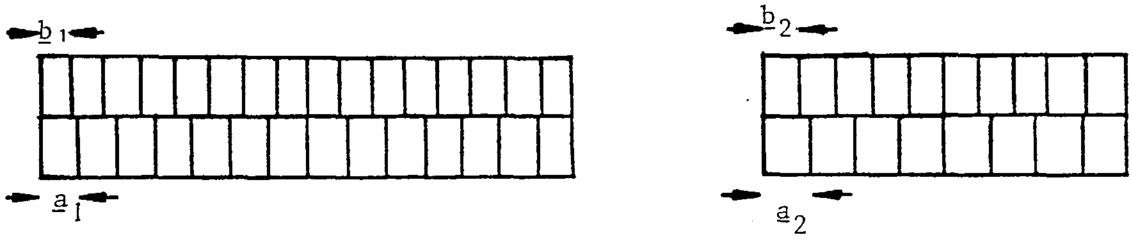

(b) Mismatch structure with $\underline{b}_1 = 7/8\ \underline{a}_1$, $\underline{b}_2 = 4/5\ \underline{a}_2$

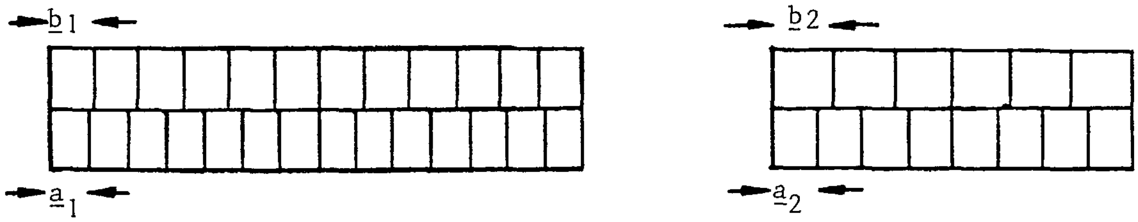

(c) Mismatch structure with $\underline{b}_1 = 7/6\ \underline{a}_1$, $\underline{b}_2 = 4/3\ \underline{a}_2$

FIG. 7.11 Possible structures for the formation of the 7 x 4 oxide pattern.

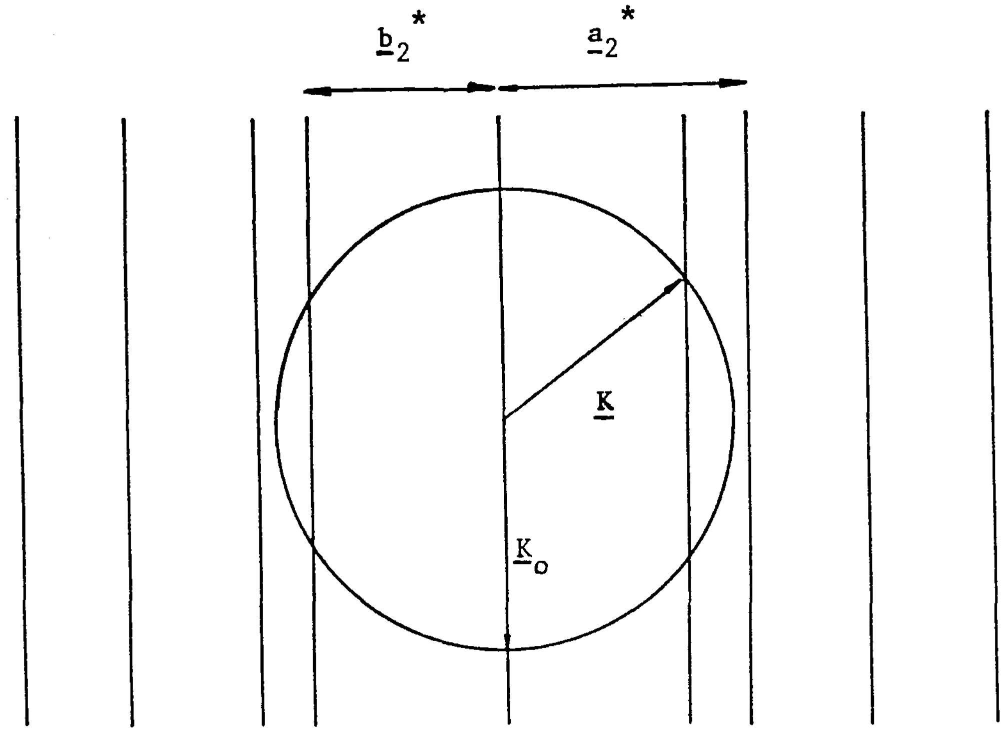

(a) Superposition of the reciprocal lattices of two different structures.

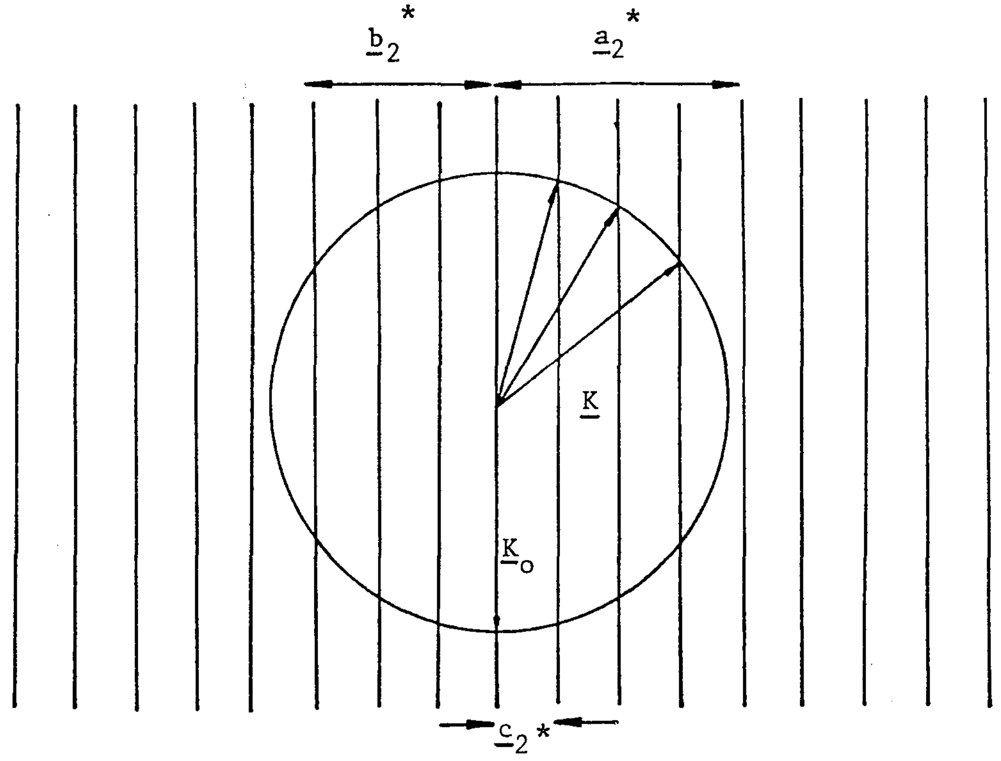

(b) Reciprocal lattice of two different structures.

FIG.7.12 (a) Superposition of reciprocal lattices of two different structures.

(b) Reciprocal lattice of two different structures ($4\underline{b} = 3\underline{a}$).

b) The surface layer could be considered to be mismatched with the tin substrate with, for instance

$$\begin{bmatrix} b_1 \\ b_2 \end{bmatrix} = \begin{bmatrix} 7/6 & 0 \\ 0 & 4/3 \end{bmatrix} \begin{bmatrix} a_1 \\ a_2 \end{bmatrix} \quad , \text{ or}$$

c) a mismatch structure with

$$\begin{bmatrix} b_1 \\ b_2 \end{bmatrix} \doteq \begin{bmatrix} 7/8 & 0 \\ 0 & 4/5 \end{bmatrix} \begin{bmatrix} a_1 \\ a_2 \end{bmatrix}$$

Combinations of these dimensions for $|\underline{b}_1|$ and $|\underline{b}_2|$ are also possible. In order to determine the correct structure solely from a spot pattern would require intensity analysis although the packing density of the oxygen atoms at low exposures makes case (a) seem unlikely.

The ringed pattern features a bright ring A (fig. 7.9) passing through the ($\pm$ 8/7 $\pm$ 5/4) spots; a faint ring B through the ($\pm$ 6/7 $\pm\frac{3}{4}$) spots; as well as many more rings. On ring A it was possible to distinguish more intense arcs at angles of $n\pi/4$ (n = 0 to 8) about the [01] axis of the reciprocal lattice. It would thus appear that the spot and ring patterns are related. As ring A is much more intense than ring B it would seem that the 7/8 x 4/5 mismatch structure is the correct structure to account for the patterns. In order to account for this structure from the ring pattern would require both the oxygen and underlying tin layers to form regions with rotational disorder during oxide growth.

7.3 SUMMARY

The clean Sn(101) surface formed a L.E.E.D pattern indicating that the surface had the dimensions of a bulk Sn(101) plane. Faint satellite spots were attributed to the presence of steps at the surface.

Below 383 - 393K oxidation resulted in the formation of an amorphous oxide. Above 383 - 393K two main structures were observed: below 1000L exposure an Sn(101) p 1 x 2 -O structure was present in the form of islands; and above 1000L an Sn(101)c 7/8 x 4/5 -O structure formed with rotational disorder.

CHAPTER 8

FURTHER DISCUSSION OF THE RESULTS

8.1 INTRODUCTION

The present study and that of G C Rider (1981) have together investigated the four lowest index single crystal surfaces of tin and their oxides. Summaries of the structures formed by the clean and oxidised surfaces have been presented in Figs. 8.1,2.

8.2 THE CLEAN Sn(001) SURFACE

The theoretical kinematic results for the Sn(001) surface models follow the trends predicted by M Henzler and H Wagner (See Section 3.4d) for the proporties of L.E.E.D. patterns from stepped surfaces. A single maximum would be expected for a particular reflection at positions of in-phase scattering from all the terraces of the surface, and multiple maxima would be expected at primary beam voltages intermediate between those required for in-phase scattering. In the present case the calculated intensity distribution curves do in fact show a single maximum for each of the {10} reflections at 35.5V, and the {11} reflections at 19.5V, these being the theoretical and experimental positions of in-phase scattering and single spots. At voltages intermediate between those for in-phase scattering the width of the splitting of the reflections increased as the terrace width increased.

Surface Plane	Study	Temperature	Structure
Sn(001)	W	115K - 473K	(001) terraces with steps along <01> directions
Sn(100)	R	200K - 473K	(100) planes with antiphase domains
Sn(101)	R	>270K <270K	(112) facets α-Sn(111) ($\sqrt{3} \times \sqrt{3}$)R30°
Sn(101)	W	135K - 473K	(101) planes with minor stepping
Sn (110)	R	>350K <350K	(110) planes (110) planes with antiphase domains. Domain boundaries were at 7° ± 2° to [110]
Foil	R	293K	Sn(001) ($\sqrt{2} \times \sqrt{2}$)R 45°

FIG. 8.1 Summary of the structures observed on low index single crystal surfaces and foil of tin. R denotes Rider's study, W the present study.

Surface plane	Study	Temperature	Oxide Structure
Sn(001)	W	130K - 473K	Amorphous
Sn(101) (facetted into (112) planes)	R	≈290K >400K	3.5Å x 4.0Å 4.8Å x 5.0Å
Sn(101)	W	>383K - 393K <383K - 393K	Amorphous Sn(101)
Sn(100)	R	≈290K ≥400K	Amorphous 4.8Å x 5.0Å
Sn(110)	R	≈290K ≥470K	3.5Å x 4.0Å 4.8Å x 5.0Å
Sn foil	R	≥290K	4.8Å x 5.0Å

FIG. 8.2 Summary of the oxide structures observed on the tin single crystal surfaces. R denotes Rider's study, W the present study.

This was expected following the arguments of section 3.4d, as was the increase in the width of the splitting the closer a particular reflection came to its position of antiphase scattering. It was not possible to distinguish separate maxima for split spots in the experimental patterns, and the lack of suitable intensity measuring apparatus made it impossible to compare the theoretical and experimental positions of intensity maxima for split spots.

The scanning electron micrographs of Fig. 4.9 indicated that extensive damage had been done to the (001) surface after argon ion bombardment. Terraced surfaces have been reported previously (M Henzler, 1970; G Schulze et al 1978) after argon ion bombardment and it seems likely that this was the cause of the terraced surface in the present case. Assuming this, it is likely that a range of terrace widths were in fact present on the surface, and that the average effects were measured.

M Henzler (1978) has investigated the effects of a distribution of terrace widths on the L.E.E.D. spot shapes produced by surfaces with one dimensional terraces. One model considered was a random mixture of equal numbers of terraces of two widths (5 and 8 atomic distances) with a step height of a random one atomic distance up or down. In the out-of-phase condition the splitting of the spot corresponded to a terrace width of 6.5 atomic distances (Fig. 8.3).

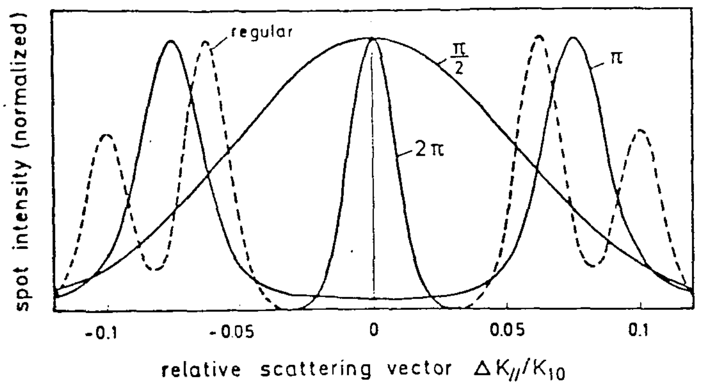

FIG. 8.3 Calculated spot shape for a random mixture of terraces of width 5 and 8 atomic distances for phase relationships of $\pi/2$, π, and 2π between terraces. Hatched curve denotes two regular arrays of these terraces (after Henzler, 1978).

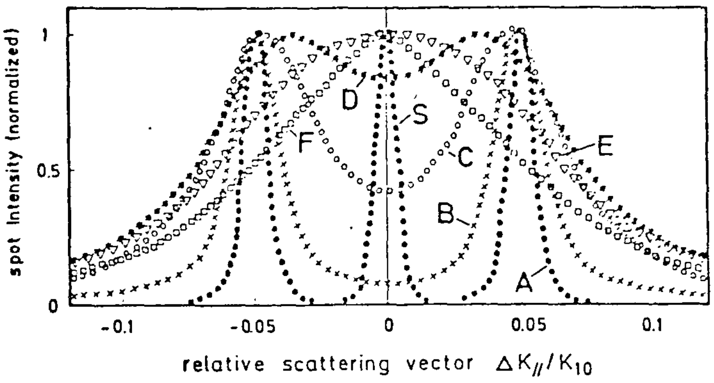

FIG. 8.4 Calculated spot shape for terrace width distributions with constant average terrace width 10 atomic distances. Letters refer to terrace width distributions in Fig. 8.5.

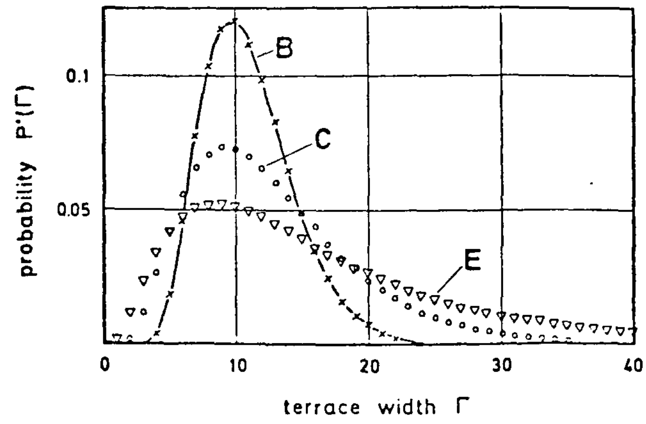

FIG. 8.5 Terrace width distributions for the calculations in Fig. 8.4.

The double spots were also broader than the single spot of in-phase scattering. For the case of two regular arrays of terraces of width 5 and 8 atomic distances, each array produced its own characteristic splitting of the spots. Random arrangements of terraces with constant average terrace width of 10 atomic distances, but different terrace width distributions were also considered (figs. 8.4,5). As the range of terrace widths considered was increased, the splitting of the spots became less well-defined, until for large distributions of terrace widths a broad single maximum was formed. Thus, in the present case, although the model with 3 atoms per terrace is the closest of the three considered to that of the real pattern, a wide range of terrace widths may be present at the surface. The presence of a range of terrace widths may explain some of the differences between the real patterns and the model patterns. The consideration of a distribution of terrace widths, and dynamical calculations may also lead to better agreement between theory and experiment at 35.5V. At this voltage the real pattern only shows single {10} spots although the theoretical patterns show split spots for other reflections with an intensity an order of magnitude less than that for the {10} spots.

A question unanswered by the techniques of the present study is why the step height was c/2 (i.e. 1.59Å), and the terrace separation a/2 (2.92Å). As the bonding in β-tin is mixed metallic/covalent one might have expected that the breaking of these bonds at the surface would have resulted in some relaxation. An understanding of the bonding at the surface may be gained by any future studies by high resolution electron energy loss spectroscopy.

8.3 THE DISAGREEMENT BETWEEN THE CLEAN Sn(101) SURFACE STRUCTURES

The discrepancy between the present L.E.E.D. results and those of G C Rider (1981) was mentioned in chapter 7. In the present study the L.E.E.D. patterns were from a surface composed of a bulk exposed (101) plane. Rider's surface was facetted into (112) planes after argon ion bombardment at room temperature. This structure underwent a reversible phase change on cooling below 290K to form a structure identified as α-Sn(111) in a $\sqrt{3} \times \sqrt{3})$ R 30° configuration. The facetting was considered to be an effect of the ion bombardment of the surface. The fact that only one of the two equivalent (112) planes formed facets was considered to be the result of the particular angle of the ion beam to the surface. As the (101) surface of the present study was bombarded under identical conditions, this explanation cannot be correct. Also, the use of an etch by Rider to remove the damaged layers after polishing does not appear to account for the surface formed as K Honda et al (1972) has shown that the etch removes (101) planes. Misorientation during preparation also seems unlikely as a vicinal stepped surface would have been expected. Thus the origin of the facetted surface is not clear.

8.4 THE OXIDES

The uptake curves for the oxidation of Sn(001) at 293K and 415K, and Sn(101) at 135K and 293K, indicated the formation of an ordered monolayer, there being little increase in oxidation beyond the formation of the monolayer.

Each of these curves levelled off at approximately the same value of O/Sn Auger peak height ratio. This was in agreement with the E.L.S. data, which indicated the same oxidation state for both surfaces. Excluding the (101) results, Rider's study also indicates that oxygen chemisorption to monolayer coverage took place on Sn(100) and Sn(101) at 290K and 450K, and on Sn(110) at 290K. AT 200K there was too much scatter in the results of the oxidation of Sn(100) for any conclusion to be made.

The ordered oxide structures formed on oxidation of Sn(101) were not related to the bulk order structures of SnO or SnO_2. The spot and ring patterns formed at post-monolayer coverage were related to each other. As the spot pattern was interpreted in terms of multiple scattering, the ring pattern was interpreted in terms of rotational disorder by both the oxygen layer, and an underlying layer of tin. Without access to techniques such as high resolution E.E.L.S., S.E.X.A.F.S., and X.A.N.E.S., no conclusions can be made as to the atomic arrangements corresponding to the ordered oxide structures of oxidised Sn(101).

The E.L.S. spectra of oxidised tin in the present study,and that of Rider, were identical for all the surfaces, even after structural changes. As the plasmon frequencies (and hence energies) are dependant on the electron density of the surface layers, the lack of change in the spectra does not indicate any changes in oxidation state or bonding accompanying these structural changes. All the E.L.S. spectra of the oxidised surfaces of both studies resembled the SnO spectrum of A J Bevolo et al (1982).

The 5eV $M_{4,5}$ $N_{4,5}$ $N_{4,5}$ Auger peak shifts measured on oxidising Sn(001) at 135K are more in agreement with the 5.5eV shifts noted by R A Powell (1979) for bulk oxides of SnO or SnO_2 than the 3 ± 1 eV for SnO and 7 ± 1 eV for SnO_2 measured by S K Sen et al (1981). The E.L.S. spectra of the present study did not indicate an intermediate oxidation state which might be suggested by Sen's values for the chemical shifts.

8.5 COMMENTS ON THE CLEAN TIN E.E.L.S. RESULTS

Most of the features of the clean tin loss spectrum are well understood as there have been many previous studies (see Chapter 2). The main discrepancy has been in the assignment of the loss at $\sim$ 5eV which has been detected in many of the studies. Initially P Bayat-Mokhtari et al (1979) considered the possibility that the loss was the result of a small amount of oxide remaining at the surface. Referring to that report, Rider also considered that possibility. It seems unlikely that this loss could be due to any hydrogen adsorbed on the surface as no detectable changes in the clean tin E.L.S. spectrum and L.E.E.D patterns were observed by Rider on surfaces exposed to hydrogen. As mentioned in Section 5.2, more recent studies have labelled this loss as a tin interband or intraband transition. This loss was always seen in the present study even after extensive argon ion bombardment. Thus the assignment of this peak to a tin transition seems the more likely explanation.

The loss spectra of the present study covered a larger energy range than previously reported. The loss seen at 50-60 eV on the clean tin spectrum, and previously unreported, has been assigned as either a double 4d interband transition or a multiple plasmon loss (or both).

CHAPTER 9

9.1 CONCLUSIONS

The (001) and (101) single crystal surfaces of tin have been studied under ultra-high vacuum conditions by low energy electron diffraction, Auger electron spectroscopy, and electron energy loss spectroscopy. Oxidation of the surfaces was undertaken at 5×10^{-7} torr at a number of temperatures.

The clean (001) surface exhibited a terraced structure. The surface consisted of terraces of the bulk (001) plane with steps of height 1.59Å both up and down along the [01] and [10] directions of the surface net. The structure was stable over the temperature range 115K to 473K. The terraced structure was predicted from kinematic theory by noting the conditions for which in-phase scattering (and thus single diffraction spots) occurred for each (hk) reflection. A model was devised for the surface based on the structural predictions of kinematic theory. The intensity distribution function was calculated at a number of primary beam voltages using this model and kinematic theory. Although this model correctly predicted the voltages at which single spots occurred, the limitations of kinematic theory for this surface were revealed by the lack of agreement between theory and experiment for the relative intensities of features in the diffraction patterns. Scanning electron micrographs of the (001) surface taken after the u.h.v. experiments indicated that extensive damage had been inflicted on the surface by argon ion bombardment.

The clean (101) surface was that of a bulk (101) plane. This structure was stable over the range 130 K to 473 K. Faint satellite spots in the electron diffraction patterns were attributed to minor stepping of the surface. Uptake curves obtained during the oxidation of the (001) and (101) surfaces at a number of temperatures indicated the formation of a single chemisorbed layer. The oxide monolayer at the (001) surface was amorphous over the temperature range 130K to 473K. An amorphous oxide was also formed on the (101) surface below 383 - 393K. Above these temperatures an Sn(101) p 1 x2 -0 oxide structure was formed at sub-monolayer exposures and an Sn(101) c 7/8 x 4/5 -0 oxide structure with rotational disorder was formed at higher exposures.

The E.L.S. spectra were identical for the oxidation of both the (001) and (101) surfaces at all temperatures considered. Comparisons with standard spectra revealed features in identical positions to those of the SnO spectrum.

Apart from the oxidation of Sn(001) at 135K, no shifts were observed in the tin Auger peaks. The shifts of 5eV in the main tin Auger transitions, and the disappearance of the clean tin bulk plasmon features during the oxidation of Sn(001) at 135K indicated the growth of a thick oxide layer at this temperature.

9.2 SUGGESTIONS FOR FURTHER WORK

There are several directions along which the u.h.v. studies on tin might proceed. One extension of the present study would be to evaporate tin onto an Sn(001) surface after ion bombardment in an attempt to obtain a surface without the terracing formed in the present study. Alternatively, ion bombardment of a freshly polished Sn(001) surface at lower beam energies may lead to a surface with less damage. It would also be worth repeating the study by Rider on the (110) surface as the phase transition observed on cooling the crystal below ∿ 350K was suggested to have been caused by slight misalignment of the surface during sample preparation. In both the present and Rider's study much reliance was placed on the use of the E.L.S. technique on characterising the surface oxides, in particular for the case of the amorphous oxides. Valence band X.P.S. studies in conjunction with A.E.S., E.L.S., and L.E.E.D. might be useful in confirming some of these conclusions. The study of work function changes during oxidation would also be useful, in particular for the (100) and (110) surfaces for which metal rich surfaces has been suggested under certain oxidation conditions by Rider, and Lin et al (1977). The use of high resolution EELS, EXAFS, and XANES would lead to a better understanding of the local atomic arrangements of the surface oxides.

The present study, and that of Rider, has concentrated on the initial stages of oxidation. Oxidation at higher pressures for longer exposures might be attempted to investigate any changes in the grown oxides. As there is disagreement in the size of the tin Auger shifts of stannous oxide (SnO) and stannic oxide (SnO_2), any further studies should consider making these measurements as they may be required for comparison with any Auger shifts obtained.

Extending the present study to the adsorption of sulphur, selenium, and the halogens, should be straightforward using molecular beams of the type used by e.g. W Heegemann et al (1975) and J S Foord et al (1982). Electronically interesting materials such as the substrate-stabilised single crystal α-tin films developed by R F C Farrel et al, and single crystals of stannic oxide (SnO_2) may also be considered to be worth further investigation.

REFERENCES

AMENT M. A. E. A., and de VROOMEN A. R.
Journal of Physics F, 4, 1359, 1974.

ANDERSON S. K., and HOWIE A.
Surface Science, 50, 197, 1975.

BARLOW S. M., BAYAT-MOKHTARI B., and GALLON T. E.
Journal of Physics C, 12 5577, 1979.

BAUER E.
Surface Science, 7, 351, 1967.

BAYAT-MOKHTARI P., BARLOW S. M., and GALLON T. E.
Surface Science 83, 131, 1979.

BEVOLO A. J., VERHOEVEN J. D., AND NOACK M.
Journal of Vacuum Science and Technology, 20, 943, 1982.

BIBERIAN J. P., AND SOMORJAI G. A.
Applications of Surface Science, 2, 352, 1979.

BIRD R. J.
Metal Science, 7, 109, 1973.

BRUNDLE C. R., AND BAKER A. D.
Electron Spectroscopy vol. 1, Academic Press, 1977.

CASTELIJNS J. H. P., van de BRUGH H. W. J. M., and de VROOMEN A. R.
Journal of Physics F, 7, 2457, 1977.

CHELIKOWSKY J. R., and COHEN M. L.
Physical Review B, 14, 556, 1976.

CHRISTMANN K., and ERTL G.
Surface Science, 33, 254, 1972.

CHUNG M. F., and JENKINS L. H.
Surface Science 22, 479, 1970.

CRAVEN J. E.
Physical Review, 182, 693, 1969.

CULLIS A. G.
Institute of Physics Conference Series No. 61, 535, 1982.

DABBS J. E.
Ph.D. Thesis, University of Southampton, 1973.

DARKEN L. S., and GURRY R. W.
Physical Chemistry of Metals, McGraw-Hill, 1953.

DAVISSON C. J., and GERMER L. H.
Physical Review, 30, 705, 1927.

de FRÉSART E., DARVILLE J., and GILLES J. M.
Solid State Communications, 37, 13, 1980.

de FRÉSART E., DARVILLE J., and GILLES J. M.
Applications of Surface Science, 11, 637, 1982.

de FRÉSART E., DARVILLE J., and GILLES J. M.
Surface Science 126, 518, 1983.

ELLIS W. P., and SCHWOEBEL R. L.
Surface Science 11, 82, 1968.

FARREL R. F. C., ROBERTSON, D. S., WILLIAMS G. M., CULLIS A. G., JONES G. R., YOUNG I.M., and DENNIS P. W. J.
Journal of Crystal Growth, 54, 507, 1981.

FARRELL T.
Metal Science, 10, 87, 1976.

FOORD J. S., and LAMBERT R. M.
Surface Science, 115, 141, 1982.

GALLON T. E.
Surface Science, 17, 486, 1969.

GROVES S., and PAUL W.
Physical Review Letters, 11, 194, 1963.

GOBBY P. L., and LAPEGUE G. J.
Proceedings of the 13th International Conference of Semiconductors, North-Holland Press, 1976.

GOBBY P. L.
Ph.D. Thesis, Montana State University, 1977.

HALL E. O.
The Mechanism of Phase Transformations in Metals, I.O.M. 1956.

HARRIS L. A.
Surface Science, 15, 77, 1969.

HARRIS L. A.
Surface Science, 17, 448, 1969.

HEEGEMANN W., MEISTER K. H., BECHTOLD E., and HAYEK, K.
Surface Science, 49, 161, 1975.

HENZLER M.
Surface Science, 22, 12, 1970.

HENZLER M.
Applied Physics, 9, 11, 1976.

HENZLER M.
Electron Diffraction and Surface Defect Structure; in
Electron Spectroscopy for Surface Analysis, Springer-Verlag, 1977.

HENZLER M.
Surface Science, 73, 240, 1978.

HERMAN F.
Journal of Electronics, 1, 103, 1955

HÖCHST H., HÜFNER S., and GOLDMANN A.
Solid State Communications, 19, 899, 1976.

HÖCHST H., and HERNANDEZ-CALDERON I
Surface Science, 126, 25, 1983.

HONDA K., and HIROKAWA T
Japanese Journal of Applied Physics, 11, 1763, 1972.

HOPKINS G. P.
Ph.D. Thesis, University of Southampton, 1976.

IHM J., and COHEN M. L.
Physical Review B, 23, 1576, 1981.

JACKSON D. C., GALLON T. E., and CHAMBERS A.
Surface Science 36, 381, 1973.

JAMIESON J. C.
Science, 139, 762, 1963.

JARZEBSKI Z., and MARTON J. P.
Journal of the Electrochemical Society, 123, 199C, 1976.

JARZEBSKI Z., and MARTON J. P.
Journal of the Electrochemical Soceity, 123, 299C, 1976.

JARZEBSKI Z., and MARTON J. P.
Journal of the Electrochemical Society, 123 , 333C, 1976.

JEAN Y. C., LYNN K. G., and CARROL M.
Physical Review B, 21 4935, 1980.

LAU C. L., and WERTHEIM G. K.
Journal of Vacuum Science and Technology, 15, 622, 1978.

LIN A. W. C., ARMSTRONG N. R., and KUWANA T.
Analytical Chemistry, 49, 1228, 1977.

LIU L., and BASSANI F.
Bulletin of the American Physical Society, 8, 51, 1963.

MACRAE R. A., ARAKAWA E. T., and WILLIAMS M. W.
Physical Review, 162, 615, 1967.

MICHEL R., GASTALDI J., ALLASIA C., JOURDAN C., and DERRIEN J.
Surface Science, 95, 309, 1980.

MORGAN W. E., and VANWAZER J. R.
Journal of Physical Chemistry, 77, 964, 1973.

NATHAN R., and HOPKINS B. J.
Journal of Physics E, 6, 1040, 1973.

PARRY-JONES A. C., WEIGHTMAN P., and ANDREWS P. T.
Journal of Physics C, 12, 1587, 1979.

PENDRY J. B.
Low Energy Electron Diffraction, Academic Press 1974.

PESSA M., VUORISTO A., VULLI M., AKSELA S., VÄYRYNEN J., RANTALA T., and AKSELA H.
Physical Review B, 20, 3115, 1979

POLLAK, R. A., LEY L., MCFEELY F. R., KOWALCZYK, S. P., and SHIRLEY, D. A.
Journal of Electron Spectroscopy and Related Phenomena, 3, 381, 1974.

POWELL C. J.
Proceedings of the Physical Society, 76, 593, 1960.

POWELL C. J.
Surface Science, 44, 29, 1974.

POWELL R. A., and SPICER W. E.
Surface Science, 55, 681, 1976.

POWELL R. A.
Applications of Surface Science, 2, 397, 1979.

POWELL R. A.
Applications of Surface Science, 2, 439, 1979.

RASIGNI G., CODACVIONI J. P., MICHAUD-BONNET J., ABBA F., and PETRAKIAN J. P.
Comptes Rendus Hebdomadaires des Seances de l'Academie des Sciences, B262, 772, 1966.

RAWLINGS K. J., and DOBSON P. J.
Chemical Physics Letters, 37, 353, 1976.

RHEAD G. E., BARTHÈS M. G., and ARGILE C.
Thin Solid Films, 82, 201, 1981.

RIDER G. C.
Ph.D. Thesis, University of Southampton, 1981.

RUSCH T. W., BERTINO J. P., and ELLIS W. P.
Applied Physics Letters, 23, 359, 1973.

SCHULZE G., and Henzler M.
Surface Science, 73, 533, 1978.

SEAH M. P.
Surface Science, 32, 703, 1972.

SEN P., HEGDE M. S., and RAO C. N. R.
Applications of Surface Science, 10, 63, 1982.

SEN S. K., SEN S., and BAUER C. L.
Thin Solid Films, 82, 157, 1981.

SEXTON B. A.
Applied Physics A, 26, 1, 1981.

TAYLOR N. J.
Review of Scientific Instruments, 40, 792, 1969.

WAGNER C. D., and Biloen p.
Surface Science, 35, 82, 1973.

WAGNER H.
Physical and Chemical Properties of Stepped Surfaces; in Solid Surface Physics, Springer-Verlag, 1979.

WATTS G. D.
Ph.D. Thesis, University of Southampton, 1974.

WEBER R. E., and PERIA W. T.
Journal of Applied Physics, 38, 4355, 1967.

WEISZ G.
Physical Review, 149, 504, 1966.

WYCKOFF R. W. G.
Crystal Structures, Interscience, 1960.

ACKNOWLEDGEMENTS

I wish to thank the members of the Surface Physics group for their advice and encouragement during the completion of this work.

I would like to thank my supervisor, Dr B J Hopkins for his advice and comments during the writing of this thesis.

I would also like to thank Sylvia and Richard Croxall for devising the computer program for my Sn(001) surface model, and Gavin Rider for explaining the use of the apparatus.

I am grateful for the technical support of Joe Lawrenson and Dave Smith.

I acknowledge the financial support of the Science and Engineering Research Council.

Finally, I wish to thank Diana Bearsford-Walker for patiently typing this thesis.

SOUTHAMPTON UNIVERSITY LIBRARY

USER'S DECLARATION

AUTHOR: WOODS, M.E. TITLE: The characterisation of clean and oxidised tin single crystal surfaces DATE: 1984

I undertake not to reproduce this thesis, or any substantial portion of it, or to quote extensively from it without first obtaining the permission, in writing, of the Librarian of the University of Southampton.

To be signed by each user of this thesis

DATE	SIGNATURE	ADDRESS